Oil & Natural Gas Technology

DOE Award No.: DE-FC26-04NT15532

Final Report

Improving Gas Flooding Efficiency

Submitted by:
New Mexico Petroleum Recovery Research Center
New Mexico Institute of Mining and Technology
801 Leroy Place
Socorro, NM 87801
(505) 835-5142

Prepared for:
United States Department of Energy
National Energy Technology Laboratory

August 11, 2008

Office of Fossil Energy

IMPROVING GAS FLOODING EFFICIENCY
FINAL REPORT

DOE CONTRACT NO. DE-FG26-04NT15532

New Mexico Petroleum Recovery Research Center
New Mexico Institute of Mining and Technology
801 Leroy Place
Socorro, NM 87801
(505) 835-5142

Report Date:	**July 15, 2008**
Contract Date:	**April 1, 2005**
Completion Date (revised):	**March 31, 2008**
DOE Total Award:	**~$800,000**
Program Manager:	**Reid B. Grigg**
Principal Investigator:	**Reid B. Grigg**
Other Major Contributors:	**Robert K. Svec**
	Zheng Wen Zeng
	Alexander Mikhalin
	Yi Liu
	Guoqiang Yin
	Solomon Ampir
	Rashid Kassim
Contracting Officer's Representative:	**Chandra Nautiyal**
Reporting Period:	**April 1, 2005–March 31, 2008**

DISCLAIMER

ABSTRACT

This document is the Final Report for the project, "Improved Gas Flooding Efficiency," Department of Energy Contract No. DE-FC26-04NT15532. This study focuses on laboratory studies with related analytical and numerical models, as well as work with operators for field tests to enhance our understanding of and capabilities for more efficient enhanced oil recovery (EOR).

Much of the work has been performed at reservoir conditions. This includes a bubble chamber and several core flood apparatus developed or modified to measure interfacial tension (IFT), critical micelle concentration (CMC), foam durability, surfactant sorption at reservoir conditions, and pressure and temperature effects on foam systems.

Carbon dioxide and N_2 systems have been considered, under both miscible and immiscible conditions. The injection of CO_2 into brine-saturated sandstone and carbonate core results in brine saturation reduction in the range of 62 to 82% brine in the tests presented in this paper. In each test, over 90% of the reduction occurred with less than 0.5 PV of CO_2 injected, with very little additional brine production after 0.5 PV of CO_2 injected.

Adsorption of all considered surfactant is a significant problem. Most of the effect is reversible, but the amount required for foaming is large in terms of volume and cost for all considered surfactants. Some foams increase resistance to the value beyond what is practical in the reservoir. Sandstone, limestone, and dolomite core samples were tested.

Dissolution of reservoir rock and/or cement, especially carbonates, under acid conditions of CO_2 injection is a potential problem in CO_2 injection into geological formations. Another potential change in reservoir injectivity and productivity will be the precipitation of dissolved carbonates as the brine flows and pressure decreases.

The results of this report provide methods for determining surfactant sorption and can be used to aid in the determination of surfactant requirements for reservoir use in a CO_2-foam flood for mobility control. It also provides data to be used to determine rock permeability changes during CO_2 flooding due to saturation changes, dissolution, and precipitation.

TABLE OF CONTENTS

LIST OF TABLES

LIST OF FIGURES

NOMENCLATURE

A = cross-sectional area of the core [cm^2]

Ads = CD adsorption density, mg surfactant/g rock

Ads_i = adsorption density after i-number of measurements, mg/g

A_i = surfactant in the rock and tubing at the i^{th} step, mg

B = Formation volume factor (L3/L3),

BR = Brine

BPR = Back Pressure Regulator

C = Compressibility (LT^2/M)

C_i and C_r = initial and residual CD concentration in solution, ppm

C/C_i = normalized concentration, fraction

C_0 = initial surfactant concentration of desorption, mg/l

CD = Chaser CD 1045™ Surfactant

CLS = calcium lignosulfonate

CMC = Critical Micelle Concentration

CO_2 = carbon dioxide

Cr_i = residual concentration after i measurements, ppm

CSG = co-injection of water and gas

CWG = co-injection of water and gas

Cc = cubic centimeter

CW = distilled water

D = Rate-dependent skin coefficient (T/L3)

dp = pressure drop [psi]

dp/ds = pressure gradient [psi/cm]

dp/dx = Pressure gradient ($ML^{-2}T^{-2}$)E = non-Darcy effect

-dp/dl = pressure gradient, psi/cm

F = Non-Darcy flow factor

Fo = Forchheimer number

f_g = gas fractional flow, fraction

f_g* = critical gas fractional flow, fraction

f = simplex function, mg/g

h = Layer thickness (L)

i = index

ID =inside diameter

IFT = interfacial tension [mN/m]

j = index

K or k = permeability [md]

k_r = Relative permeability

k_{a1} = pseudo 1st order adsorption kinetic coefficient, h^{-1}

k_{a2} = pseudo 2nd order adsorption kinetic coefficient, g/(mg •h)

k_{d1} = pseudo-first order desorption kinetic coefficient, h^{-1}

k_{d2} = pseudo-second order desorption kinetic coefficient, g/(mg •h)

L or l = sample length, cm

LS = limestone

M = molecular weight, g/mole

M = total number of measurements

M_i = surfactant left in pore and tubing at the i^{th} step, mg

Ms = mass of the solution, g

Mc = mass of the core sample, g

MMP = minimum miscibility pressure

Mt = total initial mass of surfactant in the system, mg

Ms = total initial mass of surfactant solution, g

n = number of simplex variables

N = total steps of measurements at present

N_2 = nitrogen

OD = outside diameter

p, p_b, p_w = Pressure, pressure of well block, bottom hole flowing pressure ($ML^{-1}T^{-2}$)

P = bottom hole pressure, psig

P_c = capillary pressure

P_c* = limiting capillary pressure

P_{in} = core inlet pressure [psig]

P_{out} = core outlet pressure [psig]

PV = pore volume, fraction

Q = volume flow rate, cc/hr

q = Volumetric flow rate (L^3/T)

q = *flow rate, cm^3/sec*

q = surfactant adsorption density, mg/g

q_g = gas flow rate [cc/hr or sec]

q_t = total flow rate [cc/hr or sec]

q_l = liquid flow rate [cc/hr or sec]

q_0 = initial adsorption density in desorption process, mg/g

q_{cj} =calculated adsorption density from models, mg/g

q_e = adsorption density at equilibrium, mg/g

q_i = surfactant adsorption density at the i^{th} step, mg/g

q_r = residual adsorption density in desorption process, mg/g

q_{tj} = measured adsorption density in experiments, mg/g

R = universal gas constant, 82.06 atm-cm^3/g-mole-K

R^2 = correlation coefficient

r_o, r_w = Equivalent radius of well block, wellbore radius (L)

s_k = stress sensitivity of permeability, mD/psi

s_β = stress sensitivity of non-Darcy coefficient, 10^6 1/cm/psi

SAG = surfactant solution alternating with gas

SS = sandstone

S_w = liquid saturation

T or t = time, h

V = superficial fluid velocity, cm/s or ft/d

Ve_i = effluent volume at the i^{th} step, l

V_i = total surfactant solution volume at the i^{th} step, l

W = mass flow rate, g/s

W = mass of the rock specimen, g

WAG = water alternating with gas

x, X = simplex variable

X, x = dummy variables

Y, y = dummy variables

z = compressibility factor

Greek Symbols

ρ = fluid densities [g/cm^3]

λ = simplex contracting coefficient, $0.0<\lambda<1.0$

μ = simplex expanding coefficient, $1.2<\mu<2$

u_g = *gas Darcy velocity, cm/sec*

u_w = *aqueous Darcy velocity, cm/sec*

λ_g = *gas mobility, md/cp*Nomenclature

s = Mechanical skin

β = Non-Darcy coefficient (L^{-1})

μ = Viscosity

ρ = Density

φ = *Porosity*

u_g = gas darcy velocity [cm/sec]

u_w = aqueous darcy velocity [cm/sec]

$\Sigma\{m_{si}\}$= sum of surfactant mass removed during sampling, mg

$\Sigma\{m_{li}\}$= sum of surfactant solution mass removed during sampling, g

Δ = relative change

σ = normal stress, psi

τ = octahedral shear stress, psi

Subscripts

0 = unconfined

1 = inlet

= maximum (principal stress)

2 = outlet

= intermediate (principal stress)

3 = minimum (principal stress)

100 = temperature of 100ºF

150 = temperature of 150ºF

200 = temperature of 200ºF

500 = pore pressure of 500 psi

1500 = pore pressure of 1500 psi

a = axial (stress)

c = critical

= compositional (phase sensitivity)

CO2 = CO_2

eff = octahedral effective (stress)

N2 = N_2

p = physical (phase sensitivity)

r = radial (stress)

INTRODUCTION

The objectives of this study were to acquire the information required to develop adsorption/desorption models for reservoir rock at reservoir conditions, to determine economic sweep efficiency/injectivity criteria for reservoir scale systems, to expand foam gas flooding to shallow reservoirs, and to develop models and modules for simulating CO_2 flooding mechanisms. This work devoted considerable energy to laboratory measurements to determine practical information for designing gas injection systems for a wide range of reservoir types; thus, through cost-effective and environmentally attractive means, adding to recoverable oil reserves in the US.

Expected Improvements over Existing Technologies: Despite favorable features of CO_2 flooding for EOR,[1] CO_2 flooding frequently suffers from poor sweep efficiency, high CO_2 utilization rate, the high cost of handling and recycling produced CO_2, low oil productivity due to lower-than-expected injectivity, and limited application in reservoirs that cannot be operated at pressures at or above the MMP.[2]

Poor sweep efficiency and high CO_2 utilization rate result from a high mobility ratio caused by the low viscosity of CO_2 compared to that of water or oil. The effectiveness of WAG for mobility control during CO_2 flooding is adversely influenced by gravity segregation between water and CO_2, and amplified by permeability contrasts. Foaming agents injected in the aqueous phase help control mobility. However, increased costs due to the adsorption of expensive chemicals onto reservoir rocks has limited the application of this technique. Foam quality, temperature, pressure, CO_2 injection rate and total injected volume each affects the ultimate oil recovery.[3-5] It is, therefore, advantageous to develop systems with lower concentrations of good foaming agents that will reduce the cost of using these agents. These systems are derived using a sacrificial agent; that is, a co-surfactant that reduce adsorption loss and/or concentration of the good foaming agent without reducing the effectiveness of the foam. In core tests the system of CD1045 with lignosulfonate reduces the pressure drop (increases the injectivity) while maintaining equally good sweep efficiency.[3,6,7] The combination of these two agents in small core tests appears to indicate that they could be tailored to vary injectivity, sweep efficiency, and sensitivity to oil saturation.[3,6]

To aid in predicting utilization of surfactant adsorption on pure minerals (silica, calcite, dolomite, kaolinite, and bentonite) that are common reservoir rock components, studies were performed to determine surfactant adsorption and desorption quantities, rates, mechanisms, and effects of physical parameters such as temperature, pressure, brine and surfactant composition and concentration, and pH on various rock components.[7-11] Work in this area will continue, particularly in determining adsorption values versus specific surface areas of the mineral to determine sweep efficiency in a homogeneous system. These results are required to develop models to be used in numerical simulation to predict usage in a reservoir.

WAG often reduces injectivity more than expected and the addition of mobility control agents inherently increases the severity of this problem. Any resistance increases the pressure drop, and therefore decreases injectivity.[3,13] Improved mobility control will reduce injectivity; thus, for this purpose, it is critical that the two be optimized. Causes of injectivity reduction that have been identified in ascending order of severity and amenability to remediation are: contamination, gas saturation, dissolution, and precipitation.[6,7]

Scientific and Technical Basis and Merit: Previous laboratory and field tests have confirmed the effectiveness of CO_2-foam for mobility control and fluid diversion. Areas of progress in the past include:

- Identification of foam strength in high pressure CO_2 systems,[7,14]
- Identification of properties that affect foaming agent adsorption in a porous medium: rock type,[16] surfactant type,[14] surfactant concentration,[14] and co-surfactants,[7,15]
- Identification of co-surfactants and sacrificial agents,[3,7,16]
- Effects of heterogeneity with and without capillary contact,[17]
- Identification of a number of systems with varying degrees of selective mobility reduction,[17]
- Development of models to predict reservoir response to the identified foam systems, and
- Several successful field tests.[3,7,17-27]

Benefits: Project results benefit the future of gas injection EOR. Parameters were be determined that result in improved sweep efficiency with better understanding of injectivity changes, assessing low pressure reservoir gas injection EOR potential, and some applicable simulation modules for incorporation into existing simulators. Benefits include:

- Surfactant cost reduction: optimizing sacrificial agent and high quality foaming surfactant mixtures, and decreasing primary foaming agent adsorption and required concentration,
- Extending the life of the petroleum reservoir, maintaining or increasing employment, and increasing oil recovery,
- Expanding CO_2 flooding to low pressure reservoirs,
- Delayed production of CO_2 and increased retention of CO_2 in the reservoir (carbon management),
- Improved injectivity of CO_2 and water,
- Enhanced CO_2 flooding predictions, and
- Decrease of CO_2 mobility during the alternating injection of brine and CO_2.

Carbon dioxide flooding potential has been effectively demonstrated in the US, particularly in the Permian Basin of west Texas and southeast New Mexico. Much of the research on CO_2 flooding can be applied to other gas flooding processes. Today almost 350,000 BOPD are being produced by gas injection in the US; ~70% of this oil or nearly 240,000 BOPD is from CO_2 injection projects.[28] With recent oil prices above $100 per barrel, this oil production signifies over $12 billion less in imports each year, and provides a significant number of domestic jobs as well. Out of the 350 billion barrels remaining in US oil reserves, the amount of oil presently produced by CO_2 flooding barely scratches the surface of this resource. The potential recovery is at least an order of magnitude greater.

Moderately successful use of this research will maintain current production rates, whereas good to excellent success in research, expanding market availability of CO_2 and/or sequestration incentives have the potential of increasing CO_2 use in EOR by severalfold. The potential is easily several billion dollars each year in reduced foreign imports and maximization of US resources.

EXECUTIVE SUMMARY

This document is the Final Report for the project, "Improved Gas Flooding Efficiency," Department of Energy Contract No. DE-FC26-04NT15532. This study focuses on laboratory studies with related analytical and numerical models, as well as work with operators for field tests to enhance our understanding of and capabilities for more efficient enhanced oil recovery (EOR). There are a number of publications that have resulted from this work[29-48] and more will be forth coming in the next year or so.

A high-pressure, high-temperature (HPHT) bubble chamber apparatus was modified and used to determine carbon dioxide (CO_2) and nitrogen (N_2) foam stability, interfacial tension (IFT) between HPHT gas and surfactant solutions and critical micelle concentration (CMC). A number of surfactant solutions were used in this study. In this study, changes of temperature from 25 to 90°C, pressure from 800 to 2000+ psig, and surfactant concentration from 0.005 wt% to 1 wt% were tested for foam stability, IFT and CMC. The relationship of foam stability and IFT is also discussed. IFT decreased with surfactant concentration below the CMC and was essentially constant above the CMC, increasing with the increase of temperature and the decrease of pressure. Stability of gas-foam is surfactant type and concentration-dependent.

The CO_2-CD1045 foam was stable under all tested temperatures at surfactant concentrations of 0.1 wt% and above, and decreased with increase of temperature at surfactant concentrations of 0.05 wt%. The foam was stable under all tested pressure at surfactant concentrations of 0.025 wt% and above, and decreased with increase of temperature at surfactant concentration of 0.005 wt%.

Foam behavior and adsorption, two of the mechanisms required to model surfactant requirements, are studied in this project. This study uses a commercial surfactant, nitrogen gas, reservoir conditions of 10.34 MPa (1500 psi) and 40°C (104°F), and Indiana limestone. Variables are surfactant concentration, flow rate and foam quality. At a constant gas flow rate, gas mobility decreases slightly with increasing foam quality when below the critical foam quality (f_g*) and increases with increasing foam quality above f_g*. Increased surfactant concentration leads to the decrease of gas mobility. Comparing coinjected surfactant and gas (CSG) with coinjected water and gas (CWG) shows that the mobility of CSG is an order of magnitude lower than that of CWG. Also, it took more time for CSG to reach steady state compared to CWG, even with a surfactant pad conditioning the core before surfactant and gas were coinjected.

Tests to determine CO_2 adsorption within a core were performed. They consisted of surfactant flooding in a closed system circulation system, brine-brine displacement in a multi-tap core with two brines, and surfactant adsorption tests in the multi-tap core to determine adsorption rates versus core length. All the above-mentioned experiments were conducted in a low pressure setting.

Surfactant flooding in a closed system quantified the total amount of surfactant adsorbed onto a core. Displacement of a 1% salinity brine with a 2% salinity brine was performed in order to understand the behavior of nonreactive solute transport in porous media. Cores were designed that allowed collection of samples via quarter-inch holes, three on each side of the core, that were drilled into the core. The result indicated that the waterflood bypassed some zones/parts of the core and reached breakthrough at the outlet tap before some of the taps in the last section of the core reached breakthrough. The bottom side of the core reached breakthrough earlier than the top side of the core. This was confirmed by rotating the core 180 degrees along the horizontal. There was a gravity effect.

Surfactant flooding in multi-tap core results shows that the greatest surfactant adsorption occurs at the section closest to the injection port. Surfactant adsorption was also higher in the bottom side of the core than in the top side, and exactly as the waterflood experiments, surfactant flooding bypassed some zones/parts of the core and reached maximum surfactant concentration breakthrough at the outlet tap before some the taps in the middle and last sections of the core reached plateau region in terms of concentration. The result also showed that surfactant desorption was very rapid in the first section of the core and in the bottom side of the core.

Kinetics and equilibrium adsorption were investigated by examining adsorption behavior in a system of solid phase sandstone or limestone and of an aqueous phase of surfactant in 2% brine. Effects on surfactant adsorption density for different solid to liquid ratios as well as surfactant concentration, rock type and state, and flow conditions are presented. Three systems were used: batch tests on crushed rock, circulation tests through core samples, and nonflow diffusion brine-saturated core tests. The density of an anionic surfactant adsorption onto rock is best described as a function of surfactant available in the system (concentration plus volume), rather than by surfactant concentration used by previous investigators. Experiments with solid rock were carried out to determine surfactant capacity of the porous media through flow and nonflow rock samples and crushed rock samples. Adsorption was similar for crushed sandstone

and flow tests, while significantly higher in cubed, nonflow rock systems. For limestone the crushed rock and nonflow systems were similar while the flow system was significantly lower. The time to reach equilibrium required less than one hour (generally minutes) for the crushed rock, hours to days for the flow-through tests, and weeks to over a month for the nonflow rock systems. The rate of adsorption dependent on availability (delivery) is generally much slower than the adsorption kinetics.

Results of eight series of adsorption and seven series of desorption experiments of CO_2 foaming surfactant CD1045 onto and from Berea sandstone, each with a different initial concentration, are presented. Nonlinear pseudo first and second order kinetic models for adsorption and desorption processes were derived. A simplex optimization method was adapted for the calculation of kinetic parameters of these models. This method can be used for calculating not only the kinetic model parameters, but also the absolute errors between the model and the measurements, and thus the fitness of the model. Using this simplex method and the experimental results, the adsorption and desorption processes of CD1045 onto and from Berea sandstone were found to follow a pseudo-second order adsorption model and a pseudo-first order desorption model, respectively.

The N_2 study involves both single and mixed surfactants systems. The single surfactant systems are: Enordet, Amphosol CG, Stepantan AS 1246, Formatron, CS 1040 and CS 1045. Stepantan AS 1246 + Amphosol CG and Stepantan AS 1246 + Formatron constitute the mixed surfactant systems. Evaluations of these surfactants for mobility control applications involved a series of tests that measure brine compatibility in terms of solubility, interfacial tension (IFT), foam stability, static adsorption onto reservoir rocks and flow resistance in corefloods.

The results indicate that all surfactant systems were soluble in 12.2 wt% brine except Enordet, which formed colloids and is hence recommended for use in only low salinity brine. In addition, though Stepantan AS 1246 + Amphosol mixed system has the best IFT (lowest), the mobility reduction factor (MRF) is too low and adsorption levels quite high; hence this product does not make a good choice. Furthermore, the IFT at critical micelle concentration (CMC) and above CMC, which constitute “injectible” concentrations, were virtually the same for the remaining six products; consequently, the choice then hinges on MRF. The Stepantan AS 1246 + Formatron mixed system has the highest MRF but has high adsorption levels like the other mixed system and as a result, this does not make a good choice either. Finally, these three single

systems; CS 1045, Formatron and Amphosol are recommended for detailed studies since they have appreciably satisfied all the indices of good surfactants (minimal adsorption levels, reduce IFT, yield stronger and durable foams, increase differential pressure and reduce gas mobility). The two mixed systems may also be looked at in the event that specified adsorption procedures might reduce the adsorption densities.

Laboratory tests were performed on sandstone and carbonate core samples. Two types of displacement tests were performed; gas injection to a residual brine saturation with respect to gas, followed by brine injection to a residual gas with respect to brine. The level of CO_2 saturation in the injected brine at reservoir pressure and temperature was varied from zero to over 90% saturation. Sandstone and carbonate rock samples were tested. This variation in CO_2 saturation in the injected brine determined the effect on the CO_2 saturation or plume size in the core. This information can be used in CO_2-EOR-WAG projects and for carbon sequestration into geological formations.

Injecting CO_2 into brine-saturated sandstone and carbonate core results in brine saturation reduction of 62 to 82% in the various tests. In each test, over 90% of the reduction occurred with less than 0.5 PV of CO_2 injected, with very little additional brine production after 0.5 PV of CO_2 injected. During brine injection, CO_2 production was equivalent to the rate expected from brine saturated with CO_2 at reservoir conditions, except for the first ~0.1 PV of the Queen Sandstone CO_2 production. This indicates that in each core at high endpoint brine saturation at the tested flow rate (~2 m/day) the CO_2 plume was reduced through dissolution, not displacement. With increasing CO_2 saturation in the injected brine, the brine volume required to remove (dissolve) the CO_2 plume increased proportionally. Results will be used to aid in predicting injectivity in CO_2-EOR-WAG operations and CO_2 plume migration and CO_2 dissolution in EOR and sequestration.

This report describes laboratory tests on sandstone and carbonate core samples. Two types of displacement tests were performed at reservoir conditions: gas injection into brine-saturated core until residual brine saturation is reached with respect to gas, followed by brine injection into this core until a residual saturation of gas with respect to brine is reached. In some cases the brine was injected until all the residual gas was removed by dissolution. The level of CO_2 saturation in the injected brine at reservoir pressure and temperature was varied from zero to over 90% saturation. This variation in CO_2 saturation in the injected brine determined the reduction rate of

the CO_2 saturation or plume after residual gas saturation was reached. This information can be used in CO_2-EOR WAG projects and for carbon storage into geologic formations.

The injection of CO_2 into brine-saturated sandstone and carbonate core results in brine saturation reduction in the range of 62 to 82% brine in the tests presented in this paper. In each test, over 90% of the reduction occurred with less than 0.5 PV of CO_2 injected, with very little additional brine production after 0.5 PV of CO_2 injected. During brine injection, CO_2 production was equivalent to the rate expected from brine saturated with CO_2 at reservoir conditions, except for the first ~0.1 PV of the Queen Sandstone CO_2 production. This indicates that in each core at high end-point brine saturation at the tested flow rate (~2 m/day) the CO_2 plume was reduced by dissolving gas, not displacement. With increasing CO_2 pre-saturation in the injected brine, the brine volume required to remove (dissolve) the CO_2 plume increased proportionally. Results will be used to aid in predicting injectivity in CO_2-EOR-WAG operations and CO_2 plume migration and CO_2 dissolution in EOR and sequestration projects.

Reported here are findings and comparison of five large coreflooding experimental series performed on quarried and reservoir carbonates (limestone and dolomite) with co-injected or alternating injections of CO_2 and brine at reservoir conditions. Metal chlorides were added as tracer components in injection brines for three tests and appeared in quantities well above natural levels in deposited carbonates in one test. Core segment porosity and permeability are reported to indicate dissolution and deposition. Cores were sectioned and analyzed by chemical and back-scattered electron imaging (BSEI) and chemical titration for compositional changes. In two tests fluid samples taken at reservoir conditions and neutron computed tomography (CT) were used to monitor changes in in-situ fluid compositions and the development of the 3-D porosity structure of the flooded cores, respectively.

The necessity to consider the non-Darcy effect on gas flow has been documented in the literature. In this study, the logic of the non-Darcy effect based on the Forchheimer equation has been successfully incorporated into the reservoir simulator MASTER. A method on how to implement the non-Darcy effect through the use of a non-Darcy flow factor F is presented. Sample simulation results are presented the demonstrate the need to consider the non-Darcy effect for situations involving high velocity gas flow.

Carbon dioxide is injected into deep geological formations mainly for two purposes: CO_2 enhanced oil recovery (EOR) and CO_2 sequestration. The injection of CO_2 into carbonate

reservoirs and aquifers causes pore water to change pH. The lowering of pore water pH causes a reaction between the carbonic acid and carbonate rocks, which can change porosity, permeability, and fluid chemistry. Much of the Williston Basin hydrocarbon production comes from carbonate reservoirs. With the increased interest in considering CO_2 enhanced oil recovery and CO_2 geologic sequestration within the basin, laboratory testing is necessary to limit reservoir damage and maximize production and/or storage as part of site characterization. Specifically, the changes in permeability and porosity are of importance to ensure reservoirs remain viable for continued production and future CO_2 storage. The limited availability of reservoir core samples for extensive laboratory testing requires the use of available geologic material. The Mississippian aged Salem Formation is a limestone (Indiana limestone) that has a uniform composition, texture, and structure, making it ideal for the laboratory as a calcium carbonate control. Using the Salem Formation limestone will allow for abundant data to be collected through many laboratory experiments varying injection schemes and injection rates for target reservoir conditions. Ultimately, Williston Basin core samples will become available from the future test injection site planned by the Plains CO_2 Reduction Partnership. The Williston Basin cores will be tested and compared to the data generated from the Salem Formation. The University of North Dakota Petroleum Engineering Laboratory is in the process of applying several injection strategies to Salem Formation samples at reservoir temperatures and pressures to identify the strategies that allow for maximum sequestration potential and minimum formation damage.

For experimentation the Salem Formation specimens are shaped into cylindrical plugs 25.4 mm in diameter and 50.8 mm long. Initial pressure and temperature conditions are averaged from field data in the Williston Basin; completed experiments have been run at 337.8 bar confining pressure, 248.2 bar fluid pressure, and 104.4°C. Supercritical CO_2, deionized water, and synthetic brine water are used as injection fluid in a range of Water-Alternating-Gas (WAG) Ratios. One to zero and zero to one WAG ratios are run as controls. For a completed WAG 1:1 injection experiment with an injection rate of 1 ml/min for cycles of 100 ml CO_2 and 100 ml deionized water (100 ml is equivalent to 5 pore volumes), over 250 mg of the 46.4g specimen was dissolved in a 17 hour period. With 336 and 672 hour injections scheduled to take place, significant changes in porosity and permeability are expected. Nondestructive methods are used to quantify porosity and permeability in samples by changes in acoustic velocities and

effluent chemistry during injection and Photon Emission Tomography scans before and after Sensitivities of non-Darcy flow parameters k and β to the changes of in-situ stress and fluid phase were investigated experimentally under representative petroleum reservoir conditions. Both k and β are sensitive to octahedral, i.e. average, effective stress, and insensitive to octahedral shear stress. Correlations are developed to quantify stress sensitivities of k and β. General procedures for the application of these correlations are proposed. Fluid phase changes include physical and compositional categories. Results indicate that k and β are sensitive to both physical and compositional phase changes. Compared to β, k is more sensitive to phase changes in both categories. To the same parameter, physical phase sensitivity is higher than that of the compositional counterpart. In the real world, fluid flow at near-critical conditions in the near-wellbore region may experience physical phase change due to a localized cooling effect, which may further enhance the non-Darcy flow behavior.

EXPERIMENTAL RESULTS AND DISCUSSIONS

A. SORPTION

A.1. CO_2 Foam Behavior: Influence of Temperature, Pressure, and Concentration of Surfactant

Introduction

Even though most field projects have been shown to be technically and economically successful, CO_2 flooding is associated with poor sweep efficiency, which is due to the relative low viscosity of dense CO_2 compared to that of brine and most crude oils.[49] A foam is a type of colloidal dispersion in which a gas is dispersed in a continuous liquid phase.[50] For high pressure CO_2 foam, the dispersed phase is dense CO_2 with density as high as 0.9 g/cm^3. The interface is a thin intermediate boundary between the dispersed and continuous phases. A lamella refers to the region that encompasses the thin film, the two interfaces on either side of the thin film, and part of the junction with other lamellae. The gas bubbles in foam have a large surface area, which leads to high surface energy. In order to generate stable foams with relatively low surface energy, one either adds surfactants to lower the interfacial free energy (interfacial tension), or provides sufficient mechanical energy. Using surfactants to generate stable foams is the most common method in industrial applications. Interfacial properties play an important role in foam study because of the relationship between surface energy and foam stability. Thus, it is important to test IFT between surfactant solution and dense CO_2.

This report describes the results of CO_2 foam stability and IFT tests that were conducted under the following conditions:

1. Surfactant concentration from 0.005 wt% to 1 wt%
2. Temperature from 25º to 75°C
3. Pressure from 800 to 2000 psig

The study of surfactant interfacial tension and CO_2 foam stability at various conditions will provide general information about the properties of CO_2 foam and the baseline properties of surfactants over a wide range of pressure, temperature, and surfactant concentrations. This data

can be used to develop an optimal surfactant system that has the appropriate physical properties and favorable economic potential for field applications.

Experimental Procedures

Materials. Chaser CD1045™ (CD) supplied by Chaser International was used in this study; it is a clear amber liquid that is 46.7 wt% active. Sodium chloride (NaCl) and calcium chloride dihydrate ($CaCl_2 \cdot 2H_2O$) were both A.C.S. reagent grade (98+%). Unless otherwise indicated, all experiments were conducted with CD in 2 wt% synthetic brine solution (NaCl:$CaCl_2$ at 3:1 wt ratio). Density of aqueous solutions was determined using a Mettler/Paar DMA 40 digital density meter.

IFT Measurement Methods. IFT is a measurement of the cohesive energy present at an interface, expressed in either energy/area or force/length. The common units for surface tension are milliNewtons/meter (mN/m) or dynes/centimeter.

The drop weight method of measuring the interfacial tension of liquid with respect to air (dense CO_2 in CO_2 foam) consists of determining the number of drops falling/rising from a capillary (Fig. 1). The drops are allowed to fall into a container until enough have been collected so that the weight per drop can be determined accurately. The principle of the method is that the size of the drop falling from a capillary tube depends on the surface tension of the liquid. A considerable portion of the drop (up to 40%) may remain attached to the capillary tip after the drop detaches. This effect is compensated with Harking-Brown correction factor, f,[51,52] as described by Adamson[52] (Fig. 2),

$$W = \Delta mg \quad \text{.....1}$$

where W is the weight of the drop, Δm is the differential mass between the two fluids in grams; g is the gravitational force, cm/sec^2; r is the needle radius, cm; σ is the IFT, dynes/cm. Also

$$\Delta mg = 2\pi r\sigma f \quad \text{.....2}$$

or

$$\frac{4}{3}\pi R^3(\rho_{surf} - \rho_{CO_2})g = 2\pi r\sigma f \quad \text{.....3}$$

where R is the average bubble radius, cm; ρ is the fluid densities, g/cm^3; and f is the Harking-Brown correction factor.

In this work, the calculation of the IFT measurements is analogous to that of the drop weight method.[51,52] The rate of introducing dense CO_2 is determined by the aqueous phase withdrawal rate. The number of produced bubbles per time period is recorded, from which the volume and radius of each bubble are calculated. The correction factor takes into account effects of attraction to the end of the tube and imperfections in the system, generally ranging from 0.5 to 1.0 (see Fig. 2). The correction factor in most of the experiments in this study range from 0.5 to 0.7. The drop weight method is fairly accurate and perhaps the most convenient in the laboratory for measuring both gas-liquid and liquid-liquid interfacial tensions. Design and construction of the apparatus (Fig. 3) was based on this method.

IFT and Foam Stability Apparatus and Determination. The IFT and foam stability apparatus used in this study was designed for testing surfactant properties at high pressure, thus allowing the evaluation of these solutions for reservoir use. An earlier stability apparatus[53,54] was modified with the following additions:

1. A protective frame was added,
2. The valves were fixed on a panel to reduce vibration (especially of the sapphire tube), and
3. The system was simplified without changing its functions.

The apparatus (Fig. 3) consisted of a CO_2 source tank, a visual cell made from a transparent sapphire tube, an oil/surfactant-solution cylinder, a positive displacement pump and a cathetometer for measuring the level of bubble decay versus elapsed time. The CO_2 tank and the sapphire tube high-pressure cell were contained in a temperature-controlled water bath. The pump and the oil/surfactant-solution cylinder were installed outside the water bath and their temperatures were maintained at the test temperature through an independent temperature control system.

During the stability experiment, the sapphire visual cell (Fig. 4) was first filled with the solution to be tested. The aqueous system was brought to the desired pressure by means of the Ruska positive displacement pump. The pressure difference between the CO_2 tank and the oil/surfactant-solution tank was determined by a Honeywell pressure transducer and brought to zero by fine adjustment of a Ruska positive displacement pump. At this point a valve at the

bottom of the water tank was opened that allowed flow of CO_2 into the surfactant solution as the pump is driven backward, causing the withdrawal of surfactant solution from the sapphire cell and into the oil/surfactant-solution tank. This drew the dense CO_2 upward through a needle at the lower end of the cell. Depending on the effectiveness of surfactants, the bubbles either formed a layer of foam at the top of the sapphire tube or coalesced into a clear layer of dense CO_2. During bubble generation, the number of bubbles per a set time was recorded and IFT was determined using Eq. 3. After a standard volume of CO_2 was introduced, the pump was stopped and the stability of foam determined by measuring the foam layer thickness for 90 minutes (Fig. 3). After the experiment was terminated, the surfactant portion of the contents of the sapphire tube was discarded. The CO_2 portion was blown off into the atmosphere. Finally, the sapphire tube was thoroughly rinsed with distilled water. More details on a similar system can be found in earlier publications.[53-56]

Like other types of colloidal dispersions, foams are not thermodynamically stable, Eventually they collapse, but it is possible to make surfactant-stabilized, static bubbles and films that endure for months or even years under suitable conditions. Though foams are not thermodynamically stable, they can exhibit kinetic stability, which is defined here as the CO_2 foam kinetic stability. Equation 4 shows how CO_2 foam stability was calculated from foam height measurements.

$$CO_2 \text{ foam stability} = 100 - \left(\frac{H_1(t)}{H_1(0) + H_2(0)} \times 100 \right) \quad \text{..... 4}$$

where t is time, $H_1(t)$ is the height of the CO_2 layer with time, $H_1(0)$ is the initial height of the CO_2 layer, and $H_2(0)$ is the initial height of the foam layer.

Results and Discussion

Surfactant Concentration Effect on Interfacial Tension. The surfactant was dissolved in 2 wt% synthetic brine and tested at surfactant concentrations from 0.005 wt% to 1 wt% (Table 1). The observed characteristic discontinuity in the plots of IFT against surfactant concentration (Fig. 5) corresponds to the value of the CMC (Fig. 5). For CD, IFT has been determined to decrease with surfactant concentration increases below the CMC and to be essentially constant above the CMC (Fig. 5) at 25ºC (77ºF) and 1500 psig. The CMC of CD is around 0.06 wt%.

Mechanisms for this trend for CD are as follows: at surfactant concentration below the CMC, the surfactant molecules are loosely integrated into the water structure with a monolayer forming at the interface. In the region of the CMC, the surfactant-water structure is saturated with monomers and surfactant molecules begin to build their own structures called micelles in the bulk solution. The monolayer at the interface also reaches saturation. Micelles are surfactant aggregates formed with the hydrophobic sections of the surfactant stuck together due to the limited solubility of surfactants in the aqueous phase and to the van der Waals attraction among the hydrophobic tails (or chains). The number of monomers adsorbed at the interface remains the same but the number of micelles will increase as the surfactant concentration increases above the CMC. Interfacial tension is related to the concentration of monomers at the interface and is independent of the number of micelles. Colloidal theories are based on the interfacial behavior of one pure surfactant. The surfactant solution, CD, is a commercial mixture made from different types of surfactants having a wide molecular weight distribution. Thus, the behavior of CD is more complicated and not expected to follow the theoretical predictions. Also, CMC determined by testing IFT is a measure of the saturation of the monomer's adsorption at the interface, which may possibly be lower than the theoretical CMC value that is defined as the surfactant concentration at which micelles start to form.[57]

Surfactant Concentration Effect on CO_2 Foam Stability. In our tests, coalescence of bubbles was observed only at 0.005 wt% CD concentration (Figs. 6 and 7), which indicated that foam did not collapse (Figs. 6 and 7) except at a concentration (0.005 wt%) much lower than the CMC (Fig. 5). The CO_2 foam stability of CD was insensitive to surfactant concentration over a wide range (from 0.01 wt% to 1 wt%), which is indicative of an excellent foaming agent. Figure 8

illustrated the polyhedral shape of a stable CO_2-foam. Figures 6 and 8 compare unstable foams (0.005 wt% CD) to stable foams, respectively, where the stable foams are relatively regularly-shaped polyhedrals and are homogeneous compared to the unstable foams.

The height of the foam layer decreased by a few percent with time (Fig. 9), even though the number of bubbles was constant in the foam (Fig. 8). The decrease was relatively small compared to the total foam volume and was insensitive to surfactant concentration (Fig. 9). This volume reduction occurs because liquid drains through the lamellae due to the force of gravity after foam generation (also called gravity drainage). The liquid drains by flowing downward through the liquid films. As the lamellar fluid drains and forms drier foam, the shape of the bubbles changes from spherical to polyhedral (Fig. 8).

In our test, it was noticed that the lamellae in the upper layer of the foam were thinner than those in the lower layer of the foam due to gravity drainage (Fig. 8). Draining continues until capillary forces were equal to gravitational forces. At the plateau borders (lamellae intersections) the gas-liquid interface curvature increases.[52] The increased curvature generates a low-pressure region in the plateau border area. Because the interface is flat along the thin-film region, a higher pressure resides here. This pressure difference forces liquid to flow toward the plateau borders and causes thinning of the films and motion in the foam. Film thinning is correlated to film stability (or foam stability). High speed film thinning will lead to bubble coalescence. Thus, it is important to study the effects of this on foam stability.

Temperature Effect on Interfacial Tension. Temperature is an important parameter in the application of foams in the petroleum industry. Previous studies on the effect of temperature on IFT indicated that trends observed depended on the systems studied.[58-63] According to colloidal theory, the fluidity of the hydrocarbon chains increases as temperature increases, which allows the chains to assume more favorable packing configurations to form micelles, lowering the CMC. As temperature continues to increase, however, the thermal motion of the chains increases to the point where the close packing arrangement is disrupted, causing the CMC to increase.[57] Again, similar to the surfactant concentration effect on IFT discussed earlier in this paper, this behavior with respect to temperature change was developed assuming a pure surfactant. Previous studies[58-63] also used commercial mixtures of surfactants, which explained why their results did not always agree with each other. Also, depending where in the thermal regime and on the

surfactant a particular system exists, a temperature increase might result in either an increase or a decrease in CMC.

Experiments were conducted on aqueous CD and a dense CO_2 system at different CD concentrations and temperatures (Table 2). Temperatures at which experiments were conducted ranged from 25ºC (77ºF) to 75ºC (167ºF), at 1500 psig (Table 2). The densities of the surfactant solution used in the calculating IFT were measured at atmospheric pressure and temperature. In this work, the general trend with increasing temperature was increasing IFT (Fig. 10), which indicated that thermal motion was the dominant factor controlling the IFT values. Figures 10 and 11 show that the CMC of CD is about 0.05 wt% and is insensitive to the temperature.

Temperature Effect on CO_2 Foam Stability. Foam stability under the test conditions was insensitive to temperatures at and below 60ºC for the concentrations tested, as shown in the three pictures on the left of Figs. 13 through 15, except at 0.005 wt%, the lowest CD concentration tested (Fig. 12). Tests at 75ºC saw a marked decrease in stability with rapid decay for the CD solution concentration of 0.025 wt % and 0.05 wt% (see right photos in Figs. 13 and 14). Therefore, an increase of temperature resulted in a decline in foam stability. Similar trends in temperature effect on foam stability were reported by other investigators.[64-66]

Increasing the surfactant concentration (Figs. 13 through 18) at 75ºC resulted in increased foam stability. The results imply that the temperature dependence of stability versus CD concentrations must be considered when preparing a foam system. A higher concentration of CD would be required in higher temperature reservoirs.

Bubble size became smaller and foam structure became more spherical with temperature increase. At constant temperature, the gravity drainage was relatively small compared to the total foam volume and was insensitive to surfactant concentration (Figs. 9, 19 and 20). At constant CD concentration, the gravity drainage decreased with temperature increase (Figs. 21–23).

Pressure Effect on Interfacial Tension. Previous studies on the effects of pressure on IFT observed that trends also depended on the system studied.[60-63,67-71] Experiments were conducted on aqueous CD and a dense CO_2 system at different CD concentrations (Table 3). The pressure at which experiments were conducted ranged from 800 psig to 2000 psig at constant temperature of 25ºC (77ºF). Figure 25 shows that CO_2 changes phases from gas to liquid at about 950 psig

and at 25ºC. Thus, for the pressures tested above 950 psig, CO_2 is a liquid (dense CO_2), while it is gas at 800 psig. The results showed that the IFT was dramatically higher at 800 psig compared to the higher pressures (Fig. 24). This trend is thought to be due to the increase of CO_2 density with pressure (Fig. 25), where the densities of the CO_2 and the aqueous solution became more similar. It is also observed that CMC increased with pressure increase (Fig. 26), which might be due to surfactant solubility increase in the CO_2 phase with pressure increase. A CMC increase means adsorption increases at the interface, which results in decreasing IFT with pressure increase.

Pressure Effect on CO_2 Foam Stability. Bubble size increased and gravity drainage decreased with pressure increase (contrast Fig. 9 to Fig. 27). At surfactant concentrations of 0.025 wt% and above, the foam system was stable over the testing conditions of pressure at 25ºC (Figs. 28 and 30). Foam stability decreased with pressure increase at the low surfactant concentration of 0.005 wt% (Figs. 28 and 29) at 25ºC. At high temperature (75ºC), foam stability decreased with pressure increase at CD concentration of 0.025 wt% and 0.05 wt% (Figs. 31 and 32).

In an earlier study, stable foams were usually associated with low IFT. In this study, IFT decreased with pressure increase but foam stability deceased. Presently, we do not have an explanation for this. This example demonstrates that a lower IFT does not always lead to more stable foam.

Correlation between IFT and Foam Stablity. CO_2 foam stability is surfactant concentration-dependent at low concentrations. At 1500 psig and 25ºC, IFT decreased with CD concentration below the CMC. But coalescence of bubbles was observed only at CD concentration of 0.005 wt%, well below the CMC. Thus, IFT change did not result in a change in foam stability. For example, no change was observed in foam stability at CD surfactant concentrations at and above 0.01 wt% and 2 wt% brine, while IFT decreased with concentration increase below CMC. The IFT was determined to be insensitive at CD concentration at and above 0.025 wt% at brine concentration over a range of salinities from 0 to 25 wt% NaCl:$CaCl_2$ at a 3:1 weight ratio with a minimum of ~10 wt% brine (Figs. 33 and 34). Again, for pressure increases, IFT (Fig. 24) decreased as pressure increased while foam stability (Figs. 28 and 30) remained stable at CD concentration at and above 0.025 wt%.

For all concentrations measured, IFT remained essentially constant over the intial pH range of 1 to 12 (Fig. 35). But foam stability decreased as initial pH decreased at 0.005 wt% CD (Fig. 36) and was stable at concentrations of CD at and above 0.05 wt%. Again, IFT increased with temperature increase and with CD concentration decrease (Fig. 10). At the same time, foam stability decreased with IFT increase. Thus, low IFT was favorable for the stable foam when temperature increased. A similar trend was observed when brine concentration changed at 0.005 wt% CD (Figs. 37 and 38). The IFT was fairly constant at brine concentrations of 2 wt% and below, was significantly lower at 5 wt% brine, then increased again. The values of IFT above 5 wt% brine concentration were lower than the values of IFT at brine concentration of 2 wt% and below. Correspondingly, foam was stable at and above 5 wt% brine.

As discussed above, decreasing IFT did not result in a more stable foam with increasing pressure (Fig. 24). However, foam stability decreased with pressure increase at 0.005 wt% CD (Figs. 28 and 29). Similar tends were observed at high CD concentrations at 75ºC (Figs. 31 and 32).

The above discussion indicates that IFT is one of the parameters contributing to foam stability—but it is not the only one. Foam stability cannot be predicted using IFT values alone.

Summary

- IFT has been determined to decrease with surfactant concentration below the CMC and to be essentially constant above the CMC, to increase with the increase of temperature and decrease of pressure, to remain essentially constant over the initial pH range from 1 to 12, and to be insensitive to brine concentration over a wide range with a minimum around 10%.
- Foam is stable at 60ºC and below, at all tested temperatures and CD concentrations, except at the lowest CD concentration (0.005 wt%) tested. However, foam stability increases with CD concentration at 75ºC.
- Foam is stable under all tested pressures at surfactant concentrations of 0.025 wt% and above, and foam stability decreases with increasing temperature at the surfactant CD concentration of 0.005 wt%.
- Interfacial tension (IFT) does not directly correlate to foam stability and foam stability cannot be predicted solely by the value of IFT.

Table 1. Experiment Schedule of CD Concentration Effect on IFT and Foam Stability

CD Conc. (wt%)	**0.005**	**0.01**	**0.025**	**0.05**	**0.1**	**0.25**	**0.5**	**1**
Brine	2 wt% brine (NaCl:$CaCl_2$ at 3:1 wt ratio)							
IFT	√	√	√	√	√	√	√	√
Foam stability	√	√	√	√	√	√	√	√

√ means that experiment is conducted

Table 2. Experiment Schedule of Temperature Effect on IFT and Foam Stability at Various CD Conc. (wt%)

T (°C)	0.005	0.025	0.05	0.1	0.25	0.5	1
25	√	√	√	√	√	√	√
35		√	√	√			
40	√	√	√	√	√	√	√
60	√	√	√	√	√	√	√
75		√	√	√			

Table 3. Experiment Schedule of Pressure Effect on IFT and Foam Stability at Various CD Conc. (wt%)

P (psig)	0.005	0.025	0.05	0.1	0.25	0.5	1
800	√	√	√	√			√
1100	√	√	√	√	√	√	√
1500	√	√	√	√	√	√	√
2000	√	√	√	√	√	√	√

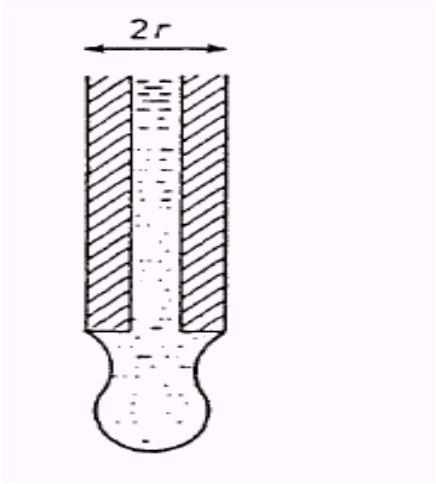

Fig. 1. Illustration of needle and drop.

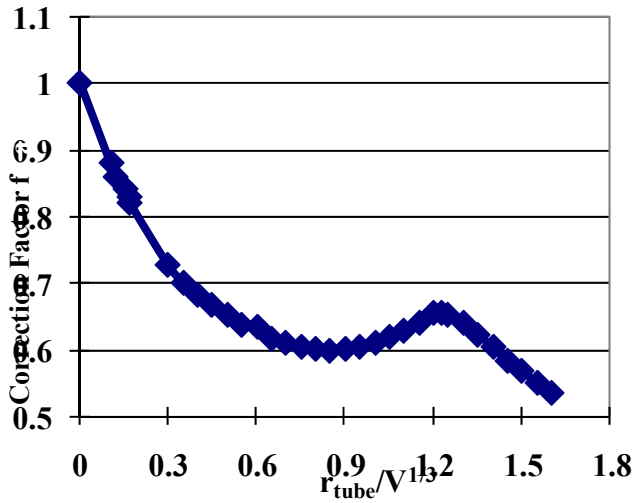

Fig. 2. Harkins-Brown correction factor for drop-weight method (after Adamson).[17]

Fig. 3. Foam stability apparatus setup.

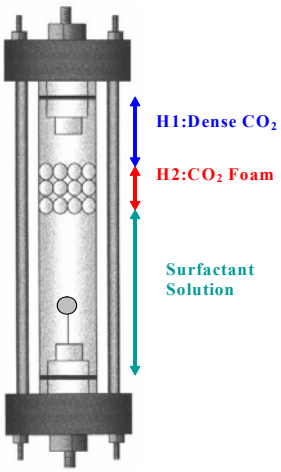

Fig. 4. CO_2 foam stability high pressure observation cell.

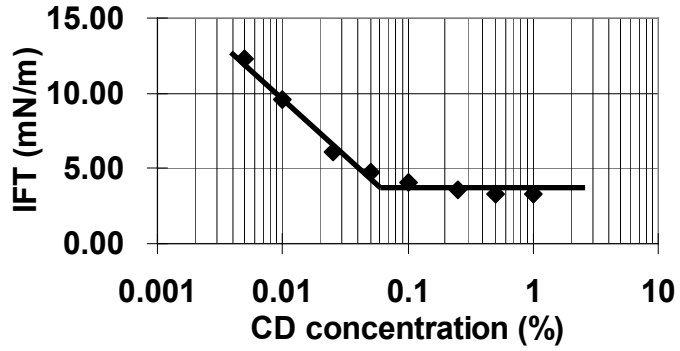

Fig. 5. CMC determination for CD.

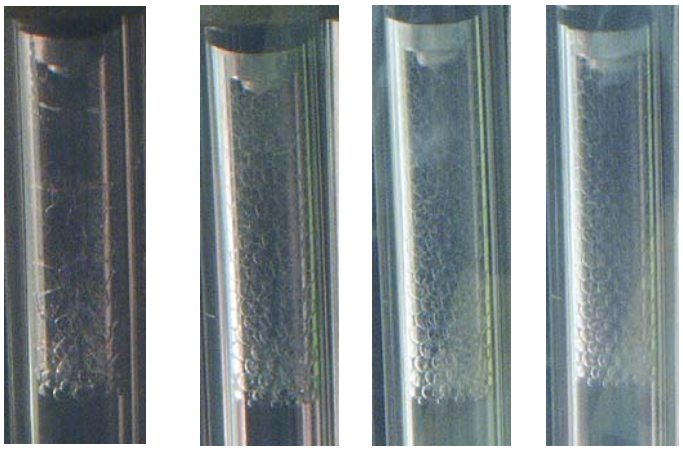

0.005 wt% 0.025 wt% 0.05 wt% 0.1 wt%

Fig. 6. Foam image at different CD concentrations at 90 min after generating bubbles.

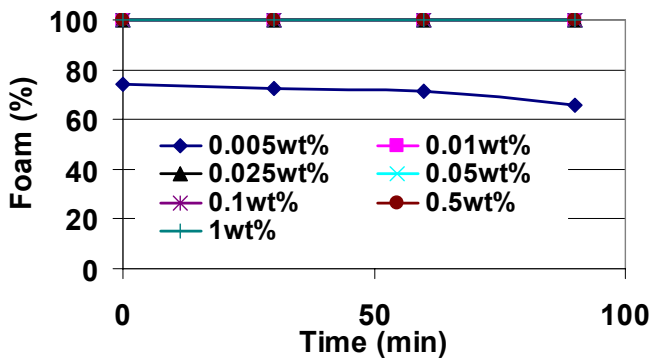

Fig. 7. Foam stability at different CD concentrations (six curves bunching at 100%).

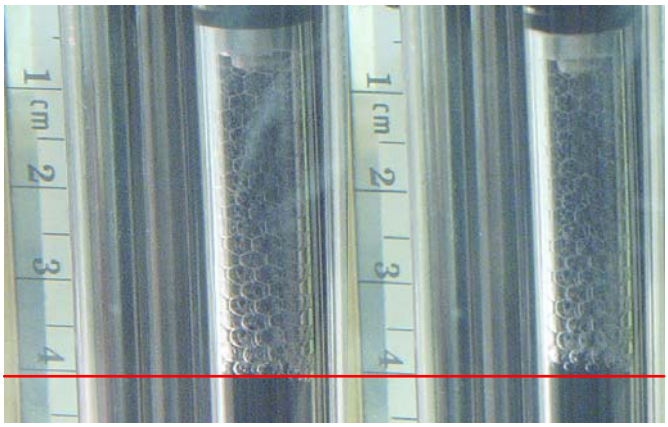

Fig. 8. Small volume changes occur with time due to gravity drainage, even for stable foams at 0.05 wt% CD.

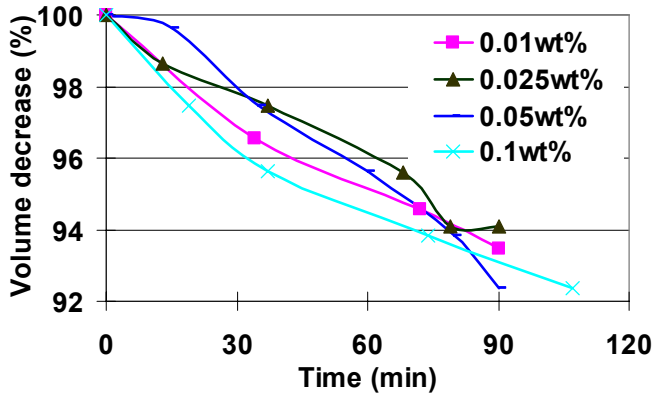

Fig. 9. Surfactant effect on gravity drainage at 25°C.

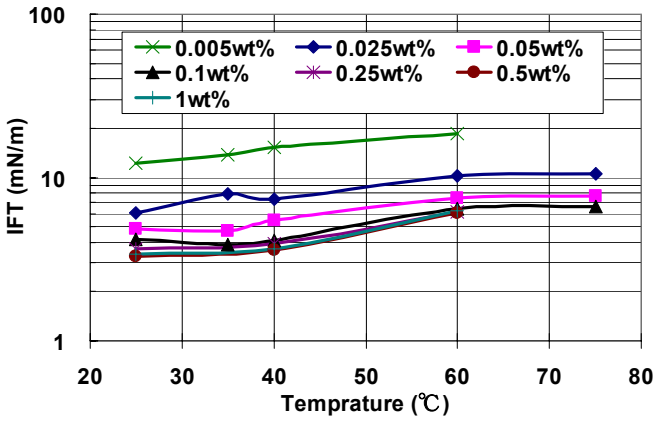

Fig. 10. IFT vs. temperature and surfactant concentration in CD solutions.

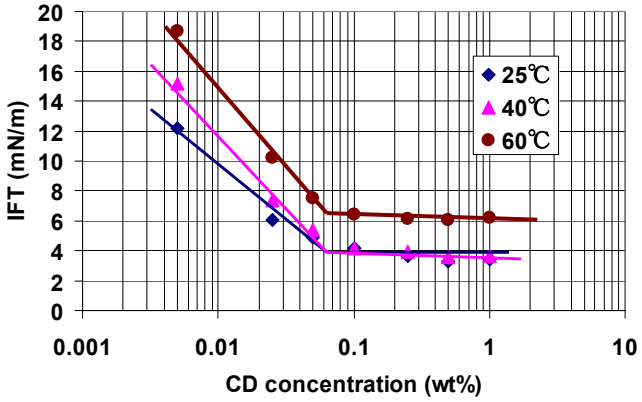

Fig. 11. CMC vs. temperature.

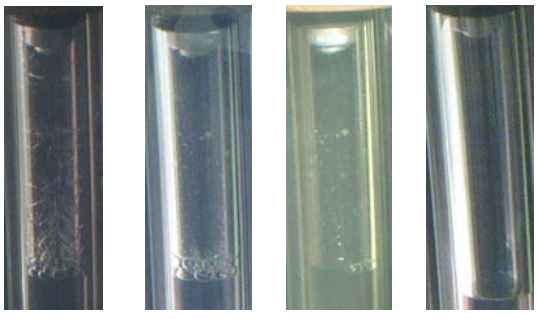

25ºC 40ºC 40ºC 60ºC

90 min 0 min 90 min 0 min

Fig. 12. Temperature effect on CO_2 foam stability at 0.005 wt% CD.

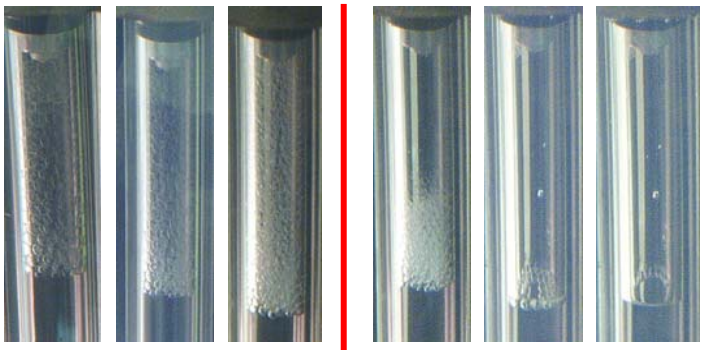

Fig. 13. Temperature effect on CO_2 foam stability at 0.025 wt% CD.

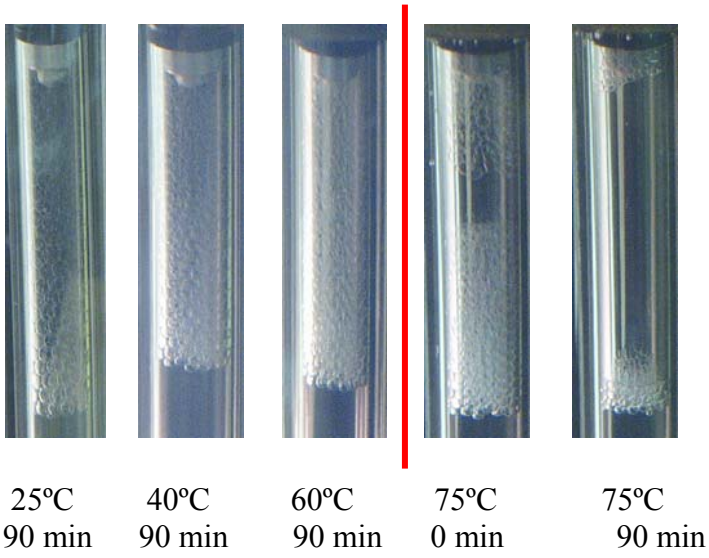

Fig. 14. Temperature effect on CO_2 foam stability at 0.05 wt% CD.

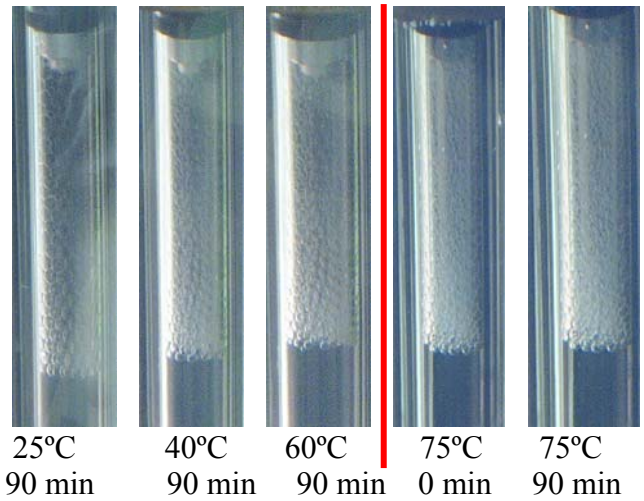

Fig. 15. Temperature effect on CO_2 foam stability at 0.1 wt% CD.

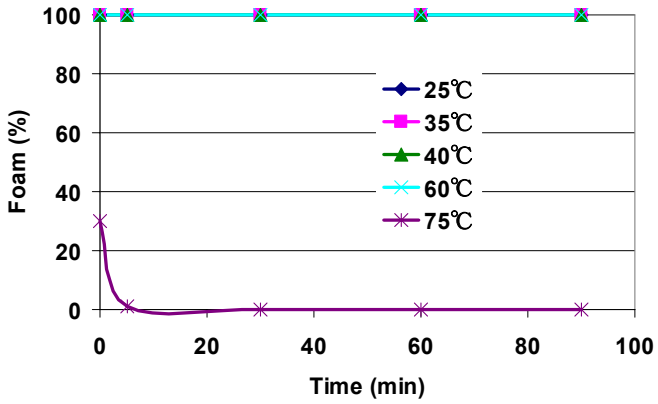

Fig. 16. Foam stability at 0.025 wt% CD (four curves bunching at 100%).

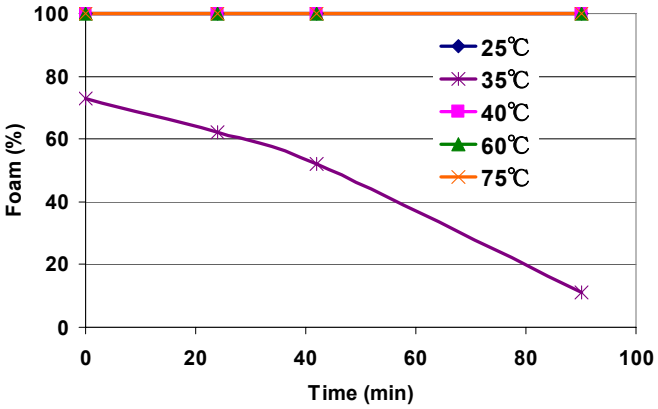

Fig. 17. Foam stability at 0.05 wt% CD (four curves bunching at 100%).

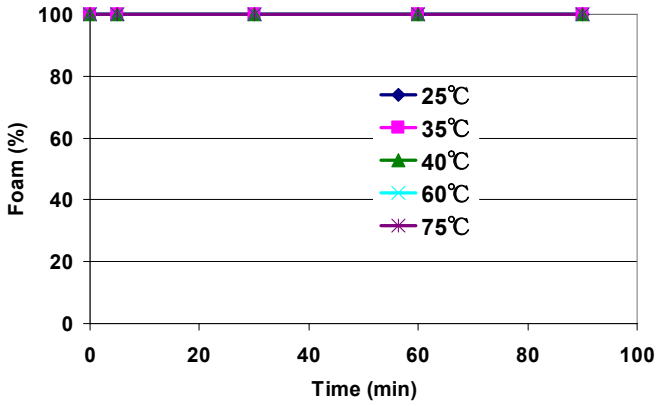

Fig. 18. Foam stability at 0.1 wt% CD (five curves bunching at 100%).

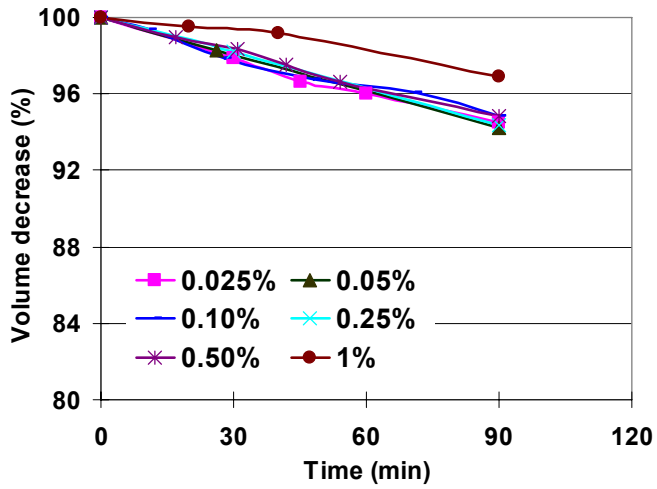

Fig. 19. Surfactant effect on gravity drainage at 40°C.

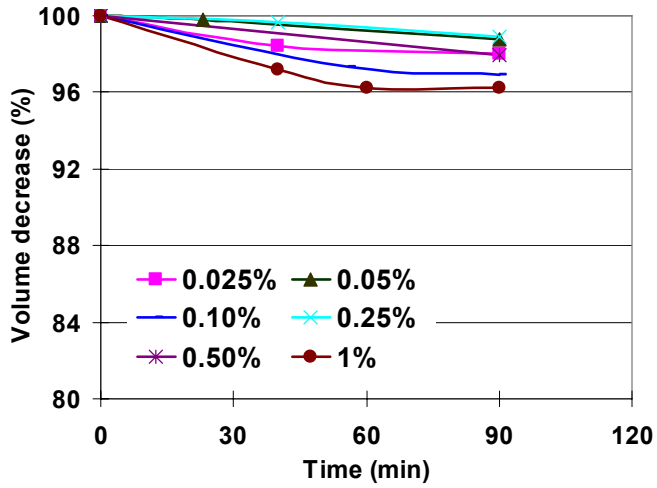

Fig. 20. Surfactant effect on gravity drainage at 60°C.

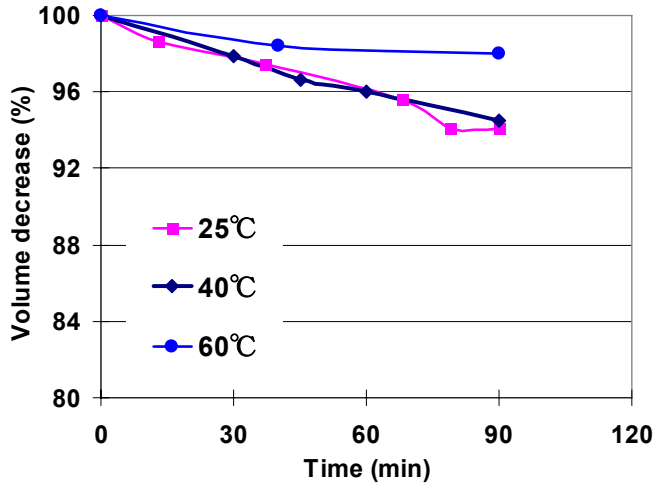

Fig. 21. Temperature effect on gravity drainage at 0.025 wt% CD.

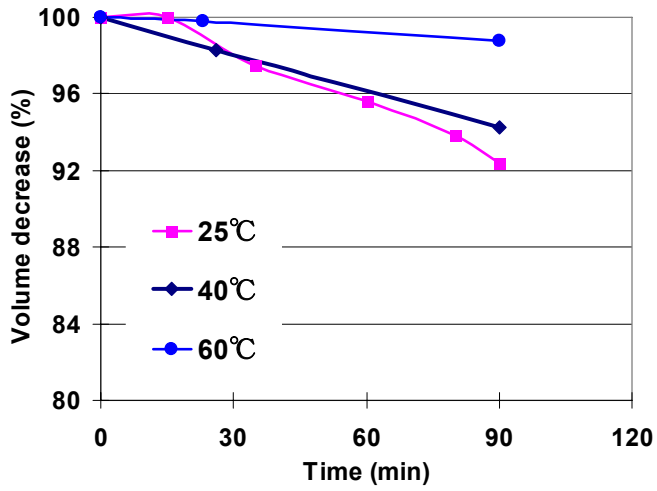

Fig. 22. Temperature effect on gravity drainage at 0.05 wt% CD.

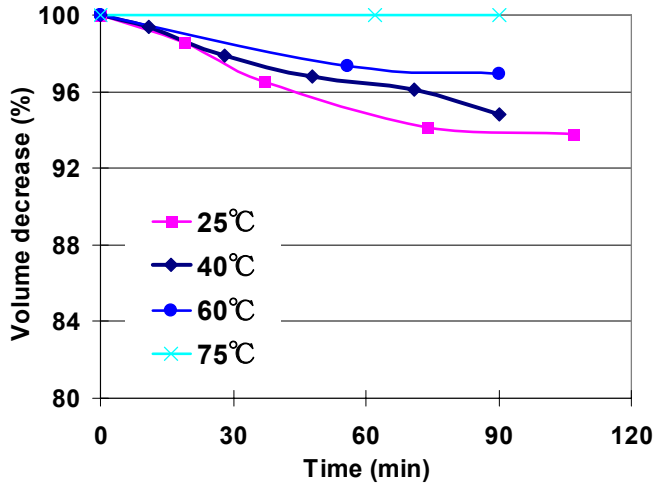

Fig. 23. Temperature effect on gravity drainage at 0.1 wt% CD.

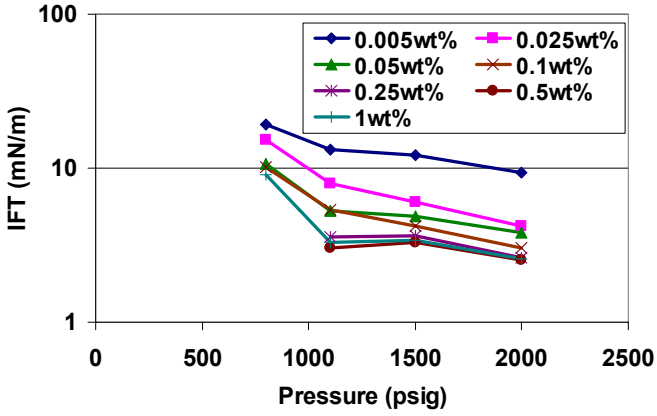

Fig. 24. Pressure effect on IFT.

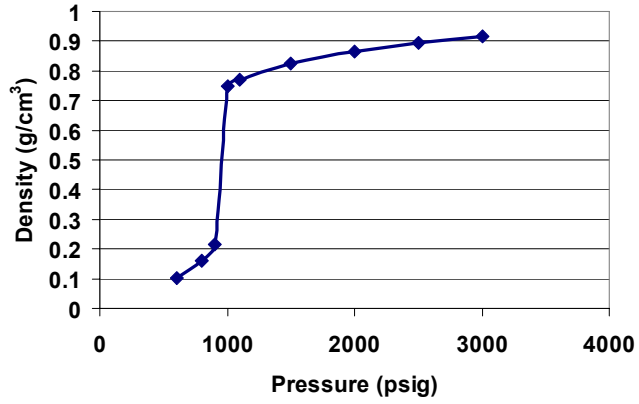

Fig. 25. CO_2 density vs. pressure at 25°C.

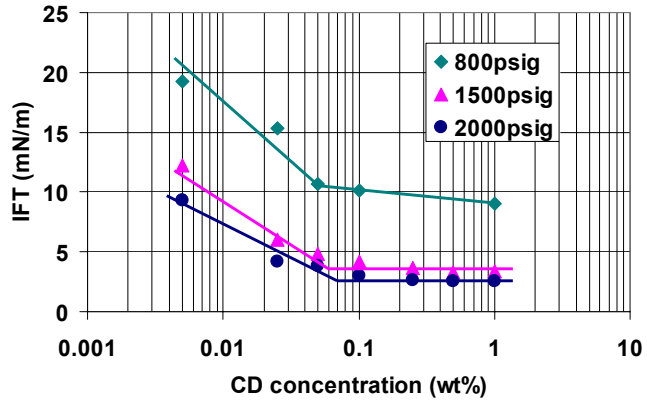

Fig. 26. Pressure effect on CMC.

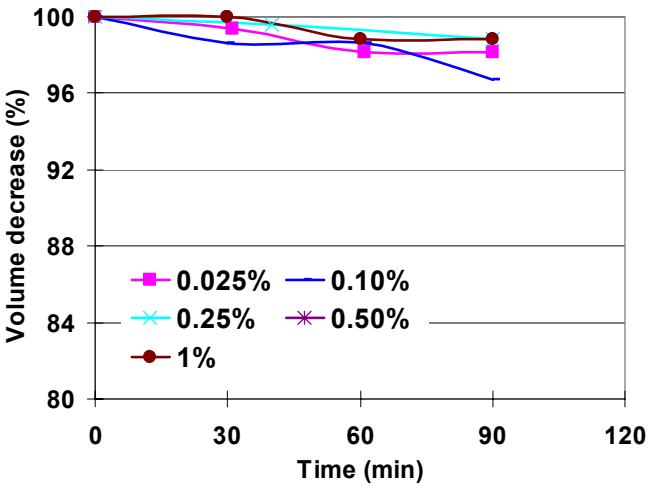

Fig. 27. Surfactant effect on gravity drainage at 800 psig.

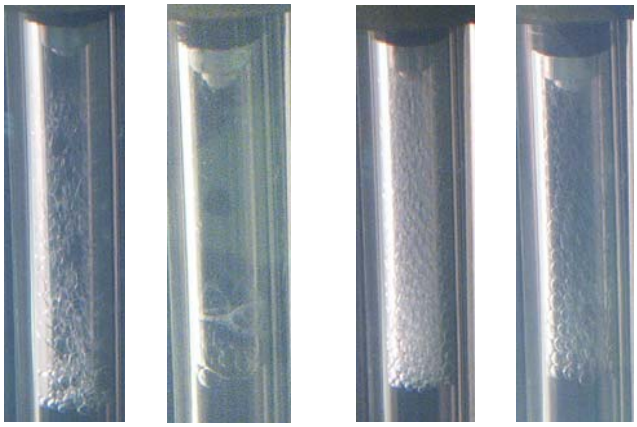

Fig. 28. Pressure effect on CO_2 foam stability at 25°C.

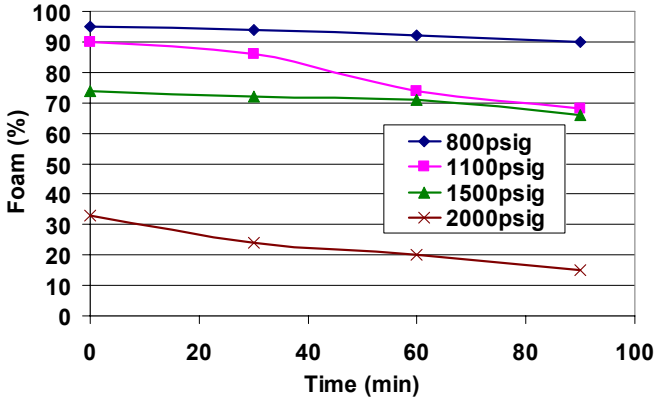

Fig. 29. Pressure effect on foam stability at 0.005 wt% CD at 25°C.

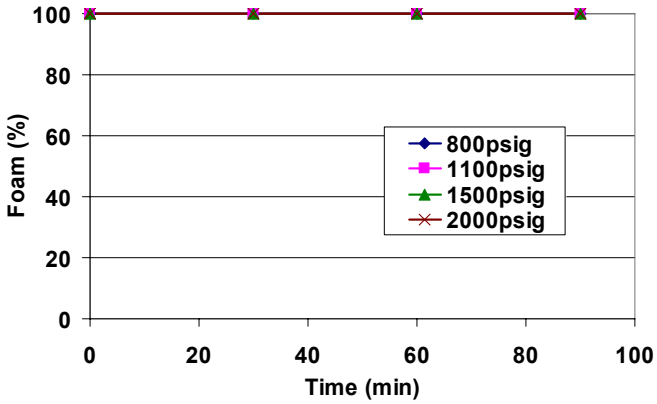

Fig. 30. Pressure effect on foam stability at 0.025 wt% CD at 25°C (four curves bunching at 100%).

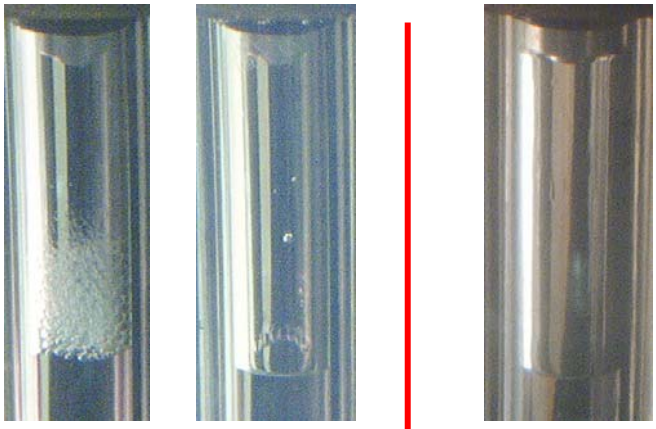

Fig. 31. Pressure effect on foam stability at 0.025 wt% CD at 75°C.

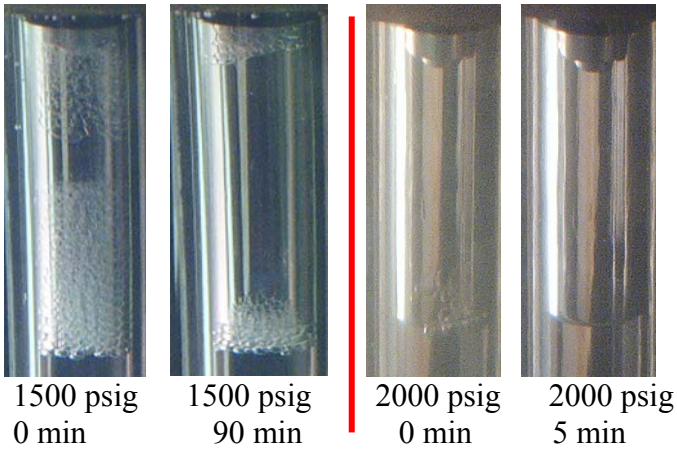

Fig. 32. Pressure effect on foam stability at 0.05 wt% CD at 75°C.

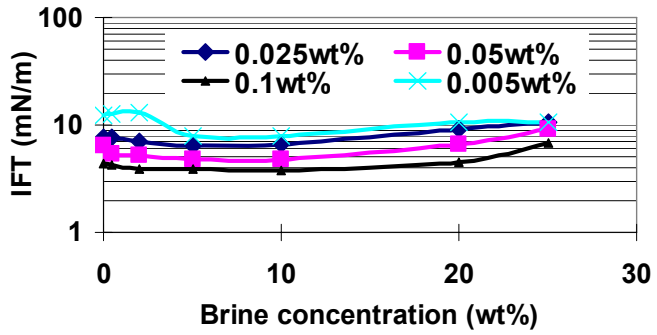

Fig. 33. Salinity effect on IFT.

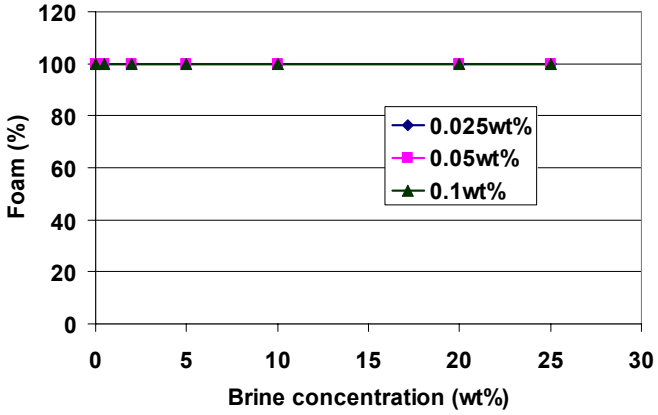

Fig. 34. Salinity effect on foam stability at indicated CD concentration (three curves bunching at 100%).

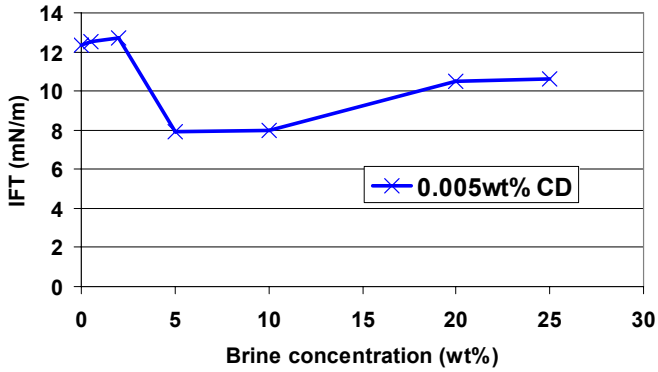

Fig. 35. Initial pH effect on IFT at different CD concentration.

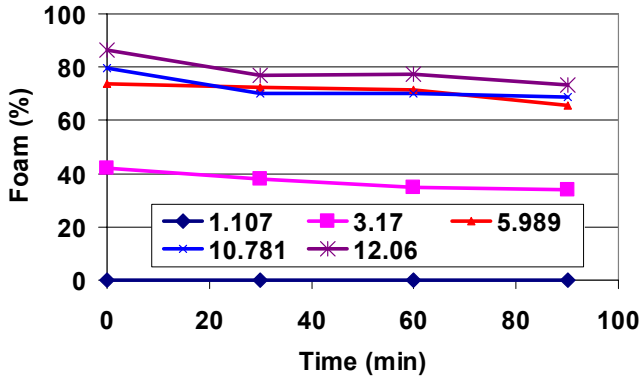

Fig. 36. Indicated initial pH effect on foam stability at 0.005 wt% CD.

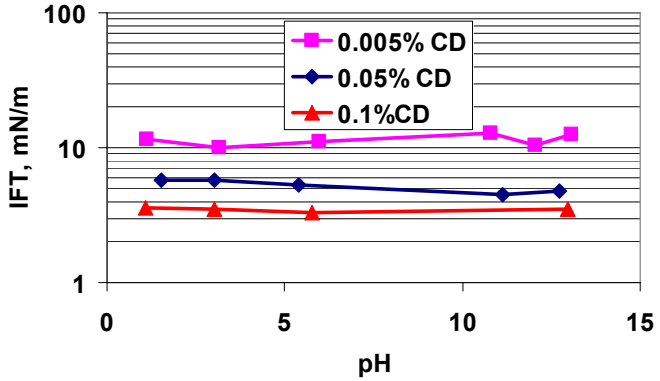

Fig. 37. Salinity effect on IFT.

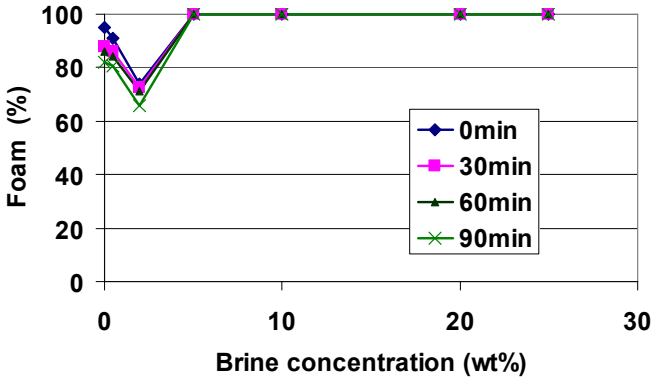

Fig. 38. Salinity effect on foam stability at 0.005 wt% CD.

A.2. Foam Mobility and Adsorption in Carbonate Core

In foam flooding, surfactant propagation is critical to foam propagation. A surfactant consists of both hydrophilic and hydrophobic parts. This unique characteristic of a surfactant molecule make it vulnerable to adsorption onto rock. The total chemical loss in the porous medium is defined as system surfactant retention. Normally we think of the primary contributor to retention being adsorption; in this work adsorption will be considered as the only contributor to retention.

The objectives of this study are:

1. To study foam behavior in the carbonate core,
2. To analyze foam durability, adsorption and desorption at high pressure and temperature, and
3. To discuss their significance.

The results can be used to optimize foam quality and injection design for various applications in the petroleum industry, including brine or surfactant solution alternating gas (WAG or SAG) injection in the field.

Experimental Setup and Procedures

Materials. Indiana limestone is a bioclastic grainstone that is rather uniform and homogeneous. In this paper, Indiana limestone was used in the coreflooding experiments. A detailed description of the Indiana limestone has been given in a previous publication.[72] The core is 5 in. long with diameter of 1.98 in. (see Table 4). Nitrogen is injected as the gas phase and surfactant solution or water is injected as the aqueous phase in our coreflooding experiments. The surfactant used in this study was CD1045™ (CD), supplied by Chaser International as 46.7 wt % active aqueous solution. The critical micelle concentration of the CD is approximately 0.06wt%.[73,74] Dimidium Bromide-Disulphine Blue Indicator, used for anionic surfactant determination, supplied by BDH Laboratory Supplies, was used to determine unknown CD concentrations and was described earlier.[75] Chloroform, HPLC grade, containing approximately 0.75% ethanol as a preservative was used as part of the process to determine CD concentrations.

Apparatus. The coreflooding apparatus (Fig. 39) was designed and built to obtain the required information while varying foam quality, flow rate and surfactant concentration. A sapphire observation cell, 2.095 in. long, 0.315 in. ID, and 0.375 in. OD, was placed at the end of the core to observe foam texture at test pressure and temperature. Three filters were placed in front of the core and acted as a foam generator and filter, the final and smallest aperture being 0.5 um. The coreholder can accommodate a core up to 2 in. in diameter and 24 in. long, with a maximum working pressure of 10,000 psi and internal pressure taps. Four Honeywell pressure transducers were incorporated in the design to measure differential pressures across core segments.

Experimental procedures. All flooding tests were carried out at 40ºC and 1500 psig core outlet pressure with 3100 psig overburden pressure. Pressure taps were set at 1 in. and 4 in. from the beginning of the core respectively. The entire core (5 in.) pressure drop (dp) and segment differential pressures across the inlet (a 1-in. segment (A, dp_A), the middle 3-in. segment (B, dp_B), and the final 1-in. segment (C, dp_C)) were recorded by four differential transducers. Two static pressure transducers were used to measure the core inlet and outlet pressures (P_{in} & P_{out}, respectively), which could also be used as a backup for the entire core pressure drop.

The CD solution and N_2 injection were controlled by two ISCO syringe pumps, each through an accumulator. The core was evacuated and the water permeability was determined. The aqueous solution was filtered and degassed. To start the experiment, the desired gas and aqueous solution flow rates were set, and the computerized data-acquisition system started to collect pressure data of P_{in} and P_{out}, pressure drop data of dp, dp_A, dp_B and dp_C and temperatures in the airbath, core holder and room.

Normally, each test interval stopped after the pressure drop through the core leveled out and the steady state of the flow was established. Next, either the solution conditions, gas to liquid injection ratio, or total flow rate was changed. At the end of a series of CD tests, the core was flushed with CD-free water until the pressure drop through the core was close to the core initial conditions at the same flow rate. The effluent from the core was collected to analyze the concentration of CD to determine the adsorption and desorption at reservoir conditions in the foam systems.

Calculations. The gas fraction (f_g) and foam quality are defined by the following equations:

$$f_g = \frac{q_g}{q_{g+w}} \quad \text{.....5}$$

$$foam\ quality\ (\%) = f_g \times 100\% \quad \text{.....6}$$

where q_g is the gas flow rate in cm^3/sec, and q_{g+w} is the total flow rate in cm^3/sec.

Many published studies[76-81] confirmed that the presence of foam did not affect the wetting-phase relative permeability. Darcy's law can be applied to calculate water relative permeability. Steady-state water saturations are different between foam and surfactant-free two-phase flow under identical flow rate conditions, while the relation between the aqueous phase relative permeability, k_{rw}, and the aqueous saturation remains the same. But the nonwetting gas phase's relative permeability will be drastically reduced when foam is present in the porous media. Therefore, the gas mobility can be used as a measure for foam flow resistance in the porous media. Also, steady-state pressure gradients in the wetting phase and the non-wetting phase are the same. Thus, the gas mobility, λ_g, in md/cp can be calculated using Eq. 3 and is defined as the ratio of the gas Darcy (or superficial) velocity, u_g, or volume per time period per cross-sectional area of the core, q_g/A, in cm/sec divided by the average pressure gradient, dP/ds across the core in atm/cm after reaching a steady state as shown in Eq. 7,

$$\lambda_g = \frac{q_g / A}{dp / ds} \quad \text{.....7}$$

Two foam-flow regimes. Figure 40 is a schematic plot for two foam-flow regimes.[82,83] The vertical dp/ds contours define the high foam quality regime, which is also known as the coarse foam regime. The horizontal contours define the low foam quality regime or stable foam regime. The mechanism behind Fig. 40 is that the capillary pressure will increase with foam quality at constant gas flow rate. However, the capillary pressure, P_c will increase up to a limiting value as f_g increases. This limiting value is defined as the limiting capillary pressure, P_c^*. The foam texture becomes coarser because the capillary pressure cannot exceed its P_c^* with further f_g increase.[84,85] In the high foam-quality regime, the pressure drop is independent of gas flow rate at constant liquid flow rate, which is controlled by P_c^*. In the low foam-quality regime, the pressure gradient remains constant with changing liquid flow rate at constant gas flow rate. The

transition zone between the two regimes is characterized by a specific value of the gas fraction, f_g*, which corresponds to the critical foam quality.

Results and Discussion

Surfactant adsorption and desorption at reservoir conditions. Two series of experiments were carried out to study gas and surfactant concentration effects on surfactant adsorption, see Table 2. CSG without a CD pad injection mode is defined as surfactant and gas coinjected into 100% water-saturated core, while CSG with CD pad injection mode is defined as surfactant and gas coinjected into a core where CD adsorption has been satisfied by an initial CD solution slug. Desorption was determined by injecting surfactant-free solution after CSG. The relation between effluent CD concentrations normalized to the injecting CD solution concentration versus pore volumes (PV) of injected CD solution is shown in Fig. 41. The high initial concentration CD (2500mg/l) propagated through the core faster than the low initial concentration CD (500 mg/l). The high concentration CD front traveled faster, driven by diffusion force due to higher concentration gradient, and the increased availability of CD satisfied adsorption demand faster than the lower concentration solution. Each CD concentration had a test with and without gas present. During the initial adsorption part of each test at 500 mg/l CD concentration both with and without a CD pad, the results were within experimental accuracy, Fig. 41. The systems at 2500 mg/l also showed similar adsorption behavior. Therefore, with or without the presence of gas, CD adsorption behavior at reservoir conditions are similar (Fig. 3). Thus, the determination and study of surfactant adsorption with foam can be performed by surfactant solution only, which requires a simpler apparatus and less expense and time.

The behavior of CD desorption compared to the adsorption for the 500 mg/l system are compared in Fig. 42. The effluent CD concentration drops rapidly after switching to the injection of CD-free solution. This rapid drop in produced CD with the long tail of low concentration corresponds to earlier studies in which desorption was seen to be slower than adsorption and not 100% reversible, at least in a comparable time frame to the adsorption.[88]

Critical foam quality determination. In order to determine critical foam quality f_g*, a series of the core flooding experiments were carried out at a constant gas flow rate of 22 cc/hr while

varying the 2500 mg/l CD aqueous phase flow rate from 0.11 to 1000 cm^3/hr. The experiment sequence is outlined in Table 7. The relationship between gas mobility, λ_g, and the gas/liquid fractional flow, $f_g/1-f_g$, at constant gas Darcy gas velocity (u_g) of 22cc/hr is shown in Fig. 43. The plot is characterized by two straight lines intersecting at critical foam quality, f_g*. At lower values of f_g, gas mobility slightly decreases or remains constant with increasing f_g, while at higher f_g the foam mobility increases with increasing f_g. The solid lines in Fig. 43 represent the trend obtained from experimental data, while the dashed lines represent the estimated trends from limited experimental data at lower constant gas Darcy velocities. Each data line represents different constant u_g. The dashed lines were plotted based on the relation between mobility and f_g at u_g and assuming that f_g* has negligible change with u_g and f_g* is a function of the characteristic surfactant formulation in the same rock. Therefore, the shape of mobility versus $f_g/(1-f_g)$ curve will be similar at different u_g. The experimentally determined f_g* is approximately 0.85 ± 0.05.

In field applications, a high fg* surfactant system is desirable. When designing foam flooding for field application, higher foam quality will reduce the total amount of surfactant injected, thereby reducing operating cost. For CD solution, 85% foam quality must be considered maximum; however more surfactant would be required in a field application to ensure foam properties remain in the preferred strong foam regime (lower quality foam).

Critical foam quality for the entire core is compared with core segments in Fig. 44. Permeability and mobility values were determined for each of the core segments. The values for f_g* were 0.84, 0.85, and 0.85 for 21 md (the middle segment-B), 29 md (the entire core), 53 md and (the ending segment-C) core, respectively (Fig. 44). Segment A, inlet, values are scattered (Fig. 44). Permeability of segment A increased over time presumable due to erosion and/or dissolution. The increased scatter in λ_g for segment C at high $f_g/(1-f_g)$ is probably due to end effects at low u_w.

Surfactant concentration effect on foam mobility. Experiments were performed at a constant flow rate of 10 cm^3/hr while varying CD concentrations and foam qualities. The experimental strategies are listed in Table 7. Surfactants can lower the interfacial tension between gas and water, lower the surface energy, and increase the membrane strength. These factors contribute to

improved foam stability with the characteristics of higher apparent viscosity and flow resistance in the porous media.

The curve of the gas mobility versus f_g at a constant flow rate of 10 cm^3/hr and varying surfactant concentrations are plotted in Fig. 45. The results show that at a constant total flow rate, the gas mobility increases with f_g. The same trend was found in Fig. 46. The 24.75 and 7 cc/hr constant total flow rate data are derived from the different constant gas flow rate data shown in Fig. 53. This agreement again supports the previously outlined assumptions for determining f_g*.

The results plotted in Fig. 7 also demonstrate that increased surfactant concentration decreases foam mobility. When comparing co-injected surfactant and gas (CSG) with co-injected water and gas (CWG), the mobility of CSG is an order of magnitude lower than that of CWG. This agrees with the foam theory and published results.[76,87-94] The time required to reach steady state was several times longer for CSG than for CWG. This is believed to be due both to the time required to reach equilibrium for surfactant adsorption and a larger displacement cross-sectional flow channel due to the higher apparent viscosity of the CSG system. Even with the longer time it took the CSG solution to reach steady state, the system reached a pressure-differential steady state long before the effluent CD concentration was equal to the injection CD concentration. For example, differential pressure across the core reached a steady state when the effluent concentration was only about 9 mg/l compared to an injection concentration of 500 mg/l. Thus a mobility steady state was reached before the adsorption plateau was achieved. This result is compatible with static foam stability experiments previously reported.[74] At 1500 psi and 40°C, the static foam durability tests demonstrated that weak foam can exist even at CD concentrations as low as 50 mg/l.[74] In foam flow tests in a porous medium, coalescing and regeneration are occurring, so even a foam of relatively short life span can be regenerating rapidly enough to result in significant mobility control. Again, this is a good implication for field applications.

The surfactant-free water and gas coinjection (CWG) experimental data was plotted into the contour plot (Fig. 47) and it was found that the f_g* in CWG is 0.1 compared to f_g* for CSG of 0.85 shown on a similar plot in Fig. 48. Values from the 1, 3, and 5 cc/hr gas flow tests shown in Fig. 43 were used to calculate the contours for the two flow regimes in Fig. 48 The value of f_g* in the surfactant system again demonstrates the advantage of foam flooding over surfactant-free gas, CWG or WAG floods.

Summary

1. At a constant gas flow rate, gas mobility slightly decreases with increasing foam quality when below the critical foam quality (fg*) and increases with increasing foam quality above f_g*.
2. Low gas mobility can be found over a wide range of foam qualities.
3. Increased surfactant concentration leads to the decrease of gas mobility. Comparing coinjected surfactant and gas (CSG) with coinjected water and gas (CWG) shows that the gas mobility of CSG is an order of magnitude lower than that of CWG.
4. Surfactant adsorption with gas present can be determined using surfactant solution alone, which lowers the expense due to simpler experimental setup and less time required.

Table 4. The Properties of Indiana Limestone

Core	*OD, in*	*Length, in*	*Pore Volume, cc*	*Porosity, %*	*Initial water permeability, md*
1	*1.98*	*5.02*	*37.75*	*14.84*	*61.66*
2	*1.98*	*5.03*	*41.53*	*16.36*	*25.61*

Table 5. The Experimental Sequence for Adsorption and Desorption

Displacing fluid sequence	*Determination*	*Injection strategy*
(1)500mg/l CD *(2)500mg/l CD and N_2* *(3)CD free water*	*CD adsorption* *CD adsorption with N_2 presents* *Desorption*	*CSG with CD pad*
(1)500mg/l CD and N_2 *(2)CD free water*	*CD adsorption with N_2 presents* *Desorption*	*CSG without CD pad*
(1)2500mg/l CD *(2)2500mg/l CD and N_2* *(3)CD free water*	*CD adsorption* *CD adsorption with N_2 presents* *Desorption*	*CSG with CD pad*
(1)2500mg/l CD and N_2 *(2)CD free water*	*CD adsorption with N_2 presents* *Desorption*	*CSG without CD pad*

Table 6. The Core Experiment Strategy for fg* Determination

Running sequence	*Gas flow rate, cm^3/hr*	*2500 mg/l CD flow rate, cm^3/hr*	*fg*
1	*22*	*0.11*	*0.995*
2	*22*	*0.22*	*0.99*
3	*22*	*0.58*	*0.974*
4	*22*	*1.22*	*0.947*
5	*22*	*2.75*	*0.889*
6	*22*	*11*	*0.667*
7	*22*	*22*	*0.5*
8	*22*	*44*	*0.333*
9	*22*	*88*	*0.2*
10	*22*	*1000*	*0.022*

Table 7. The Core Experiment Strategy for Determining Optimum fg at Constant Gas Flow Rate

CD concentration, mg/l			*Flow rate, cm^3/hr*			*fg*
CWS	*CSG*		*Total*	*Gas*	*Liquid*	
0	*500*	*2500*	*10*	*9*	*1*	*0.9*
0	*500*	*2500*	*10*	*7*	*3*	*0.7*
0	*500*	*2500*	*10*	*5*	*5*	*0.5*
0	*500*	*2500*	*10*	*3*	*7*	*0.3*
0	*500*	*2500*	*10*	*1*	*9*	*0.1*

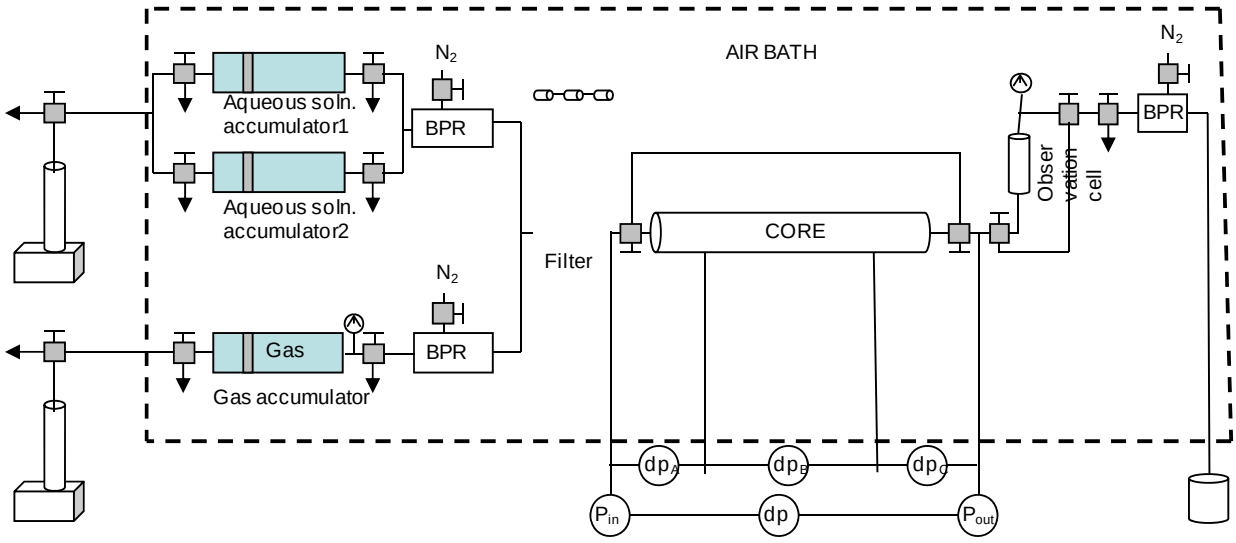

Fig. 39. Schematic plot of core flooding setup.

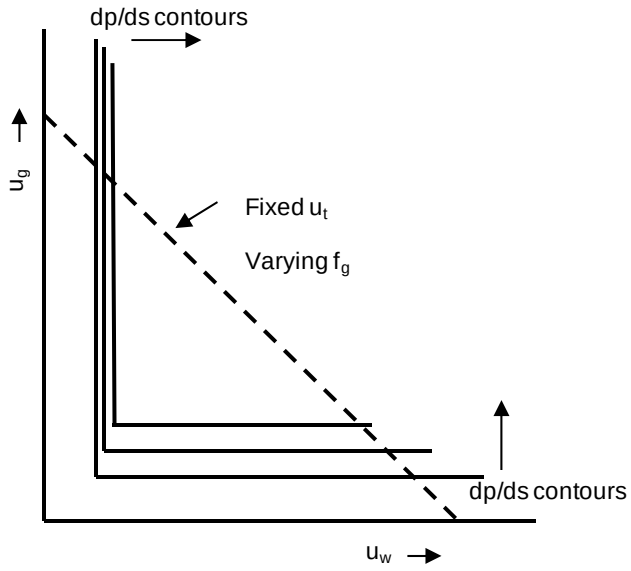

Fig. 40. Two foam-flow regime.[21-22]

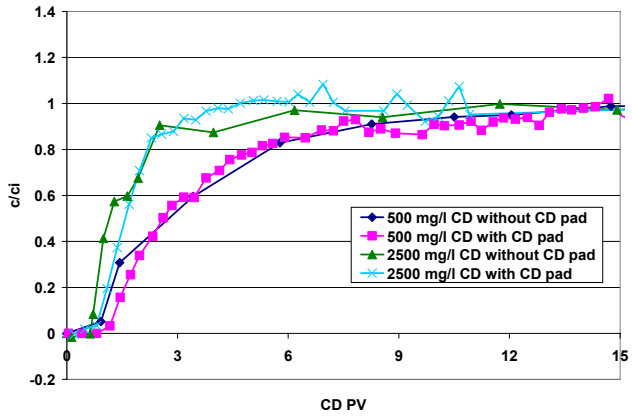

Fig. 41. CD adsorption profile.

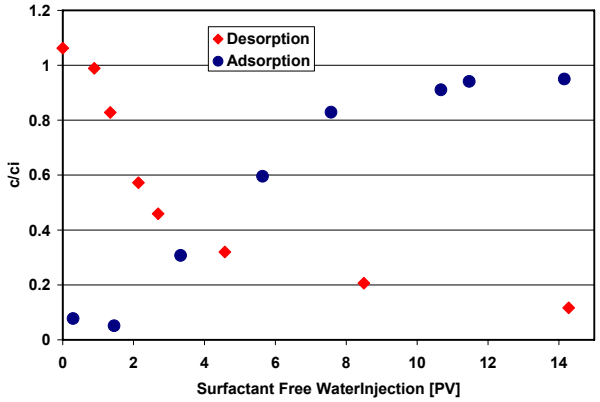

Fig. 42. Comparison of CD adsorption and desorption profiles for 500 mg/l

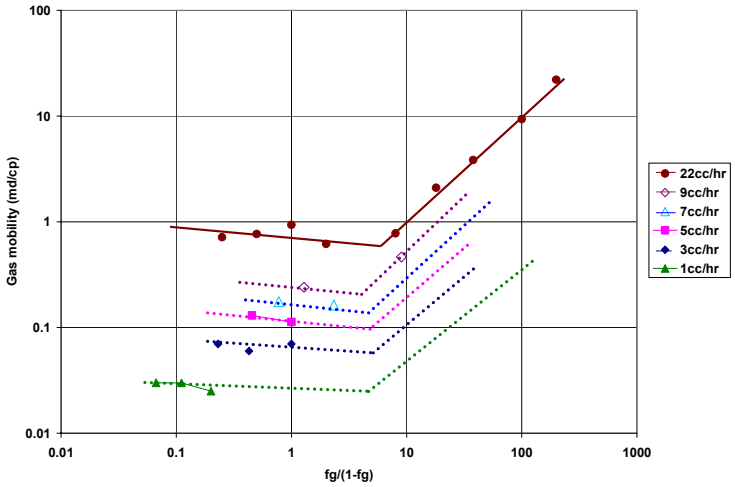

Fig. 43. Determination of f_g* at constant u_g.

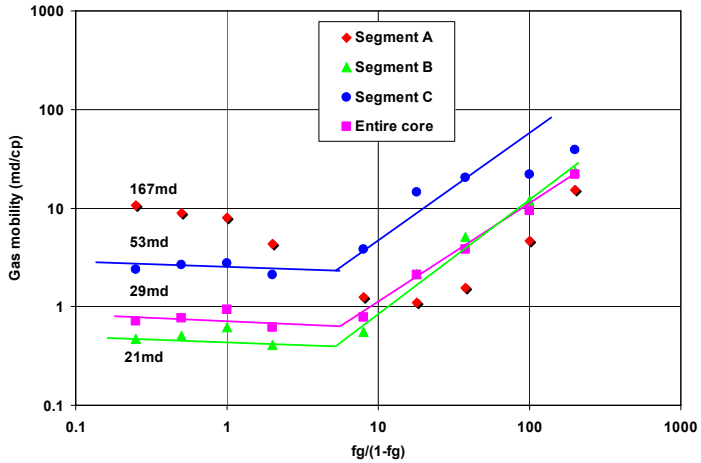

Fig. 44. Permeability effect on f_g*.

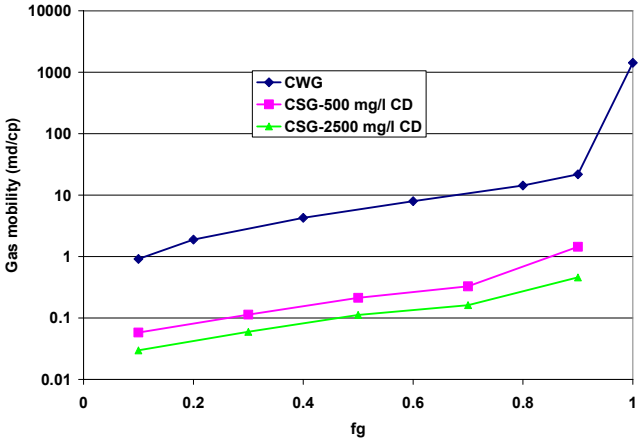

Fig. 45. The relation between foam quality and foam mobility at 10 cm^3/hr total flow rate as a function of surfactant concentration.

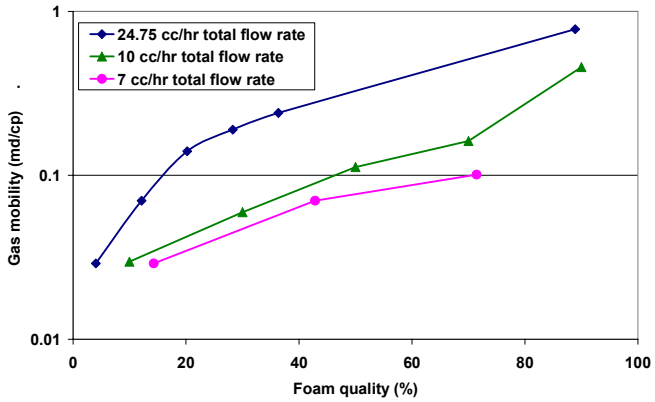

Fig. 46. Comparison of mobility obtained for Fig. 5 at constant qt=7 and 24.75 cm3/hr with mobility in Fig. 45 at qt=10 cm3/hr at 2500 mg/l CD.

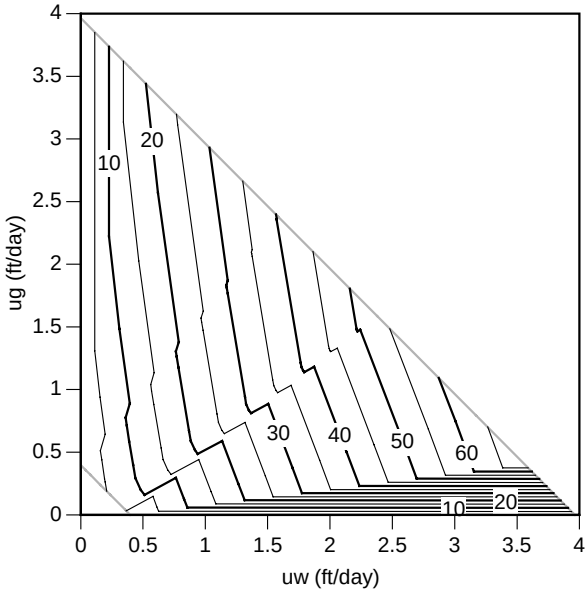

Fig. 47. CWG dp/ds contours (psi/ft) vs aqueous and gas phases Darcy velocity (ft/day).

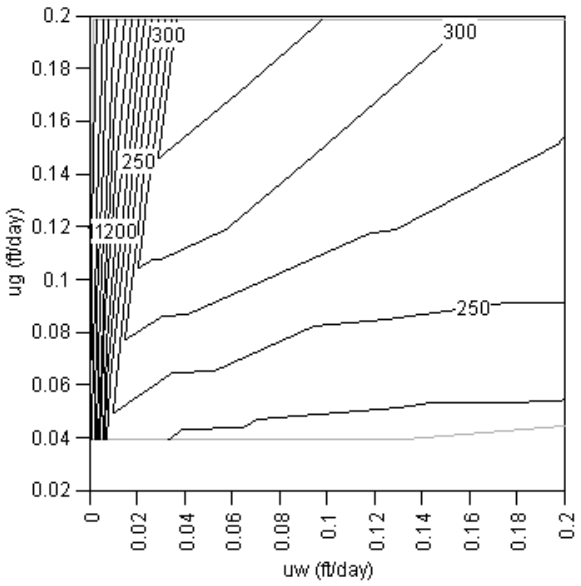

Fig. 48. CSG dp/ds contours (psi/ft) vs surfactant solution and gas phase Darcy velocity (ft/day).

A.3. Modeling of Adsorption and Desorption of Surfactant Used in CO_2 Flooding

Surfactant Flooding-Circulation Method

The circulation method was used because the experiment is a closed-system experiment; thus it was possible to observe when the maximum adsorption density had been reached. Figure 49 shows the schematic diagram of the circulation method.

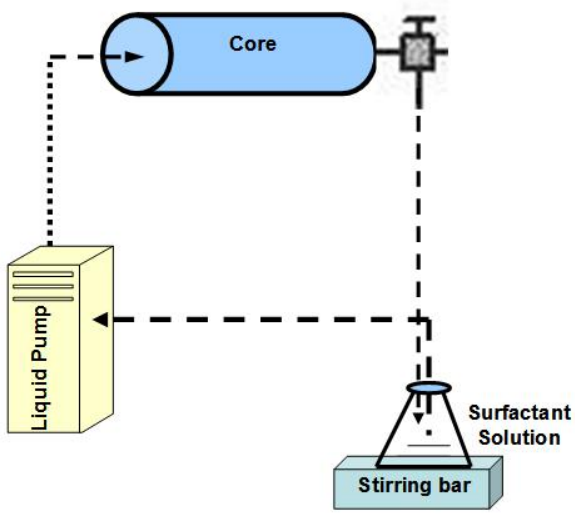

Fig. 49. Schematic diagram of circulation method.

In this experiment, brine was first circulated through the core at a constant rate until the core was completely saturated. A surfactant solution of known volume and concentration was injected and circulated through the core. Samples were taken from the surfactant solution at different time intervals for surfactant adsorption analysis. The amount of surfactant sample taken from the solution was recorded each time, but never replaced. The cycle of taking samples was repeated multiple times and the samples' concentration and surfactant adsorption density was determined using a material balance equation. The equation below gives the adsorption density after just one circulation or after taking one sample from the experiment.

$$\rho_{Ads} = \frac{((C_o - C_i) * M_S)}{(M_c * 1000)} \quad \text{.....8}$$

where

ρ_{Ads} = Surfactant adsorption density, mg/g

C_0 = Initial Surfactant concentration, mg/g

C_i = Surfactant Concentration after the i^{th} sampling, mg/L

M_S = Mass of Surfactant solution, g

M_C = Mass of the core sample, g.

Where more than one sample was taken, the above material balance equation was modified to account for all the samples taken and not replaced, in order to determine both the concentration of remaining surfactant solution after the ith sampling and the adsorption density.

$$\rho_{Ads} = \frac{[(M_t - \sum_{i=1}^{n-1} \lambda_S) - (M_S - \sum_{i=1}^{n-1} \lambda_L) * \frac{C_i}{1000}]}{M_C} \quad \text{.....9}$$

where

ρ_{Ads} = Surfactant adsorption density, mg/g

λ_s = Amount of surfactant in sample ith, mg/g.

M_t = Total amount of surfactant in the system, mg

C_i = Surfactant Concentration after the ith sampling, mg/L

M_S = Weight of Surfactant solution, g

M_C = Weight of the core sample, g

M_t = Total initial mass of surfactant, mg

λ_L = weight of sample ith, g

Surfactant Flooding: Multi-Tap Dynamic Method

Experiment Preparation and Setup

The preparation and setup for the multi-tap dynamic method required designing a coreholder that would allow taking samples while conducting surfactant flooding. This was necessary because the closed circulation system experiment could not show how surfactant concentration was changing as surfactant solution moved along the core. It was also necessary to investigate zones or sections of the core where the greatest loss of surfactant was occurring. Finally in order to take samples in the midst of surfactant flooding, the tap had to be put along the coreholder and the experiment had to be conducted under low pressure or at atmospheric pressure. The coreholder designed for the multi-tap experiment was made of PVC pipe filled with an equal ratio of sand and epoxy on the void spaces left once the core was placed inside. This made it possible to put tap along the core, collect samples

for surfactant concentration analysis, and was used at pressures as high as 100 psia. Table 8 gives the materials used in making the multi-tap core and core-holder.

Table 8. Materials Used in Making the Multi-Tap Experiment Coreholder

Material	Description	Source/Supplier
PVC Pipe	3" or 4" Regular plumbing pipe, with end caps	Ace Hardware Corp.
5 minute Epoxy	A quick-set epoxy	Ace Hardware
Polycarbonate rectangles	Rectangular shaped plastic	PRRC machine shop
Casing Epoxy	Given in tables 3-3 & 3-4	Sika Corporation of New Jersey, USA
Nylon Swagelok Fittings	Low Pressure and low Temperature fittings	Albuquerque Valve
Needles	1/16" needles	Fischer Scientific
Plastic ferrules	Sealing device	Albuquerque Valve
Wax paper	Non-stick material	Ace Hardware Corp.

The procedures for making the multi-tap experiment coreholder are as fellows:

- Place a dry and clean core on wax paper, and clearly mark position where the polycarbonate rectangles (or concentration tap) are to be placed.
- Apply t5-minute epoxy all over the core except the marked spots where the polycarbonate rectangles are to be placed.
- Apply 5-minute epoxy on the interior side of the polycarbonate rectangles and place them on the marked position on each side of the core.
- Apply 5-minute epoxy on the interior of the end cap polycarbonate squares and place them on each end of the core.
- Wait for half an hour and apply another layer of 5-minute epoxy all over the core.

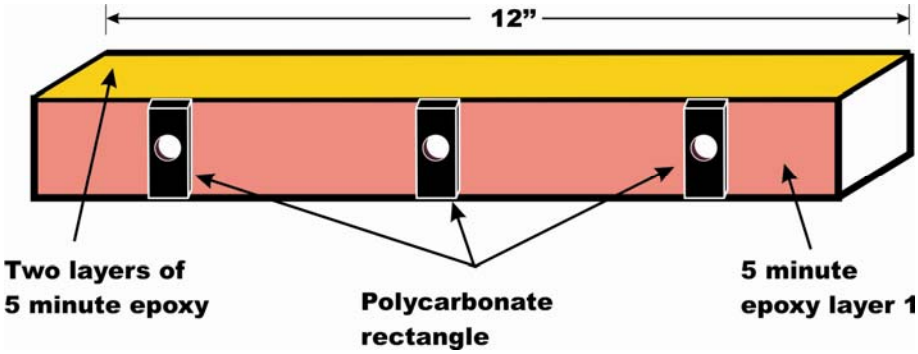

Fig. 50. Schematic diagram of early stages of multi-tap experiment coreholder design.

- Cut holes of about 29.0 mm in radius on each side of the PVC pipe at 2, 6, and 10 inches, and the PVC end caps (Inlet and Outlet) as shown by Figs. 50 and 51.
- Apply a third layer of 5 minute epoxy all over the core making sure that the layering is smooth, especially at the core edges.

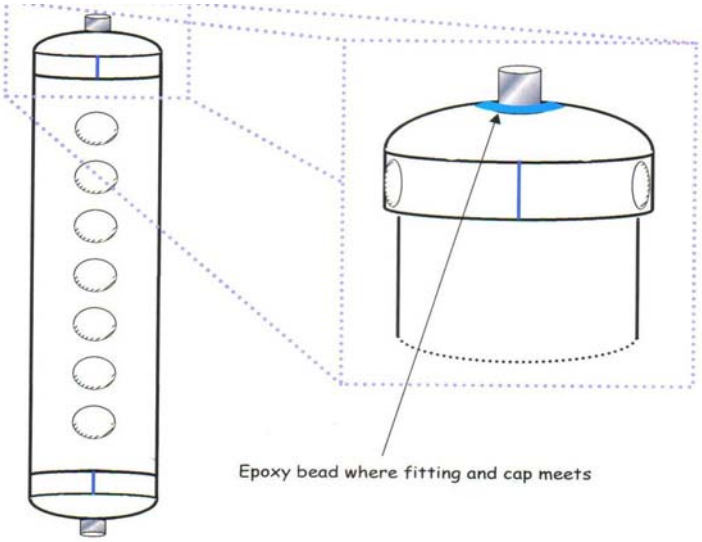

Fig. 51. PVC-pipe coreholder showing places where the holes were cut[95].

- Cut two more holes at 4 and 8 in. on each side of the PVC pipe, which are to be used for pouring the mixture of casing epoxy and sand into the core-holder as shown by Fig. 52

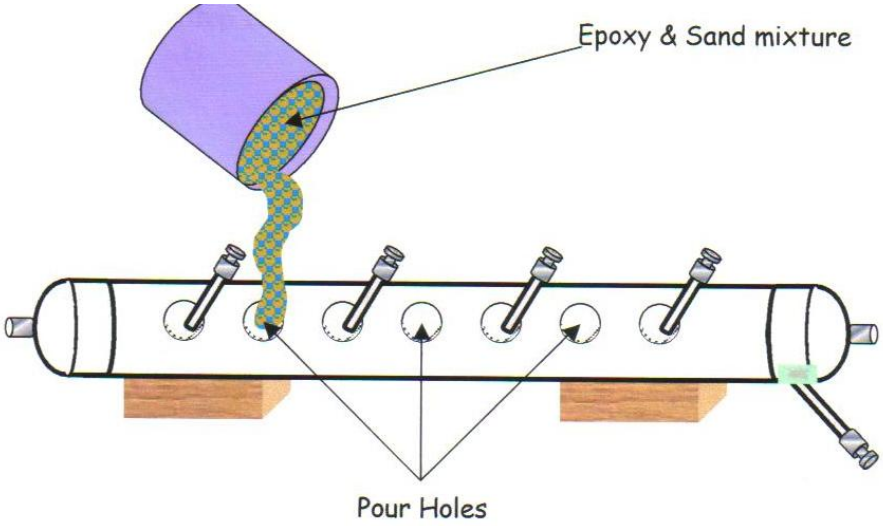

Fig. 52. Styles of pouring mixture of casing epoxy and sand into the PVC pipe core-holder[95].

- Insert Swagelock nylon fittings into the holes in the polycarbonate rectangles, and the end cap

polycarbonate squares.

- Pour mixture of casing epoxy and sand into pouring holes while the coreholder is tilted at an angle of 45 degrees. Allow about 10 hours for the casing epoxy to completely harden.
- Place the coreholder vertically and pour the mixture of casing epoxy and sand. Repeat the above step while the coreholder is positioned horizontally, allowing about 10 hours between each step.
- Place precut needles into the swagelok nylon fittings' holes and make sure the needles are touching the edge of the core.
- If holes are drilled into the core, longer needles that touch the bottom of the drilled holes must be designed and inserted into the core.
- Install syringe valves at the plastic ends of the needles for the purpose of shutting and opening the tap. Put plastic ferrules into the swagelok nylon fittings to seal it completely. The finished core and core-holder, with all the tubing's, needles and syringe valves is shown below in Fig. 53.

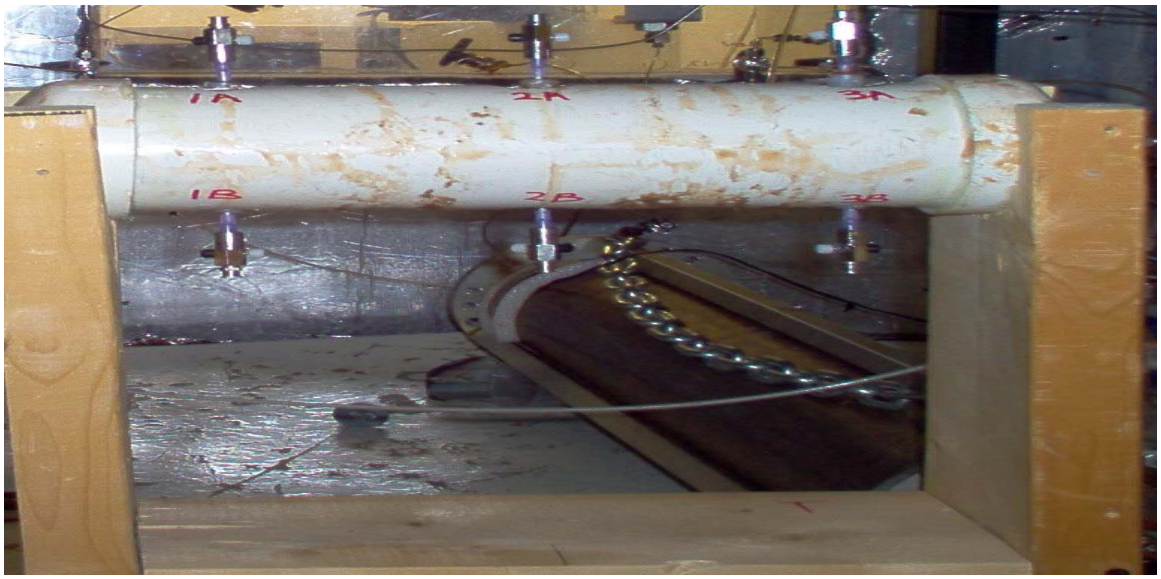

Fig. 53. Picture of the finished coreholder with all its fittings and tap.

After the core and its core-holder were built, the porosity of the core was determined using the method of mass differences between a saturated core and a dry core. The maximum pressure that the PCV pipe core-holder could be subjected was about 100 psia which was much less than the generally used pressure of 2000 psia.

Multi-Tap Dynamics Experiment: no holes drilled into core

In this experiment, needles were inserted into tap placed on the sides of a horizontally laid core. Therefore, all the samples were taken from tap placed on the surface of the core, three on each side. The multi-tap dynamic core had seven ports (tap), three on each side and one at the end of the core that samples were taken from as in Fig. 54. The experiments were performed in the following sequences:

- First, the core was saturated with 1.0 wt% brine and ports (tap) were tested to see if fluid would flow freely. The salinity of the 1.0 wt% brine was tested with a resistivity meter.
- Fives samples were taken from both the 1.0 wt% brine and 2.0 wt % and tested in order to determine the salinity of each fluid before the start of the waterflood.
- Waterflood (brine displacement) was initiated by displacing 1.0 wt% brine with 2.0 wt% brine. Samples were continuously taken from all the seven ports (tap) until all the 1.0 wt% brine was completely displaced.
- The waterflood (brine displacement) was performed while Tap "As" were at the top and Tap "Bs" were at the bottom of a horizontally laid core. The tap were labeled according to their distance from the inlet. Tap with similar numbers were equi-distant from the inlet. For instance, Tap 1A and 1B were placed 2.0 inches from the inlet. Fig. 54 shows a schematic diagram where all the seven occur along the core.

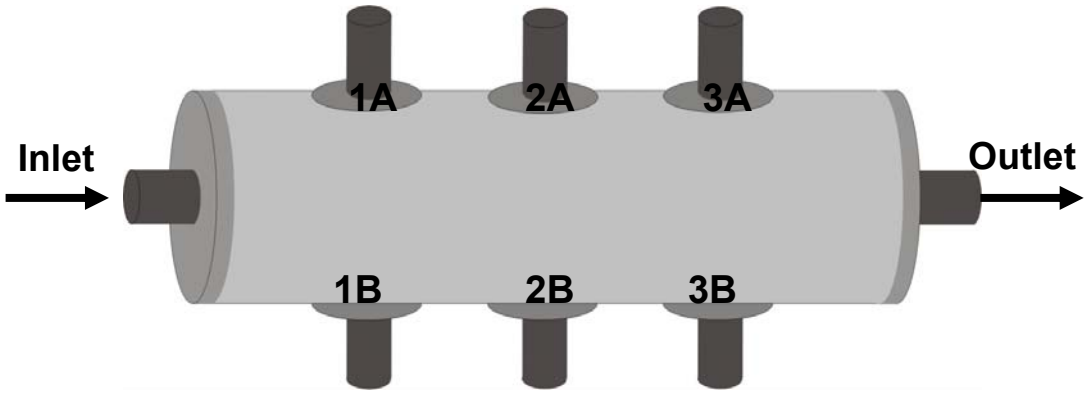

Fig. 54. Schematic diagram showing how the tap in the multi-tap dynamic experiment were labeled.

- The core was flipped (putting tap “Bs” on top and tap “As” at the bottom), saturated with 1.0 wt% brine and waterflood (brine displacement) repeated. The reason for flipping the core was to investigate the affect of gravity in the brine displacement process.
- Surfactant adsorption experiment was initiated and samples were taken from all the seven ports. Samples were continuously taken at short time intervals for about 10 hours.
- The samples collected from the surfactant flooding were analyzed using a photo spectrometer.
- Surfactant desorption experiment was initiated by flooding the core with 2.0 wt% brine. Samples were also taken from all the seven ports continuously.
- The surfactant concentrations of the samples collected were again analyzed using the photo spectrometer machine.

Multi-tap Dynamics Experiment (¼” Holes Drilled into the Core)

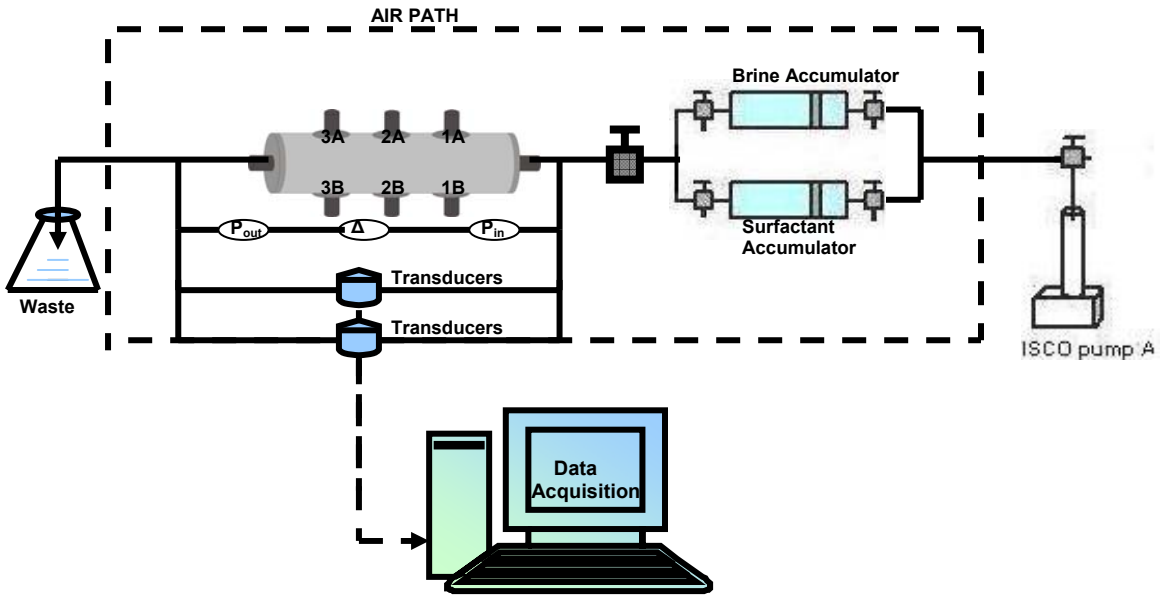

Fig. 55. Schematic diagram of the coreflooding setup.

Figure 55 shows schematic diagram of the coreflooding apparatus setup used in the multi-tap dynamic experiments. In the air path, shown by the dashed lines in Fig. 55, a constant temperature of 40°C (104°F) was maintained throughout the duration of the experiment.

Methods of Determining Chemical Concentration

Two methods were used in this study for determining changes in chemical concentration during surfactant (CD) flooding and waterflood (brine displacement). The two methods are by spectrometry which was used for determining CD concentration, and resistivity measurement, used for determining brine salinity changes. To determine CD concentration, a standard calibration curve for Chaser^{TM} CD 1045 was used. The adsorption density was calculated using a Freundlich isotherm model, an empirical equation which is generally applied to nonideal sorption that encompasses heterogeneous sorption. The equation in its general form is expressed as fellows:

$$q_e = K_F C_e^{1/n} \quad \text{..... 10}$$

where

q_e = Adsorption density onto sandstone, mg/g

K_F = Freundlich constant, (1/mg)

C_e = surfactant concentration, ppm

$1/n$ = Heterogeneity factor, or Freundlich exponent describes the degree of rock Heterogeneity in the rock. If n =1, the rock is homogeneous and the Freundlich isotherm reduces to the linear isotherm

Equation 10 can be expressed in its linear form by plotting equilibrium concentration versus adsorption density in logarithmic scale. Equation 3-8 gives Freundlich isotherm equation in log scale:

$$\log(q_e) = \log(K_F) + n\log(C_e) \quad \text{..... 11}$$

In calculating the adsorption density of the multi-tap dynamic experiment, two important assumptions were made:

- *Fluid Flow*. The first assumption was that half of the surfactant fluid injected flows through the tap at the top while the other half goes through the bottom tap. It is understood that this assumption is not entirely correct because the result of the brine displacement and the permeability measurement of the core affected fluid flow non-uniformly along the core.
- *Surfactant Retention*: It is also important to point out that surfactant flow in porous media partitions into two parts; surfactant in the fluid solution and surfactant adsorbed onto the porous

media which might have different values. Figure 56 shows a schematic diagram of how the surfactant fluid was assumed to flow through the core.

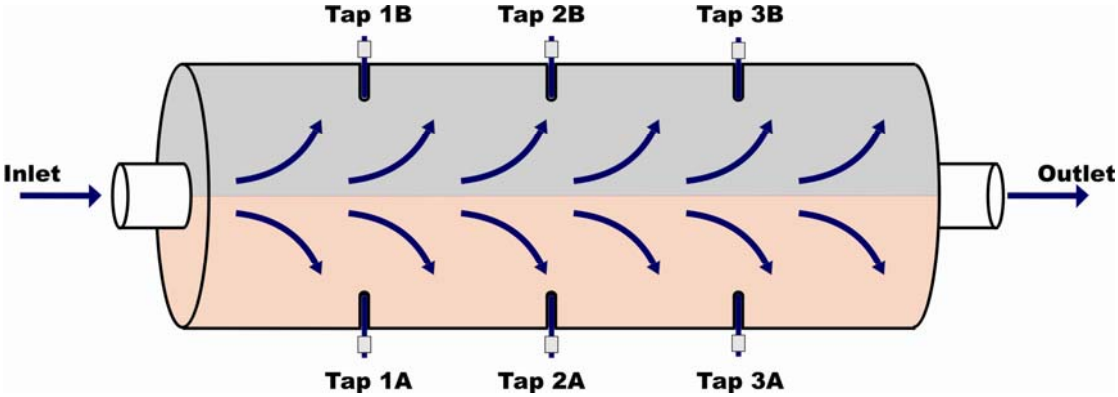

Fig. 56. Schematic diagram showing assumptions made in surfactant density calculation.

The equation used for this was

$$\rho_{AD} = \frac{(PV_i * 0.5 * C_i)/1000}{W_C * \frac{d_i}{L}} \quad \text{..... 12}$$

where

ρ_{AD} = Surfactant adsorption density, mg/g

PV_i = Surfactant pore volume injected at sample ith, fraction

C_i = Surfactant concentration of sample ith, ppm

W_C = Weight of core, g

d_i = Distance of tap nth from the port of injection, inches

L = Length of the core, inches

Surfactant retained was calculated for section one, represented by Tap 1A and 1B, and for the outlet tap, Tap 4, using the following equation.

$$\Delta R = \frac{(t_{i+1} - t_i) * 0.5 * q_f * (C_o - C_i)}{1.0E+06} \quad \text{..... 13}$$

$$R = \left(\frac{\sum_{i=1}^{n} \Delta R * K}{W_c * 0.5} + R_i\right)/2 \quad \text{..... 14}$$

where

ΔR = Change in surfactant retention, g

t = Change in time, min

q_f = Surfactant flow rate, cc/min

C_o = Original surfactant concentration, ppm

C_i = Surfactant Conc. of Sample ith, ppm

R_i = Surfactant retention at sample ith, mg/g

K = Conversion factor, 1000 ppm/mg

W_c = Weight of core, g

Resistance (Salinity) Measurements

Ohms meter was calibrated to salinity of NaCl-$CaCl_2$ (sodium chloride-calcium chloride) ratio of 3:1. Resistance is directly proportional to salinity (concentration) of the species present, assuming a constant species distribution and constant temperature.

$$S_{S_i} = \frac{(D_{M_i} - M_{V_i})}{S_{M_i}} * M_{R_i} \quad \text{..... 15}$$

$$S_{M_i} = M_{(V+S)_i} - M_{V_i}$$

where

S_{S_i} = Salinity of sample ith, ppm

D_{M_i} = Mass of diluted sample ith, g

M_{V_i} = Mass of vial ith, g

M_{R_i} = Salinity reading of sample ith, ppm

S_{M_i} = Weight of sample ith, g

Results and Discussion

Circulation Method

The circulation method was designed as a closed system where nothing was added or taken from the system except a few droplets (less than 0.5 g by weight) for sampling purposes. This method was chosen because of its straightforward material balance calculations where mass conservation for control volume formulas was used. Two types of porous media were used in the circulation method; their results are given below.

Sandstone Core Result

Figure 57 shows the result from the sandstone experiment and the adsorption density obtained from the circulation method. The results shows that as the surfactant adsorption increases (as evidenced by the increase in the adsorption density), the concentration of the surfactant in the flask decreases. The result also shows that at a given surfactant concentration, the adsorption density reaches an equilibrium where no more surfactant adsorption occurs even with continued surfactant flooding, which in this experiment was about 1.35 (mg/g). Table 8 summarizes the observed concentration change in the flask and the absorbance values obtained versus time. The result shows that surfactant adsorption was characterized by a rapid adsorption at the beginning of the experiment followed by a longer and slower adsorption process. Equation 8 was used to calculate the surfactant adsorption density given in Fig. 57.

.

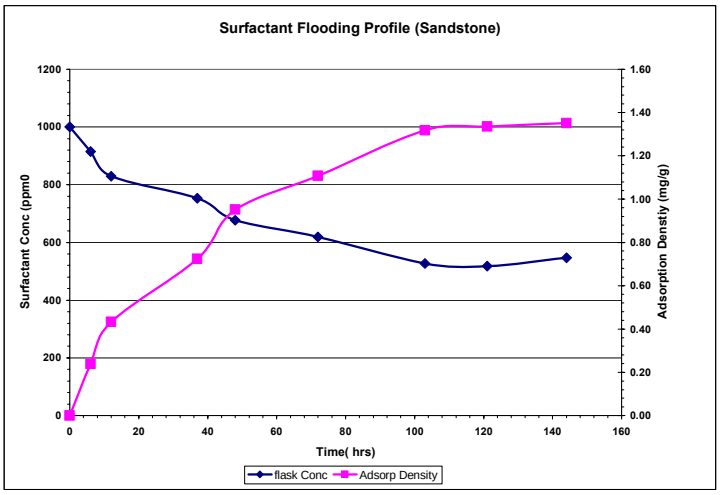

Fig. 57. Plot of surfactant adsorption density, concentration versus time in sandstone core.

Table 9. **Summary of Circulation Results from Sandstone**

Time (hrs)	Flask surfactant Conc.(ppm)	Sample weight (g)	Absorbance	Adsorption Density (mg/g)
0	1000	-	-	-
6	915	0.5013	1.691	0.2378
12	830	0.5095	1.631	0.4329
37	753	0.511	1.455	0.7236
48	677	0.5066	1.309	0.9522
72	619	0.4989	1.2	1.1071
103	527	0.5057	1.133	1.3182
121	518	0.5119	1.133	1.3354
144	547	0.5063	1.057	1.3507

Limestone Core Results

The result obtained from the limestone experiment similarly showed that as surfactant adsorption increased, the concentration of the surfactant in the flask decreased. However, one important difference between the sandstone and limestone experiment was that the rate of surfactant adsorption was higher in the sandstone even though the two experiments were performed under the same conditions such temperature, flow rate and concentration. Grigg and Bai[96] found that the degree of surfactant adsorption varied among three porous media (sandstone, limestone and dolomite) and that it took longer for sandstone to reach adsorption equilibrium. Also, Schramm[97] suggested that the composition of the porous rock, which is generally made up of mixtures of minerals such as quartz, clay, dolomite and limestone, affects surfactant-rock interactions. Figure 58 shows the result of the limestone experiment.

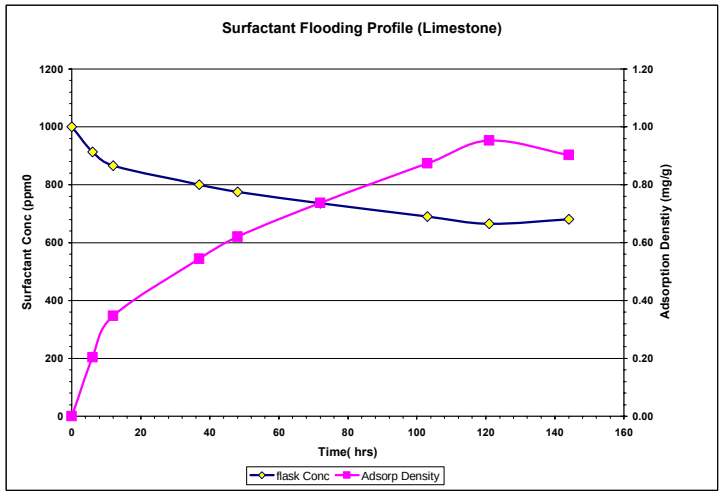

Fig. 58. Plot of surfactant adsorption density, concentration versus time in limestone core.

Table 10 shows the summary of the observed concentration changes in the flask solution and the absorbance values obtained versus time. The result also shows that the absorbance values which are directly proportional to the surfactant concentration are not decreasing as fast as they did in the case of the sandstone experiment because there was less surfactant adsorption in the case of limestone experiment. The equations used in determining the surfactant concentration of samples analyzed were Eq. 8.

Table 10. Summary of Circulation Method Results (from Limestone Core)

Time (hrs)	Flask surfactant Conc.(ppm)	Sample weight (g)	Absorbance	Adsorption Density (mg/g)
0	1000	-	-	-
6	914	0.5000	1.728	0.2042
12	866	0.5066	1.667	0.3469
37	801	0.5083	1.561	0.5442
48	775	0.5089	1.520	0.6204
72	736	0.5022	1.437	0.7375
103	690	0.5081	1.374	0.8744
121	665	0.5094	1.333	0.9523
144	681	0.5020	1.344	0.9036

Multi-Tap Experiment Results

Waterflood (Brine Displacement) Tap "As" on Top

There were two waterflood (brine displacement) experiments that were performed in the multi-tap dynamic system. The first experiment was carried while the "A" taps were on the top side of a horizontally-placed core. The results show that Tap 1B reached breakthrough before Tap 1A even though the two taps were equidistant from the port of injection. Similar results were observed for other taps such as 2A versus 2B and 3A versus 3B. These findings suggest that in the waterflood, more fluid was preferentially flowing in the bottom side of the core than in the top side. Another discovery was that Tap 4, which was the outlet tap, reached the maximum salinity plateau, which was the salinity of the injection brine (2.0 wt % brine), before Tap 3A and 3B, even though both taps were closer to the port of injection. The results indicate that factors such as gravity and anisotropic permeability are affecting the profile of the brine displacement profile, as the displacement pattern of different taps suggest.

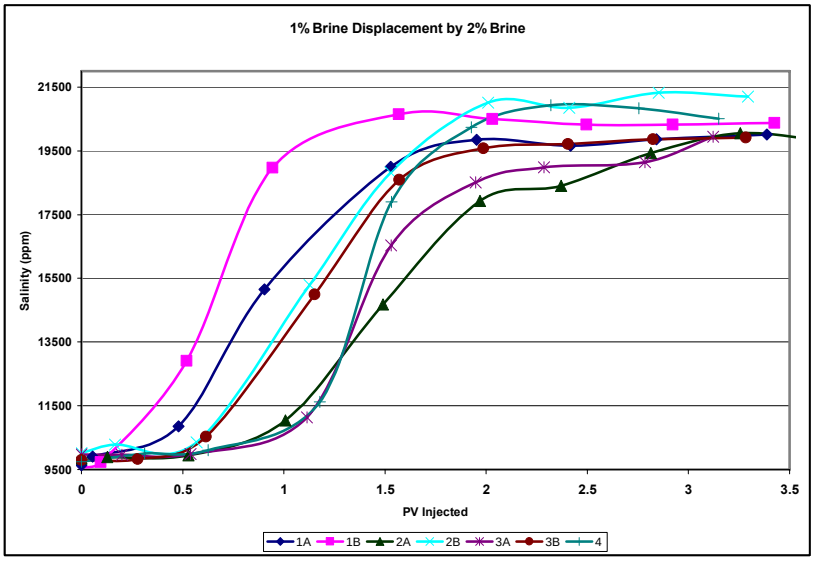

Fig. 59. Displacement profile of brine (1% by 2%) when tap "As" were top in all seven ports.

Tables 11 and 12 show the observed salinity changes in terms of part-per-million (ppm) versus pore volume of the 2.0 wt% brine injected for Tap 1A and 1B. The resistance meter used in this experiment had a maximum resistance measurement capability of 5000 ppm, while the salinities of the 1.0 wt% brine was about 10,000 ppm and the 2.0 wt% brine was about 20,000 ppm as

shown by Fig. 59. Therefore, the samples were diluted and then their resistivities were measured by multiplying the dilution factor back to the readings obtained from the resistivity meter.

Table 11. Results of Brine Displacement (1% by 2%) for Tap 1A

Sample #	PV Inj.	Time (min)	Vial Wt (g)	Vial + Sample weight	Sample Weight (g)	Sum of samples (wt)	Diluted Sample weight	Dilution Factor	Meter Rdg (ppm)	Salinity (ppm)
0	0.00	0	17.04	17.36	0.3131	0.5131	34.45	55.58	260	9634
1	0.06	2	16.83	17.17	0.3378	1.0509	34.14	51.24	290	9906
2	0.48	13	17.20	17.49	0.2939	1.5448	34.92	60.30	270	10854
3	0.91	24	17.115	17.43	0.3309	2.0757	35.01	54.11	420	15150
4	1.53	40	16.92	17.22	0.3036	2.5793	34.94	59.35	480	18993
5	1.95	51	17.16	17.46	0.2977	3.0770	34.89	59.56	500	19852
6	2.42	63	17.12	17.45	0.3274	3.6044	34.67	53.60	550	19655
7	2.84	74	17.06	17.37	0.3093	4.1137	35.13	58.42	510	19861
8	3.39	88	16.95	17.25	0.3006	4.6143	34.64	58.86	510	20012
9	3.85	100	17.04	17.35	0.313	5.1273	34.74	56.56	550	20738
10	4.36	113	17.14	17.44	0.2997	5.6270	34.99	59.54	520	20642
11	4.86	126	17.01	17.32	0.3057	6.1327	34.52	57.30	550	21008
12	5.40	140	17.07	17.40	0.3307	6.6634	35.07	54.44	550	19961
13	5.99	155	17.07	17.38	0.3092	7.1726	35.28	58.88	510	20019
14	6.57	170	17.18	17.48	0.3006	7.6732	34.94	59.10	520	20489
15	7.31	189	17.23	17.54	0.3129	8.1861	35.04	56.93	540	20495

Table 12. Results of Brine Displacement (1% by 2%) for Tap 1B

e #	PV Inj.	Time (min)	Vial Weight	Vial + Sample Weight	Sample Weight (g)	Sum of samples	Diluted Sample wt	Dilution Factor	Meter Rdg (ppm)	Salinity (ppm)
0	0.01	0	17.08	17.39	0.3131	0.5131	35.0709	57.46	250	9577
1	0.10	3	17.07	17.41	0.3396	1.0527	34.7820	52.15	280	9735
2	0.52	14	17.29	17.58	0.2953	1.5480	35.1538	60.48	320	12903
3	0.94	25	17.22	17.55	0.3242	2.0722	34.9645	54.71	520	18967
4	1.57	41	17.07	17.40	0.3307	2.6029	34.7381	53.40	580	20648
5	2.03	53	17.14	17.47	0.3276	3.1305	34.5141	53.01	580	20498
6	2.50	65	17.11	17.40	0.2923	3.6228	35.2996	62.22	490	20325
7	2.92	76	17.16	17.45	0.2874	4.1102	34.6878	60.97	500	20325
8	3.43	89	17.00	17.30	0.3026	4.6128	34.7908	58.79	520	20381
9	3.93	102	17.13	17.42	0.2816	5.0944	35.1609	64.00	480	20480
10	4.40	114	17.09	17.38	0.2932	5.5876	35.2189	61.81	500	20603
11	4.94	128	16.93	17.23	0.2930	6.0806	34.3771	59.52	510	20235
12	5.52	143	16.93	17.24	0.3066	6.5872	34.7212	58.00	520	20106
13	6.07	157	17.09	17.43	0.3387	7.1259	34.6811	51.92	590	20421
14	6.65	172	16.99	17.29	0.2979	7.6238	34.7598	59.64	520	20674
15	7.51	194	17.15	17.49	0.3368	8.1606	34.8605	52.57	600	21030

The results obtained when the “A” taps were on top for Tap 2A and 3A shows that Tap 3A had higher salinity (ppm) than 2A at about 1.5 PV even though 2A was closer to the port of injection, which means that the brine was likely bypassing some zones such as zones around the location of Tap 2A. The breakthrough times and the time waterflood reached maximum salinity of the 2.0 wt% brine in all “A” Taps were in numeric order. The result for “B” Taps, which were on the bottom side of a horizontally laid core, shows that there were no overlaps in “B” Tap displacement profiles, and the order of breakthrough times was in numeric order.

Figure 60 shows the result of brine pore volume injected before 2.0 wt % brine breakthrough was detected in all taps. The result shows that 2.0 wt % brine breakthrough was reached in Tap 1A and 1B at about 0.6 PV, while Taps 2 and 3 breakthrough times were about 1.2 PV and 1.4 PV respectively. It is interesting to note that the distance between Tap 1 and Tap 2 was equal to that between Tap 2 and Tap 3, but the progression of the breakthrough times was not linear, which suggests that there was some inherent heterogeneity in the core.

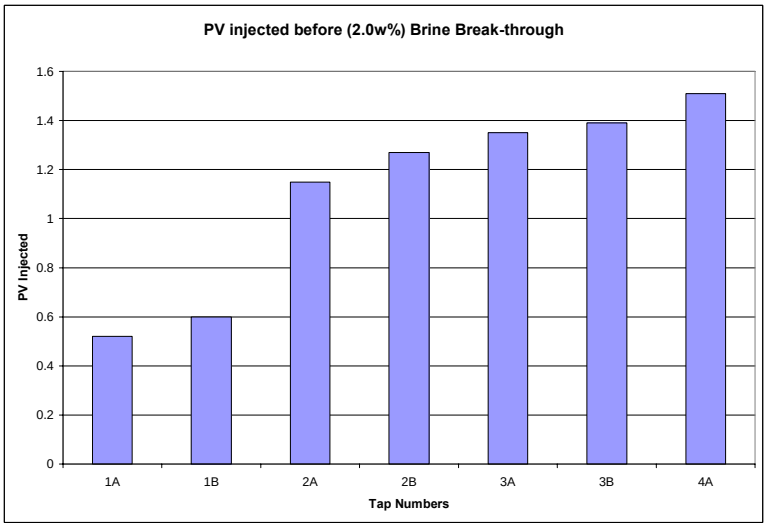

Fig. 60. Pore volume injected before salinity increase was first detected in each tap.

Figure 61 shows the results of the brine displacement profile of Tap 4 when "A" Taps were on the top side of the core (labeled as experiment 1), when "B" Taps were on the top (labeled as experiment 2), and when samples were taken only from Tap 4 (labeled as experiment 3). The number of samples taken in experiment 2 were about two-thirds of those taken in experiment 1. The results show that the effect of taking more samples on the brine displacement profile caused a shift of the graph to the right.

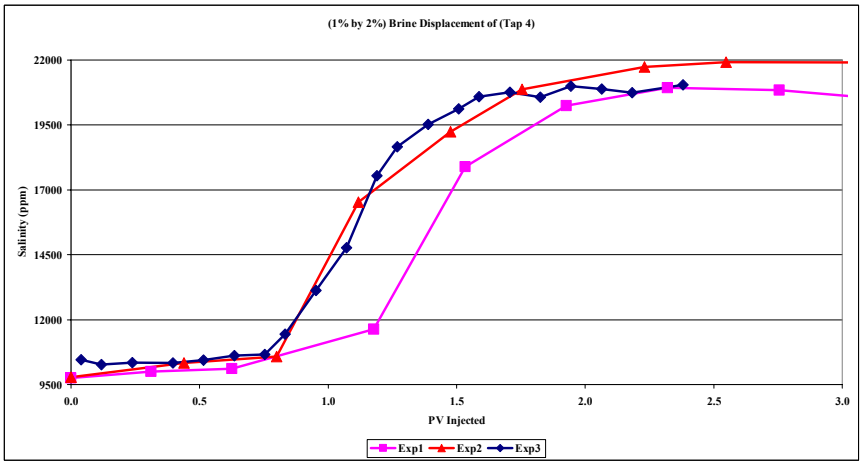

Fig. 61. Result obtained from Tap 4 in experiments 1 &2, and in experiment 3 where samples were taken only from Tap 4.

Waterflood (Brine Displacement) "B" Taps on Top

Because of the differences in breakthrough between the taps at the top, "A" Taps, and the ones at the bottom, "B" Taps, the core was flipped in order to investigate gravity effects versus heterogeneity. Figure 62 shows the result obtained when the core was flipped and "B" Taps were on top. Tap 1B was again the first tap to reach maximum salinity peak-off among all Taps, as in the previous experiment. Another observation is that the taps that were same distance from the port of injection, hence with similar tap numbers (such as 1A and 1B, 2A and 2B, and 3A and 3B), reached maximum salinity peaks almost at the same time or were very close to each other, unlike in the previous experiment, where they had clearly different timings. Another observation is that while gravity was an issue that might have contributed to some of the discrepancies observed, other factors were clearly in play. For example, if the differences in breakthrough amongst taps that were equidistant were caused by gravity alone, then how can we explain the fact that even when the core was flipped still Tap 1B was the first tap to reach salinity concentration peak? A similar result was also obtained in the case of Taps 3A and 3B, where Tap 3B reached salinity peak both times whether it was on the bottom or on the top side of the horizontally laid core. Therefore, gravity alone was not the cause of the differences observed in breakthrough; other factors such as permeability had to be investigated.

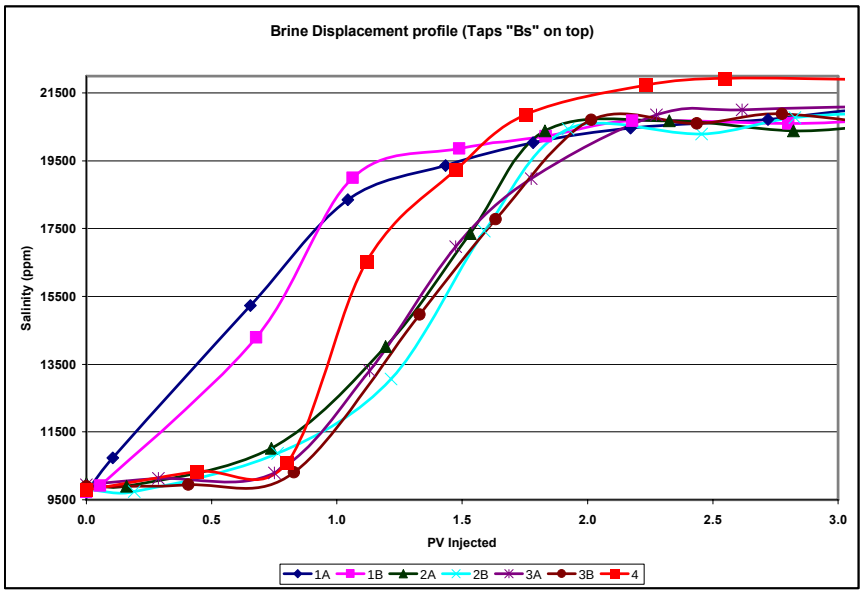

Fig. 62. Brine displacement profile (1% by 2%) when "B" Taps were on top.

Surfactant Flooding Results

Surfactant flooding of the multi-tap dynamic experiment was carried out when "A" Taps were on the top side of a horizontally laid core. There were two types of experiments that were performed in the surfactant flooding experiment; surfactant adsorption and surfactant desorption.

Figure 63 shows the observed surfactant concentration changes in all seven taps versus pore volume of surfactant injected. The result shows that there were significant differences in surfactant concentration changes amongst tap that were equidistant from the port of injection. For instance, the concentration changes of Tap 1A and 1B were quite different even though both of them were one inch from the injection port. Figure 63 also shows that the concentration of Tap 4, the outlet tap, reached the source surfactant concentration when nearly half of the other tap's surfactant concentrations were approximately 50% of the source surfactant concentration. In other words, after 18 pore volumes (PV) of surfactants injection, the concentration of the source and that of effluent (Tap 4) were the same (at about 1000 ppm). The result also shows that only four (1A, 1B, 2B, and 4) out of the seven taps reached the concentration of the source surfactant while the other three taps (2A, 3A and 3B) never reached anywhere close to the source surfactant concentration even after 18 PV of surfactants were injected. The surfactant concentration changes were normalized to the source surfactant concentration, which was about 1030 ppm.

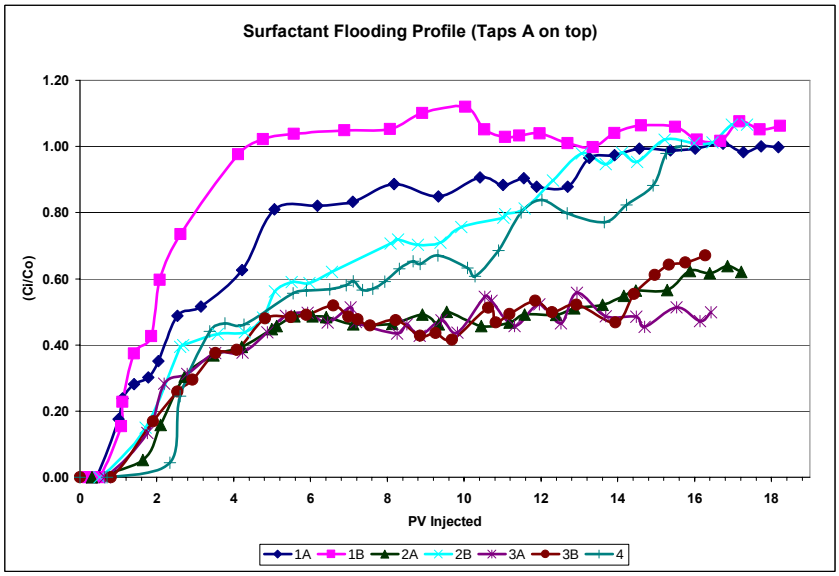

Fig. 63. Surfactant concentration changes versus pore volume injected for all seven taps.

Table 13. Surfactant Concentration Changes Observed for Tap 2A

Sample #	Time (min)	PV Inj.	Sample Wt (g)	Surfactant Mass (g)	Absorbance	Normalized Conc. C_i/C_o	Surfactant Conc. ppm
1	0	0.00	0.4947	0.00	0.085	0.00	0.00
2	10	0.39	0.3700	0.00	0.149	0.00	0.00
3	45	1.75	0.3821	20.38	0.243	0.05	53.33
4	58	2.25	0.2884	47.17	0.363	0.16	163.57
5	75	2.91	0.3346	104.78	0.621	0.30	313.16
6	95	3.69	0.2839	107.91	0.635	0.37	380.10
7	115	4.47	0.3506	142.52	0.79	0.39	406.51
8	136	5.28	0.2899	133.81	0.751	0.45	461.58
9	140	5.44	0.3510	165.08	0.891	0.46	470.30
10	153	5.94	0.3475	174.01	0.931	0.49	500.74
11	166	6.45	0.3391	169.76	0.912	0.49	500.63
12	176	6.84	0.2998	149.44	0.821	0.48	498.48
13	195	7.58	0.3117	148.33	0.816	0.46	475.87
14	222	8.62	0.3236	154.80	0.845	0.46	478.38
15	243	9.44	0.3155	159.94	0.868	0.49	506.94
16	255	9.91	0.3110	148.33	0.816	0.46	476.94
17	261	10.14	0.3518	181.38	0.964	0.50	515.57
18	285	11.07	0.3053	143.64	0.795	0.46	470.48
19	305	11.85	0.3385	163.07	0.882	0.47	481.73
20	316	12.28	0.3257	165.08	0.891	0.49	506.83
21	338	13.13	0.3152	159.27	0.865	0.49	505.30
22	351	13.64	0.3240	170.66	0.916	0.51	526.72
23	371	14.41	0.3211	172.67	0.925	0.52	537.74
24	386	15.00	0.3084	174.23	0.932	0.55	564.95
25	395	15.35	0.3270	190.08	1.003	0.56	581.30
26	417	16.20	0.3002	174.90	0.935	0.57	582.61
27	433	16.82	0.3229	207.28	1.08	0.62	641.93
28	447	17.37	0.3095	196.56	1.032	0.62	635.09
29	460	17.87	0.3006	197.45	1.036	0.64	656.87
30	470	18.26	0.3285	209.96	1.092	0.62	639.14

The surfactant CD 1045 was used. The results are shown in Fig. 63: only tap 1B reached the injection surfactant concentration (which was about 1030 ppm) at the early stages of the flooding process (at about 4 PV), and it took another 10 PV of surfactant injection for the next Tap, 1A and 2B at about 14 PV, to reach the injection surfactant concentration. This shows that surfactant efficiency, which is defined as the amount of surfactant required to produce a desired

amount of change in a phenomenon varies widely among all the taps, and that some of the taps that had low surfactant concentration may not have achieved the desired change even after 18 PV of surfactant was injected.

Table 14. Surfactant Concentration Change Results for Tap 2B

Sample #	Time (min)	PV Inj.	Sample Wt (g)	Surfactant Mass (mg)	Absorbance	Normalized Conc. C_i/C_o	Surfactant Con. ppm
1	0	0.00	0.4905	0.00	0.14	0.00	0.00
2	15	0.58	0.3912	0.00	0.142	0.00	0.00
3	47	1.83	0.3759	58.34	0.413	0.15	155.20
4	71	2.76	0.2645	107.46	0.633	0.39	406.29
5	74	2.87	0.2854	117.29	0.677	0.40	410.96
6	98	3.81	0.2639	117.74	0.679	0.43	446.14
7	117	4.55	0.3722	167.98	0.904	0.44	451.31
8	130	5.05	0.3514	174.68	0.934	0.48	497.09
9	139	5.40	0.3187	184.50	0.978	0.56	578.92
10	151	5.87	0.3424	208.17	1.084	0.59	607.98
11	164	6.37	0.3818	230.73	1.185	0.59	604.31
12	180	6.99	0.3912	249.93	1.271	0.62	638.88
13	220	8.55	0.2832	205.94	1.074	0.71	727.19
14	226	8.78	0.2935	217.10	1.124	0.72	739.71
15	240	9.32	0.3609	261.09	1.321	0.70	723.45
16	256	9.95	0.3292	240.55	1.229	0.71	730.71
17	271	10.53	0.3062	238.32	1.219	0.76	778.31
18	300	11.66	0.3291	266.01	1.343	0.78	808.29
19	302	11.73	0.3256	266.45	1.345	0.79	818.35
20	316	12.28	0.3225	270.03	1.361	0.81	837.29
21	336	13.05	0.3308	305.53	1.52	0.90	923.61
22	356	13.83	0.351	353.76	1.736	0.98	1007.87
23	373	14.49	0.307	299.50	1.493	0.95	975.58
24	385	14.96	0.3181	321.39	1.591	0.98	1010.33
25	396	15.38	0.3257	319.82	1.584	0.95	981.95
26	415	16.12	0.3128	328.53	1.623	1.02	1050.29
27	436	16.94	0.3345	347.96	1.71	1.01	1040.23
28	449	17.44	0.3091	322.28	1.595	1.01	1042.64
29	463	17.99	0.3204	351.75	1.727	1.07	1097.86
30	474	18.41	0.2975	326.74	1.615	1.07	1098.30

Tables 13 and 14 show the observed results for Taps 2A and 2B respectively. The results show that even though the two taps were equidistant from the port of injection, their surfactant concentration changes were quite different. In fact, Tap 2A never reached the source surfactant concentration even after 18 PV of surfactants were injected while Tap 2B managed to reach source surfactant concentration at about 14 PV.

Among the taps (1A, 2A & 3A) that were on the top side of a horizontally laid core, only Tap 1A reached the injection surfactant concentration while among the tapa that were on the bottom side of the core (1B, 2B and 3B), only Tap 3B did not register source surfactant concentration. This result suggests that the surfactant flooding had a preferential flow path through the core and that the lower section of the core had higher surfactant efficiency, higher surfactant adsorption, and probably higher surfactant effectiveness.

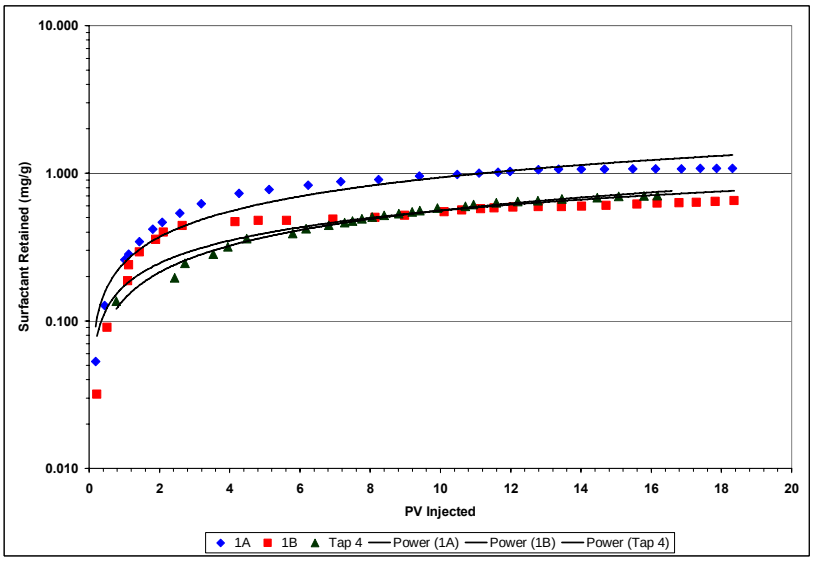

Fig. 64. Surfactant retention results from the multi-dynamic experiment of core 1.

Surfactant Adsorption Results

Table 15 shows the results of the surfactant adsorption modeling that was obtained using the Freundlich isotherm model. These results indicate two important findings; first, the highest surfactant retention was taking place near the source of injection (near-wellbore) as shown by the adsorption profiles of Taps 1A and 1B. Secondly, surfactant retention reached the plateau region when the surfactant concentration reached the source surfactant concentration. It is interesting to note that the surfactant retention profile of Tap 4, the outlet tap, which has been the basis of many surfactant retention/adsorption studies[96] in the literature, was found in this study to be

underestimating retention of surfactant near the injection port (near-wellbore). Finally, these results show that surfactant retention was characterized by very rapid retention/adsorption at the beginning of the flooding process followed by a slower and longer retention pattern.

Table 15. Results Obtained from Freundlich Isotherm Modeling for Cores 1 and 2

Tap Number	Freundlich Isotherm Equation	Freundlich Constant, K_F	Heterogeneity Factor, (n)
Core 1: 1A	$y = 0.2477 * x^{0.5774}$ $R^2 = 0.9408$	0.2477	$1/n = 0.5774$
Core 1: 1B	$y = 0.1723 * x^{0.5104}$ $R^2 = 0.8385$	0.1723	$1/n = 0.5104$
Core 1: 4	$y = 0.1403 * x^{0.6008}$ $R^2 = 0.9824$	0.1403	$1/n = 0.6008$
Core 2: 1A	$y = 0.286 * x^{0.548}$ $R^2 = 0.9242$	0.286	$1/n = 0.5480$
Core 2: 1B	$y = 0.1754 * x^{0.8425}$ $R^2 = 0.9858$	0.1754	$1/n = 0.8425$
Core 2: 4	$y = 0.079 * x^{0.8508}$ $R^2 = 0.9935$	0.079	$1/n = 0.8608$

Table 15 shows the results obtained from the surfactant retention/adsorption modeling using the Freundlich Isotherm equation. The result shows that all three taps accurately fit the Freundlich isotherm model used for nonideal retention/adsorption that involves heterogeneous retention, as evidenced by their respective correlation factors. Two things to note are that the Freundlich constant degrees from section one, represented by Taps 1A and 1B, to the outlet tap, Tap 4, which indicates that the degree of surfactant adsorption decreased along the core as surfactant flooding progressed from the tap near the port of injection to the outlet tap. Secondly, most of the surfactant retention/adsorption was taking place near the injection port as evidenced by the retention values of Taps 1A and 1B.

The heterogeneity factor, which ranges from 0 to 1, explains the degree of heterogeneity in the core chemical structure and composition. A heterogeneity factor of zero means the core is

completely heterogeneous, while a factor of one means the core is very homogeneous, and reduces the Freundlich isotherm to the linear isotherm. The average heterogeneity factor of all three taps of core 1 was about 0.56, which suggests that the core was fairly homogeneous, considering that in porous media, it is impossible to find completely homogenous rock, especially at the scale of oil and gas reservoirs. It is interesting to note that Tap 4, which represents the heterogeneity factor of the whole core, has the lowest heterogeneity factor amongst all the taps. This demonstrates that as the scale of porous media increases, its heterogeneity factor decreases.

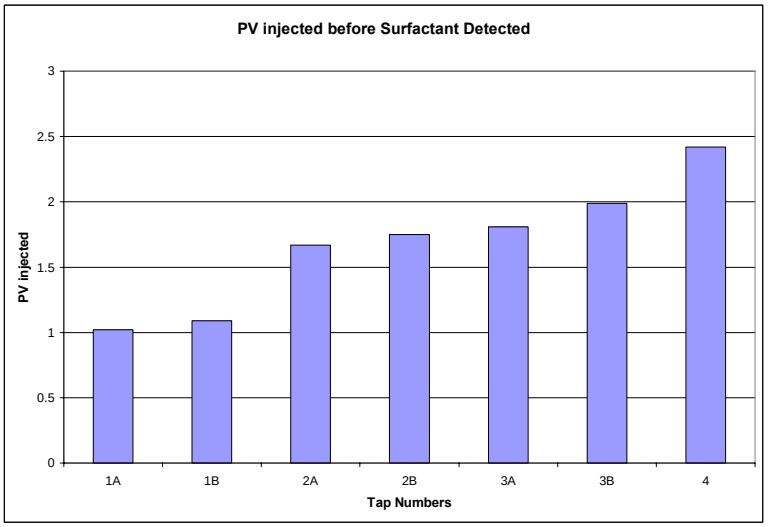

Fig. 65. Pore volumes injected before surfactants were detected in each tap.

Figure 65 represents the amount of surfactant PV injected before any surfactant was detected in any of the seven ports (taps). The result shows that about 1.0 PV of surfactant had to be injected before any surfactant was detected in the Taps (1A & 1B) that were closest to the injection source. The results also show that it took about 2.5 PV of surfactant injection before any surfactant was detected at the outlet port (Tap 4) and that the process of surfactant detection in all taps was in chronological order where the tap closest to the port of injection came first, followed by the tap in the middle, and lastly the tap at the end of the core. Figure 66 represents the amount of surfactant injected in each section, in terms of its PV, before any surfactant was detected. More importantly, the results shows that about 6.3 PV had to be injected in section one, the section closest to the port of injection (wellbore), which clearly reinforces the view that most

surfactant loss occurs near the port of injection and that surfactant does not propagate further into the core (or reservoir), especially if only 1.0 PV is injected.

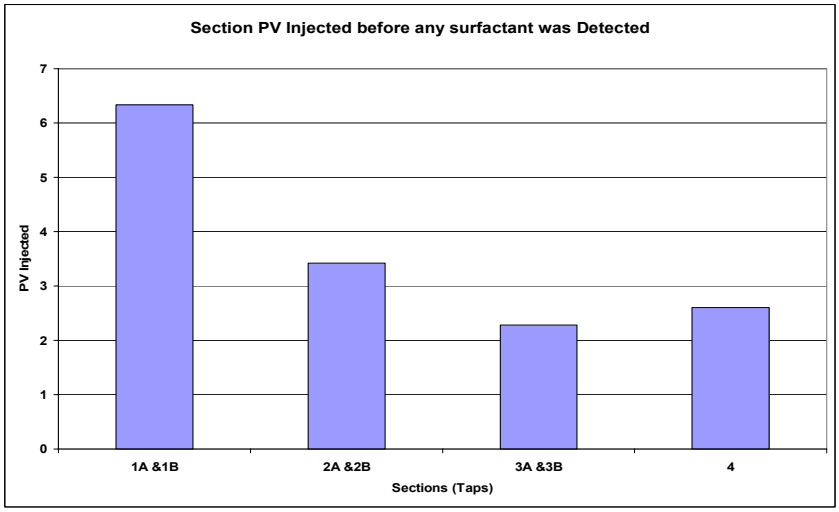

Fig. 66. Average section PV injected before any surfactant was detected.

Surfactant Desorption Results

Figure 67 shows the results obtained from the surfactant desorption experiment conducted with "A" Taps on the top side of a horizontally-laid core. The results show three important findings; first, surfactant desorption was characterized by rapid desorption at the beginning, especially in high surfactant concentration zones/section, followed by a slower and longer desorption. Secondly, the desorption process was nonuniform among the core ports. The "B" Taps on the bottom side of the core had more surfactant desorption than the "A" Taps , which were on the top. In fact, the taps with the lowest surfactant concentration at the end of the desorption experiment were all from the bottom side of the core (1B, 2B and 3B). Thirdly, there was very little surfactant desorption in zones/section that had low surfactant concentration at the beginning of the experiment. For instance, Taps 2A and 3A, which had the lowest surfactant concentration at the beginning of the surfactant desorption experiment, ended up having the highest surfactant concentration at the conclusion of the desorption experiment. It is important to note that the surfactant desorption experiment was done ten days after the surfactant flooding experiment, which was roughly the time it took to analyze the concentration of the samples collected. Table 16 shows the effect of the 10 days shut-in on the concentration of the surfactant in the core. Surfactant concentration in all taps declined except that of Tap 3A, but the biggest change occurred in the tap that had reached maximum surfactant

concentration at the end of the surfactant flooding experiment. The cause could be attributed to the effect of surfactant diffusion and/or surfactant bio-degradation. Grigg and Mikhalin[12] found that it takes hours to days for flow-through surfactant flooding, and week to months for no-flow (diffusion dominated) to reach equilibrium.

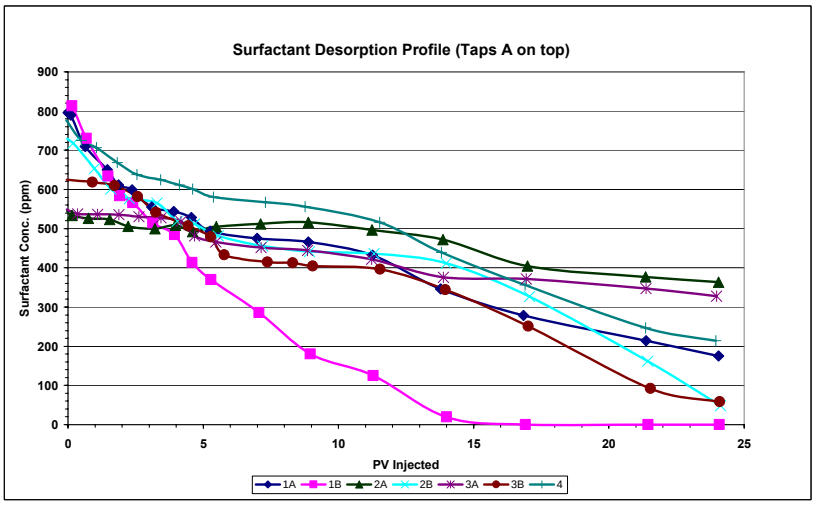

Fig. 67. Surfactant desorption profile of Core_1 multi-tap.

Table 16. Effect of 10 Days of Shut-In on the Surfactant Concentration in the Core

Tap Number	Conc. At end of surfactant flooding (ppm)	Conc. At beginning of Desorption Exp(ppm)	Concentration Change (%)
1A	1027	795	-22.6%
1B	1094	817	-23.5%
2A	639	544	-14.7%
2B	1098	729	-33.6%
3A	513	548	6.8%
3B	690	624	-9.5%
4	1031	776	-24.7%

Figure 68 shows a comparison of the surfactant desorption profile of Tap 1A and 1B, which were the closest taps to the port of injection and had the highest surfactant concentration at the beginning of the experiment. There was complete desorption in 1B, which was at the bottom side of the core, while Tap 1A had about 180 ppm of surfactant concentration after 25 PV of brine injection. Another important finding was that in previous studies, researchers[4] reported that desorption was biphasic; a rapid process at the beginning, and a slower and longer process that never reached zero concentration. In this study we found that surfactant desorption of the taps that

were closest to the port of injection and were on the bottom side of the core actually approached zero as shown by Figures 68 and 69. It is important to point out that in previous studies, researcher based their conclusion of "no zero desorption reached" on the profile of the outlet tap, Tap 4, and did not have a concentration tap along the core that showed whether some parts of the core had indeed reached zero desorption.

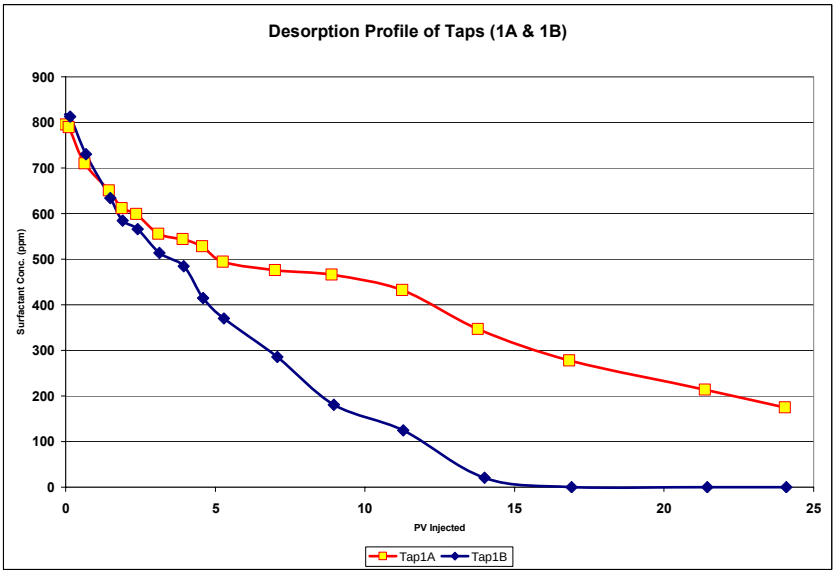

Fig. 68. Comparison of surfactant desorption profile of tap 1A and 1B, which are closest to the port of injection.

Tables 17 and 18 show experimental results of surfactant desorption data for the Tap 1A and 1B which were closest to the port of injection. The results shows that even though the surfactant concentration of the two taps were almost equal at the beginning of the desorption experiment and that the two taps were equidistant from the port of injection, their desorption results were totally different. In the waterflood (brine displacement), it was found that gravity had an effect on the brine displacement profile and breakthrough times, but could not have caused such massive discrepancies in the desorption profile of equidistant taps. Another factor that was thought to be playing a role in the discrepancies observed in both the adsorption and desorption results, and that warranted some investigation, was the affect of anisotropic permeability. The result obtained from the permeability investigations are given in the Mini-Permeameter Measurement section.

Table 17. Surfactant Desorption Experiment Result for Tap 1A

Sample #	Time (min)	PV Inj.	Sample Wt (g)	Surf. Mass (mg)	Absor.	Norm. Conc. C_i/C_o	Sur. Conc. (ppm)
0	0	0.0	0.3294	261.99	1.325	0.77	795.35
1	3	0.1	0.3115	245.91	1.253	0.77	789.44
2	17	0.7	0.305	216.43	1.121	0.69	709.62
3	38	1.5	0.3309	215.09	1.115	0.63	650.03
4	49	1.9	0.2978	182.05	0.967	0.59	611.30
5	62	2.4	0.3369	178.47	0.951	0.58	599.31
6	81	3.1	0.3137	186.96	0.989	0.54	554.94
7	102	4.0	0.3093	170.43	0.915	0.53	543.30
8	119	4.6	0.3275	163.29	0.883	0.51	527.93
9	137	5.3	0.3194	161.73	0.876	0.48	493.82
10	182	7.1	0.3215	151.90	0.832	0.46	475.58
11	231	9.0	0.3232	149.89	0.823	0.45	466.22
12	292	11.3	0.3075	139.62	0.777	0.42	431.99
13	357	13.9	0.3142	106.57	0.629	0.34	346.57
14	436	16.9	0.3001	87.37	0.543	0.27	278.06
15	553	21.5	0.2983	64.14	0.439	0.21	213.74
16	622	24.2	0.3034	52.09	0.385	0.17	174.61

Table 18. Surfactant Desorption Experiment Result for Tap 1B

Sample Number	Time (min)	PV Injected	Sample Weight (g)	Surfactant Mass (mg)	Absorbance	Normalized Conc. Ci/Co	Surfactant Conc. (ppm)
0	0	0.0	0.366	299.06	1.491	0.79	817.09
1	4	0.2	0.2916	236.98	1.213	0.79	812.68
2	18	0.7	0.3464	253.06	1.285	0.71	730.53
3	39	1.5	0.3011	190.75	1.006	0.62	633.53
4	50	1.9	0.3583	209.29	1.089	0.57	584.12
5	63	2.4	0.2971	168.20	0.905	0.55	566.14
6	82	3.2	0.3244	152.57	0.835	0.50	513.53
7	103	4.0	0.3253	157.26	0.856	0.47	484.77
8	120	4.7	0.3334	134.71	0.755	0.40	414.10
9	138	5.4	0.3355	123.32	0.704	0.36	369.88
10	184	7.1	0.3415	95.85	0.581	0.28	285.70
11	233	9.1	0.2887	61.69	0.428	0.18	180.64
12	293	11.4	0.3281	36.01	0.313	0.12	124.72
13	363	14.1	0.3081	6.53	0.181	0.02	19.91
14	438	17.0	0.2974	0.00	0.117	0.00	0.00
15	555	21.6	0.306	0.00	0.121	0.00	0.00
16	623	24.2	0.3057	0.00	0.137	0.00	0.00

Figure 69 shows the result of the brine PV injected before the surfactant concentration of each tap reached 50% of its initial concentration (that is, the concentration of each tap at the beginning of the desorption experiment). Desorption was much slower in “A” Taps, which were on the top side of the core, than in “B” Taps, which were on the bottom side. In fact, some of the taps (2A and 3A highlighted in dark blue) never reached 50% of their initial concentration at the conclusion of the desorption experiment. The results also show that taps which had the highest surfactant adsorption at beginning of the surfactant flooding experiment ended up having the fastest surfactant desorption pattern.

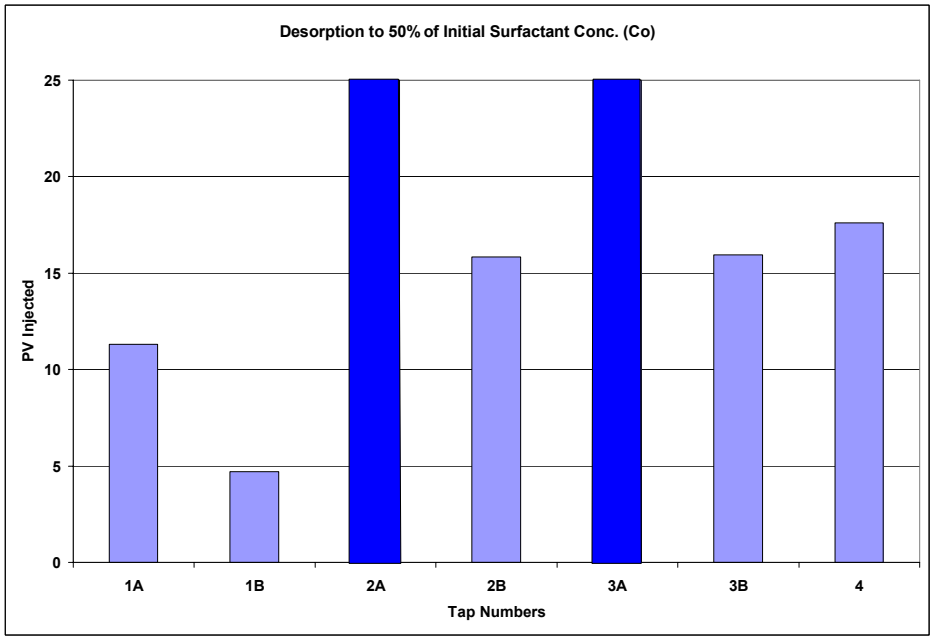

Fig. 69. Brine pore volume Injected in each tap before its concentration reached 50% of its initial surfactant concentration.

Multi-Tap Dynamics Experiment (Quarter-Inch Holes Drilled into Core-HDC)

This experiment was similar to the first multi-tap dynamic experiment, except quarter-inch holes were drilled into the core, three on each side of the core. This was done in order to mitigate the effect of the boundary layer, which was evident in the multi-tap dynamic experiment. Next, a longer core was designed in order to increase the separation distance between the taps so that a clear distinction on the profile of brine displacement, surfactant flooding and surfactant desorption could be observed among all taps. Five experiments were performed in this setup; waterflood (Tap A on top), waterflood (Tap B on top), surfactant flooding (at $q_s = 100 cm^3 / hr$), surfactant flooding (at $q_s = 150 cm^3 / hr$), and surfactant desorption.

Waterflood (Brine Displacement) Tap A on top

Figure 70 shows the result obtained from the waterflood (brine displacement) which was conducted while the "A" Taps were on the top side of the core. The results show three important findings; first, the taps at the bottom of the core (1B– 3B) reached breakthrough earlier than their counterparts on the top side of the core (1A– 3A). Secondly, the last tap to reach breakthrough was Tap 3A, and not Tap 4, the outlet tap, located at the end of the core. This suggests that the waterflood was bypassing

some zones of the core. Thirdly, it took about 1.6 PV of brine injection for all taps to reach break-through, which was half the time it took in the first experiment. It is important to point out that the first detection of brine salinity increases among the taps was not in numerical order, which suggests that the fluid flow along the core was not homogeneous and/or uniform. For instance, salinity increases were detected in Tap 3B earlier than in Tap 3A or even Tap 2A. A similar result was also observed for Tap 4, the outlet tap, which increased ahead of Tap 3B.

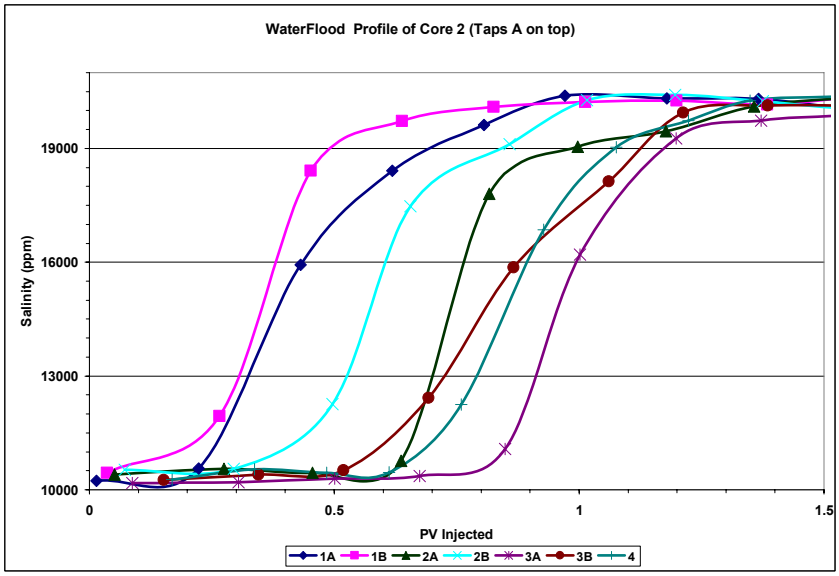

Fig. 70. Results of the brine displacement of core 2 performed when "A" taps were on top.

Waterflood (Brine Displacement) with "B" Taps on Top

Because of the differences observed in the salinity increase detection times and also in break-through times, the core was flipped in order to investigate whether the discrepancies were caused by gravity. Figure 71 represents the results obtained when the core was flipped and the "B" Taps were on the top. There were three important findings: first; Taps 1A and 1B, and 2A and 2B, switched positions, but the gap between 2A and 2B was much smaller than that observed in the previous experiment where "A" taps were on top. Secondly, unlike the previous experiment, there are clearly defined displacement profiles among the three sections of the core represented by Tap sets 1, 2, and 3. Thirdly, Taps 3A and 3B did not switch positions when the core was flipped, which suggests that other factors such as anisotropic permeability might be affecting the results. It is also important to point out that Tap 4, the outlet tap, reached breakthrough before tap

3A, as in the previous experiment. This result suggests that the waterflood is primarily bypassing the top part of the last section of the core where Taps 3A and 3B were located.

Comparison of the two waterflood experiments showed that for salinity increase detection, there were similar results in sections one and two, where in each case the taps that were on the bottom came first, but there were differences in results for the last section where in the first waterflood experiment Tap 3B was the first tap, while in the second experiment Tap 4 came ahead of Taps 3A and 3B.

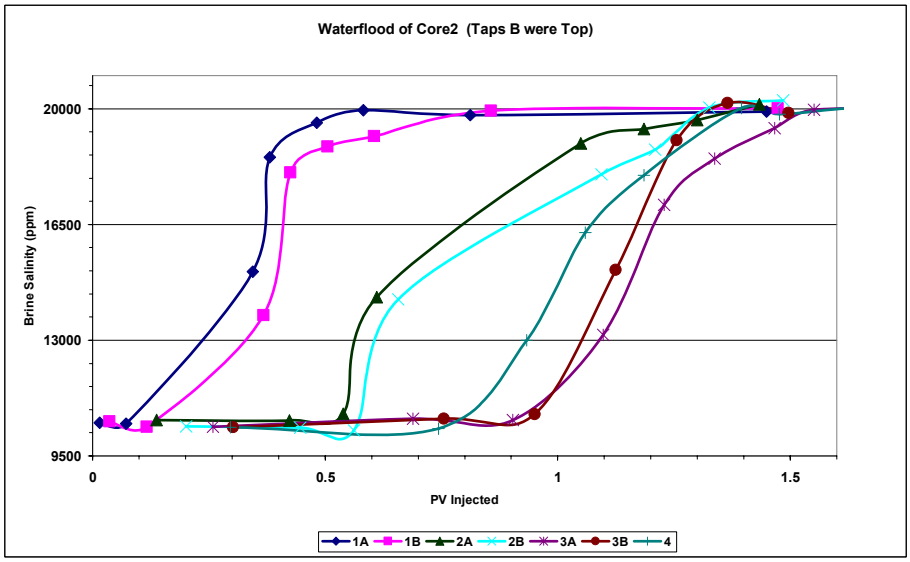

Fig. 71. Brine displacement results profile of core 2 when tap B were on the top.

First Surfactant Flooding at (q_s = 100 cm^3/hr) of Core 2

The surfactant flooding experiment was conducted when "A" Taps were on the top side of a horizontally-laid core. Figure 72 shows the results obtained from the surfactant flooding experiment. These results completely agree with the findings of the previous experiment. First, surfactant concentration was higher in the "B" Taps, which were on the bottom side of the core. This was probably due to multiple factors such as gravity and anisotropic permeability. Secondly, the concentration of Tap 4, the outlet tap, was higher than those of Taps 2A, 3A and 3B, but lower than those of Taps 1A, 1B and 2B. This suggests that the concentration at the effluent tap, Tap 4, which was what most previous researchers[96] have based their analysis of

surfactant flooding and surfactant adsorption, is actually close to the average surfactant concentration of the core.

In this experiment only one tap, 1B, reached the maximum available surfactant concentration after 9.0 PV of surfactant injection. The important question to ask, is when to stop surfactant flooding, especially if surfactant is being produced at a higher concentration. The answer to this question would depend on many factors: surfactant efficiency, the depth and distance of the phenomenon to be altered by the surfactant, economics, and the availability of surface handling equipment.

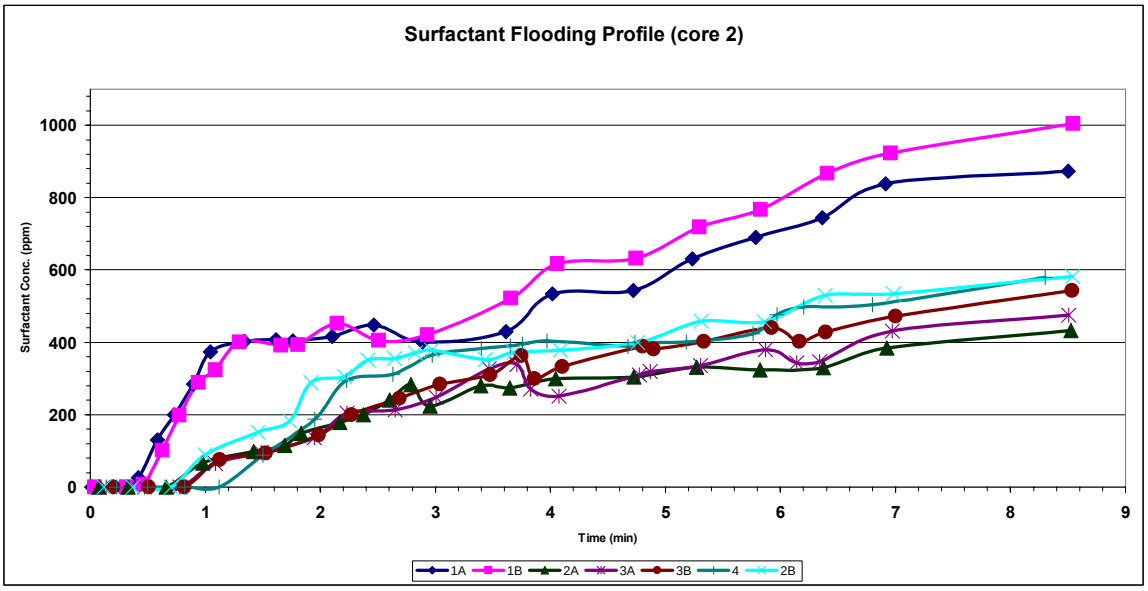

Fig. 72. Result of surfactant flooding of Core 2.

Figure 72 represents the average surfactant PV injected into each section, in terms of sectional PV, before surfactant was detected. The results show that section one (1A and 1B), the section closest to the port of injection, required more than 2.5 PV before surfactant was detected. This finding shows that most surfactant loss occurs near the source of injection, especially when only 100–200% PV is used. In the previous experiment it took about 7 PV before surfactant was detected in Taps 1A and 1B, as shown by Fig. 65.

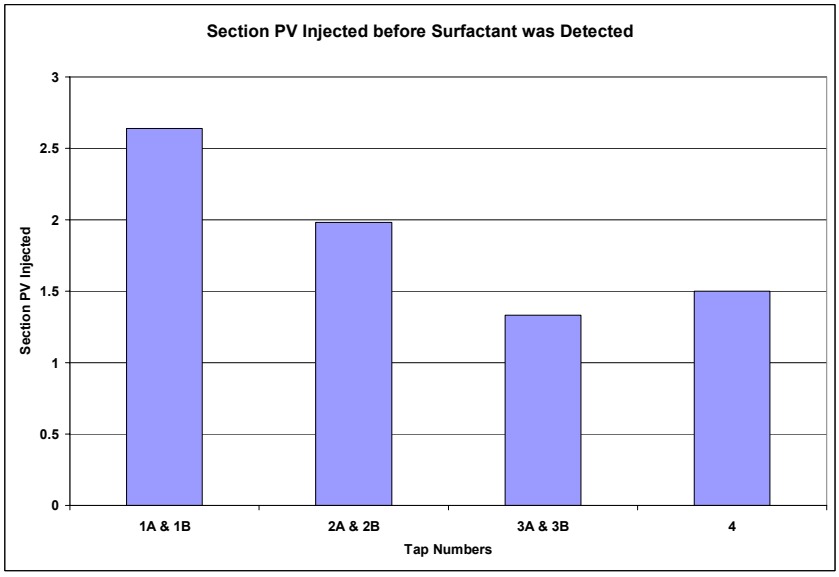

Fig. 73. Average amount of surfactant injected in each section before surfactant was detected in terms section PV.

In surfactant flooding, the concentration of the surfactant reaching different parts of the core (reservoir) has a direct impact on the amount of change it can produce in a given phenomenon. In this study and in previous studies [7] it was found that surfactant concentration at the outlet tap stays around 50% of the injection surfactant concentration for a long time before it gradually increases. Figure 74 shows the amount of surfactant PV injected before the concentration of the surfactant in each tap reached 50% of the original surfactant concentration. Taps 2A and 3A, highlighted in dark blue, did not reach the 50% threshold at the conclusion of the experiment. The result shows that it took much longer for the middle section of the core, represented by 2A & 2B, and to a lesser extent the last section (3A & 3B), to reach the 50% threshold. This finding reinforces the notion that there was less surfactant available in the middle section and also the last section of the core because of surfactant loss in the first section where a lot of surfactant adsorption was taking place.

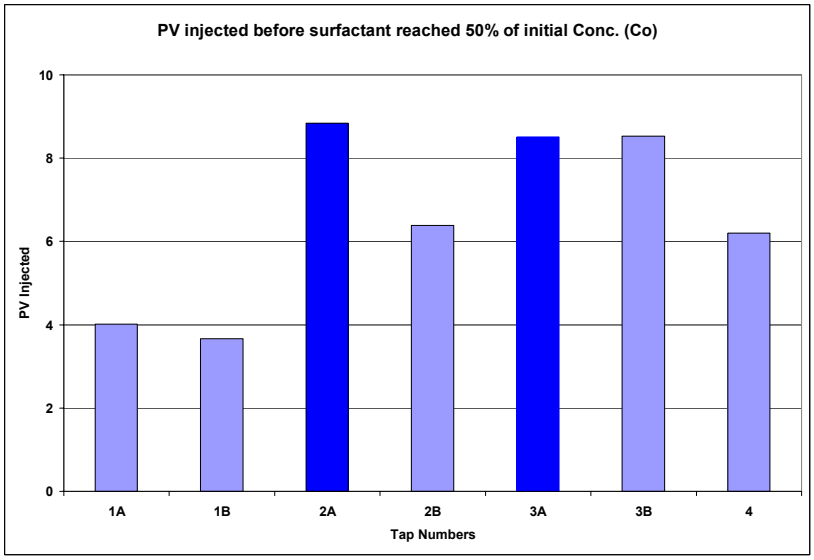

Fig. 74. Amount of PV injected before surfactant concentration reached 50% of Initial Conc.

Surfactant retention density defined as the amount of surfactant retained per unit mass of the rock was calculated using Eqs. 14 and 15. Figure 75 shows the results of surfactant retention versus surfactant PV injected. Three important findings, which were also noted in the previous surfactant retention/adsorption modeling experiment, are: First, the surfactant retention profile of different sections of the core had a distinguishable retention pattern where the retention/adsorption profile of equidistant taps were slightly different. This was probably due to multiple factors such as gravity and anisotropic permeabilities, considering that factors such as fluid pH, flow rate, and temperature were held constant throughout the experiment. It is also worth mentioning that the waterflood experiments showed the existence of a gravity effect when the core was flipped. Secondly, most of the surfactant retention/adsorption was taking place at the zones closest to the source of injection, as evidenced by the retention isotherms of Taps 1A and 1B. This was especially true at the beginning of the surfactant flooding process. Thirdly, surfactant retention was characterized by biphasic adsorption; very rapid at the beginning of the surfactant flooding process, followed by a slower and longer retention pattern

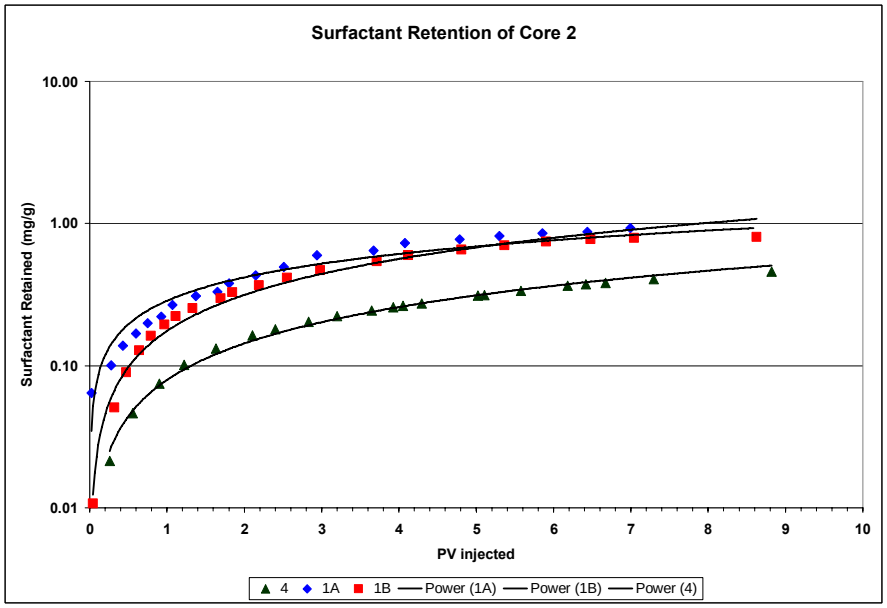

Fig. 75. Surfactant retention using Freundlich isotherm modeling result for Core 2.

Second Surfactant Flooding at (q_s = 150 cm^3/hr) of Core 2

Another surfactant flooding experiment was carried out to investigate the amount of surfactant injection required for all taps to reach the maximum surfactant concentration. Figure 76 shows the results of the surfactant flooding experiment where the flow rate was increased to $q_s = 150 cm^3 / hr$. The results of this experiment revealed two new findings; first, some sections of the core attained concentrations higher than that of the surfactant concentration that had been injected. For example, Taps 1A and 1B registered surfactant concentrations of about 1250 pmm while the concentration of the source surfactant injected was about 1000 ppm. This result suggests that there was a lot of surfactant adsorption in section one which continued even when the concentration of the fluid passing those zones reached the source surfactant concentration. Secondly, the results also show that no matter how much surfactant PV was injected into the core, there would be some parts of the core that might never reach the maximum surfactant concentration. For instance, the surfactant concentration of tap 3A, which was located on the top side of the last section, plateaued at about half the original concentration (500 pmm). This was probably due to the proximity of a pressure sink, the outlet tap that was open to atmospheric pressure, which made it difficult for fluids to flow to the top end of the core. It is also important to point out that at 20 PV, samples from Taps 1A, 1B and 2B were no longer taken, after it was

determined that they had reached the maximum concentration. The last samples collected from all the taps was at about 35.0 PV.

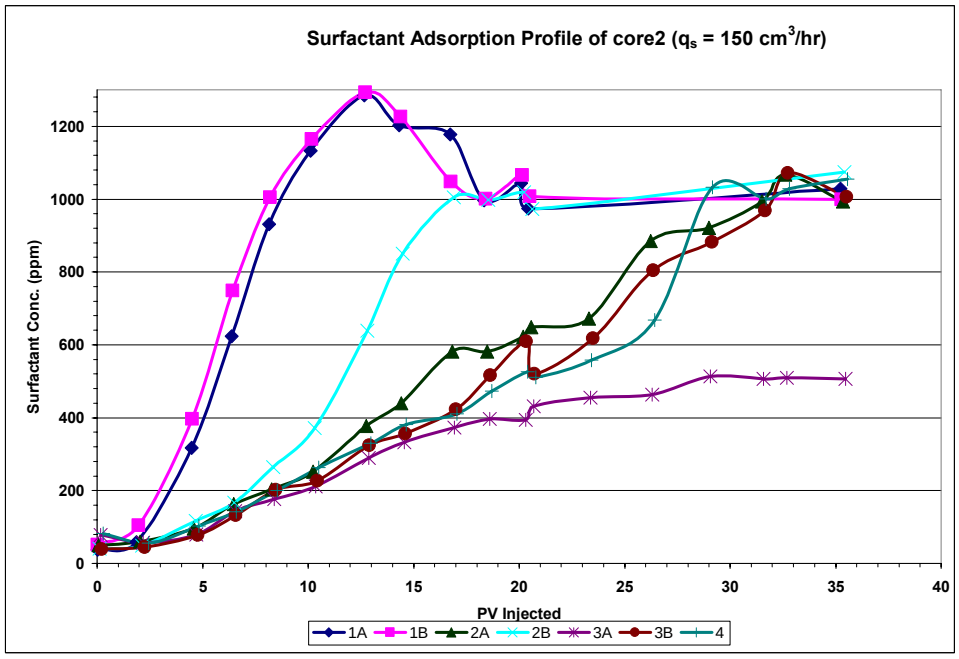

Fig. 76. Result of the second surfactant flooding of Core 2.

Surfactant Desorption

The surfactant desorption experiment was performed in order to investigate the desorption behavior of CD 1045 at an elevated temperature and low pressure settings. Figure 77 shows the results obtained from the surfactant desorption experiment. These show that; first, surfactant adsorption was very rapid at the beginning of the experiment, especially in high surfactant concentration zones as evidenced by the desorption profiles of Taps 1A and 1B. Secondly, while some parts of the core were de-absorbing, other sections of the core were adsorbing. This result suggests that during the surfactant desorption, there were simultaneous adsorption and desorption processes that were taking place within the core. For example, while the surfactant concentrations of Taps 1A and 1B were decreasing at about 1.0 PV, the concentrations of Taps 2A, 2B, 3A, 3B, and 4 were increasing, which suggests that the surfactant that de-adsorbed from section one (1A and 1B) was re-adsorbed by the sections that came after it. Thirdly, the tap with the highest surfactant concentration at the beginning of the experiment ended up having the lowest surfactant concentration at the end of the desorption experiment. This result suggests that

two new parameters influenced the behavior of desorption isotherms; first, proximity to the port of injection, and surfactant concentration at the start of the desorption experiment.

It is also interesting to note that during the surfactant flooding experiment, about 9.0 PV of surfactant was injected into the core, and in the subsequent desorption experiment, a similar amount of brine (~ 9.0 PV) was injected into the core. But as Fig. 77 shows, there was a significant amount of surfactant still remaining in the core, which suggests that surfactant desorption was much slower than surfactant flooding/adsorption.

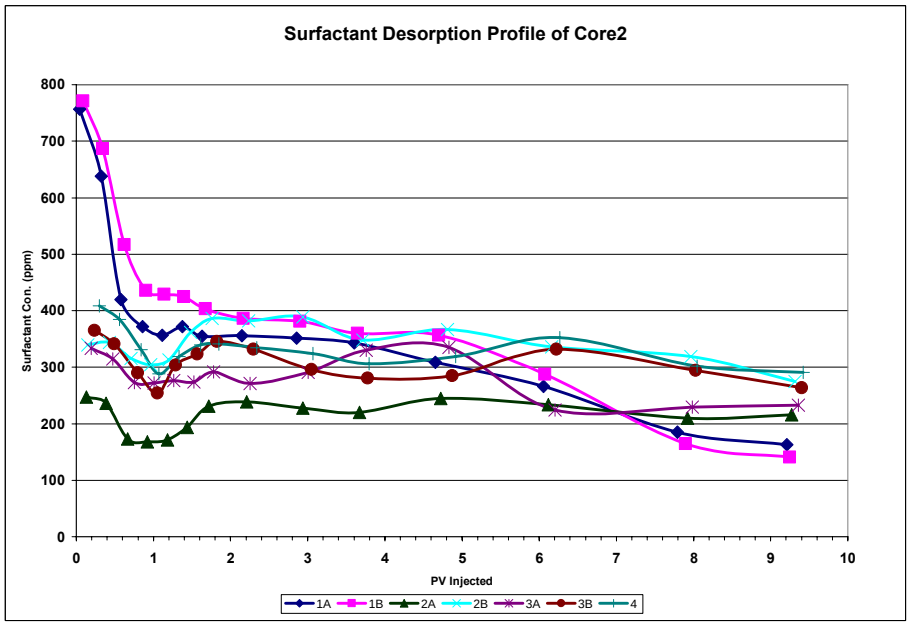

Fig. 77. Surfactant desorption experiment result of Core 2.

Permeability Measurement Results of Core2

The effect of permeability on the waterflood (brine displacement), surfactant adsorption, and surfactant desorption of core 2 was investigated using a minipermeameter. There was a coloration mark at the spot where Tap 2B was located, which we believe was caused by the casing epoxy seeping into the core. There were three layers of 5-minute epoxy on the core that were designed to prevent the casing epoxy, a very corrosive chemical agent, from ever reaching the core, but apparently on that spot it penetrated into the core. Figure 78 shows the permeability measurement result of both sides of the core. The result, surprisingly shows some very important findings; first, there was a permeability difference between the two sides of the core, and that on average, the permeability of Sside B was higher than that of Side A. Secondly, the results show that the

permeability of 2B was lower than that of 2A, but that was caused by the casing epoxy seeping into the core. More importantly, the area affected by the casing epoxy was quite small and had limited effect on the behavior of the fluid flow around Tap 2B, as shown by the surfactant flooding results, which clearly showed that Tap 2B reached maximum surfactant concentration much earlier than Tap 2A.

The result of the permeability measurement reinforces the findings of the waterflood experiments and the surfactant flooding experiment, which showed that the taps on the bottom side of the core were outpacing their counterparts on the top side, on breakthrough times, on reaching the salinity plateau region, and in surfactant concentration increases.

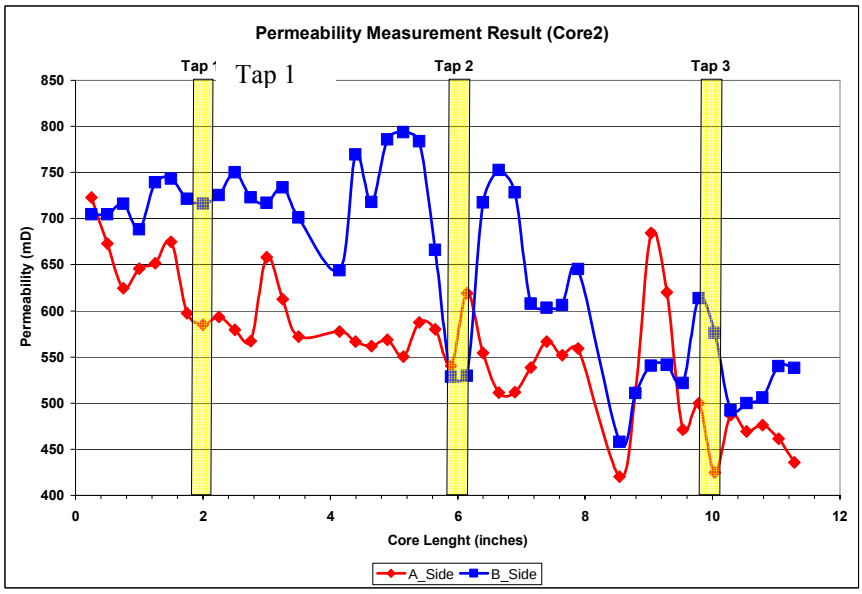

Fig. 78. Permeability measurement results of Core 2 showing locations of taps.

Figure 79 shows a contour plot of the permeability measurement results of core 2 versus the core length (in.). This shows that the permeability of section three, represented by Taps 3A and 3B, was lower than that of other sections. This finding agrees with the result of the second surfactant flooding experiment which showed that Section 3 had the lowest surfactant concentration increase. In fact, Tap 3A, which was located at the end of the top side of the core was the only tap that did not reach maximum surfactant concentration. Knowing that section 3of the core had low permeability, it is reasonable to conclude that most of the fluids that were injected probably side-tracked that section of the core.

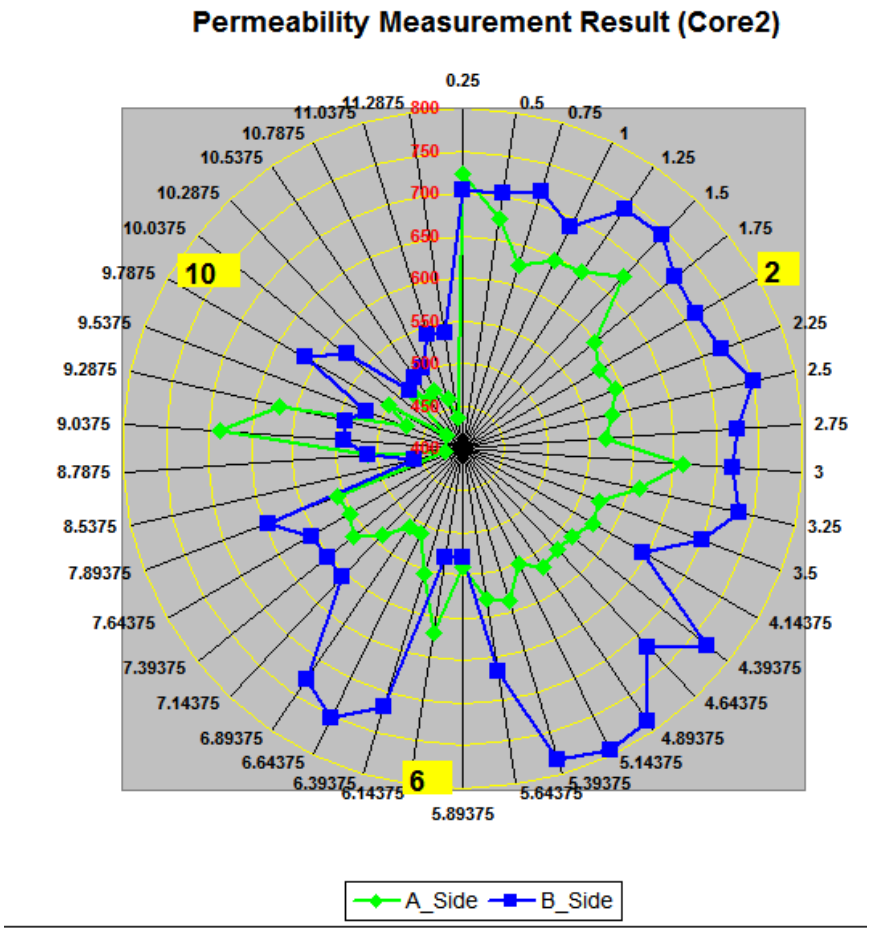

Fig. 79. Contour-plot of the permeability measurement results of core 2.

Experimental Error Analysis

Table 19 shows the result of the experimental error analyses for the different experiments performed in this study. The results show that there were two major types of experimental errors that were encountered in this study. First, the greatest error was due to the equipment used in analyzing collected samples. For instance, the resistivity meter, which was used to measure resistance, a property which is directly proportional to salinity, had an error of about 5%. The photospectometer also had fairly high uncertainty, especially in the second core's surfactant flooding and desorption analysis. On the other hand, experimental error due to mistakes by experimenters were very small and thought to have been in the range of 1%–2%, which were mostly from sample preparation, laboratory equipment cleaning methodologies, and probably due to experimenter inexperience.

Table 19. Experimental Error Analysis of the Different Experiments Performed

Experiment type	Average sample wt (g)	Error	Average salinity meter	Salinity Error	Spectro. Error	Other Errors	Total Error	Core #
Water flood Tap A Top	0.3117	0.32%	472.95	4.23%	0.00%	1.50%	4.50%	Core 1
Water flood Tap B Top	0.3187	0.31%	473.81	4.22%	0.00%	1.50%	4.49%	Core 1
Surfactant Flooding	0.3222	0.31%	0	0	3.12%	1.50%	3.47%	Core 1
Surfactant Desorption	0.317	0.32%	0	0	3.12%	1.50%	3.48%	Core 1
Water flood Tap A Top	0.3283	0.30%	453	4.42%	0.00%	1.50%	4.67%	Core 2
Water flood Tap B Top	0.3422	0.29%	458.51	4.36%	0.00%	1.50%	4.62%	Core 2
Surfactant Flooding 1	0.3308	0.30%	0	0	4.66%	1.50%	4.90%	Core 2
Surfactant Desorption	0.3089	0.32%	0	0	4.66%	1.50%	4.91%	Core 2
Surfactant Flooding 2	0.3295	0.30%	0	0	3.12%	1.50%	3.47%	Core 2

Conclusion

Coreflooding experiments and simulations were carried out in this study in order to further the understanding of the broad topic of fluid flow in porous media, especially waterflooding and surfactant flooding. There were three different sets of laboratory experiments that were performed in this study in order to understand some of the factors that influence surfactant flooding, such as gravity and anisotropic permeability, and to determine where the greatest surfactant loss occurs within the purview of the core. All the results obtained in this study were directed towards mitigating the problem of surfactant loss, especially in enhanced oil recovery where surfactant flooding has a huge potential.

Circulation method experiment

1. In the circulation method, under the same conditions such as surfactant concentration, temperature, salinity, and pressure, the surfactant adsorption density was higher in sandstone than in limestone.
2. The adsorption density of the both the sandstone and limestone reached a plateau where there was little or no increase at all after a certain period of time. The concentration of the surfactant in the flask also did not change after the adsorption density reached a plateau.

Waterflood (Brine Displacement) Experiments

1. In the waterflood experiments, the 2.0 wt % brine was found to be bypassing some zones and reaching breakthrough at the outlet tap before some of the taps in the third (last) section of the core, taps 3A and 3B, registered breakthrough, which suggests that the core was not as homogeneous as previously thought.
2. In the waterflood experiments, earlier breakthroughs were recorded in the bottom side of the core than in the top side of the core. The taps at the bottom registered early breakthrough and salinity peak-off faster than their counterparts on the top side, which means brine flow was preferentially faster in the bottom side. This was probably due to gravity
3. In the multi-taps dynamic (NHDC) experiments, the boundary layer effect was found to be influencing flow fluid along the edges of the core where samples were taken.
4. An anisotropic permeability was found to influence brine displacement profile.

Surfactant Flooding Experiments

1. The surfactant flooding profiles of all the taps were well predicted by the predecessor experiments, the waterflood. Taps that had early breakthrough in the waterflood experiment also had early surfactant concentration breakthrough. Therefore, the flow pattern of surfactant flooding effectively mirrors that of the waterflood.
2. Surfactant flooding was found to be bypassing some zones and reaching breakthrough at the outlet tap before half of the taps in the core reached the breakthrough surfactant concentration. This was probably due to anisotropic permeability.
3. Surfactant adsorption was greatest in the zones closest to the port of injection.
4. Surfactant adsorption was found to be higher in the bottom side of the core than in the top side of the core. This was most likely due to gravity.

5. The surfactant adsorption isotherm of CD 1045 on sandstone was found to depict the highly regarded four-region adsorption isotherm model.

Surfactant Desorption Experiments

1. Surfactant desorption was greatest at section 1, represented by Taps 1A and 1B, which were closest to the port of injection.
2. Surfactant desorption (depletion) was found to be higher in the bottom side of the core than in the top side.

A.4. Effects of Flow Conditions and Surfactant Availability on Adsorption

Introduction

Foam application involves injecting a surfactant along with water and gas into the reservoir. Normally, the surfactant is dissolved in the aqueous phase, though surfactants dissolved in CO_2 are also being considered.[98] To aid in the selection of a suitable surfactant for the reservoir, laboratory data is collected to characterize the surfactant performance. The economics of foam flooding depend significantly on the quantity of surfactant required to generate and propagate foam. Surfactant loss through partitioning into the crude oil phase and through adsorption onto the rock surfaces often consumes more than 90% of the surfactant in the system.[99] Surfactant loss through partitioning into the crude oil can be responsible for surfactant losses of as much as 30%. However, for the very hydrophilic surfactants chosen for many foam flooding applications, the partitioning onto crude oil is near zero.[100]

More serious losses are demonstrated from the results of a number of studies of the adsorption properties of surfactants suitable for foam flooding.[101-103] These have shown that effective foam forming surfactant may exhibit adsorption levels from near zero to up to quite high levels on the order. For example one test determined adsorption rates of 2.5 mg/g (mg of adsorbed surfactant for each gram of rock in the system). A mile-square, 10-ft thick reservoir saturated with surfactant would require 55,000 tons (50,000 tonnes) of surfactant at 2.5 mg of surfactant per g of rock. Adsorption does not depend on the nature of the surfactant alone, but also (though not inclusively) on temperature, brine salinity and hardness, rock type, wettability, and the presence of the residual oil phase. These factors will lead to vastly different distances of foam propagation into a reservoir, so selection of foam-forming surfactant formulation with acceptable adsorption levels at reservoir conditions is critical.

In this study the effect on surfactant adsorption for different solid to liquid ratios, surfactant concentration, rock type and state, and flow conditions are determined. The goal for this work is to quantify equilibrium values and kinetics in order to predict adsorption and desorption under reservoir conditions.

Material, Procedures, and Definitions

Materials

Anionic surfactant Chaser International CD 1045™ (CD), which has been identified as one of the best foaming agents,[104-106] was used in this study. It was supplied by Chaser International as 46.7 wt% active aqueous solution. The anionic surfactant indicator Dimidium Bromide–Disulphine Blue was used in this study to determine an unknown concentration of CD solution. The base stock was supplied by BDH Laboratory Supplies. The working solution was prepared as outlined in an earlier publication.[107] Chloroform with 1% ethanol was used in this study. The brine used to prepare the surfactant solution was 2 % (wt) synthetic brine composed of 1.5 wt% NaCl and 0.5 wt% $CaCl_2$.

Two types of cores were used as porous adsorbents: Berea sandstone and Indiana limestone. The powdered or crushed rock was prepared in-house by crushing the corresponding solid core with a maximum size determined by passing the crushed rock through a standard Number 60 sieve (~0.4 mm diameter).

Description of test procedures

All the adsorption experiments were preformed at 40ºC and atmospheric pressure. In the case of the flow-through test the outlet core pressure was atmospheric and the inlet pressure dependent on the flow rate and system permeability. For each determined CD adsorption density onto crushed limestone or sandstone, surfactant solution and crushed rock were added together in a test tube. The test tube was then placed in the shaker and placed in the thermostatic air bath. Samples of surfactant solution were taken from test tubes after at least 24 hours of exposition to determine residual CD concentrations at equilibrium. Initial surfactant concentrations tested were 500, 750, 1000, 1250, 2000 ppm. The solid to liquid weight ratios ranged from 1:1 to 1:5. Usually, 1 gram of solid was used for each combination of surfactant concentration and solid to liquid ratio.

Dynamic adsorption experiments were performed to determine adsorption densities of limestone and sandstone brine-saturated cores via circulation of a fixed volume of surfactant solution through the core. Samples of solution were taken from the flask periodically until no change in surfactant concentration was observed. Initial surfactant concentrations tested were 1000 and 2000 ppm and the range for solid to liquid ratios was from 1:1 to 1:5. The amount of

surfactant-free brine in each core at the start of the experiment was included in calculations when equilibrium adsorption was determined in the system. The flow rate of surfactant solution was 15 ml/hr for each circulation experiment. Details of the crushed and flow-through tests have been presented earlier.[108-110]

To measure adsorption by diffusion of surfactant from a CD solution to brine-saturated sandstone and limestone cubes the following equipment was used: glass jars with a screw cap, magnetic stirrers, and a thermostatic air bath. The CD adsorption density calculated during each diffusion test into limestone or sandstone brine-saturated cores was determined on cubes that were covered with epoxy on five sides, leaving one side of the cube exposed. After the epoxy hardened, cubes were evacuated and saturated with surfactant-free brine. After determining by weight change the amount of brine imbibed into the core and the PV, each cube was immersed into surfactant solution in a glass jar that was then closed with a screw cap to prevent evaporation and put on magnetic stirrer in the air bath. Samples of the surfactant solution were taken periodically to determine residual CD concentration. Initial surfactant concentrations tested were 1000 and 2000 ppm and the range for solid to liquid weight ratios varied from 1:1 to 1:5. The initial brine in each cube was included when calculating the total amount of liquid and surfactant available in each system.

Formulas used to calculate adsorption density

The amount of surfactant absorbed (adsorption density) was expressed as the unit mass of CD adsorbed per 1 gram of rock (mg/g). Adsorption density of crushed rock was calculated by the following formula:

$$Ads = (Ci - Cr)*Ms/(Mc*1000), \quad (17)$$

where:

Ads – CD adsorption density, mg/g

Ci, Cr – initial and residual CD concentration in solution, ppm

Ms – mass of the solution, g

Mc – mass of the core sample, g.

During an experiment when it was necessary to take several samples to measure residual concentration in surfactant solution, material balance and adsorption density were calculated using the following formula:

$$Ads_i = [(Mt - \Sigma\{m_{si}\}) - (Ms - \Sigma\{m_{li}\})*Cr_i/1000]/Mc, \qquad 18$$

where:

Ads_i – adsorption density after i-number of measurements, mg/g

Mt – total initial mass of surfactant in the system, mg

Ms – total initial mass of surfactant solution, g

$\Sigma\{m_{si}\}$ – sum of surfactant mass removed during sampling, mg

$\Sigma\{m_{li}\}$ – sum of surfactant solution mass removed during sampling, g

Cr_i – residual concentration after i measurements, ppm

Mc – mass of the core sample, g

Surfactant availability in the system

In this study, when adsorption isotherms were constructed as adsorption density versus amount of surfactant available in the system, availability of surfactant in the system was defined as the total amount in mg of CD in solution per 1 g of solid. The term "surfactant availability" is used here in lieu of the approach for presenting adsorption isotherms as a function of surfactant adsorption density versus equilibrium surfactant concentration. This approach was selected because it is shown that by increasing the volume of surfactant solution the adsorption density generally increases at a fixed equilibrium surfactant concentration; thus the adsorption density might have different values for a given equilibrium concentration.

Presentation of data and results

CD adsorption onto crushed rock

The first set of tests was performed on crushed limestone and sandstone. These are essentially small chucks of rock at or less than 0.4 mm in diameter (No. 60 sieve). From a previous study the crushed rock pieces are shown to be in the order of one to three grain diameters in size.[20] These tests were designed to determine adsorption kinetics in porous media with minimal diffusion.

The results from the experiments with crushed limestone indicate that CD adsorption was near completion in about 10 minutes for initial CD concentration of 1000 ppm and solid to liquid

ratios from 1:1 to 1:5 and completed in less than one hour for initial concentration of 2000 ppm (Fig. 80). For sandstone the crushed rock reached 95% of maximum adsorption within one hour for an initial CD concentration of 2000 ppm (Fig. 80). The adsorption experiments with a weight ratio of 1:1 between surfactant solution and crushed limestone showed that with a linear increase of surfactant concentration the CD adsorption density increases linearly from 0.450 mg/g to 1.796 mg/g over the range of initial CD concentrations from 500 ppm to 2000 ppm (available surfactant of 0.5 to 2.0 mg/g) (Fig. 81). Crushed sandstone demonstrated a similar trend. Adsorption density for crushed sandstone in the range of initial concentration 500 to 2000 ppm (available surfactant of 0.5 to 2.0 mg/g) and solid to liquid ratio of 1:1 increased linearly from 0.107 mg/g to 1.35 mg/g (Fig. 82).

It was found that CD adsorption density increases when the available volume of surfactant solution increases while holding the initial CD concentration constant. The results are plotted in Fig. 81 where the availability of CD per gram of rock varies from 0.5 mg/g (1:1 @ 500 ppm) to 10mg/g (1:5 @ 2000 ppm). The increase in adsorption is independent of concentration and approximately linear until about 4 mg/g of surfactant is available. After reaching an adsorption density of 3.0 mg/g at 4 mg/g of surfactant available, adsorption increases only slightly with increasing availability of surfactant. Over the tested CD concentrations and solid to solution ratios, CD adsorption density on crushed limestone is a function of CD available in the system rather than a function of surfactant concentration.

Figure 82 shows a number of adsorption isotherms plotted as a function of availability of surfactant with an apparent dependence on initial surfactant concentration. Adsorption density for crushed sandstone in the range of initial concentrations of 500 to 2000 ppm and solid to liquid ratio from 1:1 to 1:5 increased with availability of surfactant with a significant change of slope at 4 mg/g of surfactant available. The maximum adsorption was above 3 mg/g. The plotted curves of CD available versus adsorption density have an increasing slope with increasing CD concentration (Fig. 82). The slope increases from about 0.3 to 0.7 going from CD concentrations of 500 ppm to 2000 ppm. For the lower concentrations the availability (liquid to solid ratio) was not high enough to reach a plateau. Thus further tests are required to determine if the plateau would be similar for all concentrations, though it appears that the plateau for 1250 ppm is lower than for 2000 ppm, etc.

In general, crushed limestone demonstrated higher CD adsorption densities compared to crushed sandstone for all corresponding initial CD concentrations and solid to liquid ratios, compare Figs. 81 and 82.

CD adsorption by diffusion into brine saturated cores

In the second series of tests there was no injection into the test cubes, thus fluid within the core was static and diffusion was expected to play the major role in adsorption rates. The only mechanical mixing was in the bulk solution to maintain a homogeneous solution as explained in an earlier section. Adsorption dynamics and equilibrium tests data for brine saturated cubes of limestone and sandstone are summarized in Tables 20 and 21, respectively. Time required for CD adsorption to reach equilibrium by diffusion into brine saturated rock was about three orders of magnitude longer than in the crushed rock (400-600 hours for brine saturated cubes versus one or less hours for the crushed rock, see Fig. 80).

Figure 83 compares the final values of CD adsorption density on crushed and nonflow solid cubes for limestone. The two systems types had similar adsorptions at the same surfactant availability. Figure 84 compares the final values on crushed and nonflow solid cubes for sandstone. There is a higher adsorption for the cubed nonflow systems. The difference might be due to the fact that the Berea sandstone rock samples used to prepare the crushed and cubes samples were from different blocks. All tests were performed at CD concentrations of either 1000 or 2000 ppm.

There is a similar point in both the limestone (Fig. 83) and sandstone (Fig. 84) that is significantly lower than adjacent points. Each were at a solid to liquid ratio of 1:3 and initial surfactant concentration of about 2000 ppm (6 mg/g surfactant availability). The two tests were performed concurrently and when compared with tests that preceded and followed them had significantly different adsorption isotherms (Fig. 85). Their final adsorption densities were lower than systems with both less and more available surfactant. Also, the initial 100 hours had an unusual “S” shaped curve in the isotherm. It is suggested that these two points be weighted less when determining adsorption density trends and at a future date be retested.

Effect of flow conditions on CD adsorption

The third set of tests comprised flow tests similar to tests that have traditionally been performed to determine adsorption onto rock. During the flow test surfactant solution is circulated through the core until equilibrium or steady state is achieved. One difference from traditional tests was that not only were surfactant concentrations varied, but the amount of solution or as explained earlier the solid (rock) to liquid mass ratios were varied. Tables 22 and 23 summarized the CD adsorption values and conditions measured in the circulation experiments with limestone and sandstone cores.

Time for CD adsorption to achieve equilibrium by circulation through brine saturated cores was at least one order of magnitude greater compared to the crushed rock (20–50 hours for brine saturated cores versus one hour or less for the crushed rock) and an order of magnitude less compared to nonflow brine saturated core tests (Fig. 80).

Values of CD adsorption density on limestone were significantly lower in the circulation experiments compared to those measured in crushed rock and nonflow saturated core tests (Fig. 86). Since these were prepared from samples of the same rock sample, the differences might be explained from the energy required for mono- versus multi-layer adsorption. The electrostatic interaction between surfactant molecules and solid surface as well as the lateral chain-chain interactions between the adsorbed surfactant molecules contribute to the driving force of adsorption.[111] Energy due to hydrophobic attraction of the surfactants to form surface aggregates is of the same order of magnitude as the energy of micellization of surfactants (~1 kcal/mol) while energy of electrostatic interaction between surfactant molecules and solid surface is around 20-30 kcal/mol, which is an order of magnitude greater than the energy of hydrophobic interaction. Therefore the difference in CD adsorption densities due to the flow conditions, shown in Fig. 86, might be interpreted as the inability of surfactant aggregates formed outside the near surface adsorption on the solid to resist surface washing by the flow of liquid in porous space. This result will be significant when determining adsorption in nonflow regions of the rock compared to flow paths. This may imply varying adsorption capacity versus flow rate. Thus an understanding of flow and diffusion rates are required for accurate adsorption density calculations onto limestone.

The results for the sandstone systems had similar equilibrium time compared to the limestone, but found little difference in the total adsorption in flow versus nonflow systems (Fig.

87). Unlike the solid cube sandstone samples, the flow tests were prepared from the same lot as the crushed samples. In earlier studies it was found that the adsorption on pure silica was less than on sandstone.[109] The increase was dependent on the amount of clay in the system, which generally has a much higher adsorption capability than sandstone due to increased surface area and composition.[109] This and the discussion from the last paragraph indicates that different CD adsorption mechanisms and adsorption energy levels that occur on sandstone and limestone surfaces should affect adsorption density and result in adsorption density as a function of parameters such as flow conditions, rock type, and rock impurities (clays, etc).

Conclusions and Implications

1. Values of CD adsorption density on crushed and non-flow solid limestone cubes were found to be the same and best described as a function of surfactant availability (mass of surfactant available per mass of solid) in the system.
2. The shape of the adsorption isotherms on crushed sandstone comparing surfactant availability with adsorption density suggests the slopes and possibly the density plateau depend on surfactant concentration and availability.
3. Adsorption time dynamic depends on the state of solid and flow conditions. Time to reach equilibrium in nonflow core volumes was an order of magnitude greater compared to circulation experiment, and 3 orders of magnitude greater compared to the crushed rock. Thus the rate of adsorption is dependent on the availability of surfactant with the kinetics and equilibrium being comparably very rapid.
4. When comparing flow versus nonflow systems in cube or core samples, the adsorption density on limestone underwent a significant decrease due to the flow in porous media while adsorption density on sandstone remained the same. This might be an indication of different adsorption mechanisms and/or energy levels that occur on limestone and sandstone surfaces. Tests such as heats of adsorption that are planned for the future should shed some light on the cause of these differences.
5. The results should be considered when determining reservoir adsorption requirements.

Table 20. CD Adsorption by Diffusion Into Brine Saturated Limestone Cubes

Test #	Ratio S:L	CD mg/g	Core [g]	Pore Vol. [cc]	Mass of Surf. Solution [g]	Initial CD Conc. [ppm]	Duration of the exp. [hrs]	Res. CD Conc.* [ppm]	CD Ads. density* [mg/g]
1	1:1	1	146.3	6.2	140.4	1021	167	94	0.850
2	1:2	2	141.6	8.9	274.2	1012	167	74	1.796
3	1:3	3	147.5	8.2	434.2	999	600	202	2.330
4	1:4	4	142.5	8.5	561.4	1016	743	158	3.356
5	1:5	5	121.9	7.5	601.9	1013	644	356	3.163
6	1:1	2	162.6	9.5	153.0	2126	166	441	1.585
7	1:2	4	142.5	8.5	276.4	2062	576	604	2.821
8	1:3	6	157.7	9.1	463.9	2040	360	1338	2.094
9	1:4	8	138.0	8.4	543.5	2031	431	1112	3.643
10	1:5	10	129.1	7.8	637.6	2025	547	1273	3.738

(* at the end of experiment)

Table 21. CD Adsorption by Diffusion Into Brine Saturated Sandstone Cubes

Test #	Ratio S:L	CD mg/g	Core [g]	Pore Vol. [cc]	Mass of Surf. Solution [g]	Initial CD Conc. [ppm]	Duration of the exp. [hrs]	Res. CD Conc.* [ppm]	CD Ads. Den.* [mg/g]
1	1:1	1	105.8	9.6	96.2	1023	167	25	0.886
2	1:2	2	108.1	10.7	205.4	1032	167	67	1.809
3	1:3	3	109.2	11.2	316.3	1015	600	264	2.158
4	1:4	4	105.5	11.5	410.4	1028	743	148	3.392
5	1:5	5	103.5	11.1	506.3	1022	644	284	3.584
6	1:1	2	107.0	11.3	95.6	2239	166	501	1.537
7	1:2	4	107.2	11.6	202.7	2115	576	429	3.158
8	1:3	6	105.8	11.6	305.7	2077	360	1177	2.590
9	1:4	8	102.9	11.5	400.0	2058	431	708	5.241
10	1:5	10	105.9	11.3	518.1	2044	547	1262	3.823

(* at the end of experiment)

Table 22. CD Adsorption by Circulation of Surfactant Solution Through Limestone Cores

Test #	Ratio S:L	CD available [mg/g]	Core mass [g]	Pore Volume [cc]	Mass of Surfactant Solution [g]	Initial CD Conc. [ppm]	Duration of the experiment [hrs]	Residual CD Conc.* [ppm]	CD Ads. density* [mg/g]
1	1:1	1	141.6	8.9	132.6	1046	22	524	0.488
2	1:2	2	141.6	8.9	274.2	1012	70	544	0.898
3	1:3	3	144.4	9.9	443.0	980	103	665	0.952
4	1:4	4	115.8	7.7	455.4	997	71	692	1.193
5	1:5	5	110.0	7.9	542.0	1015	30	781	1.148
6	1:1	2	125.5	8.0	117.4	2096	24	1251	0.792
7	1:2	4	120.6	8.7	232.4	2118	35	1351	1.484
8	1:3	6	114.4	8.5	334.6	2052	21	1575	1.396
9	1:4	8	115.8	8.3	454.8	2037	44	1531	1.988
10	1:5	10	112.6	8.7	540.0	2086	18	1672	1.982

(* at the end of experiment)

Table 23. CD Adsorption by Circulation of Surfactant Solution Through Sandstone Cores

Test #	Ratio S:L	CD available [mg/g]	Core mass [g]	Pore Volume [cc]	Mass of Surfactant Solution [g]	Initial CD Conc. [ppm]	Duration of the experiment [hrs]	Residual CD Conc.* [ppm]	CD Ads. density* [mg/g]
1	1:1	1	137.2	9.8	127.4	1055	50	492	0.515
2	1:2	2	138.2	10.0	266.1	1017	46	533	0.923
3	1:3	3	115.0	10.2	345.0	980	103	532	1.335
4	1:4	4	108.3	9.1	424.0	1001	71	587	1.611
5	1:5	5	103.0	9.2	505.7	1018	50	700	1.558
6	1:1	2	112.1	8.3	103.7	2120	24	729	1.277
7	1:2	4	115.6	9.3	221.8	2128	35	1076	2.013
8	1:3	6	107.2	8.5	313.0	2055	21	1380	1.966
9	1:4	8	110.3	9.9	431.2	2046	22	1436	2.385
10	1:5	10	104.8	9.9	514.0	2039	18	1553	2.382

(* at the end of experiment)

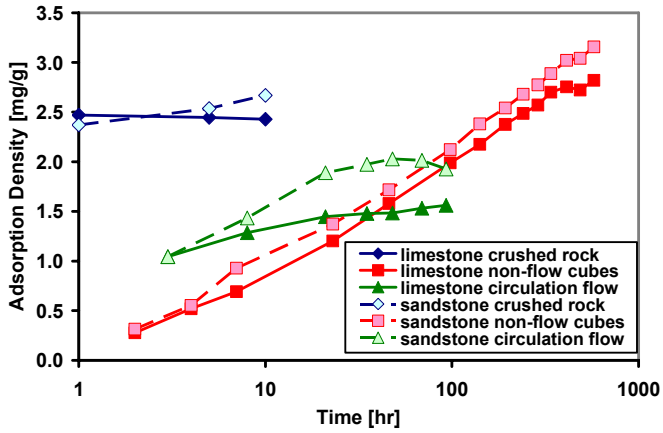

Fig. 80. Comparison of equilibrium time versus adsorption density for crushed rock, nonflow cubes, and flow-through core for limestone and sandstone systems.

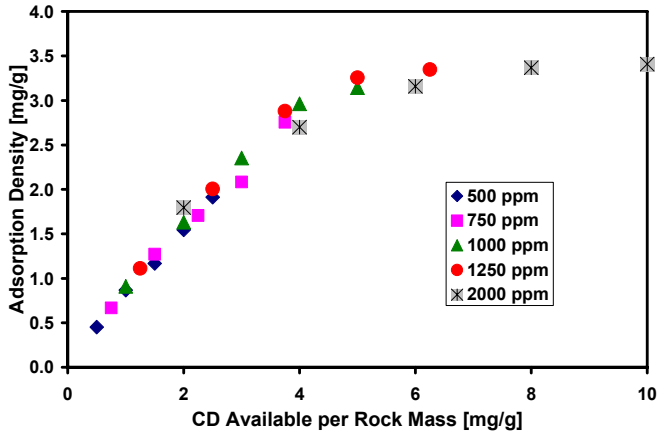

Fig. 81. CD adsorption density versus mass of CD available per gram of crushed limestone.

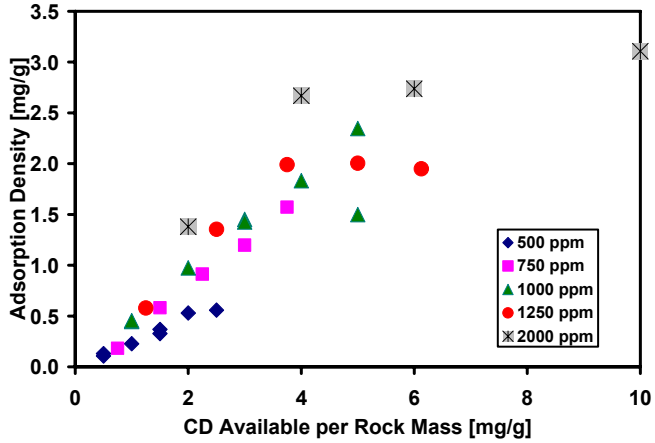

Fig. 82. CD adsorption density versus mass of CD available per gram of crushed sandstone.

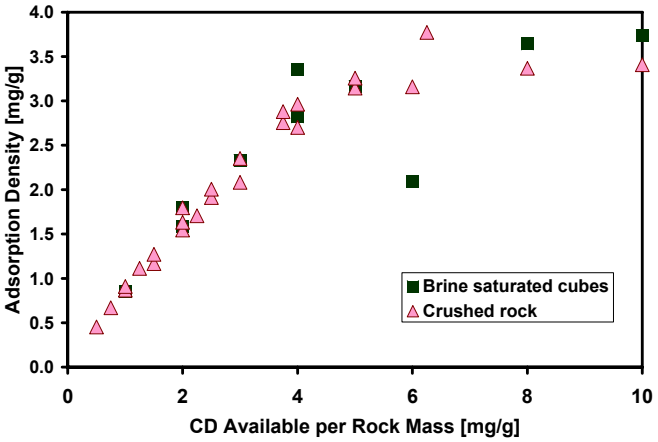

Fig. 83. Comparison of CD adsorption density onto crushed limestone and solid limestone cubes, both nonflow tests.

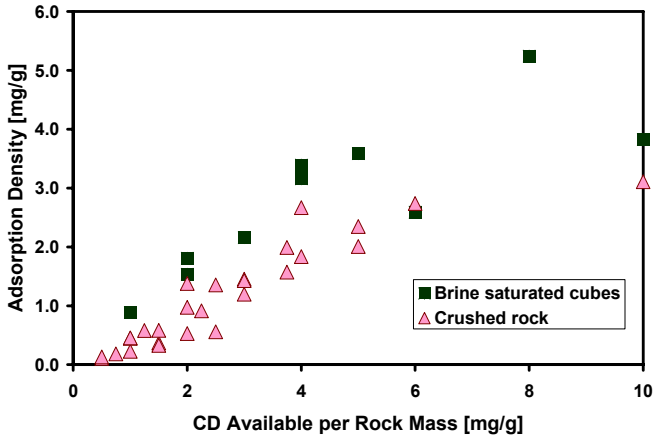

Fig. 84. Comparison of CD adsorption density onto crushed sandstone and solid sandstone cubes, both nonflow tests.

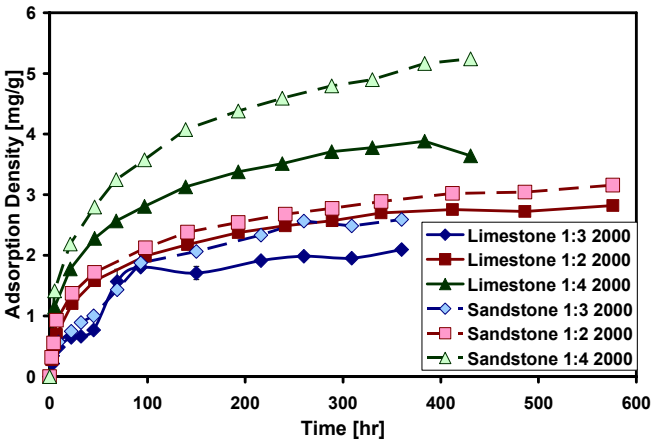

Fig. 85. Comparison of equilibrium time for several limestone and sandstone non-flow cube tests at 2000 ppm CD concentration.

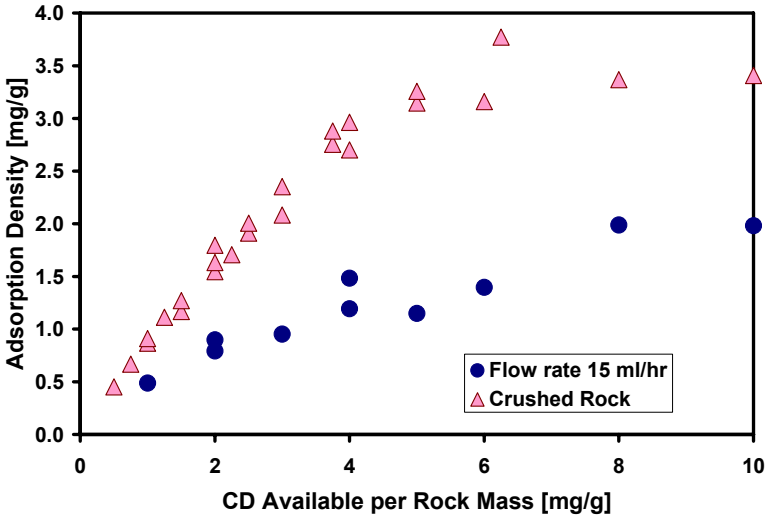

Fig. 86. Comparison of CD adsorption density for crushed limestone and flow-through limestone core tests.

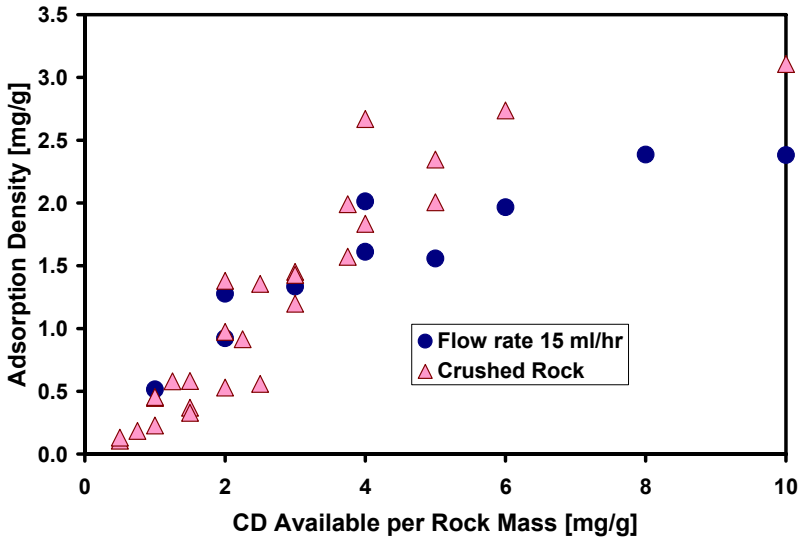

Fig. 87. Comparison of CD adsorption density for crushed sandstone and flow-through sandstone core tests.

A.5. Screening of Surfactants for Use in N_2 Flooding

Introduction

Over the years, surfactants have been extensively used to augment recoveries in old and new reservoirs in most foam-flooding processes. They are applied as single surfactant systems or dual surfactant systems. This study looks at nitrogen (N_2) flooding at immiscible conditions. It considers six single surfactants and two mixed surfactant systems. The experiments conducted were in four distinct categories, each contributing to the overall effort to evaluate the salient parameters that influence the selection of suitable surfactant systems. The area of interest that was covered included interfacial tension (IFT), foam stability, static adsorption, and core flooding (gas mobility reduction factors (MRF), differential pressures (DP), and pore volume liquid produced (PVLP)).

Interfacial Tension (IFT)

All experiments were conducted at 95°C and 1000 psi. Wei et *al.*[112] reported IFT of 56.49 mN/m for distilled water (DW) and N_2 under the stated conditions above. The system used for the ensuing experiments had 55.2 mN/m for DW and N_2. This is a deficit from Wei et *al*[112] of 2.3% and indicates that the system has no major dysfunction. The 12.2 wt% brine however, has 63.9 mN/m IFT value. These IFT values are shown in Fig. 88.

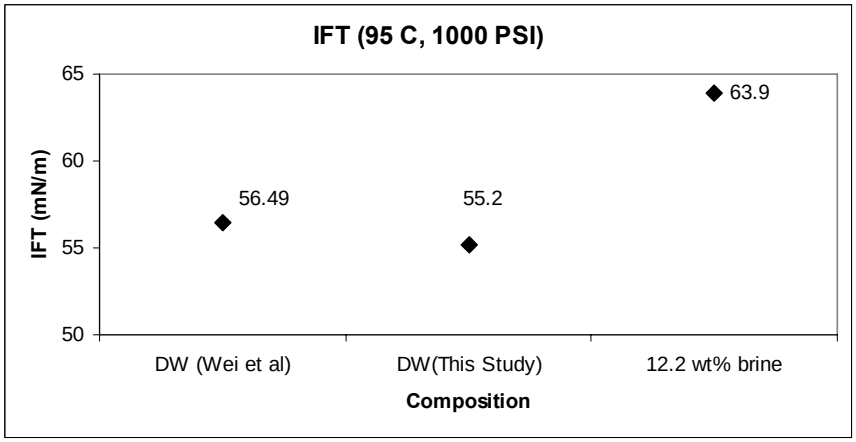

Fig. 88. IFT comparison (Wei et al.[112] and This Work).

In surfactant flooding, surfactants concentrations greater than the Critical Micelle Concentration (CMC) do not reduce IFT significantly,[113] but have a net effect of improved displacement efficiency by lowering overall Gibb's free energy at the surface. To be able to

identify the CMC and distinguish between "injectible" and "noninjectible" concentrations, each surfactant is dissolved in 12.2 wt% brine and tested at surfactant concentrations from 0.02 wt% to 1 wt%. "Injectible" concentrations here are concentrations greater than the CMC and "noninjectible" are concentrations less than the CMC. Table 24 and Fig. 89 show IFT results for both single and mixed surfactant systems. Appendix 3-1 shows a typical spreadsheet for IFT evaluation as well as other important input parameters and Appendix 3-2 indicates IFT results for individual systems at different surfactant concentrations.

Table 24. Interfacial Tension (IFT) in mN/m (With N2 @ 95°C & 1000 PSI)

	0.02 wt%	**0.05 wt%**	**0.1 wt%**	**0.5 wt%**	**1 wt%**
Surfactant	IFT	IFT	IFT	IFT	IFT
CS 1045	25.7	19.7	18.7	17.9	17.7
CS 1040	28.6	20.6	18.7	18.2	18.2
Amphosol CG	29.5	24.4	23.7	22.8	21.8
Stepantan AS1246	31.7	22.3	19.9	19.6	20.3
Formatron D74	29.3	23.1	22.1	20.6	20.2
Enordet	33.6	30.6	23.6	19.0	19.0
Step+Ampho	37.9	8.9	4.3	2.9	2.7
Step+Format	34.1	20.7	18.6	17.1	17.3

NB: CMC IFT @ 0.05 wt%. Enordet CMC at 0.5 wt%

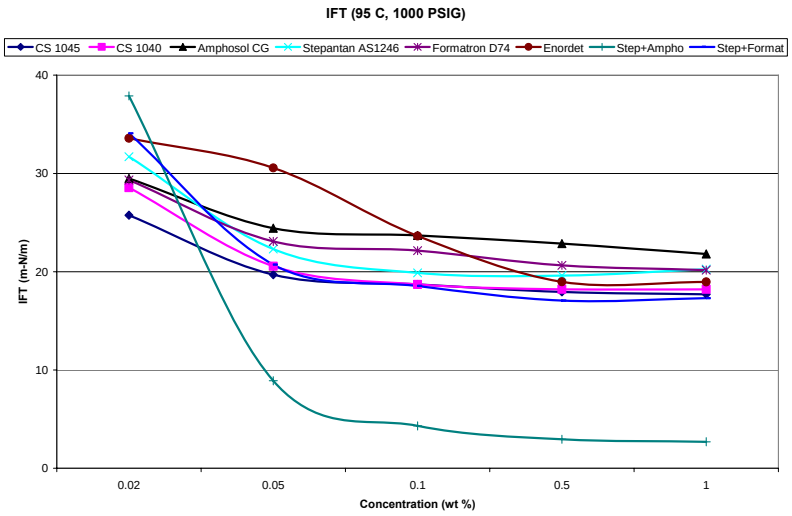

Fig. 89. IFT results.

Injecting chemically untreated synthetic brine at reservoir condition has 63.9 mN/m IFT (Fig. 88). The surfactant injection has the tendency to reduce IFT (Fig. 89). Adding 0.02 wt% concentrations of surfactant to the brine almost halved the brine IFT. Figure 89 also indicates that increasing the surfactant concentrations from 0.02 wt% to 0.05 wt% has significantly reduced the IFT for all surfactants. Further increments from 0.05 wt% to 1 wt% have no significant impact on IFT; hence, it can be argued that for most of the products tested the CMC is 0.05 wt%, except Enordet which has CMC around 0.5 wt%. CMC values are reported in Table 24 and can be observed in Fig. 89 as well.

A closer look at Fig. 89 reveals that of all the chemicals tested, the mixed surfactant systems lowered the IFT the most, with a mixture of Stepantan AS 1246–Amphosol being the best product. The results show that Stepantan AS 1246–Amphosol reduced IFT from 63.9 mN/m to 4.3 mN/m at 0.1 wt%, a significant 93.3% (Fig. 90). The percentage reduction for the remaining seven systems is around 70–63 % at 0.1 wt%; with 2.3% deficit in this study compared with Wei et *al,*[112] it could be argued that there is no significant differences in IFTs. Thus, the mixed systems offer the best choice of surfactants based on the IFT experiments alone.

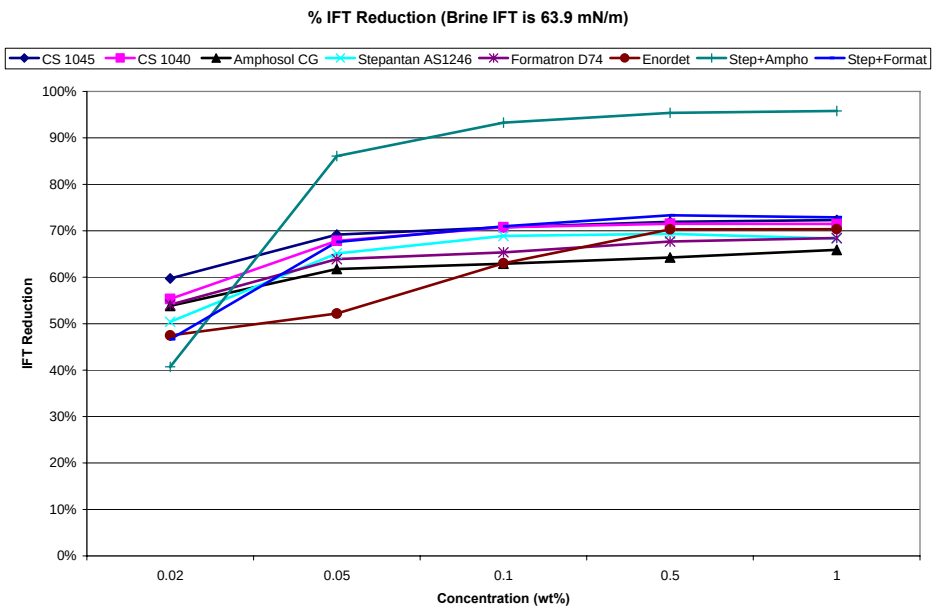

Fig. 90. Percentage IFT reduction from 63.9 mN/m.

Foam Stability

Two separate testing procedures, the drop weight method (DWM) and the bench foam test (BFT) were used to determine the stability of foams for the eight surfactant systems by measuring their lifetimes. Heller et *al*[114] recounted that these lifetimes of static foams are determined by the times of drainage (of the bulk aqueous liquid, from the lamellae into their plateau boundaries, and through that network into the bulk phase) and by the critical minimum thickness the films can maintain.

For a surfactant to be effective for mobility control, it is important for the lamellae to have some degree of durability but it is not clear that surfactants which make very long-lasting bubbles is better than one whose bubble lifetime merely exceeds some minimum time. Thus, Schramm[113] indicated that surfactants must be present at a concentrations greater than the Critical Micelle Concentration (CMC) in order to improve foam stability which is essential for effective sweep since foam volume is larger than equivalent liquid volume for that matter will contact much more reservoir volume. Foam also will have lower mobility compared with liquid and will delay breakthrough.

Drop Weight Method (DWM)

The same apparatus used for IFT determination (Fig. 89) was used for this experiment. It is a HPHT apparatus which houses a sapphire observation cell within, with which the N_2 foam heights were measured with a cathetometer. Just as in IFT experiments, the surfactants were dissolved in 12.2 wt% brine and tested at 0.02 wt% to 1 wt% concentrations. The lifetimes of N_2 foam at reservoir conditions of temperature (95°C) and pressure (1000 psig) were monitored at 90 minutes and at 30 minutes intervals thereafter, with the results shown in Figs. 91–95.

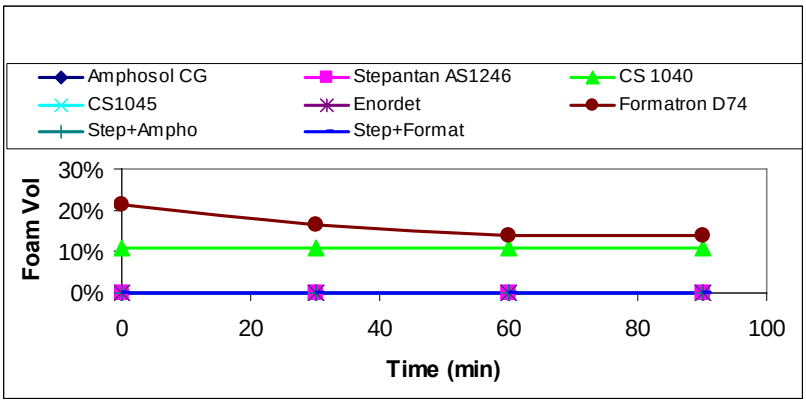

Fig. 91. Foam stability for 0.02 wt% concentration.

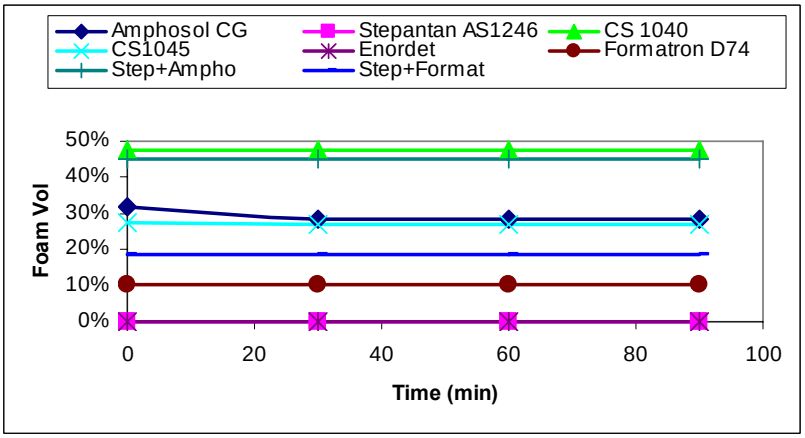

Fig. 92. Foam stability for 0.05 wt% concentration.

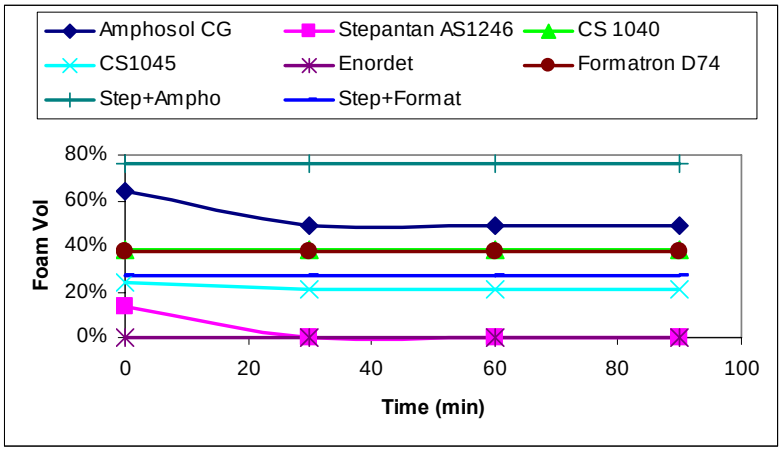

Fig. 93. Foam stability for 0.1 wt% concentration.

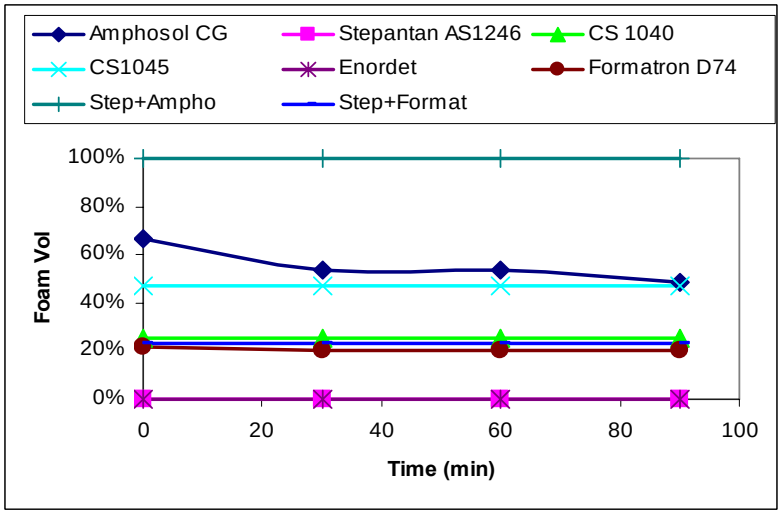

Fig. 94. Foam stability for 0.5 wt% concentration.

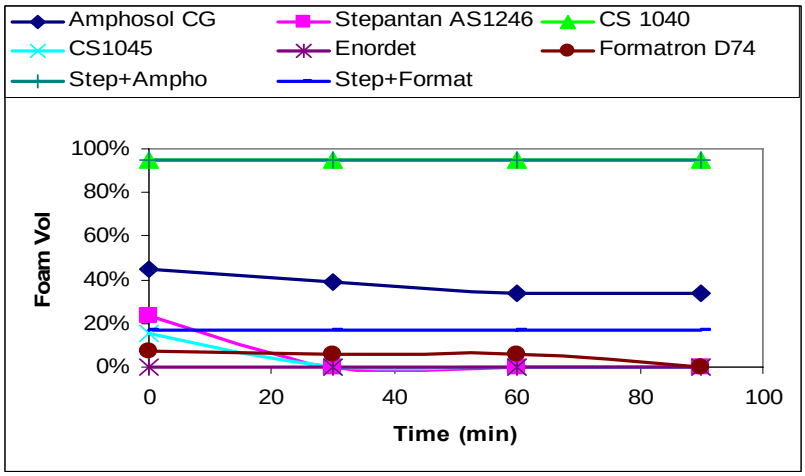

Fig. 95. Foam stability for 1.0 wt% concentration.

It is not surprising that at very low concentrations of 0.02 wt%, most of the surfactants did not form stable foams, except for CS 1040 and Formatron D74. This phenomenon could be explained according to Israelachbvili,[115] as the surfactant concentration is below CMC; the molecules are loosely integrated into the water structure with a monolayer forming at the fluid-fluid interface. However, a gradual increase in concentration from 0.02 wt% to 0.1 wt% saw slight improvements in the stability of foams for most of the products; yielding 25% or more stable foams except Stepantan AS 1246 and Enordet. Surfactant concentrations greater than 0.1 wt% show a gradual decrease in foam stability (Figs. 94 and 95). One possible reason is that, as surfactant concentrations increased, the foam structure becomes smooth and weak and the percentage of stable foam for most of the products is less than 20%. Figures 91–95 demonstrate that there is no explicit relationship between concentrations and foam stability. This confirms Liu's[116] earlier report that foam stability did not demonstrate a direct relationship with concentration. In summary, Figs. 91–95 show that the foam drainage rate was not rapid for most of the products that form substantial foams since the initial stable foam volume at 90 minutes

hardly decayed, but a quick observation is that Stepantan AS 1246 and Enordet never formed any substantial stable foam.

Bench Foam Test (BFT)

This procedure, also called a low pressure test, was conducted under the atmospheric pressure and concentrations of 0.02 wt% to 1.0 wt% in 12.2 wt% brine. The initial foam volumes were reported at room temperature of 27°C after shaking the configuration (specific concentration and volumes in test tube and placed in holders) for 30 seconds. The configuration was then put into a constant temperature bath of 95°C and subsequent volumes were reported at this temperature. The results are shown in Figs. 96–100.

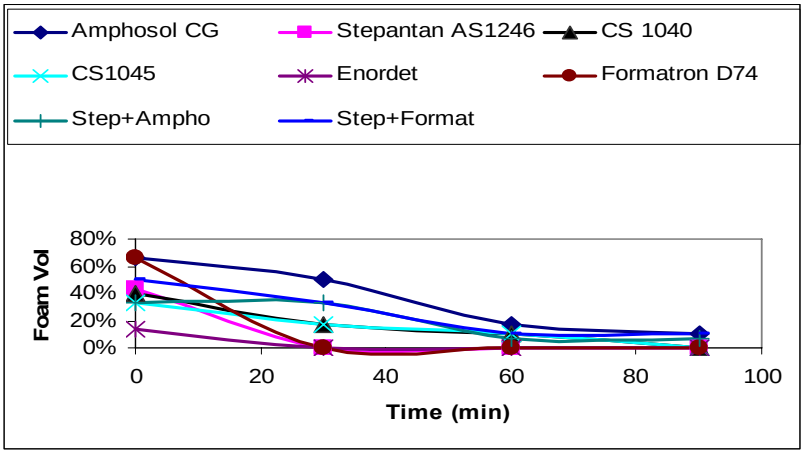

Fig. 96. Foam stability for 0.02 wt% concentration.

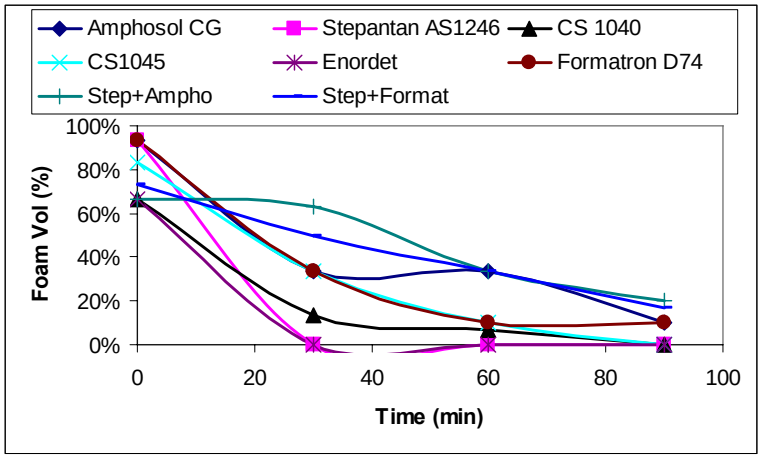

Fig. 97. Foam stability for 0.05 wt% concentration.

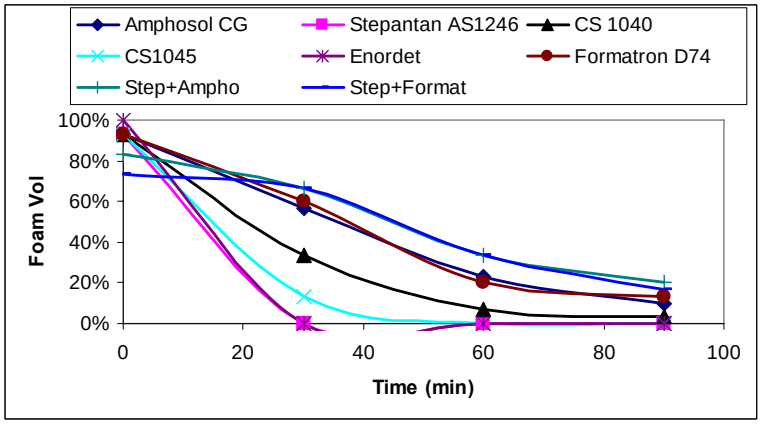

Fig. 98. Foam stability for 0.1 wt% concentration.

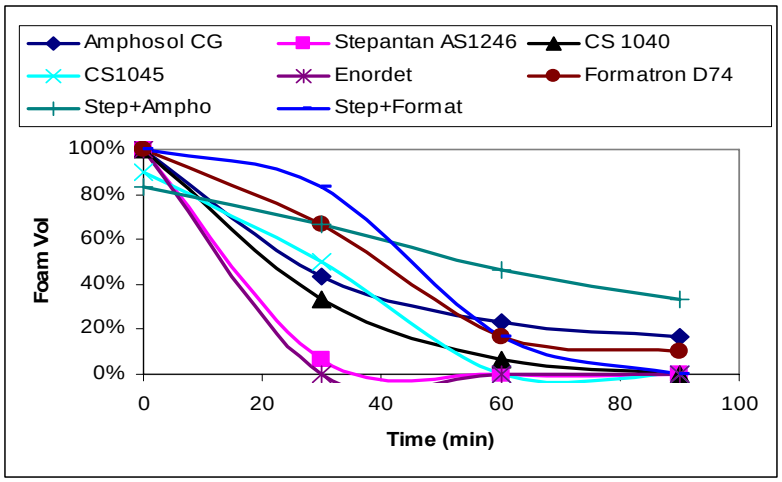

Fig. 99. Foam stability for 0.5 wt% concentration.

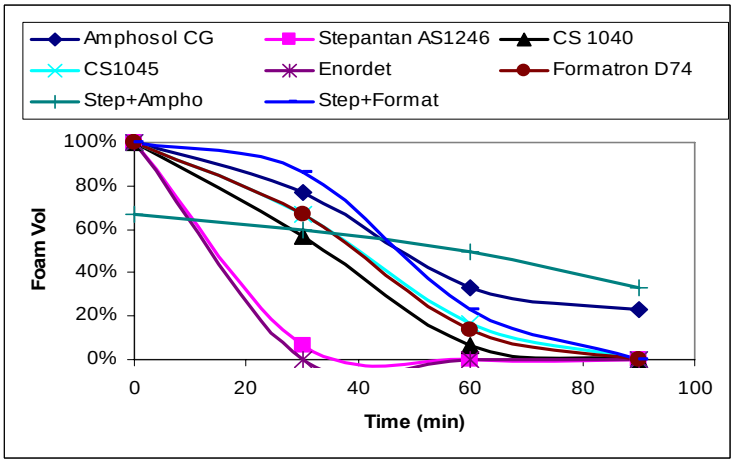

Fig. 100. Foam stability for 1 wt% concentration.

Though this experiment used a different strategy, the results confirmed the DWM. For instance, the percentage of stable foam at zero time increased as the concentration of surfactant increased from 0.02 wt% to 1 wt%. At the CMC, five products achieved 5% or more foam stability but this number decreased to two at 1 wt% concentration in 90 minutes. The results also show rapid increase in foam drainage as a function of time for all surfactants at all

concentrations. Stepantan AS 1246 and Enordet never formed any substantial stable foam after 30 minutes, just as in DWM.

In summary, all the surfactant systems except Stepantan AS 1246 and Enordet have proven the tendency to form stable foams under high or low pressure and both testing methods have confirmed this.

Static Adsorption

All adsorption experiments were conducted at 40°C with 12.2 wt% brine. Surfactant concentrations vary from 0.02 wt% to 0.1 wt%. For lack of experimental procedures for the adsorption exercise, as stated earlier, the standard method for Chaser^{TM} CD 1045 was used. Two approaches were used: chloroform baselines and brine baselines. Figures 101 and 102 show the results of adsorption density in milligrams of surfactant per gram of rock vs. residual concentration for both chloroform baseline and brine baseline adsorption experiments. The residual concentrations are equilibrium concentrations. Bai[116] stated that for many surfactants, the adsorption isotherm will plateau at surfactant concentrations greater than its CMC. The maximum concentration used in this study was 0.1wt%, and this is greater than the CMC of most of the products except Enordet. The adsorption isotherm for a single surfactant species consist of two distinct regions; an adsorption plateau for concentrations in excess of the CMC and a line of slope connecting the origin to the plateau with the intersection of the two curves being at the CMC and that no further adsorption occurs above the CMC (Fernandez et al[117]). The results show that the adsorption plateau is reached or almost reached at a solution concentration that is almost the same as the CMC determined from IFT experiments, and this supports the hypothesis that the monomer determines the adsorption.

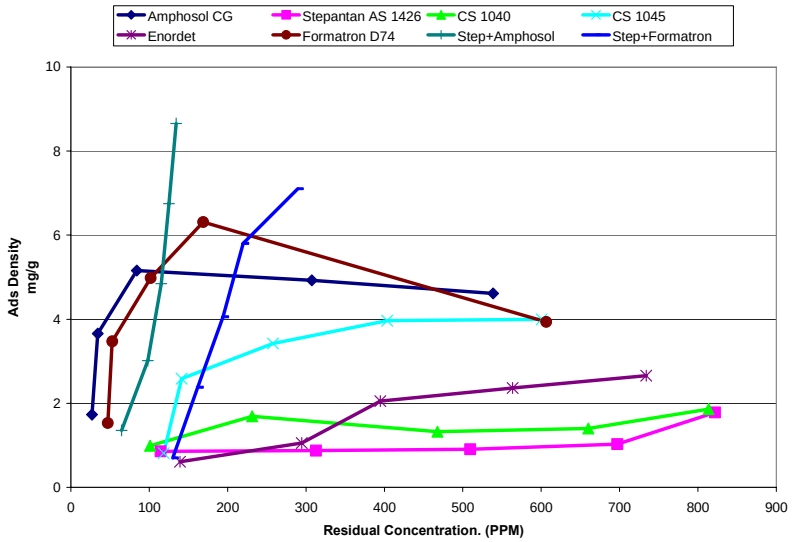

Fig. 101. Adsorption isotherms for chloroform baselines.

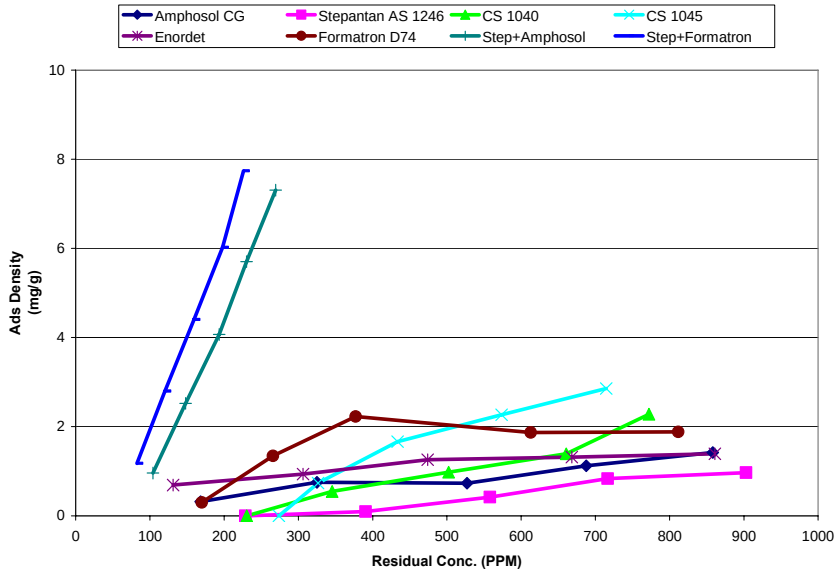

Fig. 102. Adsorption isotherms for brine baselines.

The single surfactant systems in Figs. 101 and 102 can also be compared to a typical four-region isotherm for a monoisomeric anionic surfactant. Though these regions are not distinctly defined due to the number of data points, at least the trend is obeyed. The results show that the surfactant adsorption increases with increasing initial concentration. The result also demonstrates

that at a given surfactant concentration, in this case near the CMC, the adsorption density reaches an equilibrium where little additional surfactant adsorption occurs for most of these surfactants. These peak adsorption values are shown in Fig. 103.

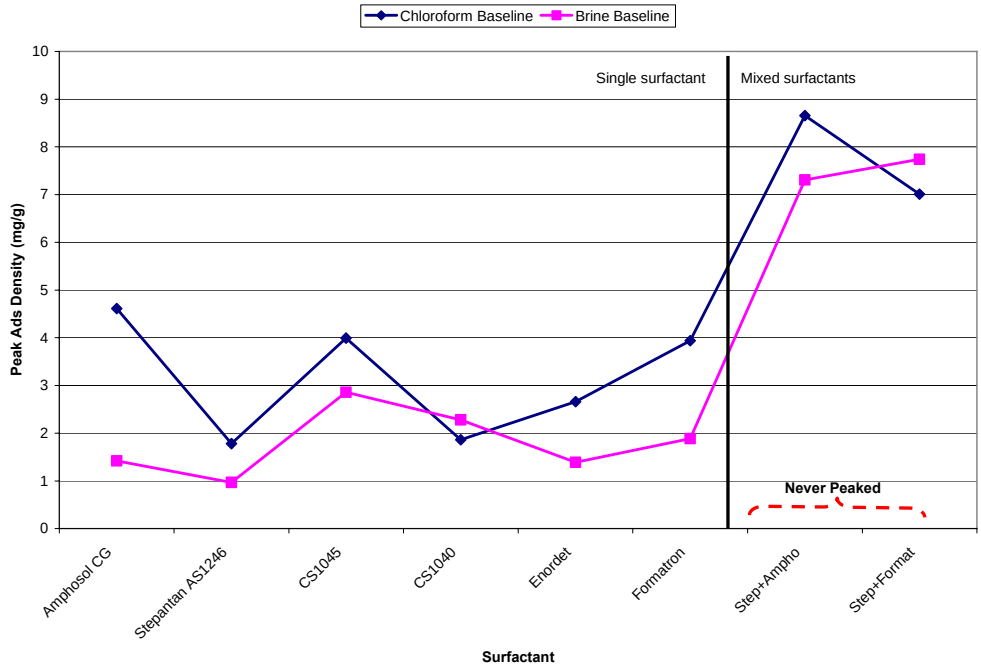

Fig. 103. Peak adsorption densities for both baselines.

For surfactant flooding, moderately low adsorption or very low cost surfactant is a requirement for field applications. Clearly, from Fig. 102, Stepantan AS 1246 and CS 1040 have adsorption densities of less than 2 mg/g (using chloroform baselines). The rest have adsorption densities greater than 2 mg/g. For brine baselines, all but the Chevron chemical (CS 1040, CS 1045) have densities less than 2 mg/g.

The mixed surfactant systems (Figs. 101 and 102) can be compared to typical mixed adsorption isotherms of $C_8SO_4/C_{12}SO_4$ onto α- alumina.[113] According to Fernandez et al,[117] adsorption from solutions containing surfactant mixtures is assumed to depend on the monomer concentration and composition, but not on the micellar concentration and composition. Recall

also, that Harwell and Scamehorn[118] mentioned that mixed surfactants systems have mixed micelle adsorption behavior and that adsorption in Region I, which has no interaction with surfactant molecules, tend to behave like pure components; but as the surfactant concentration increase, the position of Region I/Region II break shift relative to the single component adsorption isotherms. Regions II, III, IV positions, however, are functions of the types and amounts of surfactants in the mixture relative to the adsorption isotherms of a pure component. Figure 96 shows that the system does not seem to peak no matter the relative amount of each constituent in the mixture for both baselines and at CMC, their adsorption densities were greater than 7 mg/g for both baselines (Fig. 103). As a result of their high densities, the mixed systems may not make a good pick since they might be too expensive for field application.

Figure 103 illustrates that, though both methods used different strategies, the results assumed a similar trend, as there are no significant differences in peak adsorption densities, but these values can only serve as guidelines until specified procedures are used to confirm or refute them.

Coreflooding Experiments

There were two major types of experiments, S01 and S02 defining the cores used. The two experiments were classified based on the total Darcy velocities of 14.12 ft/d and 28.25 ft/d respectively. N_2/brine injection and N_2/surfactant solution injection have a gas-liquid volumetric ratio of 1.1, corresponding to 50% foam quality. The salinity of the injected water was 2 wt% and 0.1 wt% of each surfactant at 40°C. For 28.25 ft/d coinjection, the system was not purged after successive runs. For 14.12 ft/d coinjection, the system was purged with 1000 cc, approximately 50 PV after successive runs and 7.25 PV of new product injected before

introducing the gas. The order of the runs is believed to play some role in S01 core results but it is difficult to evaluate. The numbers in parentheses next to the curves indicate the order in which the surfactants were injected (Fig. 106 and Fig. 108). The order is not as critical as in the S02 core study because more attention was given to restoring the core to its original condition before testing the next surfactant. For each case, multiple PV were injected to achieve steady state conditions. The coreflood performances for these cases will be subdivided into pore volume liquid produced (PVLP), differential pressures (PD), and gas mobility reduction factors (MRF).

Pore Volume Liquid Produced (PVLP)

Figures 104 and 105 show the results of PVLP for both cases. In Fig. 104, brine or surfactant injection alone (approximately, 7.25 PV) shows no apparent differences in PVLP as against PVLI for all products. Thus, before stable foam was generated in the core the PVLP is equivalent to PVLI. Contacting surfactant solution with N_2; (after 7.25 PV in Fig. 104) and Fig. 105 results in foam formation and that will translate into cumulative reduction in PVLP for "good foamers." On the other hand a "poor foamer" or "weak foamer" will show little or no reduction in cumulative PVLP and will maintain an apparent direct relationship between PVLI and PVLP. Essentially, this approach for distinguishing "good foamers" from weak ones has no mathematical implication. This is a crude method to differentiate between surfactants but can be helpful.

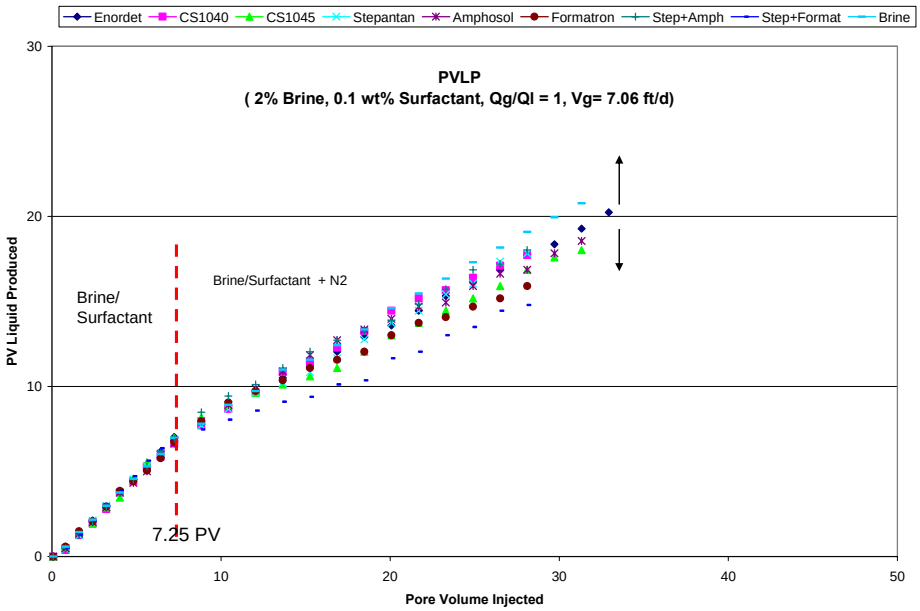

Fig. 104. Pore volume liquid produced (PVLP) vs. total pore volume injected (Vg = 7.06 ft/d).

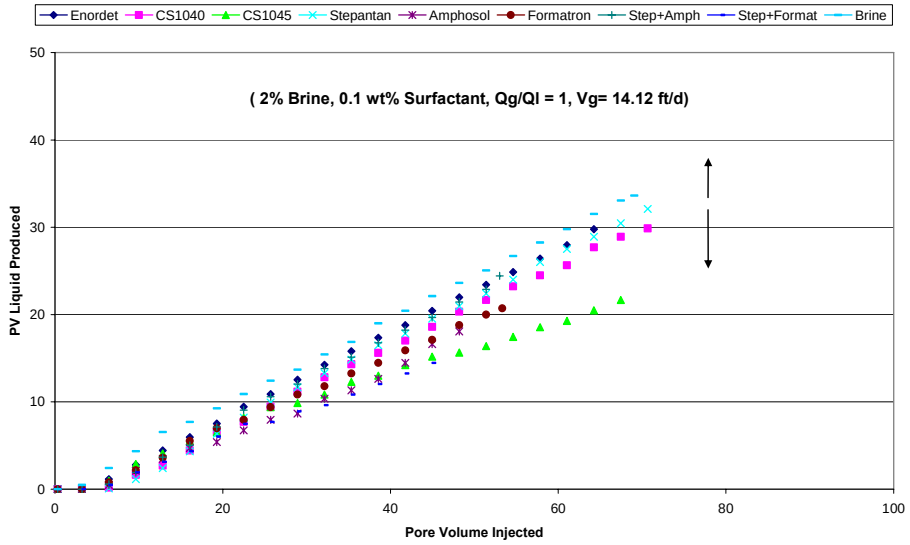

Fig. 105. PVLP vs. total PV injected (Vg = 14.12 ft/d).

Assuming a straight line through the middle of both graphs to split PVLP into two groups, CS 1045, Formatron, Step+Amphosol and Step+Formatron are in one category and the rest in the other category (Figs. 104 and 105). The first group could be termed “good foamers”

lying at the bottom of the hypothetical line and the other group "poor foamers" lying at the top of the hypothetical line. The reason for decreasing PVLP can be attributed to the fact that more foams are produced instead of liquid and difficult to quantify. "Weak foamers" on the other hand will have cumulative PVLP almost directly proportional to PVLI (Figs. 104 and 105). Summarily, the first group of surfactants resting below the hypothetical line will make a good choice compared with the other group.

Differential Pressures (DP)

Figures 105 and 107 are the results of differential pressures for Vg of 7.06 ft/d and 14.12 ft/d respectively. Approximate steady state differential pressures corresponding to the respective flow rates are shown in Figs. 107 and 109. As indicated earlier, about 7.25 PV of new surfactant solution was injected after purging the system (Fig. 106). This illustrates the fact that injecting surfactant solution alone is like injecting brine since there was no significant surge in differential pressures. However, with simultaneous injection of N_2 and surfactant solution, foam is formed inside the core when conditions favorable for stable foam are met. After foam was formed and as the bubble density increased the differential pressures increased substantially for "good foamers" before steady state was reached for both flow rates. "Poor foamers," however, have their differential pressures increased; the increment is of a comparatively lower proportion. Here again, certain chemicals stand out, having their differential pressures increased by over three-hundred fold. These are Step+Formatron, CS 1045, Formatron and Amphosol. The other category of moderately "good foamers" is CS 1040, Step+Amphosol and Stepantan AS 1246. The results of Enordet have consistently indicated that it is a "poor foamer" as both its injection rates and its differential pressures are equivalent to brine injections.

Choice of surfactants based on differential pressures could be dicey in the sense that though high differential pressures are required, it is likely that those surfactants with extremely high differential pressures might not make a good pick since they could fracture the reservoir. In that vein, it is imperative that more detailed studies are conducted to verify the compatibility of those surfactants having extremely high differential pressures with specific reservoirs, so as not to damage them. In that regard, it will be worthwhile to pick for application those surfactants with moderately high differential pressures (Stepantan AS 1246–Amphosol, Stepantan AS 1246 and CS 1040) for the same reasons mentioned earlier. In summary, extremely high differential pressures alone do not make surfactants a better choice but must be looked at in the broader picture of the type, strength and other reservoir conditions before committing to a particular surfactant for application.

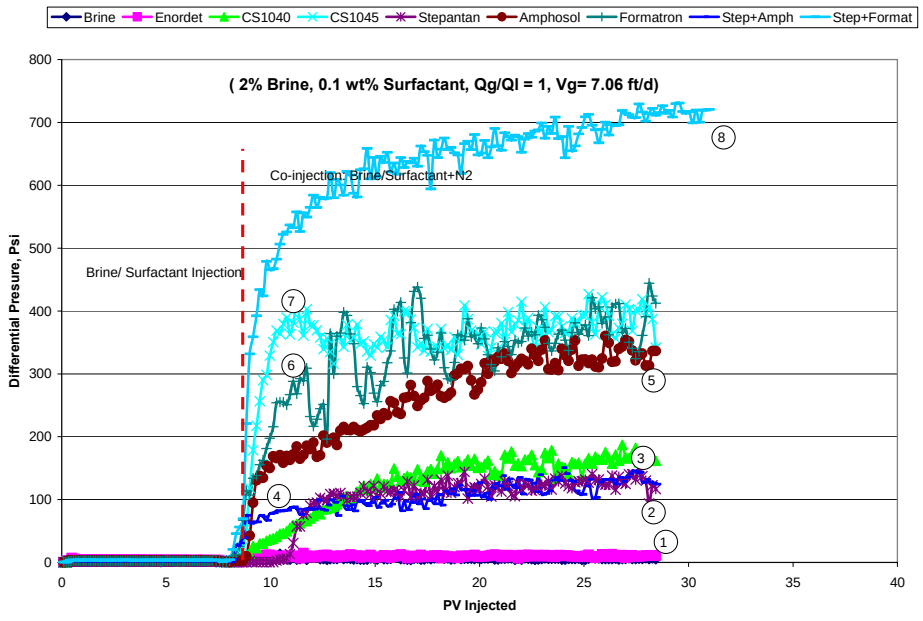

Fig. 106. Differential pressures vs. total PV injected (Vg = 7.06 ft/d).

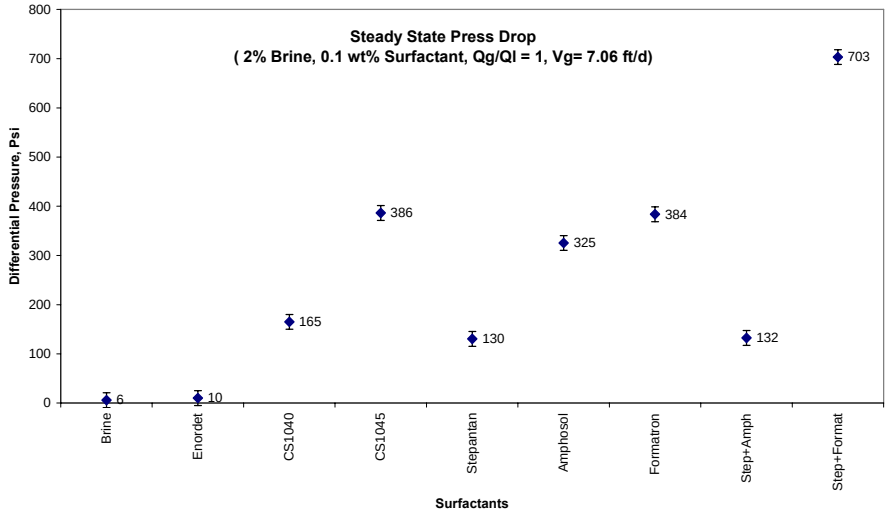

Fig. 107. Steady state differential pressures (Vg = 7.06 ft/d).

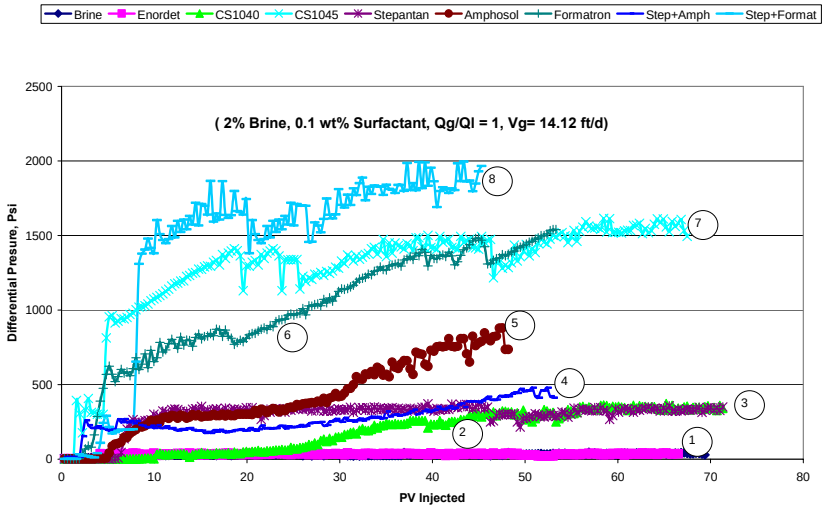

Fig. 108. Differential pressures vs. total PV injected (Vg = 14.12 ft/d).

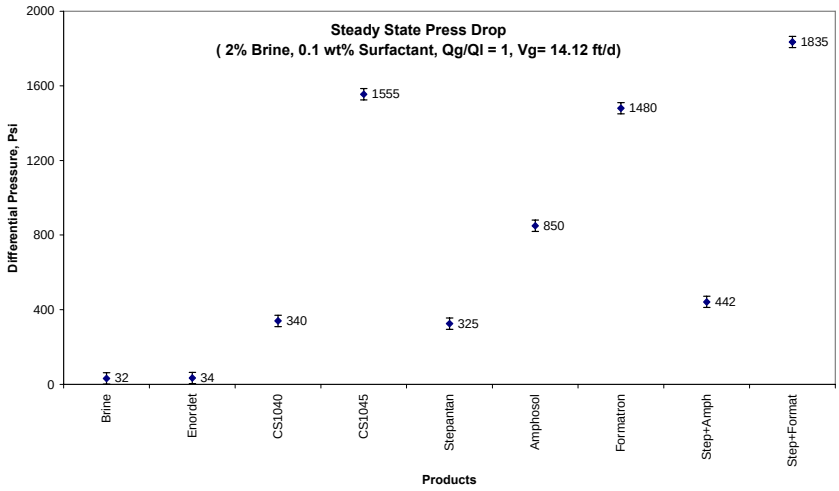

Fig. 109. Steady state differential pressures (Vg = 14.12 ft/d).

Mobility Reduction Factors (MRF)

Steady state total mobility (M) for both instances of injection rates are shown in Figs. 110 and 111. Coinjection of brine and N_2 yielded the highest total mobilities of 189.5 md/cp and 69.7 md/cp corresponding to total flow rates of 14.12 ft/d and 28.25 ft/d, respectively. There was no foam generated in the core; hence, mobility was not retarded. Both figures illustrate the significance of foam formation in the reservoir as evident in substantial reduction in total mobilities by virtue of foam formation. Total mobilities were reduced from 189.5 md/cp and 69.7 md/cp to single digits for most of the surfactants. This is good because most reservoirs are heterogeneous and mobilities need to be reduced to have significant influence on sweep efficiency. That is, the smaller the mobilities, the more uniform the front, the less viscous fingering and the better the sweep. The smaller the mobilities, the better also the foam forming qualities of the surfactants and that will translate into reducing early breakthrough. Apart from Enordet, all the other systems have substantially reduced mobilities and the Stepantan AS 1246 + Formatron mixed system shows superior mobility reduction compared to the injection of other

systems. However, mobilities around 1.0 md/cp might take a long time to produce or might not move at all, for that matter; those around 10 md/cp, which are moderate mobilities, may be preferred.

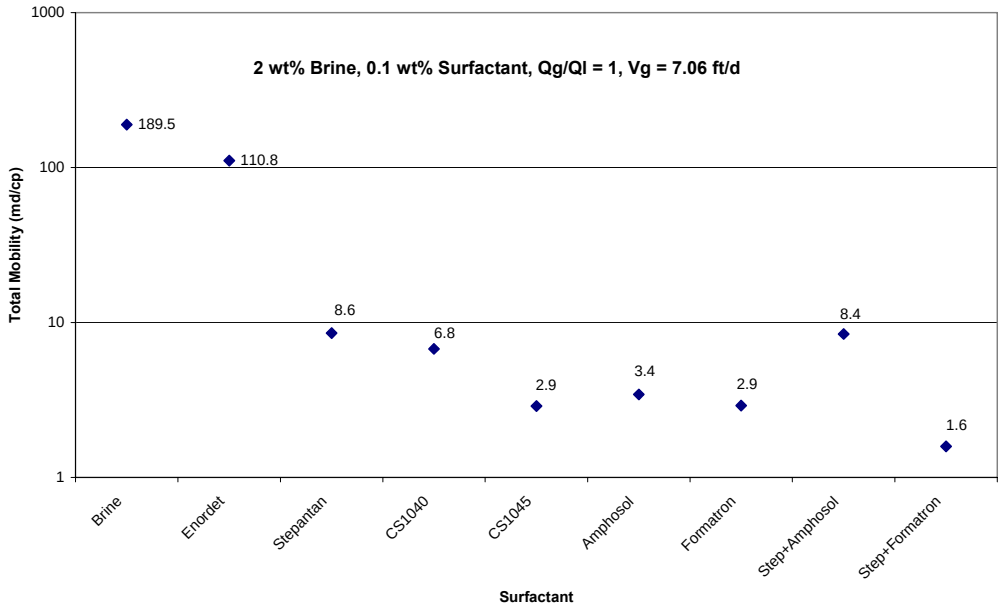

Fig. 110. Steady state total mobility (Vg = 7.06 ft/d).

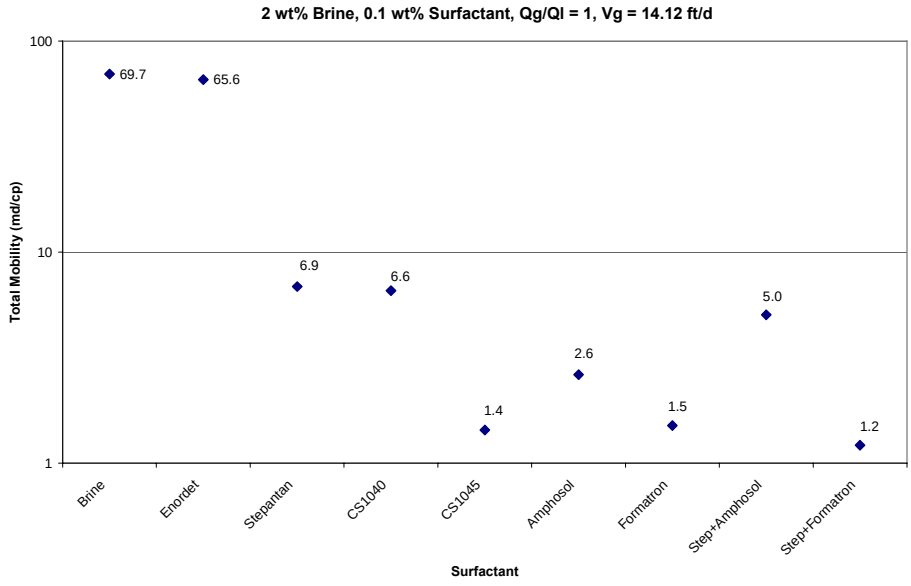

Fig. 111. Steady state total mobility (Vg = 14.12 ft/d).

The mobility reduction factors (MRF) are shown in Figs. 112–115 for respective dynamic and steady state differential pressures for respective flow rates. The results show considerable decrease in gas mobility when steady state was reached (Figs. 113 and 115) for most of the surfactants. The results also confirm the conclusion by Chang and Grigg[119] that the foam resistance factor decreases with increasing flow rate. For both flow rates, Stepantan AS 1246-Fomatron mixed system show superior qualities in reducing mobility. It reduced gas mobility by 119 times for Vg = 7.06 ft/d and 57 times for Vg = 14.12 ft/d but these figures may be too high and furthermore, may take a long time to produce. However, these results confirm the report by Tsau et al[120] that favorable foaming stability and selective mobility reductions are observed when mixed surfactants are coinjected with CO_2. Other good surfactants are CS 1045, Amphosol and Formatron; their respective MRF are shown in Figs. 113 and 115. These high mobility reduction factors are especially important in heterogeneous systems where improvement in oil recovery is caused by blockage of the high-permeability channels and diversion of N_2. Enordet in particular was very poor in generating foam in-situ and has the lowest MRF of 1.71 and 1.06 for Vg = 7.06 ft/d and 14.12 ft/d respectively.

Low mobilities, which are equivalent to high mobility reduction factors, are essential for effective sweep but extremely low mobilities and extremely high MRF may reduce flow abnormally so that it might be difficult to produce. In the light of these, it is prudent to further analyze these surfactants with specific reservoir rock before one can commit to any for application.

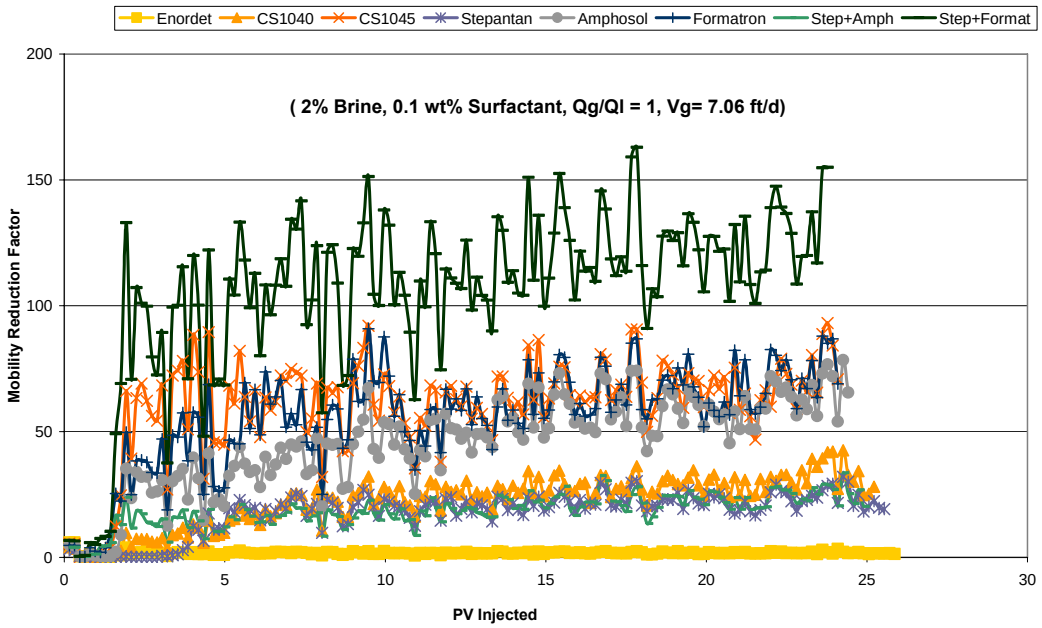

Fig. 112. MRF vs. total PV injected (Vg = 7.06 ft/d).

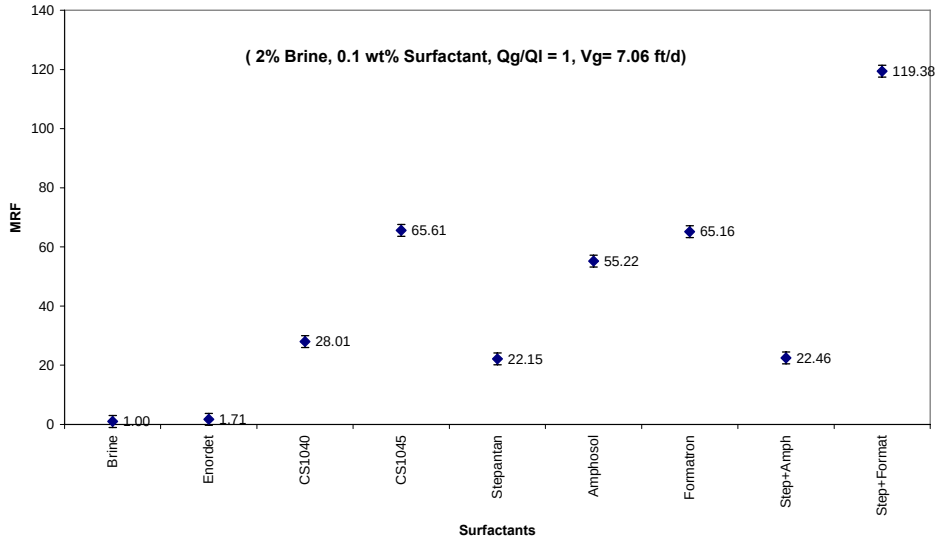

Fig. 113. Steady-state MRF vs. total PV injected (Vg = 7.06 ft/d).

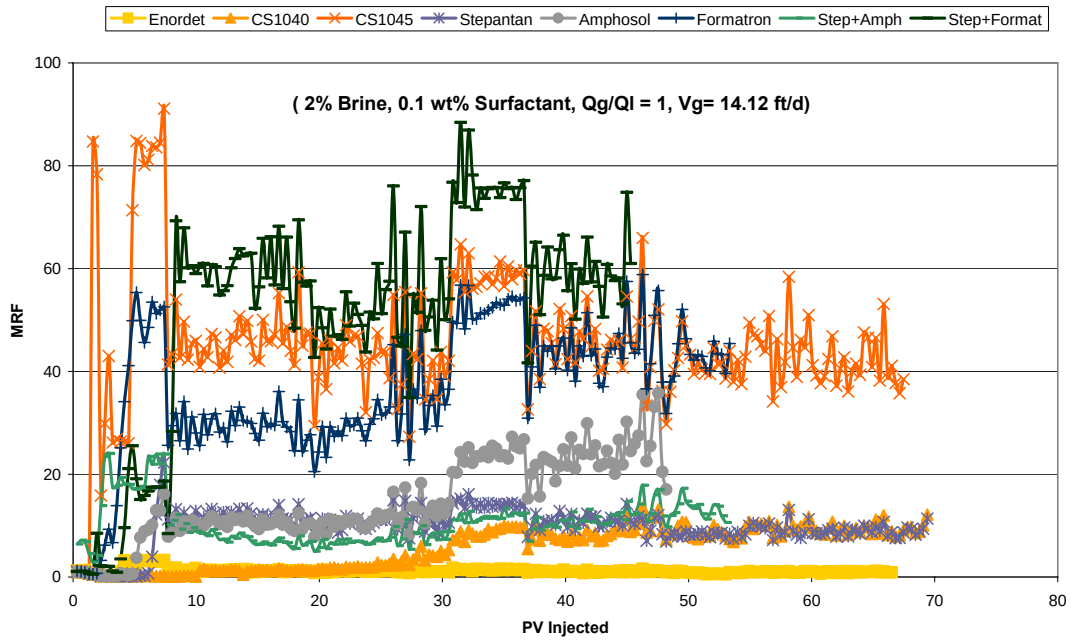

Fig. 114. MRF vs. total PV injected (Vg = 14.12 ft/d).

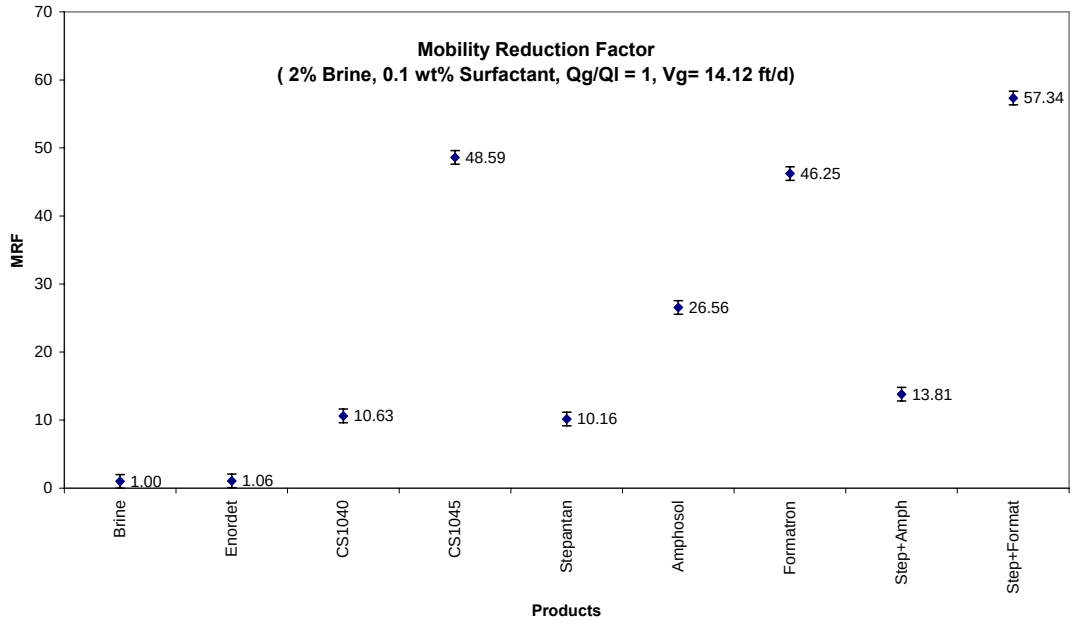

Fig. 115. Steady-state MRF vs. total PV injected (Vg = 14.12 ft/d).

A.6. Modeling Adsorption Density in the Adsorption Process

The measured adsorption density during the adsorption and desorption processes was calculated from the results of these experiments. The measured adsorption density in the circulation experiment is calculated according to the following equation:

$$q_i = \frac{\sum_{i=1}^{N}(C_{i-1} - C_i)\cdot V_i}{W} \quad \text{.....19}$$

where q_i is the surfactant adsorption density at the i^{th} step, mg/g; W is the mass of the rock specimen, g; C_i is the surfactant concentration at the i^{th} step, mg/l; V_i is the total surfactant solution volume at the i^{th} step, l; and N is the total steps at present.

The surfactant solution was sampled and tested more often at the beginning. Table 23 shows the results of Ads. Test 1, of which initial surfactant concentration was 196 mg/g.

Adsorption Density in Desorption Process

For the desorption process, the adsorption density at each step was calculated using the following equation group:

$$\begin{cases} A_1 = q_0 \cdot W + C_0 \cdot PV \\ A_i = A_{i-1} - C_{i-1} \cdot Ve_{i-1} \quad (\mathrm{i} = 2,...,\mathrm{N}) \\ M_i = C_{i+1} \cdot PV \\ B_i = A_i - M_i \\ q_i = \dfrac{B_i}{W} \end{cases} \quad \text{.....20}$$

where A_i is the surfactant in the rock and tubing at the i^{th} step, mg; q_0 is the initial surfactant adsorption density in the desorption process, mg/g; W is the mass of the rock specimen, g; C_0 is the initial surfactant solution concentration in the desorption process, mg/l; PV is the volume of the pore space and the tubing, l; Ve_i is the effluent volume at the i^{th} step, l; M_i is the surfactant left in the pore space and the tubing at the i^{th} step, mg; and N is the total steps at present.

Similarly, the effluent was analyzed more frequently at the beginning. Table 24 shows the results of Des Test 1, corres-ponding to Ads Test 1.

In total, 8 series of circulation experiments for adsorption were conducted, and 7 series of flow- through experiments for desorption were performed. From the measured adsorption density at different steps during the adsorption and desorption processes, the adsorption and desorption kinetics of the surfactant can be determine.

Derivation of Kinetic Equations

Assuming rate dependence of surfactant sorption, the pseudo- first and second order kinetic models for adsorption and desorption are derived as follows.

Pseudo First Order Adsorption Model

If the adsorption process obeys the pseudo first order adsorption model, it can be written in the following differential equation:[121]

$$\frac{dq}{dt} = k_{a1}(q_e - q) \quad \text{……..…….....……..21}$$

where q is the surfactant adsorption density, mg/g; t is the time, h; k_{a1} is the pseudo first order kinetic coefficient of adsorption, h^{-1}; and q_e is the surfactant adsorption density at equilibrium, mg/g.

The initial condition is $q = 0$ at $t = 0$. Using this condition, the solution for Eq. 3 is obtained as follows:

$$q = q_e\left(1 - e^{-k_{a1}t}\right) \quad \text{…….....} \ 22$$

Pseudo Second Order Adsorption Model

The differential equation for the pseudo second order adsorption model can be written as:[121]

$$\frac{dq}{dt} = k_{a2}(q_e - q)^2 \quad \text{…….…..……..23}$$

where k_{a2} is the pseudo second order kinetic coefficient of adsorption, g/(mg •h); and t, q, and q_e are the same as in Eq. 21.

Integrating Eq. 23 at the initial condition of $q = 0$ at $t = 0$, the following solution is obtained:

$$\frac{1}{q_e - q} - \frac{1}{q_e} = k_{a2}t \quad \text{..... 24}$$

Rearranging Eq. 6 leads to:

$$q = \frac{k_{a2} \cdot q_e^2 t}{1 + k_{a2} \cdot q_e t} \quad \text{.....25}$$

Pseudo First Order Desorption Model

The differential equation of the pseudo first order kinetic model for desorption process can be defined as:[122]

$$\frac{dq}{dt} = k_{d1}(q - q_r) \quad \text{.....26}$$

where k_{d1} is the pseudo first order kinetic coefficient of desorption, h^{-1}; and q_r is the residual surfactant adsorption density at the end of the desorption process.

The initial condition is $q = q_0$ at $t = 0$, where q_0 is the adsorption density at the start of the desorption process. Solving Eq. 26 based on this initial condition gives:

$$q = (q_0 - q_r)e^{k_{d1}t} + q_r \quad \text{.....27}$$

Pseudo Second Order Desorption Model

The differential equation of the pseudo-second-order kinetic model for desorption process can be defined as:

$$\frac{dq}{dt} = k_{d2}(q - q_r)^2 \quad \text{.....28}$$

where k_{d2} is the pseudo second order kinetic coefficient of desorption, g/(mg •h).

With the initial condition $q = q_0$ at $t = 0$, Eq. 28 is solved as follows:

$$\frac{1}{q - q_r} = \frac{1}{q_0 - q_r} - k_{d2}t \quad \text{.....} \quad \text{.....} \quad 29$$

It can be further simplified as:

$$q = \frac{q_0 - q_r}{1 - k_{d2} \cdot (q_0 - q_r) \cdot t} + q_r \quad \text{.....} \quad 30$$

Using the experimental data obtained in last section, Eqs. 22, 25, 27 and 30 can be used to test whether the adsorption and desorption processes can be described by these models; and if a specific model is applicable, what the kinetics parameters' values are. In return, knowing the kinetic model and their parameters, the change of the surfactant concentrations in the solution can be predicted, and thus the foaming processes.

Simplex Nonlinear Optimization

It can be seen that in Eqs. 22, 25, 27 and 30, adsorption density and time are related nonlinearly. Previous efforts to test nonlinear models through simplification and linearization have limitations. For instance, only two unknown parameters can be determined. For nonlinear equations with three and more unknown parameters, the linear correlation method does not apply. The correlation coefficient, R^2, is a relatively relax condition. No absolute errors are given in this type of correlation. In order to overcome these limitations, a simplex method for nonlinear optimization is adapted here for testing the models and determining their parameters.

The simplex method refers to two different mathematical optimization approaches: simplex linear programming[123] and simplex nonlinear optimization.[124] While sharing the same name, these two approaches are completely different.[125] This paper focuses on the method of simplex nonlinear optimization.

Function Definition

A properly defined function is the basis of simplex nonlinear optimization. Assuming an objective function is defined by *n* variables as

$$f = f(X) = f(x_1, x_2, ..., x_n) \quad \text{.....31}$$

Now the task is to find a set of variables, $X^0(x_{1\eta\eta}, x_2, ..., x_n)$, that minimizes the simplex function *f*.

Mathematical Procedures

The general idea of the simplex method is to minimize the simplex function of the *n* variables by comparing function values at *(n+1)* points, which forms a polyhedron, or simplex, in the *n*-dimensional space. In each step of iteration the point that makes the function maximum and minimum are termed as the worst point, *W*, and the best point, *B*. The worst point is replaced by a new point calculated through the simplex operation. The procedures are as follow:

Step 1. Initialize *(n+1)* feasible solutions to define the initial simplex.

Step 2. Calculate the function value at each point. Find the best and the worst point which makes the function value minimum and maximum, respectively.

Step 3. Calculate the possible new point to substitute for the worst point.

Step 4. Substitute the worst point by a new point according to the simplex operation rules.

Step 5. Repeat Step 2 through Step 4 until a previously defined criterion is satisfied.

These procedures are achieved by four basic operations: reflection (*R*), expansion (*E*), contraction (*C*) and shrinking (*S*), as demonstrated in Fig. 116 by a *2*-variable simplex. In Fig. 3, *BMW* is the initial simplex, in which *B* represents the best point, *W* the worst, and *M* the intermediate. The dashed lines represent the simplex operations, *R* refers to the reflected point of *W*, *E* the expanded point of *R*, *C* the contracted point of *W*, and S_1 and S_2 the shrunk points of both *M* and *W*. Whether the initial simplex *BMW* becomes *BMR*, *BME*, *BMC* or BS_1S_2 is decided by the following simplex operations.

Simplex Operations

Initialize the Simplex. Assuming the initial simplex is composed of the following *(n+1)* points:

$$X_i = (x_{1i}, x_{2i}, ..., x_{ni}) \qquad (i = 1,2,...,n+1) \quad \text{.....32}$$

Each of the X_i must be both mathematically and physically valid to Eq. 31. The simplex function value at each point is:

$$f_i = f(X_i) \qquad (i = 1,2,...,n+1) \text{ ……..33}$$

Rank the Function Values. The function value of each point is calculated. Then the best point, $B(X_B)$, and the worst point, $W(X_W)$, are determined by the following formula:

$$\begin{cases} f_B = f(X_B) = \min(f_i) \\ \qquad\qquad (i = 1,2,...,n+1) \text{ ……..34} \\ f_W = f(X_W) = \max(f_i) \end{cases}$$

Calculate the Reflection Point. The reflection point, $R(X_R)$, of the worst point, $W(X_W)$, is calculated as follows:

$$\begin{cases} X_R = 2X_F - X_W \\ X_F = \dfrac{1}{n}\displaystyle\sum_{\substack{i=1 \\ i \neq w}}^{n+1} X_i \end{cases} \text{ ……...35}$$

Substitute the Worst Point. The substitution of the worst point is conducted according to the following simplex rules:

a. If $f_R < f_B$, then $R(X_R)$ is expanded to $E(X_E)$, by the following formula:

$$X_E = (1+\mu)X_R - \mu X_F \text{ ……..36}$$

where μ is the expanding coefficient, $1.2<\mu<2$.

Now if $f_E < f_B$, then $W(X_W)$is substituted by $E(X_E)$; otherwise, $W(X_W)$ is substituted by $R(X_R)$.

b. Else, if $f_B < f_R < f_W$, then $W(X_W)$ is substituted by $R(X_R)$.

c. Otherwise, if $f_R >= f_W$, then $R(X_R)$ is contracted to $C(X_C)$, by the following formula:

$$X_C = \lambda X_W + (1-\lambda) X_F \quad \text{.....37}$$

where λ is the contracting coefficient, 0.0<λ<1.0.

Now if $f_C < f_W$, then $W(X_W)$ is substituted by $C(X_C)$; otherwise, the whole simplex is shrunk by half toward the best point, $B(X_B)$, to form a new simplex by the following formula:

$$X_i^{'} = \frac{1}{2}\left(X_i + X_B\right) \qquad (i = 1,2,...,n+1) \quad \text{.....38}$$

where $S_i(X_i^{'})$ is the new points of the simplex.

After the above substitution steps, a new simplex is formed. The function value of each point of this new simplex is again calculated by Eq. 31, and the simplex operations from ranking to substitution are repeated until a predefined criterion is satisfied.

Simplex Algorithm for Sorption Kinetics

In the previous section, equations of the pseudo first and second order adsorption and desorption models were derived. From Eqs 22, 25, 27 and 30, it is seen that adsorption models have two unknown parameters, and desorption models have three unknown parameters. Using the above simplex method and the experimental data of Ads Test 1 and Des Test 1 shown in Tables 25 and 26, this section will demonstrate the testing of the models and determination of the kinetic parameters.

Test of Pseudo Second Order Adsorption Model

Defining the Function. The pseudo second order adsorption model, Eq. 25, has two unknown parameters, k_{a2} and q_e, so the simplex will have three points, (k_{a2i} , q_{ei}) ($i = 1, 2, 3$). In Table 25, there are 12 measurements, (t_j, q_{tj}) where ($j = 1, 2, \ldots, 12$). Further, for each measurement time, t_j, a theoretical adsorption density, q_{cj}, can be calculated using Eq. 25 with each assumed value of (k_{a2i} , q_{ei}). Now the goal is to find the best point (k_{a2b} , q_{eb}) that can minimize the cumulative

difference between the measured and the calculated adsorption densities. With these considerations, the function is defined as:

$$f_i = \sum_{j=1}^{M} \left| q_{tj} - \frac{k_{a2i} \cdot q_{ei}^2 \cdot t_j}{1 - k_{a2i} \cdot q_{ei} \cdot t_j} \right| \quad \text{.....39}$$

where j is the index of measurements; i is index of simplex points; and M is the total number of measurements, $M=12$ in Ads Test 1.

Initiated Simplex. Theoretically, the simplex algorithm is independent of the initial values of (k_{a2i} , q_{ei}) where (i = *1, 2, 3*). However, a reasonable set of initial values would speed up the search for the solution. In order to give reasonable initial values for (k_{a2i}, q_{ei}) where (i = *1, 2, 3*), a rough estimate of the ranges of these parameters is helpful. If the adsorption process is rate independent, k_{a2} would be zero; otherwise, k_{a2} could be any positive value. If there is no adsorption, q_e would be *zero*. From Table 25, q_e could be very well constrained within *0* and *1*. Based on this rough estimation, three pairs of initial values are given in Table 27.

Initial values in a larger range have been tested and same results have been repeated.

Solution Criterion. Two criteria were applied: the absolute error and the maximum iteration of simplex operations. The first is the function value defined by Eq. 39 divided by the number of measurements. It is the error between the measured and calculated values. This criterion was set at *0.005 mg/g* for Ads Test 1. The second criterion was set to avoid dead loop in case of an incorrect model or unrealistic error level. A maximum iteration of 1000 was set in this case.

Results of Ads Test 1. Using the above defined function, initial simplex and criteria, a computer program was developed for the simplex operation. Table 28 shows part of the results. The same results were repeated by changing the initial simplex values and the criteria. This proves that the algorithm is robust, and the results are reliable.

It can be seen that the solution was obtained by the 200th iteration. After that, the solution and the error did not change. It can also be seen that the error criterion of *0.005 mg/g* has not been

met. Instead, the program stopped when the maximum iteration was reached and did not change after 100 iterations.

Applying the k_{a2} and q_e of Table 28 and the time of Table 25 into Eq. 25, the calculated adsorption density at each time can be obtained. Figure ? compares the measured and modeling results for this case. The model matches the test results well except for the third test point that was taken at 6 hours. The experimental results are more erratic in the time period of rapid transition. This is where the experimental and modeled results deviate. This occurred and was probably due to the experimental accuracy where adsorption rate changes rapidly.

Results of Ads Test 2-8. Following the same procedure, Ads Tests 2–8 were analyzed. Table 29 summarizes the final results of all the tests. Fitness of the measured and modeled results is shown in Fig. 118.

The low absolute error, the close match between the measurements and the modeled results indicate that a pseudo second order model can describe the adsorption kinetics of CD1045 onto Berea sandstone under the specific conditions.

Test of Pseudo First Order Desorption Model

Desorption experiments shown in Table 30 were found to be best fitted by the pseudo first order desorption model. The simplex procedure is similar to that for the test of the pseudo second order adsorption model. Applying Eq. 27 to replace the counterpart in Eq. 39, the simplex function for the desorption model is defined as:

$$f_i = \sum_{j=1}^{M} \left| q_{tj} - \left[\left(q_{0i} - q_{ri} e^{k_{d1i} \cdot t_j} \right) + q_{ri} \right] \right| \text{.....40}$$

In Eq. 40, there are three unknowns, k_{d1}, q_0, and q_r. Therefore, the simplex is a *3*-dimensional tetrahedron. The initial simplex has *4* points, each with *3* values for each of the three unknowns. Table 30 shows the initial values for Des Test 1.

With the above modifications of the simplex computer program, the parameters of the pseudo first order model for Des Test 1 are obtained as shown in Table 32. The fitness of the measured data and the modeling results are shown in Fig. 119.

Des Test-2 to -7 in Table 30 were also processed in the same way. Table 34 summarizes the final results of all the desorption tests. The fitness of the model to the measured results for desorption Test 2 to 7 is shown in Fig. 120. It can be seen that all desorption tests can be well fitted by pseudo first order model except Des Test 6. This is due to the fact that Des Test 6 had three different flow rates, as shown in Table 30.

Test of Pseudo First Order Adsorption and Pseudo Second Order Desorption Models

The adsorption and desorption experimental results were also tested with pseudo first order adsorption model, Eq. 22, and pseudo second order desorption model, Eq. 30. The models did not converge, and gave no indication that they would do so, even though the iteration limit of 10,000 was used. Therefore, these experimental data cannot be described by these models.

Conclusions

Through the work described in this section, the following conclusions were arrived:

1. The pseudo first and second order kinetic models for adsorption and desorption were derived in a mathematically complete format. These models are nonlinear. The adsorption models have two unknown parameters, and the desorption models have three unknown parameters.
2. A simplex nonlinear optimization method was adapted for the determination of the unknown parameters for these kinetics models. This algorithm can be applied to determine not only the parameters of these nonlinear models, but also the absolute error between the model and the measured results.
3. The adsorption and desorption processes of surfactant CD1045 onto and from Berea sandstone were found to obey a pseudo second order adsorption model and the a pseudo first order desorption models, respectively. More experimental work under different conditions will be carried out to better understand the influences of different factors on the sorption processes.

Table 25. Measurements of Ads Test 1

Step	Time (h)	Adsorption density (mg/g)
1	1	0.009
2	3	0.046
3	6	0.109
4	24	0.106
5	30	0.115
6	36	0.122
7	48	0.121
8	72	0.138
9	96	0.138
10	120	0.139
11	144	0.139
12	168	0.137

Table 26. Measurements of Des Test 1

Step	Time (h)	Adsorption density (mg/g)
1	0.5089	0.1089
2	0.9749	0.0918
3	1.4368	0.0907
4	1.8972	0.0906
5	2.5097	0.0903
6	3.3083	0.0903
7	4.3241	0.0895
8	5.3496	0.089
9	5.6694	0.0888
10	9.9094	0.0868
11	18.2027	0.0842

Table 27. Initials for Ads Test 1

I	k_{a2} (g/(mg·h))	q_e (mg/g)
1	0	0
2	0	1
3	5	0

Table 28. Simplex Operation Results of Ads Test-1

Iteration	k_{a2} (g/(mg·h))	q_e (mg/g)	Error (mg/g)
100	0.9782	0.1458	0.007
200	0.9781	0.1458	0.007
400	0.9781	0.1458	0.007
600	0.9781	0.1458	0.007
800	0.9781	0.1458	0.007
1000	0.9781	0.1458	0.007

Table 29. Simplex Results of Ads Test 1-8

Ads. Test	Surf. conc. (mg/g)	Itera-tion	k_{a2} (g/(mg·h))	q_e (mg/g)	*Error* (mg/g)
1	196	200	0.9781	0.1458	0.007
2	493	100	0.6145	0.2691	0.014
3	727	200	0.7866	0.4254	0.006
4	1034	100	0.7940	0.5581	0.009
5	1627	100	0.2462	0.7578	0.012
6	2114	200	0.1386	0.9847	0.026
7	3123	200	0.3061	1.376	0.040
8	485	200	1.3826	0.3174	0.011

Table 30. Desorption Experiment Conditions

Des. Test	Surf. conc. (mg/g)	Flow rate (cm^3/h)	Temp. (°C)	Pressure (kPa)
1	196	15	40	101.3
2	727	15	40	101.3
3	1627	15	23	101.3
4	3123	15	40	101.3
5	493	30	40	101.3
6	1034	30	40	101.3
7	2114	60→4→60	40	101.3

Table 31. Initials for Des Test-1

I	k_{d1} (h^{-1})	q_0 (mg/g)	q_r (mg/g)
1	0.1	0.15	0.5
2	5	0.3	0.1
3	1	0.5	0.1
4	5	0.5	0.5

Table 32. Simplex Operation Results of Des Test-1

Iteration	k_{d1} (h^{-1})	q_0 (mg/g)	q_r (mg/g)	Error (mg/g)
100	-4.5458	.2856	0.0895	0.001
200	-4.5759	.2886	0.0895	0.001
400	-4.5759	.2886	0.0895	0.001
600	-4.5759	.2886	0.0895	0.001
800	-4.5759	.2886	0.0895	0.001
1000	-4.5759	.2886	0.0895	0.001

Table 33. Adsorption Experiment Conditions

Ads. Test	Surf. conc. (mg/g)	Flowrate (cm^3/h)	Temp. (°C)	Pressure (kPa)
1	196	15	40	101.3
2	493	15	40	101.3
3	727	15	40	101.3
4	1034	15	40	101.3
5	1627	15	40	101.3
6	2114	15	40	101.3
7	3123	15	40	101.3
8	485	15	23	101.3

Table 34. Simplex Results of Des Test 1-7

Des. Test	Surf. conc. (mg/g)	Iter-ation	k_{dl} (h^{-1})	q_0 (mg/g)	q_r (mg/g)	*Error* (mg/g)
1	196	200	-4.5759	0.2886	0.0895	0.001
2	493	1000	-2.9550	0.2821	0.0903	0.002
3	727	500	-0.0881	0.3476	0.3017	0.001
4	1034	200	-0.0476	0.5738	0.3042	0.002
5	1627	1300	-0.0805	0.8204	0.3035	0.005
6	2114	300	-0.5127	0.9306	0.4858	0.028
7	3123	3100	-0.0664	1.0595	0.7215	0.013

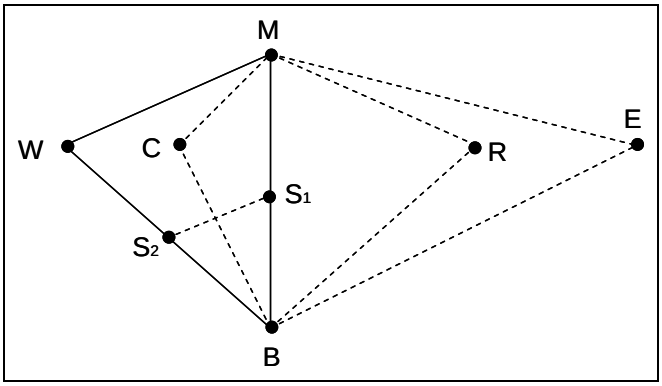

Fig. 116. Simplex operations in a 2-variable case.

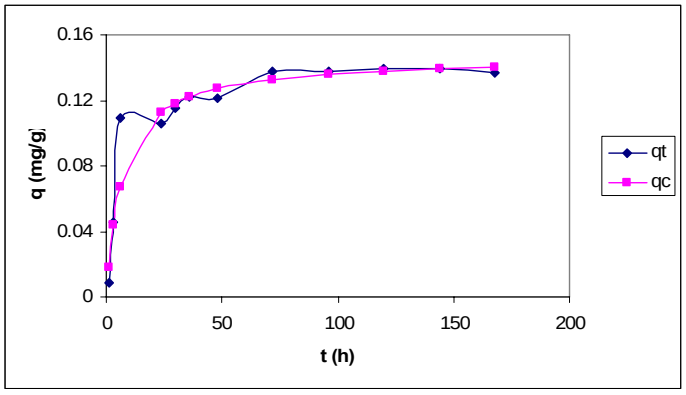

Fig. 117. Comparison of Ads Test 1 and pseudo second order modeled adsorption.

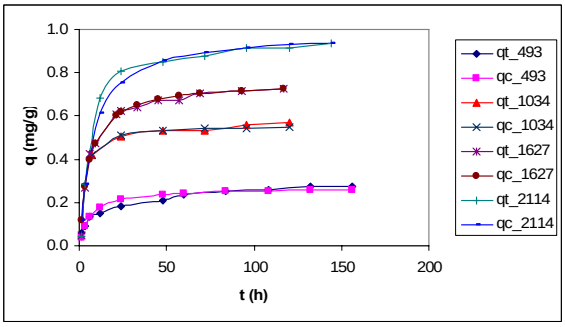

(a)

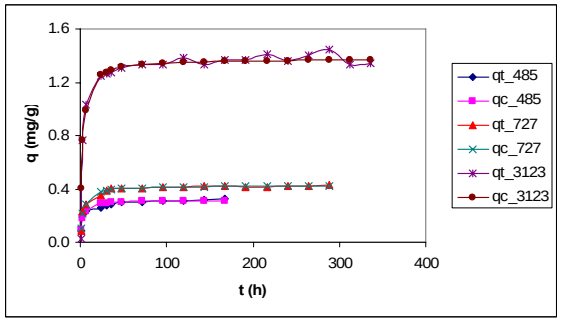

(b)

Fig. 118. Experimental results, qt, compared to pseudo second order model calculated adsorption density, qc, in Ads Test 2-8: (a) Ads Test-2, -4, -5, and -6; (b) Ads Test-3, -7, and -8.

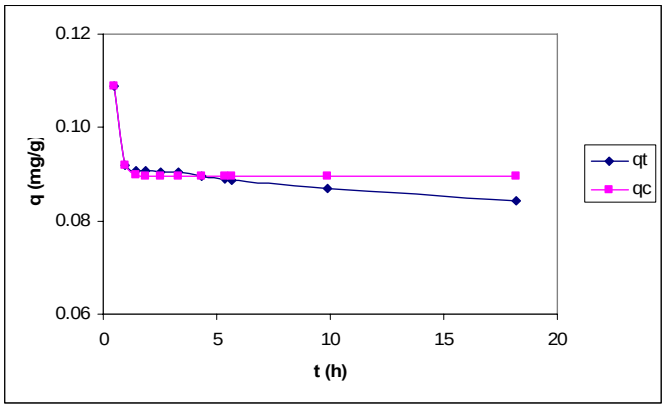

Fig. 119. Comparison of measured qt and modeled qc results of Des Test 1.

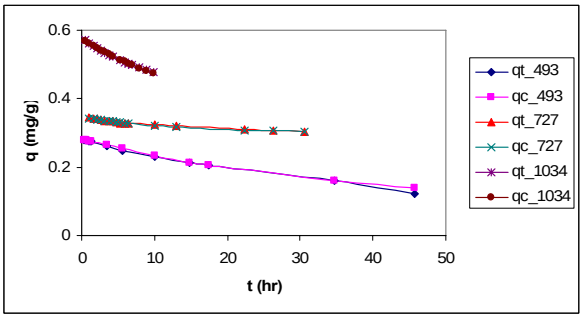

(a)

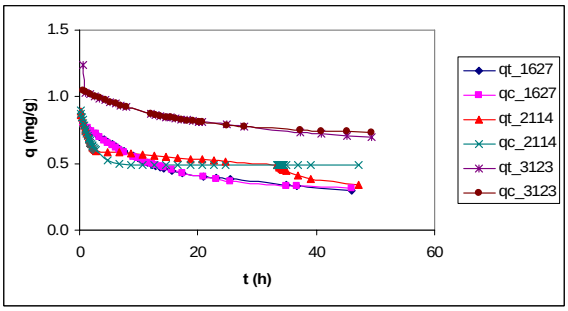

(b)

Fig. 120. Experimental results, qt, compared to pseudo first order model calculated adsorption density, qc: (a) Des Test-2, 3 and 4; (b) Des Test-5, 6 and 7.

B. RELATIVE PERMEABILITY and PHASE BEHAVIOR

B.1. CO_2 Retention and Injectivity Changes: Laboratory Tests

Introduction

Residual CO_2 saturation is suspected to be a significant factor for reducing injectivity during many water alternating with gas (WAG) processes for CO_2 EOR projects.[125] Also, there is increasing interest in minimizing CO_2 (greenhouse gas) emissions by sequestrating CO_2 in depleted oil and gas reservoirs or in saline aquifers.[126] The interest in increasing CO_2 injection into geological formations requires a better understanding of mechanisms and extent of CO_2 plume development and subsequent dissolution into formation brine. This study describes laboratory tests on Frio and Queen Sandstones, Indiana limestone, and Lockport dolomite. Several types of displacement tests were performed; gas injection into a core until no additional free brine was produced, thus to a pseudo-residual brine saturation with respect to gas injection, followed by brine injection into a core partially saturated with gas. The level of CO_2 saturation in the injected brine at reservoir pressure and temperature was varied from zero to over 90%. This variation of CO_2 saturation in the injected brine was to determine the effect on the CO_2 saturation or plume size in the core.

Determination of CO_2 saturation in a core was sought after injection of CO_2 into a core that was originally saturated with brine. This was then followed by the injection of brine into the core while differentiating brine displaced of free-phase CO_2 versus producing CO_2 dissolved in brine. Currently in the field, CO_2 is being injected into reservoirs nearing their waterflood economic limit and into aquifers; thus CO_2 is being injected into geological formations containing high brine saturation. To aid in conformance control and reduce the amount of CO_2 required for injection, CO_2 and water are alternately injected into oil reservoirs. Also, it is being proposed to inject CO_2 into innumerable aquifers for carbon sequestration. Thus tests are required for both the understanding of how brine and CO_2 streams flow through porous media and how their mutual solubilities change their saturations with time.

Experimental

Material

Frio cores used in these tests were obtained from depths of 2493, 2496.6, and 2497.8 m in the Felix Jackson # 62 Well, located south of the S. Liberty DOE CO_2 pilot site in Chambers County, Texas. These cores were selected because they were consolidated sandstone (see Frio Core Parameters listed in Table 35). The DOE carbon sequestration test site south of Houston is at a shallower depth and the test horizon is in poorly consolidated rock. These tests were performed in the consolidated core to simplify the development of test procedures. Table 36 lists the composition of the synthetic brine used in these tests, which is intended to represent the Frio reservoir brine. Indiana limestone is from a quarry near Victor, Indiana. The parameters for this core are also listed in Table 35. More details of the Frio sandstone and Indiana Limestone are found in an earlier publication.[127] The Queen sandstone core used in these tests was obtained from the West Pearl Queen Field, southeast New Mexico, Stevison Federal well #1 at 1375.0 m. The permeability was measured at 21.61 md by minipermeameter estimation (+/- 5.86). The whole core permeability was then determined by brine injection to be 15 md before the first test and 17 before the second test. Both compare well with minipermeameter tests performed using air; one on the whole core and the other at the end of the core and the other on the whole core. Other parameters are found in Table 35 with the brine used listed in Table 36. The dolomite core is Lockport dolomite. The core parameters and brine are listed in Table 36.

Pore System Characteristics

The mercury injection data show the sandstone has a measured porosity of 29.7% and a calculated Klinkenberg permeability of 2700 md (see Fig. 121). Most of the PV consists of intergranular pores (19.6% by point count) that appear to be well interconnected. Point count data indicates that secondary intraparticle and leached grain pores make up 3.6 vol % pore space, or an estimated 12% of the total PV (see Fig. 123). Micropores are created by partial to complete dissolution of susceptible detrital grains (mostly feldspars and volcanic grains) and are associated with authigenic clay cements. The difference between the mercury injection porosity (29.7%) and the point count porosity (23.2%) is generally a measure of pore space tied up as micropores (6.5%) or 22% of the total PV. The mercury injection of the sandstones show an initial invasion pressure of about 3.5 psi and sharp shoulder that leads to a flat slope from 5.0 to

9.0 psi where 50% of the pores (mostly large to medium sized intergranular pores) are filled. The injection curve begins to ramp up pressure until about 35–40 psi, where the mercury is estimated to invade the micropore space. The mercury injection pore throat radius distribution chart estimates 18% of the total porosity as micropores (assuming a 0.5 micron radius cutoff), which is close to the point count estimation of micropores, which is 22% of the total pore space.

Thin section observations show the Indiana limestone has a trimodal pore system of larger vugs and moldic pores, intergranular pores and micropores in partially leached ooids and peloids (see Fig. 124). The limestone sample has a measured porosity of 16.0% and a calculated Klinkenberg permeability of 118 md. Most of the PV consists of well connected intergranular pores (8.0% by point count) and secondary moldic pores and vugs (3.6% by point count). Fracture pores (2.0% by point count) are probably artificial and not included in these calculations. Micropores are created by partial dissolution of susceptible grains like ooids, algae, peloids and intraclasts. The difference between the mercury injection porosity (16.0%) and the intergranular and moldic point count porosity (11.6%) is generally a measure of pore space tied up as micropores (4.4%) or 28% of the total PV.

The mercury injection of the Indiana limestone shows an initial invasion pressure of about 3 psi and a gentle slope from 5.0 to 30.0 psi where the pressure begins to ramp up with little invasion (see Fig. 122). At about 110 psi the mercury begins to invade the micropore system. Assuming a 0.5 micron radius pore throat cutoff, the estimated micropore volume is 44% of the total PV. The point count estimation of micropores is lower at about 28% of the total pore space. This difference is likely due to sample heterogeneity, with the thin section sample having less ooids and occasionally having plucked grains artificially counted as vugs. The sample used for the mercury injection sample may have had more ooids and a higher percentage of equant calcite cement.

Core Flooding Apparatus

The core flooding apparatus is located in a temperature-controlled air bath, with a syringe pump and separator system outside the air bath (see Fig. 125). The dead volume of this system (non-flow path volume) and non-core volume (determined to be 4.3 cc) was minimized by reducing the number of pressure control devices, pressure transducers and valves in the system. All the cores were prepared by wrapping them longitudinally in a lead (Pb) foil which functioned as a diffusion barrier between the core and the overburden sleeve. In this way the diffusion of the

CO_2 from the core into the overburden fluid is minimized and the mass balance is optimized. During the analysis care was taken to capture all the water using an ambient condition separator (liquid trap) to catch the brine/water and a salt breaker (vapor trap) to capture water vapor. For a volume check the liquid and vapor traps were weighed before and after each test and in a couple of cases at an intermediate point. The wet-test meter was used to determine gas production at ambient conditions. Included in the gas calculations were corrections for gas displaced by brine/water in the separator.

Test Procedures

Frio sandstone tests were performed at the reservoir conditions of about 62.8°C (145°F) and 15.3 MPa (2200 psig), except for a couple of comparison tests at 37.8°C (100°F) that will be indicated. The overburden pressure was maintained at 27.7 MPa (4000 psig). The brine was prepared with the composition indicated in Table 36. In some cases the brine had CO_2 dissolved in it to represent brine that had been in contact with CO_2. The brine will be indicated as dead brine (no dissolved CO_2), 50% CO_2-brine (brine saturated to about 50% CO_2), and 90% CO_2-brine (brine saturated to about 90% CO_2). Brine saturated to 100% CO_2 was not used to ensure no new free CO_2 occurred from CO_2 evolving from the brine. Pressure drop across the core and/or dissolved solid changes in the brine due to dissolution of core material or water vaporizing into the CO_2 phase could perturb brine 100% saturated with CO_2 and result in small but undesirable amounts of free CO_2 forming from the injected fully saturated brine.

In all but one case the coreflood was initiated in core 100% saturated with dead brine. Dehydrated CO_2 was then injected into the core until no free brine was produced for several PV. The CO_2 was stored outside the air bath at ambient temperature and injected at rates from 10 to 200 cc/hr (20 cc/hr was used unless otherwise indicated) at ambient temperature and about 15.3 MPa. The CO_2 injection volume at 63°C was about 65% higher than at ambient temperature; both at 15.3 MPa. The temperature of the air bath, core, and injection pump were recorded. The head plus end volume of the core system is 4.3 cc; thus in Figs. 126, 127, 129, 130, and 132 the volumes are shown starting at -4.3 cc.

All Indiana limestone tests were performed at about 37.8°C (100°F) and pore pressure of about 15.2 MPa (2200 psig). In the first four tests the core was initially saturated with dead brine and displaced with CO_2 until no free water was being produced; usually requiring 2–3 PV after

the last production of free water was detected. In all but the third tests, the CO_2 injection rate was 20 cc/hr at room temperature or about 21.7 cc/hr at core conditions. In series three the injection rate was initially 21.7 cc/hr and then increased incrementally to 43.4, 86.8, and 130.2 cc/hr.

All Queen tests were performed at the reservoir conditions of about 35°C (95°F) and 14.5 MPa (2100 psig). The overburden pressure was maintained at 21.5 MPa (3100 psig). The brine was prepared with 220,000 ppm NaCl with no dissolved CO_2 before injection into the core. In each test the core was initially 100% saturated with dead brine. Dehydrated CO_2 was then injected into the core until no free brine was produced for several pore volumes (PV). The CO_2 was stored outside the air bath at ambient temperature and injected at 20 cc/hr at ambient temperature and about 14.5 MPa. The CO_2 unit volume at 35°C was about 8% higher than at ambient temperature or a lower density; both at 14.5 MPa. There is a slight reduction in permeability indicated from 17 to 15 md before and after the first test series.

The Lockport dolomite tests were performed at room temperature which varied from 18° to 23°C (65° to 73°F) and elevated pressures from 24.2 to 28.7 MPa (3500 to 4142 psia), see Table 36. The overburden pressure was maintained at about 34.6 MPa (5000 psig). The core was initially 100% saturated with dead water (degassed, distilled water). CO_2 was injected at 20 cc/hr into the core until free brine production had essentially stopped. Though water production does continue as water vapor in the produced CO_2, it is at a slow rate.

Discussion of Results

Results – Frio Sandstone

Figure 126 compares two tests of CO_2 displacing brine in Frio Core A. In both about 7 cc of brine was produced before CO_2 breakthrough. After CO_2 breakthrough there was a small quantity of brine produced and then brine production stopped except for water dissolved in the CO_2. Usually over 95% of the brine production occurred before 1 PV of CO_2 had been injected. Any continued production after less than 1 PV of CO_2 had been injected was from vaporized water. The salt vapor trap (Fig. 125) was weighed only at the end of the test and this value was added evenly over the duration of the test scaled to the injection rate in the brine/water production plots. The time when the vapor was actually produced is not known. In Fig. 126 the first system had an injection rate increase from 20 to 100 cc/hr after 200 cc of CO_2 had been injected. There was additional free brine produced following the injection rate increase. During

the second test, injection was continued overnight at a reduced injection rate of 10 cc/hr and then increased to 100 cc/hr for a short time at the end of the test.

In each case the saturations reached what might be considered stable pseudo-end point saturation. However this stable saturation changed by increasing the flow rate, decreasing pressure, and by evaporating water. What is the definition of an end point or residual water saturation? For this paper it will be referred to as a pseudo-end point. After completion of CO_2 injection, brine was injected into the core to displace the CO_2. Figure 127 compares the first two brine injection tests which used dead brine in Frio Core A after CO_2 injection in each test (see Fig. 126). In each about 4.3 cc of reservoir condition CO_2 was produced (the same as the end plate dead volume), then the CO_2 production rate decreased significantly. After this change in production rate, approximately 4 to 5 cc of additional CO_2 at reservoir condition were produced at a fairly constant rate. Using values from Wiebe and Gaddy[128] adjusted for dissolved solids,[129] these rates are what would be expected from CO_2 dissolved in Frio brine fully saturated with CO_2 at the test conditions. The CO_2 produced after the dead volume was produced was not a free phase. The final value of produced CO_2 from the system, including blowdown to ambient pressure, was equal to the brine produced during CO_2 injection; thus a good material balance was obtained throughout the experiments.

The second set of experiments was performed on Frio Core B. In this set the tests used the same procedure as for Frio Core A, except that CO_2 dissolved in the injected brine varied from 0 to 90% of CO_2 saturation. In each case the production rate of CO_2 in cc/cc of brine produced was around 24. This was what would be expected from saturated brine. Figure 128 compares the production rate of CO_2 during the injection of brine into Frio Core B during three different tests. Excluded in Fig. 128 was the first PV of brine injection where the production of free CO_2 was occurring, which exceeded 150 cc/min during free-phase CO_2 production. Each of the three tests shown in Fig. 128 followed the injection of CO_2 into the core saturated with dead brine. The three tests differ in the concentration of CO_2 in the injected brine. During the early time period the production rates are essentially equal for all three scenarios. The brine produced from this 6.1 cm core was saturated with CO_2 and did not depend on the CO_2 concentration of the injected brine. Thus the brine was saturated with CO_2 over a relatively short flow path.

The injection test using 90% CO_2-brine was not continued until free CO_2 was depleted in the core as in the other two cases. Injection and production continued long enough to verify the

production rate of CO_2 during the first part of the injection. From Fig. 128, CO_2 depletion in the core during the dead brine injection shows a rapid decline in the CO_2 production rate after most of the CO_2 had been produced. In the 50% CO_2-brine the drop is slower and as might be expected the system stabilizes at a rate of about 3 cc/min, which is the same as the content of the brine being injected. When the pressure was released on the 50% CO_2-brine system the produced CO_2 was equal to about that which would be evolved from 1 PV of brine saturated to 50% CO_2, indicating that all the free-phase CO_2 had been removed.

The production of CO_2 during the injection of 50% CO_2-brine at 37.8 and 62.8°C were similar, but the lower temperature appeared to be about 10–15% higher. This compares well with the higher solubility of CO_2 in brine at lower temperatures. The final set of Frio tests was in core C. Figure 129 has an expanded production rate scale to demonstrate the rate comparison during free-phase CO_2 production and production evolving from CO_2 dissolved in brine at reservoir conditions. In these tests the first step was started with a dry core. This was then saturated with 100% dehydrated CO_2; then dead brine was injected into the core. In this test about 9 cc of CO_2 at reservoir conditions were produced before production stabilized. This rate was equal to that of CO_2 evolved from brine saturated with CO_2 at 37.8°C and 15.2 MPa and 20 cc/hr flow rate. Then an additional 11 cc (reservoir conditions) of CO_2 were produced at a rate of about 8 cc/min at ambient conditions. This totals 20 cc of produced CO_2. Subtracting the 4.3 cc dead volume yields 16 cc or almost 90% of the 18.1 cc core PV. Another 2 cc were produced during the remaining injection period and subsequent blowdown. This test required about 4 cc of brine or 0.22 PV to establish a brine flow path. Shortly after brine breakthrough, it appears that only CO_2 dissolved in the brine was produced.

Results – Limestone

Several tests on Indiana limestone were conducted using the same procedure used for the Frio sandstone. All tests were performed at about 37.8°C and pore pressure of about 15.2 MPa. In the first four tests the core was initially saturated with dead brine and displaced with CO_2 until no free-phase water was being produced; usually requiring 2–3 PV after the last production of free-phase water was detected. In all but the third tests, the CO_2 injection rate was 20 cc/hr at room temperature and core pressure or about 21.7 cc/hr at core conditions. In series three the injection rate was initially 21.7 cc/hr and then increased incrementally to 43.4, 86.8, and 130.2 cc/hr while

the incremental produced water was 7.8, 0.3, 0.1, and 0.1 cc, respectively. Again, the first 4.3 cc produced was from the line volume resulting in brine production from the core of about 4.0 cc and vapor production caught in the salt trap of 1.4 for a total of about 5.4 cc of brine from the core. The brine/water production in the third test is compared to the other three tests in Fig. 130. There is a contrast of the production at similar injection rates between the first two and last two tests of almost 1 cc (Fig. 130). This is believed to be due to the formation of a solution channel in the limestone core.

Figure 131 compares flow tests at three different times during these tests that indicates a permeability change (increase). As the number of tests and PV of fluid injected into the core increased, the pressure drop versus flow rate increased. This is an indication that the core permeability was decreasing with time or PV of fluid injected. Tests performed after the last test indicated almost no pressure drop at all tested flow rates (20–200 cc/hr), indicating a very high permeability. In earlier tests with limestone, total core permeability increased over time until a solution channel through the core had been formed, and then the permeability drastically increased.[130,131] In each case there had been plugging or deposits advancing ahead of the solution channel.

Figure 132 compares the reservoir volumes of CO_2 produced for each test during the injection of brine. For Tests 1 and 2 dead brine was injected and for both there was a good material balance. For Tests 3 and 4, a 50% CO_2 saturated brine was injected. Again in both cases there was a good material balance, but a decrease in CO_2 production. This is also shown in Fig. 133 where the production rate in the later tests dropped before the free CO_2 was dissolved and produced, indicating the brine was not being saturated when a channel formed. In Tests 1 and 2 the core had very little CO_2 remaining at blowdown. For Tests 3 and 4 the production dropped much more quickly to the baseline for the 50% CO_2-brine and at blowdown both had significant amount of CO_2 remaining. Test 4 had almost 3 cc compared to about 1 cc remaining in Test 3 (Fig. 123). It is believed that the difference is due to the formation of the solution channel, where most of the flow bypassed the bulk of the core.

Results - Dolomite

As with the other rock types, the core was first saturated with water and water permeability was determined. Also, during CO_2 flooding of carbonate rock, dissolution and subsequent precipitation can occur. Both fines movement and precipitation results in permeability decreasing while dissolution increases permeability. From experience we have found that decreases in permeability in the early stages predominates over dissolution increases in permeability and later dissolution predominates.[130,131] In these tests the permeability decreased during the series of test.

Figure 134 shows a plot of data from Flood 1. In this test the core saturated with water had CO_2 injected at 20 cc/hr at the indicated conditions (Table 37). Plotted versus time are the differential pressures (left y-axis) and produced water, produced CO_2 at reservoir conditions, and injected CO_2 at reservoir conditions (right y-axis). The fluid production volumes were only recorded until gas breakthrough. At this point the separator top blew off several times and lost fluid, so the results were not considered accurate from that point. In Fig. 134 it is shown that this is a pressure increase as CO_2 displaces water and two-phase flow occurs. After CO_2 breakthrough, the average pressure drops is similar to the starting differential pressure across the core, except less stable. The initial condition is single-phase flow of brine at 100% brine saturation; postbreakthrough, it is single-phase flow of gas, but with two-phase saturation. Thus, under these conditions the relative permeability of the core to the less viscous CO_2 after breakthrough is similar to the permeability of the more viscous single-phase water before gas injection.

Dolomite Flood 2 is shown in Fig. 135. The pressure differential, cumulative CO_2 injection, cumulative water production, and cumulative CO_2 production plots all look similar to Flood 1 (Fig. 134), except some post-gas breakthrough data was obtained. No difference can be distinguished between the two.

Results - Queen

Figure 136 compares two tests of CO_2 displacing brine in the West Pearl Queen Core. In both just over 9 cc of brine was produced before CO_2 breakthrough (9.02 and 9.15 cc, respectively). Subtracting the 4.3 cc dead space leaves 4.72 and 4.85 cc or 0.373 and 0.383 PV, respectively (PV = 12.65 cc). After CO_2 breakthrough there was a small quantity of brine produced and then brine production stopped except for water dissolved in the CO_2. About 90% of the brine

production occurred before one PV of CO_2 had been injected. Much of the production after one PV of CO_2 was injected was from vaporized water. The salt vapor trap was weighed only at the end of the test and this value was added evenly over the duration of the test scaled by injection rate to the brine/water production plots. There were 0.6 and 0.2 grams of water captured in the vapor trap during the two tests, respectively. The time when the vapor was actually produced is not known. The flow rate was not changed in any of the tests as was done in some of the earlier tests. Figure 137 compares the pressure drop across the core during the injection of CO_2.

After completion of CO_2 injection, brine was injected into the core to displace the CO_2. Figure 138 compares the two brine injection tests, which both used dead brine after the CO_2 injection in each test (see Fig. 136). In each, about 4.3 cc of reservoir condition CO_2 was produced (the same as the end plate dead volume), then another 0.94 to 1.14 cc of the free-phase CO_2 was produced before the rate decreased; this seemed to indicate a residual CO_2. After this break, additional CO_2 was produced at a fairly constant rate. Using the values of Wiebe and Gaddy[128] adjusted for dissolved solids,[129] these rates are as expected from CO_2 dissolved in the brine fully saturated with CO_2 at test conditions. The final reservoir volume of produced CO_2 from the system, including blowdown to ambient pressure, was within 5% of the brine produced during CO_2 injection; thus a fair material balance.

Figure 139 compares the production of CO_2 during the injection of brine for the two tests. The production rates are essentially identical until the blowdown in the first test. The rate of about 170 cc/min at ambient is equivalent to the production of CO_2 at ambient conditions from a core at 14.5 MPa and 35°C. Then as the free CO_2 production ends the rate settles at about 8cc/min, which is about the solubility of CO_2 in brine.[129] At 58 minutes into Queen Test #1, blowdown started. During Queen Test #2 injection was stopped at 62 minutes and restarted at 73 minutes and continued until stopping injection at 140 minutes. Blowdown started at 153 minutes. For both tests the total CO_2 produced was equivalent and about equal to the reservoir volume of brine displaced. The 0.94 and 1.14 cc of free-phase CO_2 produced represent 0.074 and 0.090 PV in Queen Tests #1 and #2, respectively. This is compared to no free-phase CO_2 from the core seen in the Frio sandstone and Indiana limestone tests. This leaves a CO_2 residual saturation of 0.309 and 0.283 PV respectively, where any additional CO_2 production was from CO_2 dissolved in the brine.

The laboratory findings from the corefloods on Queen sandstone were performed at the same pressure and temperature conditions as the West Pearl Queen reservoir. This study also supports the results from the West Pearl Queen Reservoir Huff-n-Puff pilot.[132-134] In the pilot scenario, after CO_2 was injected and allowed to soak for several months, the subsequent production was relatively high for the first couple of weeks, but much slower thereafter. A prolonged, slow, consistent production occurred after the first couple of weeks. At reservoir conditions, assuming the produced brine is saturated, the production rate would be about 24 m^3 of CO_2 per m^3 of produced brine (135 scf of CO_2 per barrel of produced brine). During the first three months of production, 17% of the injected 2000 tons of CO_2 had been produced.[134] At that point a fairly steady production rate of 15 barrels of brine (2.4 m^3) and about 1 barrel (.16 m^3) of oil per day was being produced. If the produced brine and oil are saturated with CO_2 at reservoir conditions of about 35°C and 14.5 MPa (95°F and 2100 psig), it is expected that CO_2 production from solution would be about 60 m^3 and 40 m^3 from brine and oil, respectively, or 100 m^3 per day. Thus if the production of CO_2 is higher than 100 m^3/d, some would be derived from free-flowing CO_2. The total injection into the field was 2000 tons (~1,000,000 m^3). At the present rate, the remaining 83% of the injected CO_2 would take over 20 years to produce. After CO_2 in the reservoir is reduced to residual CO_2 the later production rates of CO_2 will be from CO_2 dissolved in the produced brine and oil. Since there are a number of zones, and within zones a range of permeabilities and porosities, production from free-flowing and dissolved CO_2 may be occurring simultaneously.

A consideration that was discussed earlier in the paper was the effect on injectivity of two-phase relative permeabilities near the wellbore, and how long this effect might persist. Some CO_2/brine relative permeabilities are reported by Bennion and Bachu[135] with some having similar end points, as reported in this work. In all cases, with CO_2 saturations in the 20 to 30% range the brine relative permeability ranges from 0 to 0.4. Each case could affect injectivity depending on the length of time required to remove CO_2 from the near-wellbore region. A quick calculation indicated that it would take about ten times as long in a WAG process to dissolve the residual CO_2 as it took to inject it into a region radial around a wellbore. This would be the case if the end-point saturation is the same as the residual CO_2 saturation. If half the CO_2 was free-flowing phase CO_2 then it would only take five times as long to remove the CO_2 as it took to place it. Thus a CO_2 saturation is persistent and will decrease injectivity significantly longer than

most WAG half- cycles. The assumption used was a solubility of about 2 mole % of CO_2 in brine. This represents a fairly low-salinity brine. The time would increase with increasing salinity. A related issue is that with relatively large volumes of CO_2 flowing through or near the brine near the wellbore, the evaporation of the water will create a dry zone around the wellbore that will increase the time to clear the near-wellbore area of CO_2 after the start of the brine injection cycle of WAG. Again, similar phenomena will occur with CO_2 storage in an aquifer, if the aquifer is flowing—which most do at some rate though generally slowly in comparison to the injection rate of a CO_2 EOR project. Nonetheless, this behavior should be considered when looking at the longer-time frames considered for sequestration.

Summary and Conclusions

These were relatively short cores (5.71 to 8.17 cm), about 3.8 cm in diameter, and therefore care must be taken when extrapolating results to reservoir scale. These findings of end-point saturation are significant parameters in determining flow patterns, retention rates, and injectivity changes and their longevity that will enable improved predictions of CO_2 behavior in reservoirs for EOR and/or sequestration considerations.

Conclusions from this work include:

1. In the range of 0.2 to 0.3 PV fraction of CO_2 saturation was required to establish a CO_2 flow path, after which there was little brine production except through evaporation, which is a slow process. The CO_2 saturation can be increased by increasing the flow rate and by water evaporation.
2. At the end of CO_2 injection there was relatively low CO_2 saturation and high brine saturation in the core; thus no reduction in CO_2 saturation was required to return to brine flow. Only in the Queen sandstone was there free flowing CO_2 with subsequent free CO_2 produced during brine injection.
3. Brine is equilibrated with CO_2 in a short time frame over a relatively short distance. Only when a solution channel was formed was brine produced that was not saturated with CO_2, while a significant residual CO_2 remained in the core.
4. The injection of brine into a 100% CO_2 phase required 0.2 to 0.3 PV fraction saturation to establish a brine flow path.

5. The sandstone and carbonate systems initially performed similarly. This changed when, through dissolution of the rock matrix, a solution channel was formed in the limestone, creating a dominant flow path that significantly altered the flow behavior of the core.
6. This work estimates that the removal of CO_2 saturation near a wellbore will take ten times as long as it took to establish it.

Table 35. Core Parameters

	Frio Sandstone			*Queen Sandstone*	*Indiana Limestone*	*Lockport Dolomite*
	Frio A	*Frio B*	*Frio C*			
Depth [m]	*2493.0*	*2496.6*	*2497.8*	*1375.0*	*Quarried*	*Quarried*
Diam [cm]	*3.73*	*3.66*	*3.73*	*3.81*	*3.84*	*3.78*
Length [cm]	*6.08*	*6.10*	*5.71*	*7.21*	*7.95*	*8.17*
Bulk vol [cc]	*66.44*	*64.18*	*62.39*	*82.20*	*92.07*	*91.68*
Pore vol [cc]	*18.51*	*18.01*	*18.29*	*12.65*	*16.28*	*15.72*
Por [%]	*27.9*	*28.1*	*29.3*	*15.4*	*17.7*	*17.1*

Table 36. Synthetic Brine Composition

Component (mg/L)	*Frio and Limestone*	*Queen*	*Dolomite*
NaCl	*82,753*	*220,000*	*-*
$CaCl_2$	*8,584*	*-*	*-*
$MgCl_2$	*2,152*	*-*	*-*
KCl	*362*	*-*	*-*
$NaHCO_3$	*186*	*-*	*-*
			-
Total Dissolved Solids	*94,037*	*220,000*	*0*

Table 37. Flooding Parameters

	Frio Sandstone	*Queen Sandstone*	*Indiana Limestone*	*Lockport Dolomite*
Pressures (MPa)	*15.17*	*14.45*	*15.17*	*24.14 – 28.62*
Temperatures (°C)	*37.8 & 62.8*	*35.0*	*37.8*	*18.3 – 22.5*
Flow Rates (cc/hr)	*10 - 200*	*20*	*20 – 120*	*20*
Brine (% CO_2 sat.)	*0, 50, & 90*	*0*	*0 & 50*	*0*
System Dead Vol. (cc)	*4.3*	*4.3*	*4.3*	*4.3*

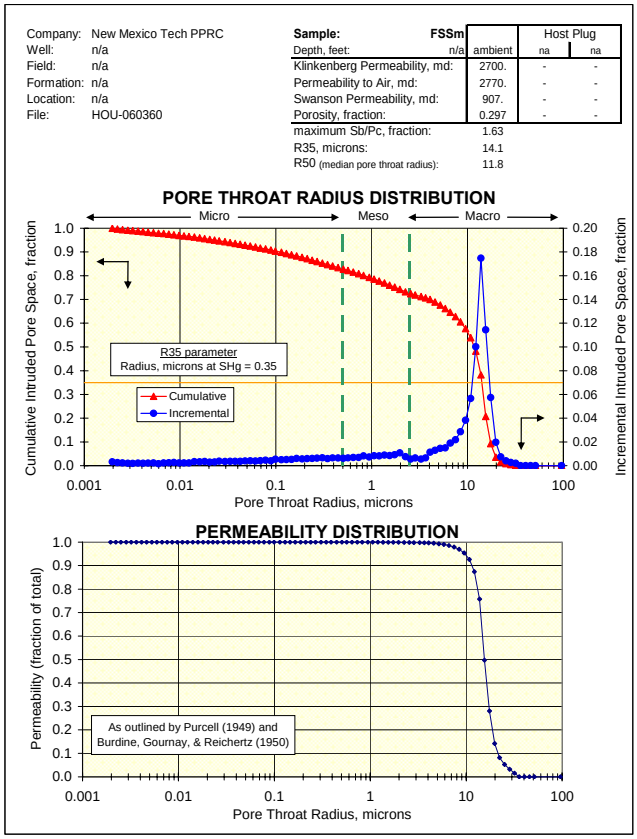

Fig. 121. Mercury injection pore throat and permeability distribution plots for Frio sandstone.

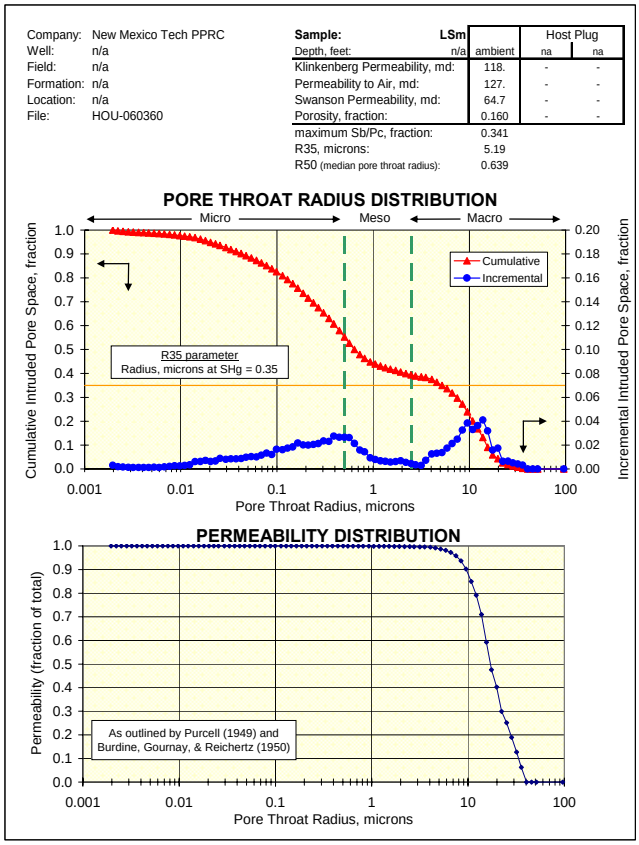

Fig. 122. Mercury injection pore throat and permeability distribution plots for Indiana limestone.

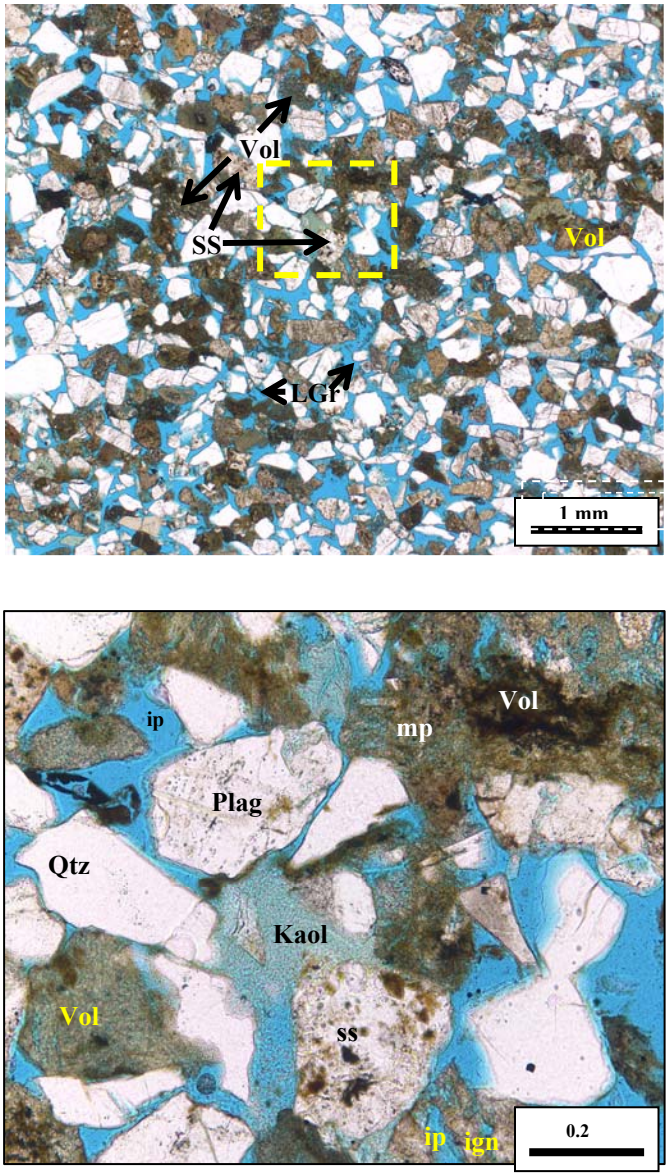

Fig. 123. Frio sandstone thin sections. Key: intergranular pores (ip), leached grain pores (LGr), micropores (mp), volcanic (Vol). kaolinite (Kaol), quart (Qtz), plagioclase (Plag), igneous (Ign), and sandstone (SS).

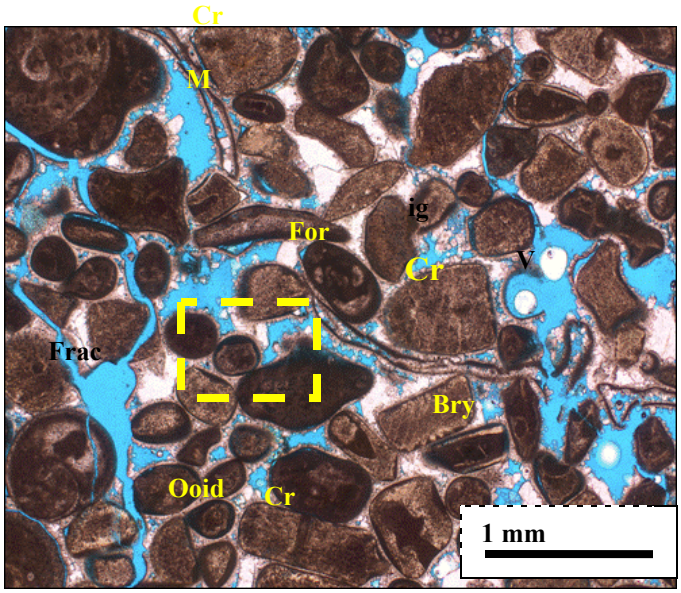

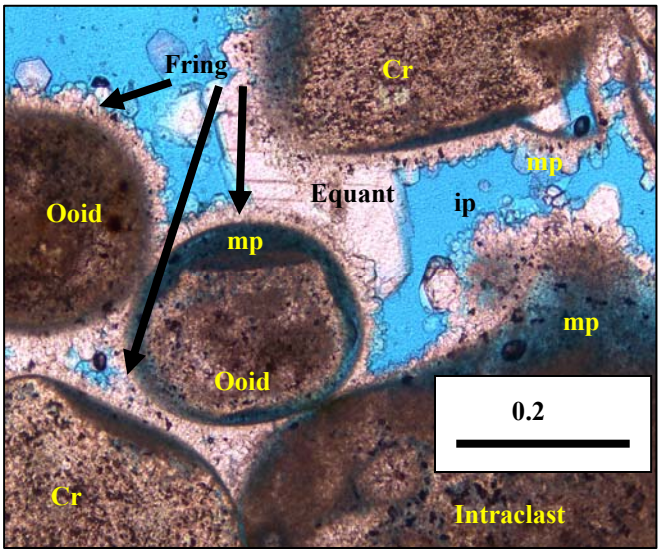

Fig. 124. Indiana limestone thin sections. Key: intergranular pores (ig) pores, micropores (mp)I, ooids (Ooid), secondary moldic pores (M), vugs (V), crinoids (Cr), intraclasts (Intraclast), bryozoans (Bry), forams (For), fractures (Frac), and fringing (Fring) and equant (Equant) calcite cement.

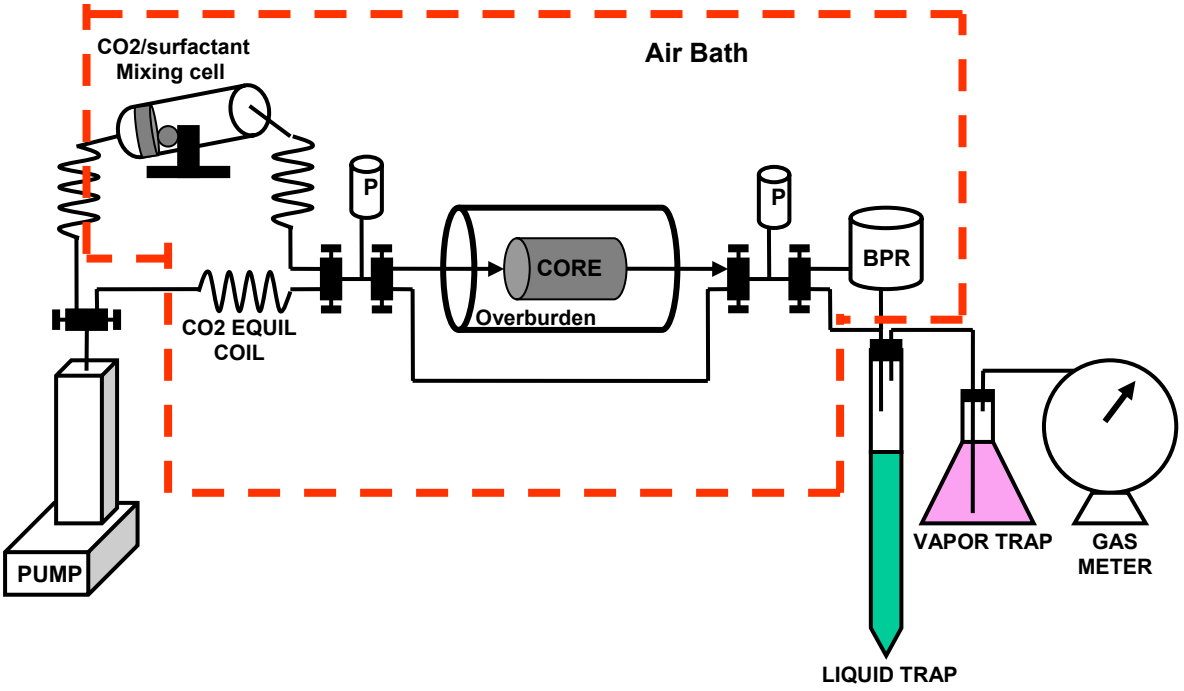

Fig. 125. Coreflooding apparatus.

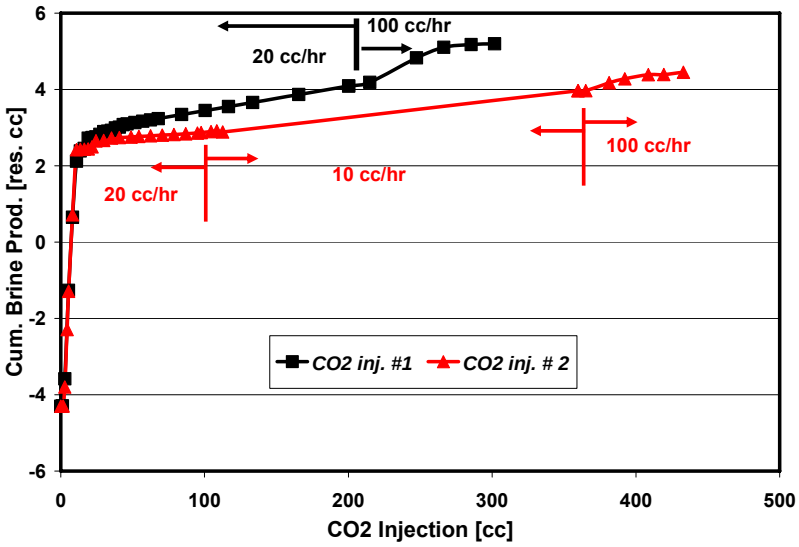

Fig. 126. Comparison of brine production during CO_2 injection of two tests in Frio Core A.

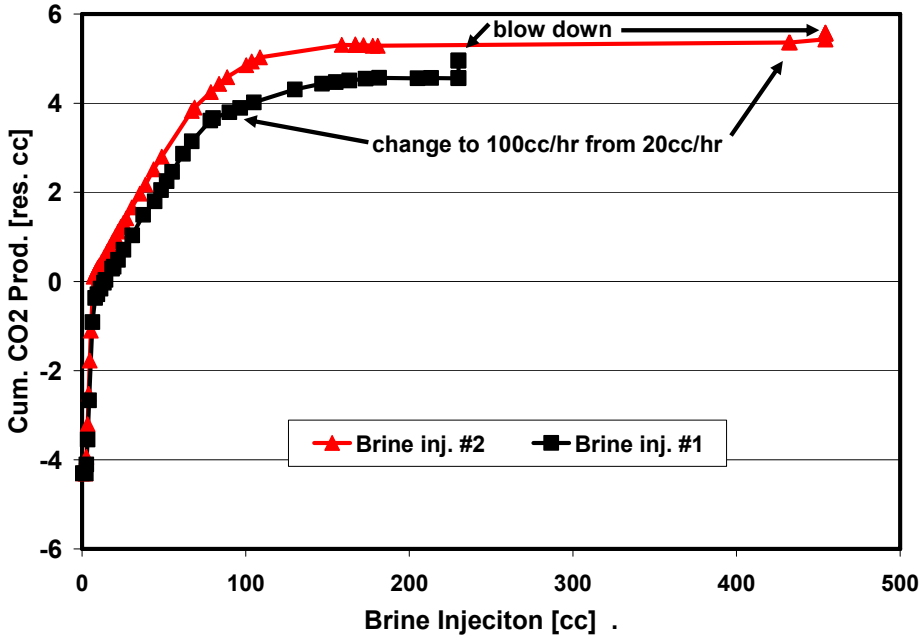

Fig. 127. Comparison of CO_2 production during brine injection for two tests in Frio Core A.

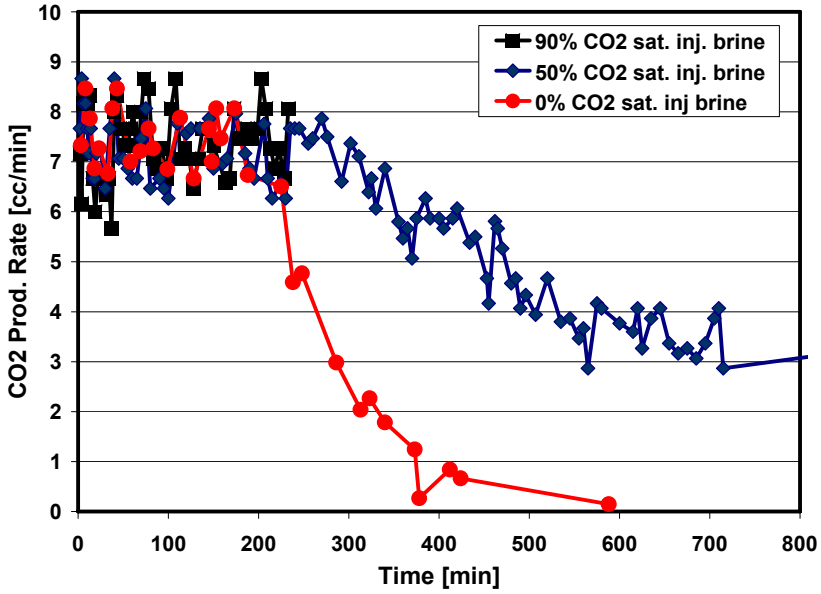

Fig. 128. Production rate of CO_2 during the injection of brine into Frio Core B for three different tests, each at different concentrations of CO_2 in the injected brine.

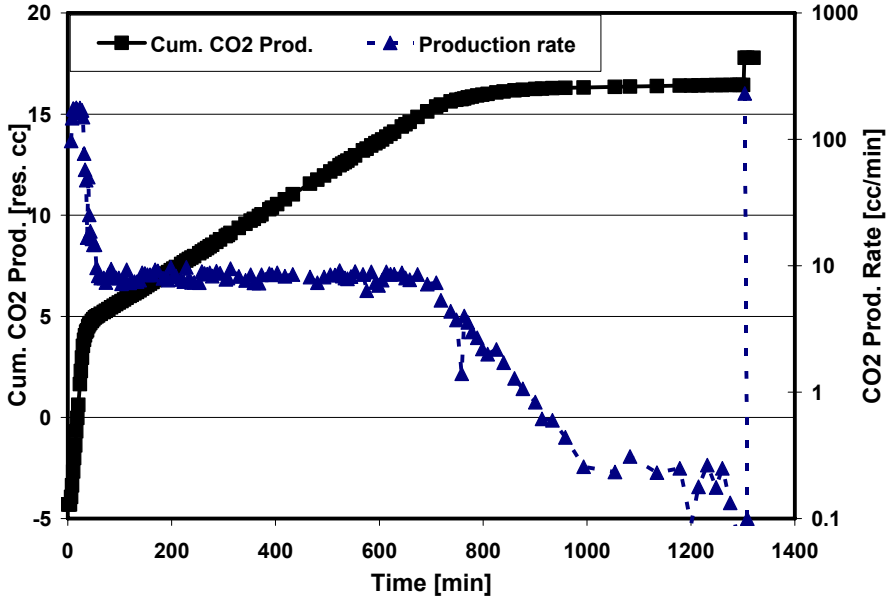

Fig. 129. Comparison of total CO_2 production rate at reservoir and ambient conditions at 37.8°C for Frio Core C.

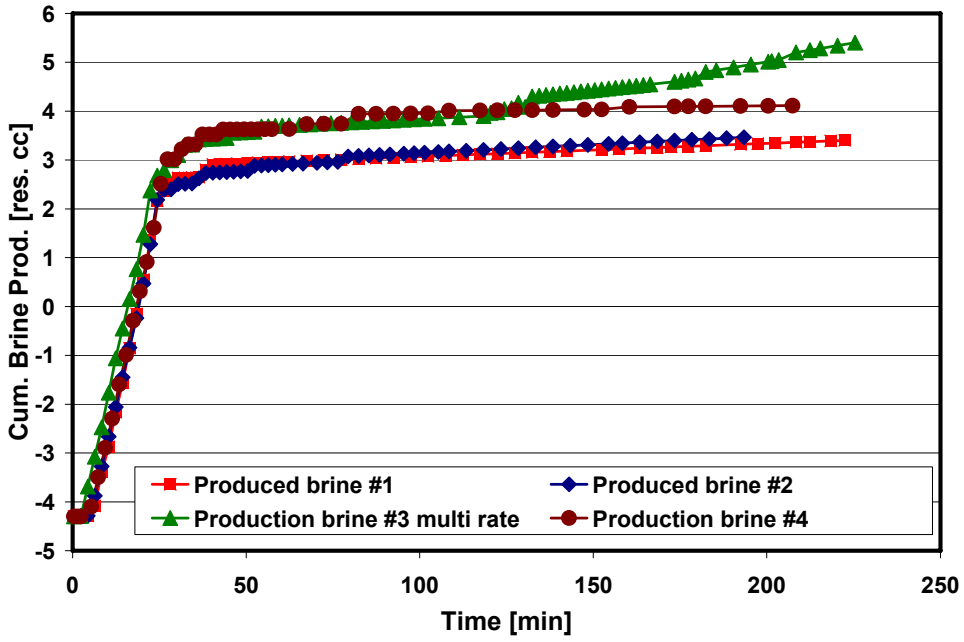

Fig. 130. Comparison of brine production during CO_2 injection of four tests in Indiana limestone.

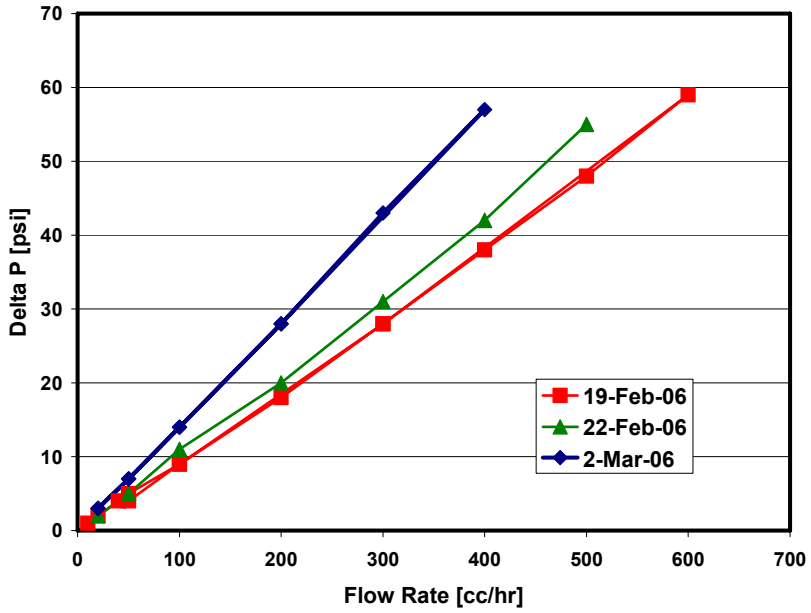

Fig. 131. Pressure drop versus flow rate for Indiana limestone on three different days. The indication was a decrease in permeability with time.

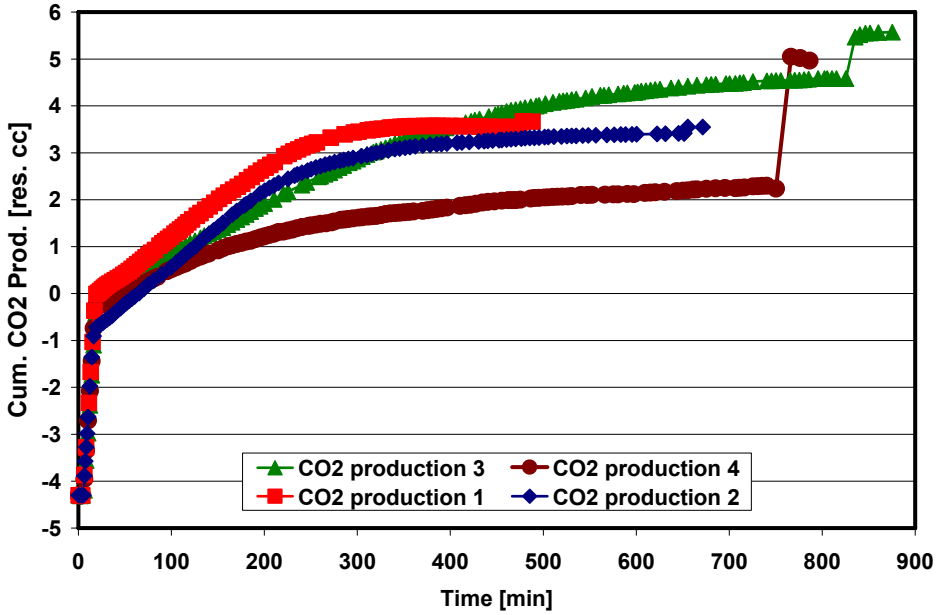

Fig. 132. Comparison of CO_2 production during brine injection for four tests in Indiana limestone.

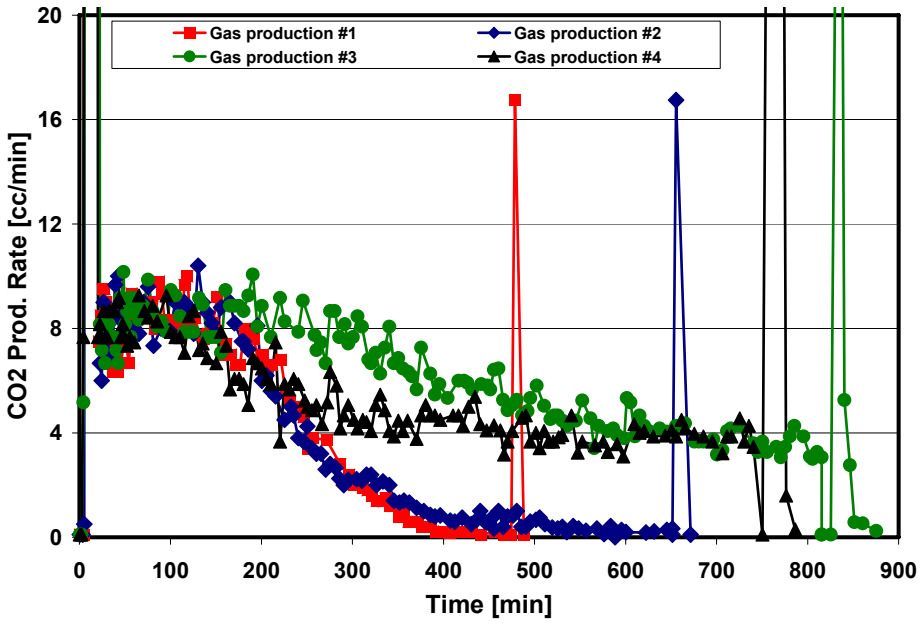

Fig. 133. Production rates for CO_2 at ambient conditions at a brine injection rate of 20 cc/hr in Indiana limestone.

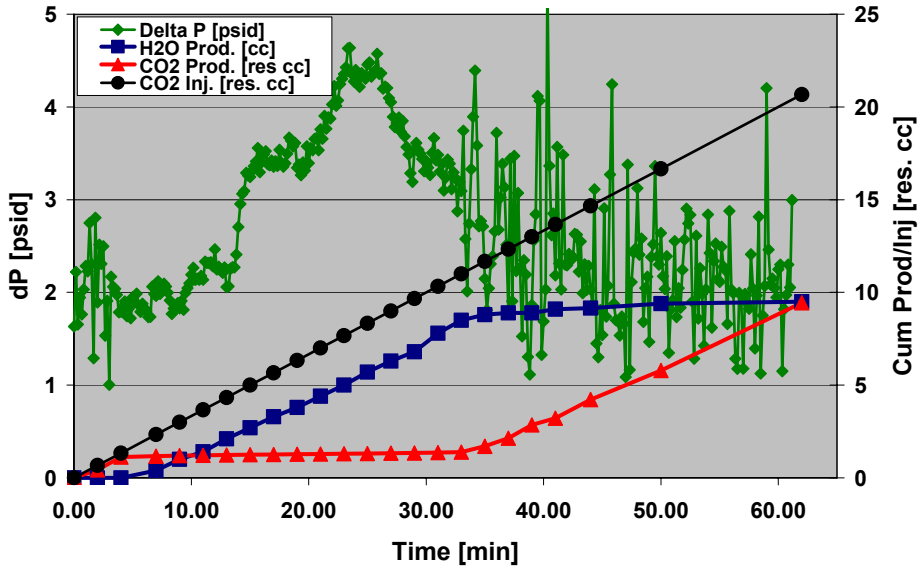

Fig. 134. Dolomite Flood 1 showing the injection and production of CO_2, production of water, and differential pressure until CO_2 breakthrough.

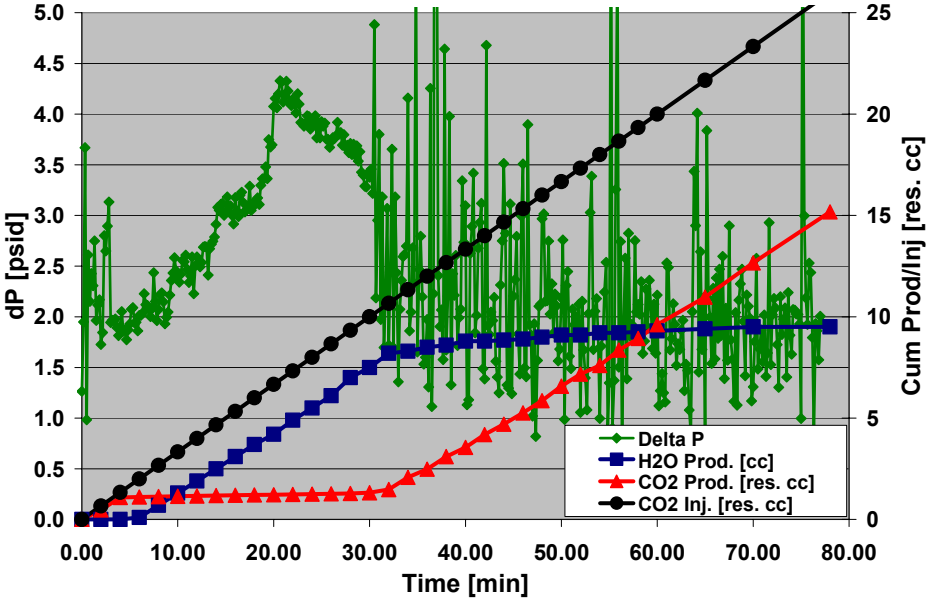

Fig. 135. Dolomite Flood 2 is similar to Flood 1 except production of CO_2 and water were recorded after CO_2 breakthrough.

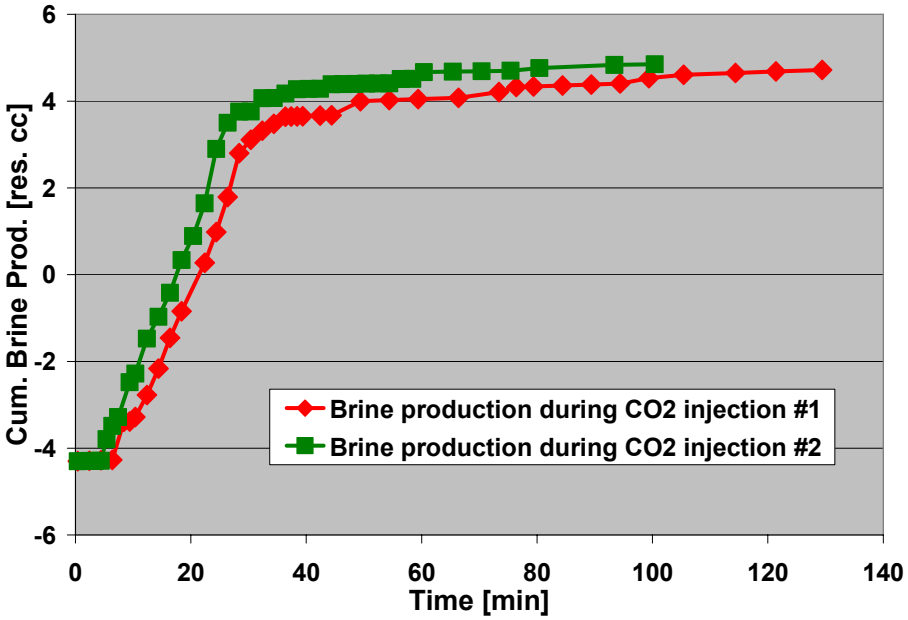

Fig. 136. Comparison of brine production versus time for both CO_2 injection Queen tests. One PV of injection is equal to about 38 minutes of injection.

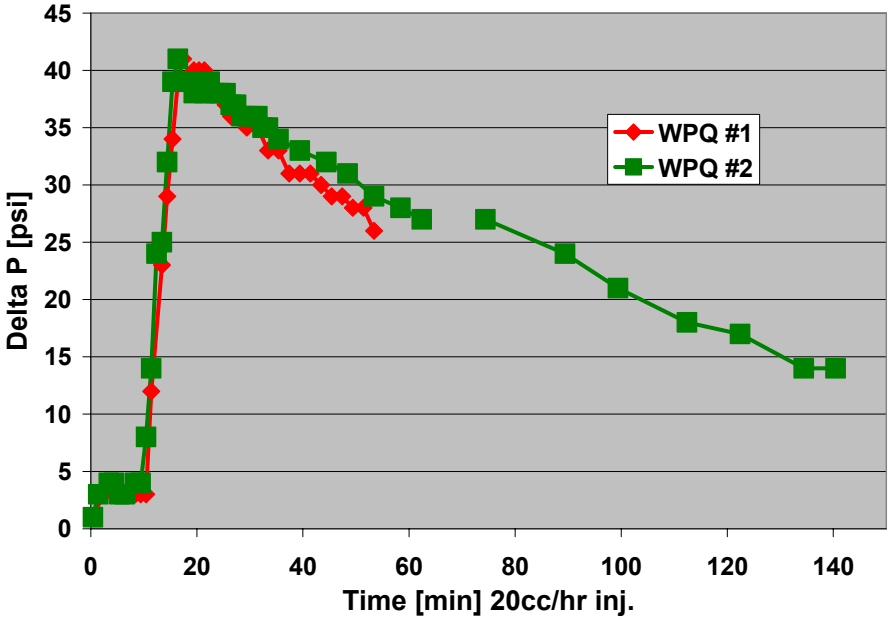

Fig. 137. Comparison of pressure drop across the core during CO_2 injection versus time during brine injection for both Queen tests. One PV of injection is equal to about 38 minutes of injection.

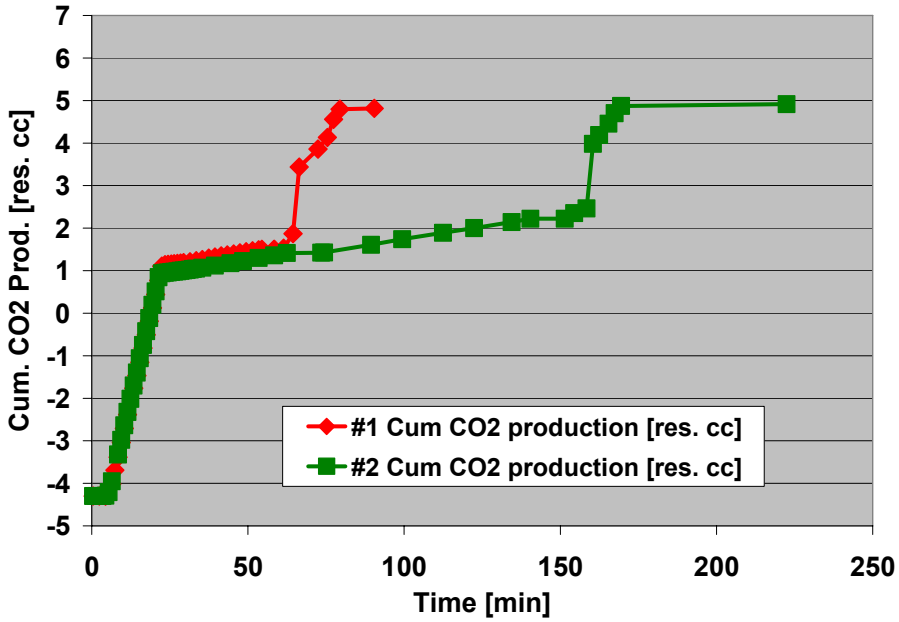

Fig. 138. Comparison of CO_2 cumulative production versus time during brine injection for both Queen tests. One PV of injection is equal to about 38 minutes of injection.

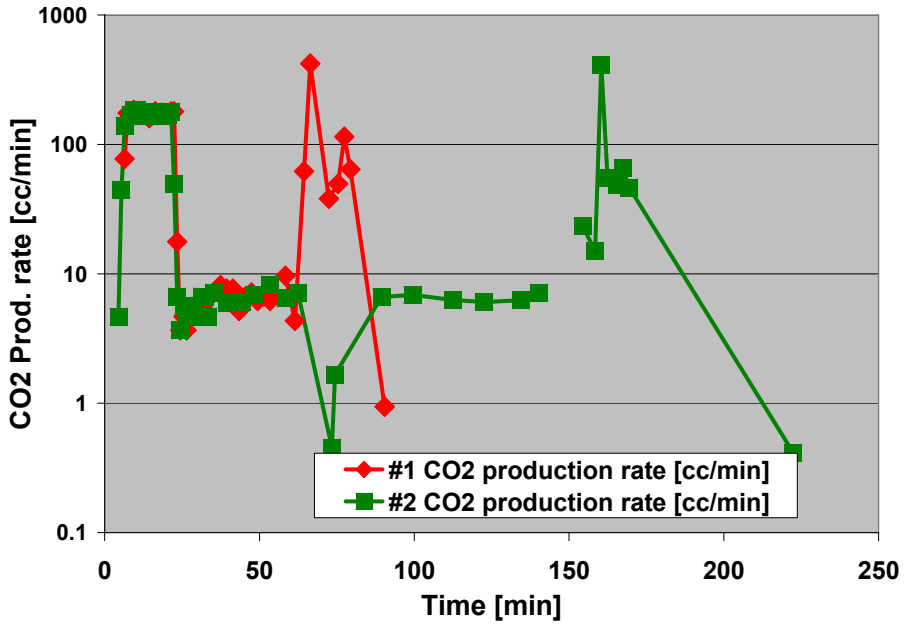

Fig. 139. Comparison of CO_2 production rate versus time during brine injection for both Queen tests. One PV of injection is equal to about 38 minutes of injection.

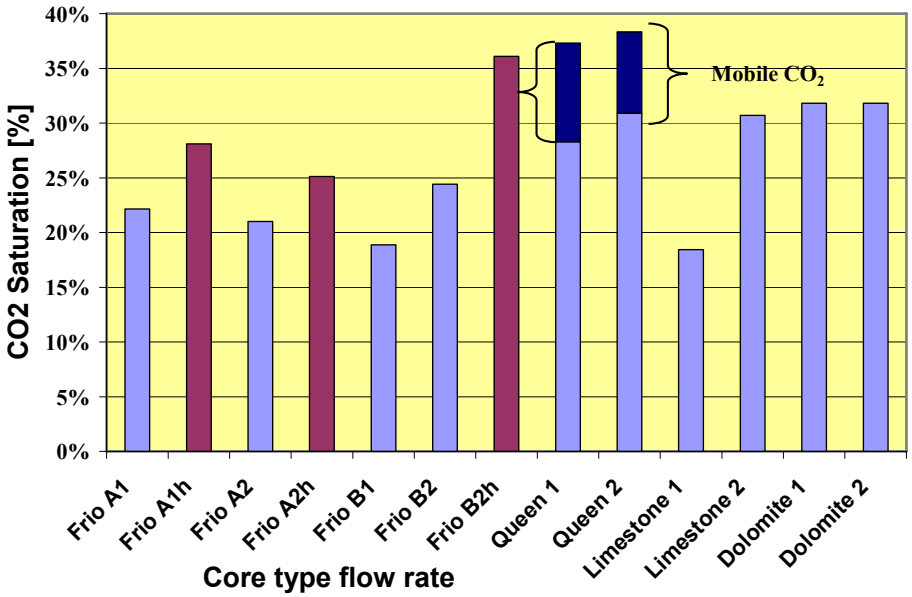

Fig. 140. CO_2 saturation in several core types. For all systems, the original injection rate was about 20 cc/hr; for each Frio system it was then increased to 100 cc/hr (200 cc/hr for Frio B2h) with the indicated increase in saturation indicated by the "h". Only for Queen was there mobile CO_2.

B.2 Laboratory Observation of CO_2 Phase Transition Induced Seismic Velocity Change

Introduction

Seismic imaging has been considered one of the most promising methods for monitoring injected hydraulic fracturing fluid and CO_2 in petroleum reservoir formations.[136,137] Whether or not this tool can be used to monitor CO_2 phase change depends on the existence of detectable change in seismic velocities during CO_2 phase transition. This section presents the results of a study to experimentally investigate changes in compressional (P-) and shear (S-) wave velocities when a CO_2 saturated Indiana limestone sample is heated and cooled across the CO_2 critical temperature while the pore pressure is maintained above the critical pressure.

Experimental System

Laboratory experiments to investigate the change of seismic velocities of a rock due to CO_2 phase transition can be performed using an in-house developed, multipurpose triaxial acoustic coreflooding system.[138] Figure 141 shows the system diagram with some individual components. The core represents a sample material cored from a reservoir well. This sample can be under varied geological conditions such as temperature, in-situ stresses, pore pressure, fluids, etc. All these geological conditions can be independently simulated and applied to the rock sample by means of this in-house developed system. The system mainly consists of the injection pump, back pressure regulators (BPRs), triaxial acoustic core holder, air bath (oven), axial and radial in-situ stress (confining pressure) pump, digital oscilloscope, data acquisition board, and control box.

In Fig. 141, flow lines correspond to steel tubing that can carry the injected fluid and the confining pressure fluid up to 15,000 psia. Data lines represent cables from different subsystems, sensors, and transducers. Depending on where the cables are connected, they carry digital and analog signals. The control box shown in Fig.142 was designed to carry multiple functions and serve as an interface between the electrical connections of the hardware components and a local computer.[139]

All pressure transducers, thermocouples, acoustic waveforms and pump readings are routed via the control box. A digital oscilloscope is used in place of a data acquisition board (DAQ) with a high sampling rate to digitize the acoustic waveforms from the piezoelectric (PZT) transducers. Only one set of the piezoelectric transducers is connected to the oscilloscope at a

time, which is switched through the control box after the waveform data are sent to the computer for processing.

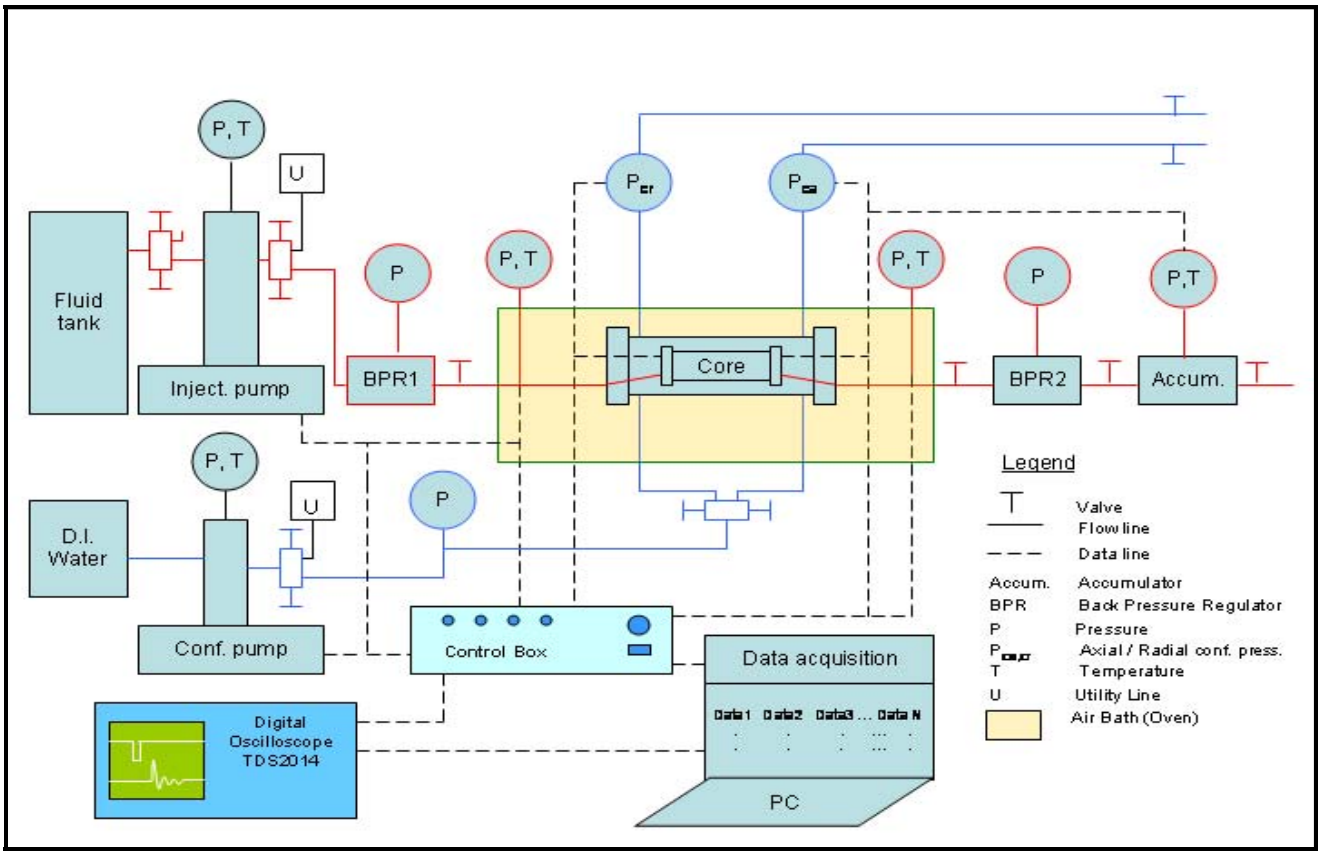

Fig. 141. Multipurpose triaxial acoustic coreflooding system (modified from Zeng, 2006[138]).

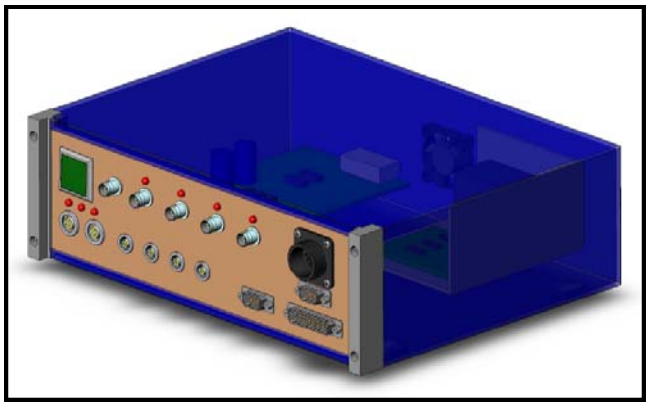

Fig. 142. The control box.

Two BPRs are used to maintain a pressure threshold at the inlet and outlet of the core holder. The injection pump supplies the fluid to the core holder in which the sample is being tested. Having the injection pump in the system adds some advantage to maintaining a constant flow rate or constant pressure and allows the system to continuously monitor the amount of fluid being injected.

The core holder is a fixture that consists of a cylinder, a piston and a cap. The cap seals the cylinder and the piston can be adjusted to provide a specific axial in-situ stress (confining pressure) to the sample. Also, the cylinder can be filled with a fluid, usually deionized water, to provide a desired radial in-situ stress (confining pressure). A VITON rubber sleeve holds the sample straight between the cap and the piston and also seals the injected fluid from the confining fluid. In this way the axial, radial, and pore pressures can be controlled separately and set to the desired values based on the geological conditions of any proposed formation. Figure 143 shows the components of the core holder in detail.

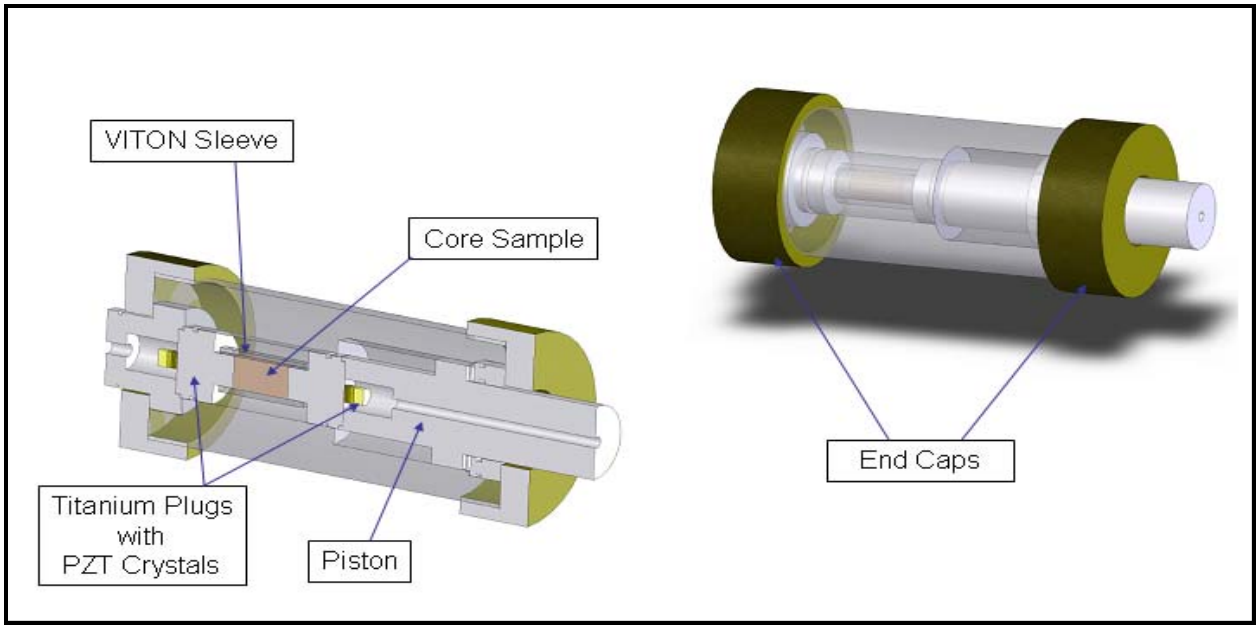

Fig. 143. Triaxial acoustic core holder.

Both the cap and the piston have a set of PZT transducers mounted inside. These transducers are made of PZT crystal disks: one for P- and two for S-wave. Diameter of the crystal disk is 0.875-in. Central frequency of the transducer is 1 MHz for P-wave and 500 KHz

for S-wave. The transducers are used to generate non-destructive ultrasonic waves and to convert the ultrasonic (mechanical) vibrations back to electrical signal in order to measure the seismic velocities of the sample. The three PZT disks are polarized in the *X*-, *Y*- and *Z*-axis. The transducer polarized in the *X*-axis will generate P-waves; and the *Y* and *Z* polarized transducers will produce the vertical and horizontal shear waves (*Y*-vertical and *Z*-horizontal), also known as S1- or SV- and S2- or SH-wave, respectively. Figure 144 shows each disk along with its polarization. One set is used as a source by applying an electrical pulse to each individual disk and the other set is used as a sensor to detect the corresponding wave. Because of their piezoelectric effect, a piezoelectric transducer can serve as both a source and a receiver.

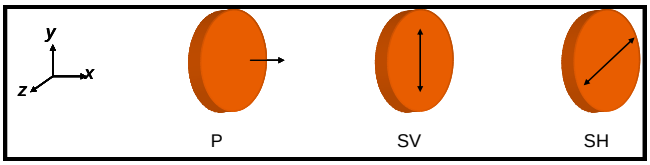

Fig. 144. Piezoelectric transducers.

Acoustic velocity is calculated using full waveform cross-correlation. An electrical pulse from the control box is simultaneously sent to the source transducer and the oscilloscope. The pulse travels through the rock specimen to the receiving transducer. At the same time the pulse activates the data acquisition board via the oscilloscope. The waveform is digitally sampled. Sampling rate is programmable to match the transducer's central frequency. At the beginning of the measurement, a template waveform is manually selected to define the start and end of the signal for each transducer. Figure 145 shows a set of typical P-, SV- and SH-waveforms, and the definition of the template waveform for the start and end of the signal. Using the template waveform, the same type, i.e. P, SV or SH, of subsequent waves are compared to their corresponding template waveforms using cross-correlation to determine the velocity via high speed signal processing.[139] Each velocity measurement needs about 5 seconds. The control box switches the velocity measurement among P-, SV- and SH-waves automatically. The velocities of all three waveforms are calculated and stored in about 20 seconds. Once all three waves are measured, the control box will restart the measurement at a programmable interval from 1 to 10 minutes. This allows continuous measurement of the P-, SV- and SH-wave velocities of the rock

specimen when other processes, such as compaction and fluid injection, are independently in operation.

While confining pressure and pore pressure are controlled by pumps, the temperature is established by an air bath. The core holder is placed inside the air bath with a temperature controller, which can be adjusted by the computer to a desired temperature. The oven element is switched on and off from a solid-state relay, which is controlled from the Acoustic Core Holder Measurement System (ACHMS) software. Six thermocouples are installed throughout the system to measure temperatures at different points during experiments. They monitor the temperatures of the ISCO pump cylinder, the room, the air bath, the core holder, the inlet fluid, and the outlet fluid.

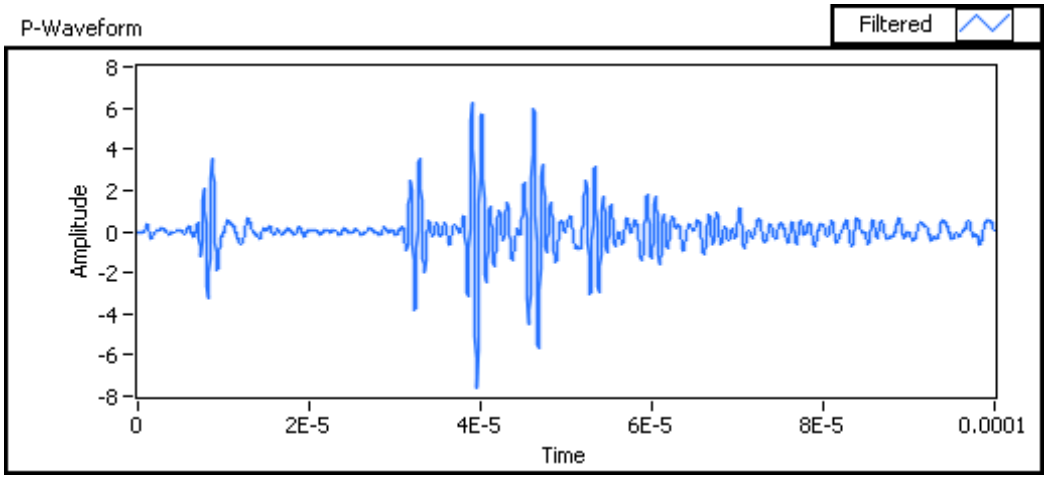

(a)

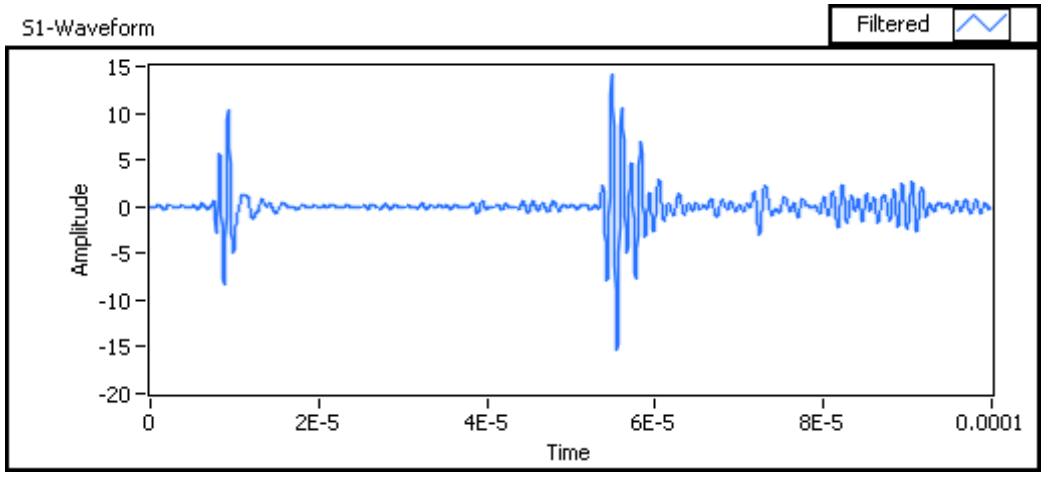

(b)

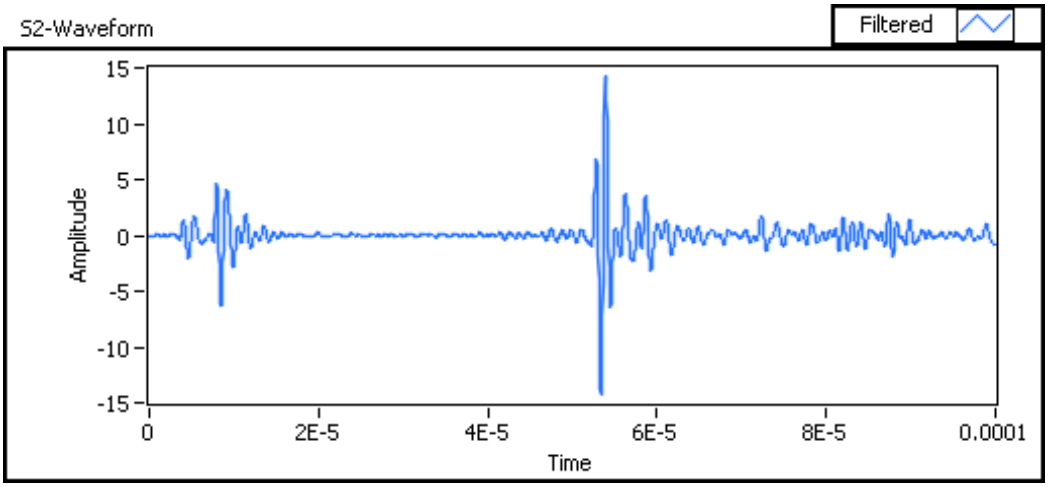

(c)

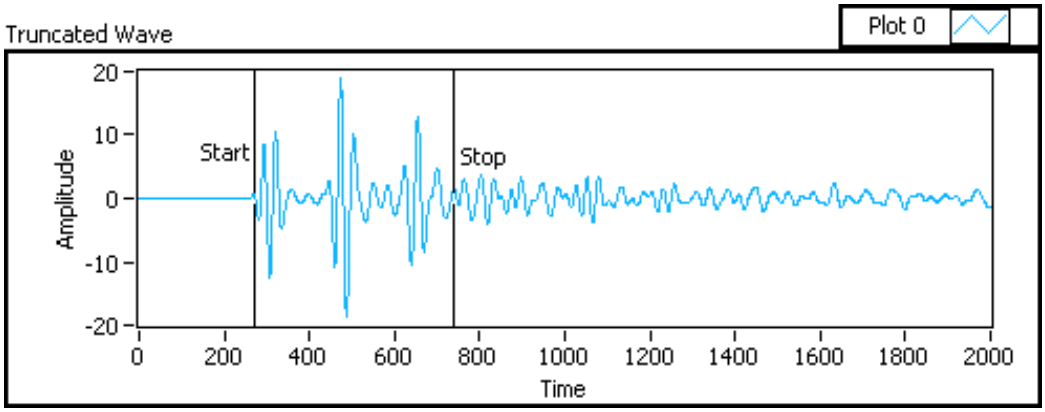

(d)

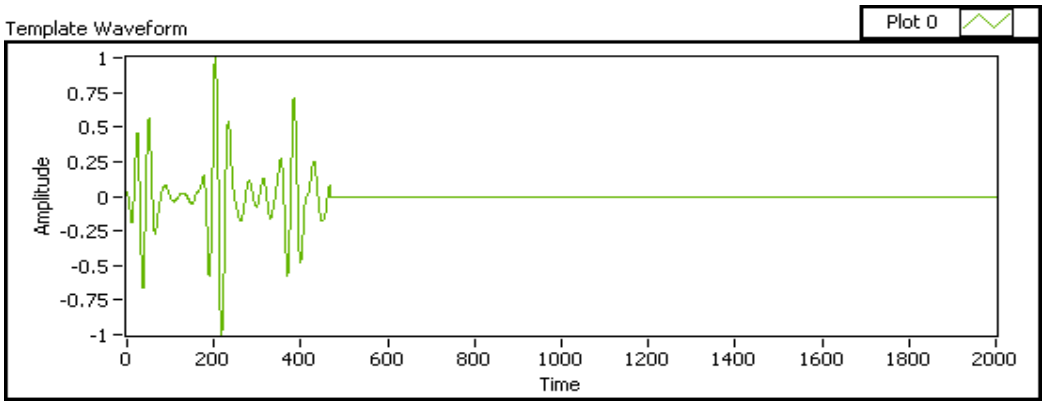

(e)

Fig. 145. Waveforms and definition of template for travel time. (a) P-wave. (b) SV-wave. (c) SH-wave. (d) Truncated waveform for defining the travel time. (e) Template waveform. Time unit is "second" in (a), (b) and (c), and "40 nanoseconds" in (d) and (e).

The ACHMS software is implemented in National Instrument's LabVIEW, and runs on a local computer under the Windows XP operating system. The main function of this application is to communicate with the control box, pumps and oscilloscope. It controls them and collects data from them. A few algorithms are implemented in ACHMS to filter the noise from the sensors and calculate petrophysical, seismic, and geomechanic properties of the sample being tested. All this information is then stored in a local database for documentation and other post analysis. The software provides a graphical user interface (GUI) with controls and data entry points for the user to be able to monitor and setup the experiments in real-time locally and remotely through other computers connected to the Internet. Figure 146 shows two photographs of the injection pumps, the triaxial core holder in the air bath, the digital oscilloscope, the control box and the ACHMS software during operation.

(a)

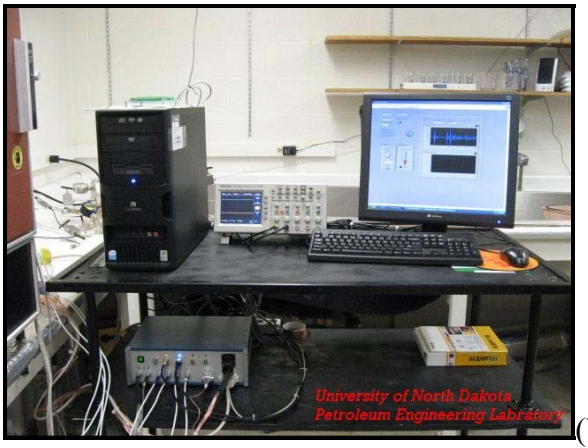

(b)

Fig. 146. The triaxial acoustic velocity core flooding system. (a) Hardware. (b) Control box and software in operation.

System Calibration

In order to avoid inaccurate measurements it is important that the system is calibrated frequently. This is usually done with a known reference value that is compared against the sensor reading. Over time, most of the sensors will drift from their original readings due to temperature effect and their state of operation. This change is a nonlinear effect in most cases. Therefore, their readings must be compensated either through modifications in the signal conditioning circuits or through the software. Usually, it is more convenient to modify the digital reading through software rather than changing the hardware every time a sensor drifts.

As mentioned previously, the system consists of pressure transducers, ultrasonic transducers, temperature sensors, data acquisition board, ISCO Syringe pumps and the TDS2014 digital oscilloscope. Each of these devices requires calibration and some have built-in calibration

functions. The data acquisition board and the TDS2014 have internal calibration modules for improved measurement accuracy. The manufacturer recommends that the TDS2014 oscilloscope be calibrated every time there is a temperature change of 5ºC or more in the operating environment. The calibration of the oscilloscope can be done in two different ways following the user's manual.

Each ISCO syringe pump has three sensors, which the controller uses for pump operation, and which also report their readings to the ACHMS for other measurement calculations. Pump pressure, remaining volume and flow rate sensors are calibrated from the manufacturer. The read-out for each sensor is already provided in a digital format, therefore no conversion is necessary. Also the pressure transducers are calibrated using the readout from the pump as a reference.

Calibration of pressure transducers is performed in the lab using the ISCO pump and the Calibration Module program. The ISCO pump provides a specific pressure and the Calibration Module does the acquisition of the voltage output for each pressure transducer. After a set of data is collected, a linear curve fitting scheme is applied to calculate the coefficients of a linear function, $y = ax - b$, which are entered in the individual conversion modules. Figure 147 shows voltage acquisition for each pressure transducer vs. the ISCO pump pressure. The inlet and outlet pressure transducers are of two brands; thus the calibrating curves shown in Figure 147 are different.

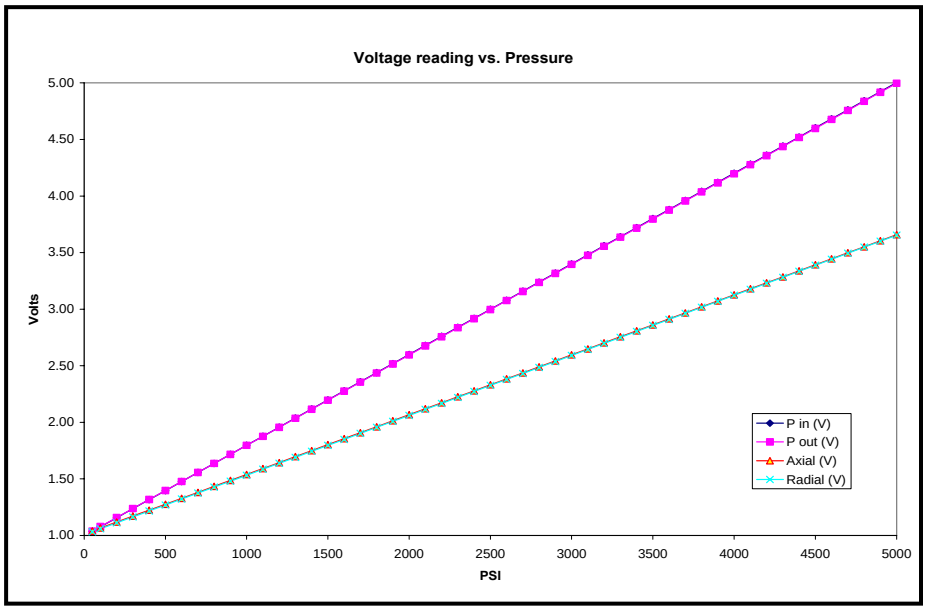

Fig. 147. Voltage acquisition of each pressure transducer.

The coefficients, *a* and *b*, are found from the collected data and their results are presented in Table 38. These coefficients are used in signal processing routines.[139]

Table 38. Calibration for Pressure Transducers

Pressure Transducer	*a*	*B*
P-in	1250	1244.50
P-out	1250	1245.38
P-axial	2000	2020.00
P-radial	2000	2005.00

A similar procedure is followed for each thermocouple. Table 39 shows the results.

Table 39. Calibration for Thermocouples

Thermocouples	*a*	*B*
Pump Injection Temp	100	19.40
Core Inlet Temp	100	18.25
Core Outlet Temp	100	17.90
Core Holder Temp	100	17.01
Room Temp	100	17.60
Air Bath Temp	100	16.27

Calibrating the core holder acoustic transducers can be performed in several different ways. Since this calibration involves measuring the correction time delays for titanium coupling, both titanium plugs are attached head to head to measure the time delay for each wave. This requires an almost perfect alignment and some external coupling paste is used to allow waves to propagate with minimal loss. Another method is to use a known homogenous material, such as aluminum or steel, and prepare two cylinders, one inch in diameter at two different lengths. Each cylinder can be placed inside the core holder with a confining pressure between 500 psia to 2000 psia, which ensures better surface attachment between the sample and the titanium plugs. The total time delay is then measured for each wave.

$$TD_{total,i} = \Delta t_{sample,i} + \Delta t_{correction,i} \qquad 41$$

$$V_{1,i} = V_{2,i} \Rightarrow \frac{l_1}{TD_{1,i}} = \frac{l_2}{TD_{2,i}}. \qquad 42$$

Substituting Eq 41 into Eq 42 and solving for $\Delta t_{correction,i}$ obtains Eq 43

$$\Delta t_{correction,i} = \frac{l_{2,i} TD_{1,i} - l_{1,i} TD_{2,i}}{l_{1,i} - l_{2,i}}, \qquad 43$$

where i is P, S1 or S2, and l_1 and l_2 are the sample lengths. Each wave has its different correction time. Table 40 lists the correction times for the P, S1 and S2 waves measured at 700 psia confining pressure and room temperature.

Table 40. Titanium Plugs' Correction Times

Wave	$\Delta t_{correction}$ (μs)
P	16.06111
S1	27.83136
S2	27.28077

System validation

System Measurements

Five different aluminum samples with different lengths were tested under 500 psia radial pressure and 700 psia axial pressure at 65ºF. The motivation for this experiment was to acquire some data for the velocities and derive statistical analysis from different sample lengths. Each sample was tested for one hour and ACHMS was set to record the velocities every minute. The system collected approximately 60 data points for each sample, and the mean and standard deviation were calculated for each velocity. Tables 41–43 show the maximum, minimum, average, and standard deviation for each wave.

Table 41. Aluminum P-Wave Velocity Statistics

Length (mm)	V_P (m/s)			
	Max	Min	Avg.	Std
26.90	6652.00	6614.38	6633.65	7.96
34.98	6694.73	6660.32	6680.61	7.00
45.30	6642.33	6612.28	6629.63	5.65
49.30	6896.96	6548.98	6575.38	41.71
53.13	6646.32	6618.17	6631.75	5.30

Table 42. Aluminum SV-Wave Velocity Statistics

Length (mm)	V_{SV} (m/s)			
	Max	Min	Avg.	Std
26.90	2798.69	2785.65	2790.66	2.28
34.98	2842.75	2827.12	2833.04	2.22
45.30	2897.78	2787.07	2794.05	14.39
49.30	3041.61	2945.63	2951.66	11.71
53.13	2847.47	2837.29	2841.91	1.65

Table 43. Aluminum SH-Wave Velocity Statistics

Length (mm)	V_{SH} (m/s)			
	Max	Min	Avg.	Std
26.90	3142.44	3123.46	3132.42	3.16
34.98	3106.02	3095.58	3101.14	2.34
45.30	3122.37	3111.21	3118.14	2.33
49.30	3240.80	3154.14	3159.74	10.56
53.13	3022.83	3014.94	3019.32	1.76

The results also show that vertical and horizontal shear wave velocities are not the same, which indicates that the aluminum is not isotropic. The variations of velocities for different lengths are due to the coupling between the titanium plugs and the surface of samples.

Temperature Effect

Three different experiments with three sample materials were tested under a constant confining pressure in a varying temperature environment. One steel sample with length 50.00 mm, one Dakota sandstone sample with length 50.74 mm and one Indiana limestone sample with length 45.96 mm were placed in the core holder under a confining pressure of 3000 psia. The air bath was heated to a temperature of 150ºF (65.5ºC). No fluid was injected; therefore samples were considered dry. The confining pressure was maintained constant as the temperature was changed and the P- and S- wave velocities were measured. Figures 148 through 150 show the plots for velocities versus temperature for each sample. From observing the plots, the change is

moderately small, and the temperature has the largest influence on Dakota sandstone and the least effect on the steel sample. This change is due to the thermal expansion between the different particle grains in the solid matrix. Steel is denser and has zero porosity, making it more consistent during thermal expansion compared to Dakota sandstone and Indiana limestone.

Velocities of CO_2 Saturated Indiana Limestone

Velocities Across Critical Temperature

This experiment involves measuring velocities during CO_2 phase transition in an Indiana limestone sample. To create the phase transition, the sample is first saturated with liquid CO_2 at room temperature, *Tr*, (65ºF). It is then heated up to *Tg* (100ºF). The pressure of injected CO_2 is 1100 psia. According to the CO_2 phase diagram, phase transition occurs at around 88ºF, as shown in Fig. 151. The system is set up to maintain a constant injection rate of CO_2 at 0.5 ml/min. and gradually change the temperature between *Tr* and *Tg*. The confining pressure is maintained constant at 3200 psia.

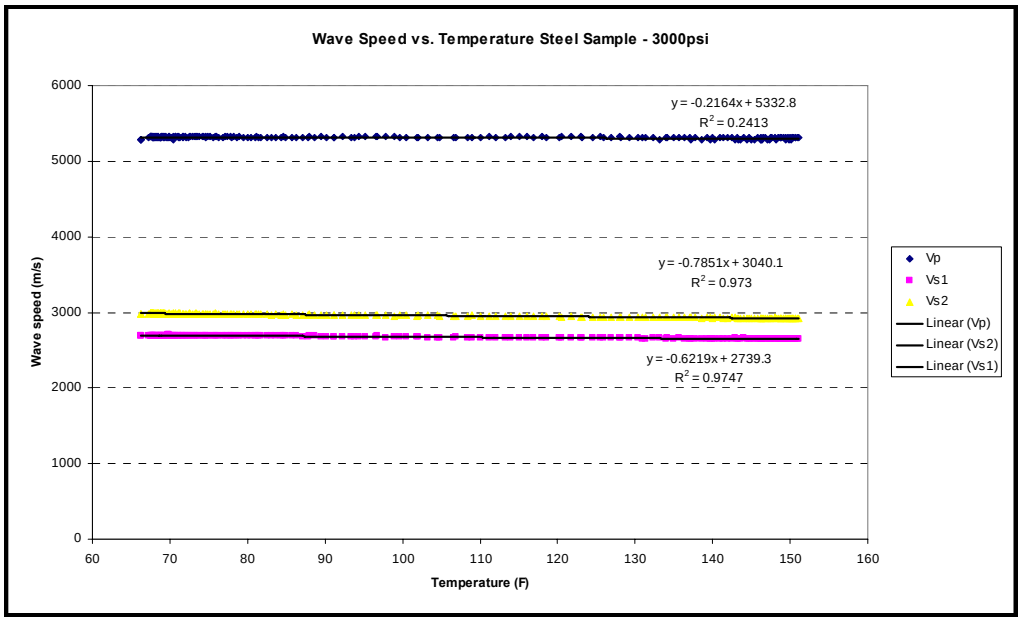

Fig. 148. Stainless steel sample velocity vs. temperature.

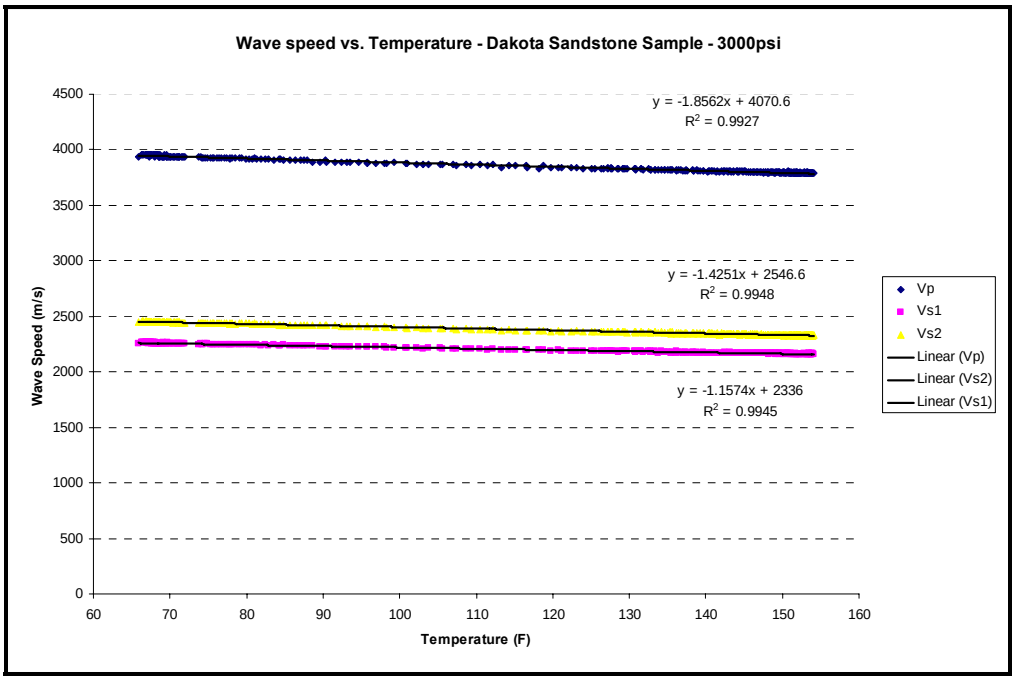

Fig. 149. Dakota sandstone velocity vs. temperature.

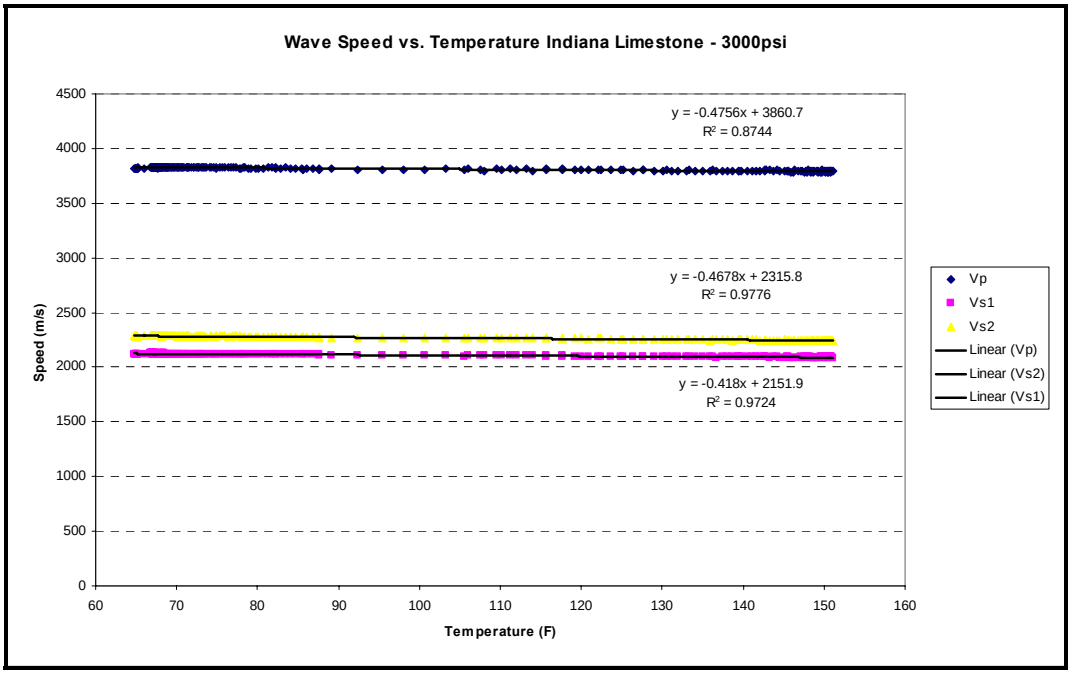

Fig. 150. Indiana limestone velocity vs. temperature.

The core holder temperature is measured instead of the core sample since there is no thermocouple mounted inside the core holder. The core holder was initially heated and then cooled. This process was repeated twice. Figure 151 shows the core holder temperature and the velocities for each wave.

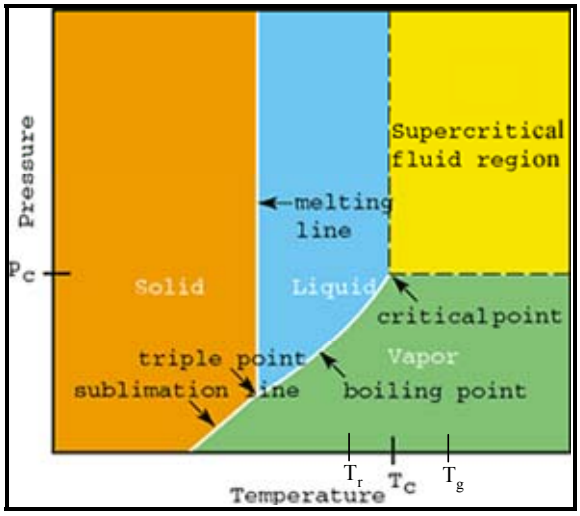

Fig. 151. CO_2 phase diagram.

It is observed that there are obvious changes in all seismic velocities during the phase transitions of the saturating fluid (CO_2) from subcritical to supercritical state (heating up), and from supercritical to subcritical state (cooling down) in the Indiana limestone.

Velocities at Critical Temperature

To further verify that the above observed seismic velocity changes were due to CO_2 phase transition, a similar experiment which maintained the core holder temperature around 88ºF was conducted. The sample did not show large variations in seismic velocities. In fact the overall velocities remained unchanged on average. Figures 152 and 153 show these velocities when core holder temperature was kept at CO_2 critical point (88ºF).

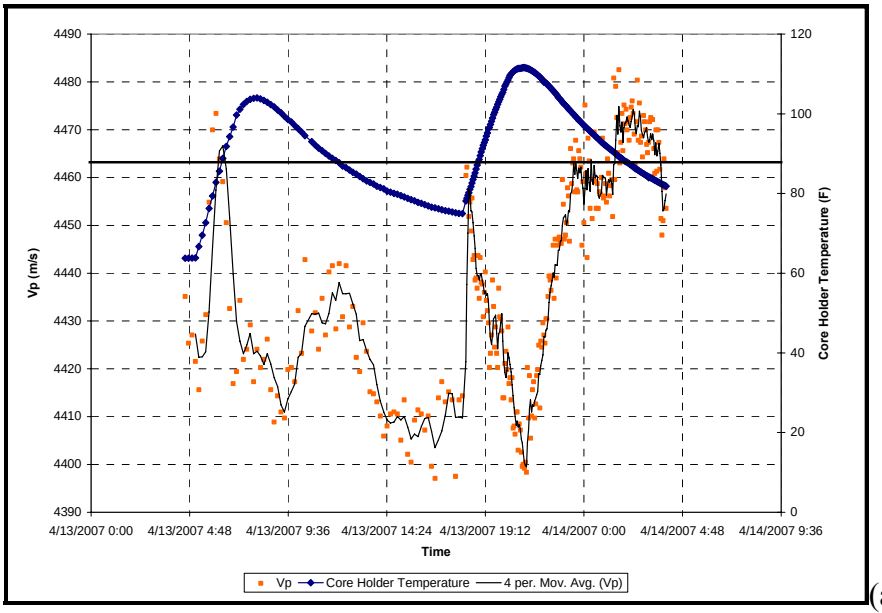
Vp (m/s)
Core Holder Temperature (F)
Time
4/13/2007 0:00
4/13/2007 4:48
4/13/2007 9:36
4/13/2007 14:24
4/13/2007 19:12
4/14/2007 0:00
4/14/2007 4:48
4/14/2007 9:36
Vp
Core Holder Temperature
4 per. Mov. Avg. (Vp)

(a)

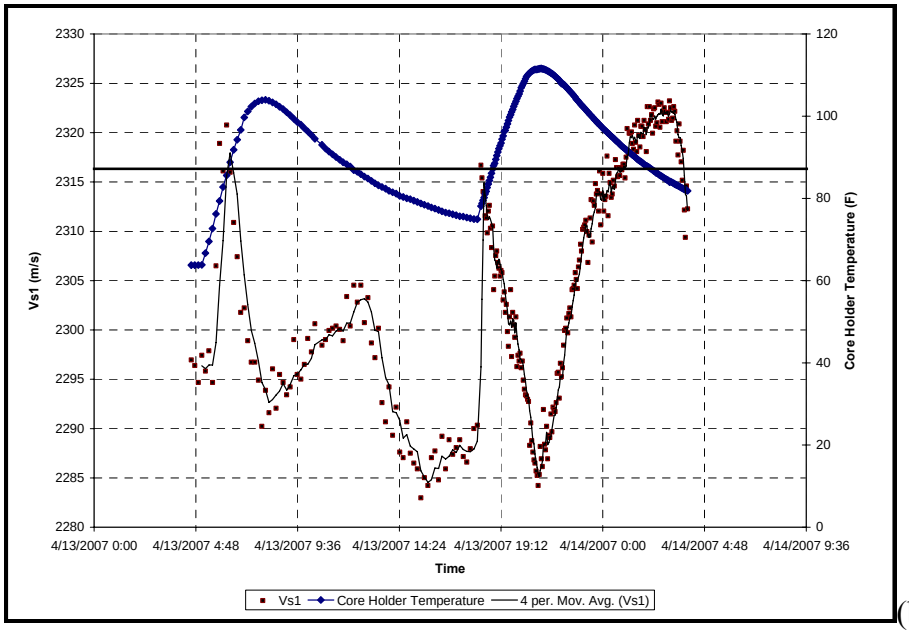
Vs1 (m/s)
Core Holder Temperature (F)
Time
4/13/2007 0:00
4/13/2007 4:48
4/13/2007 9:36
4/13/2007 14:24
4/13/2007 19:12
4/14/2007 0:00
4/14/2007 4:48
4/14/2007 9:36
Vs1
Core Holder Temperature
4 per. Mov. Avg. (Vs1)

(b)

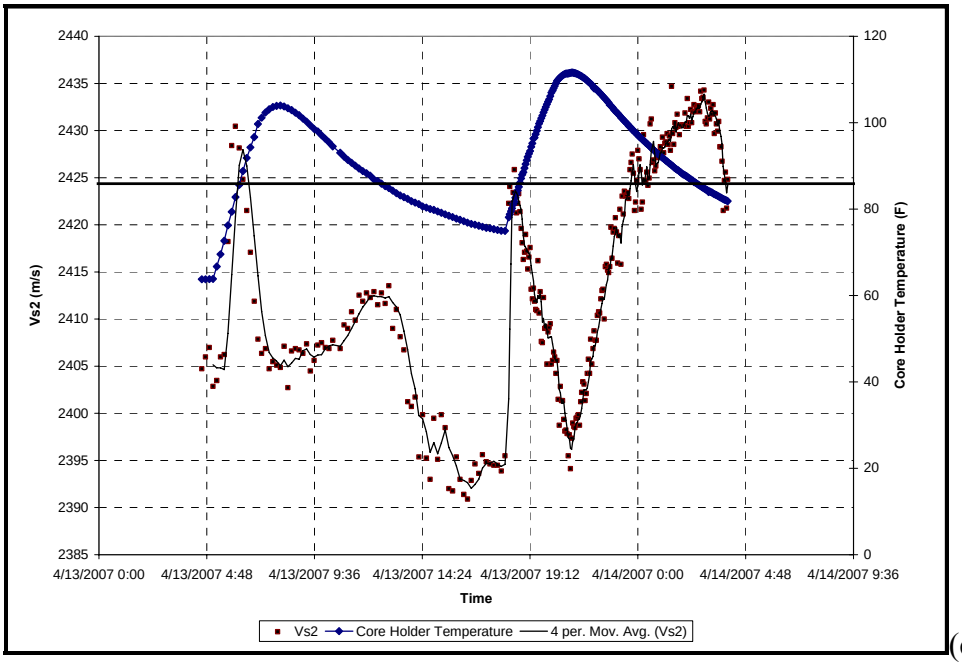

(c)

Fig. 152. Velocities of CO_2 saturated Indiana limestone across critical temperature. (a) P-wave. (b) SV-wave. (c) SH-wave.

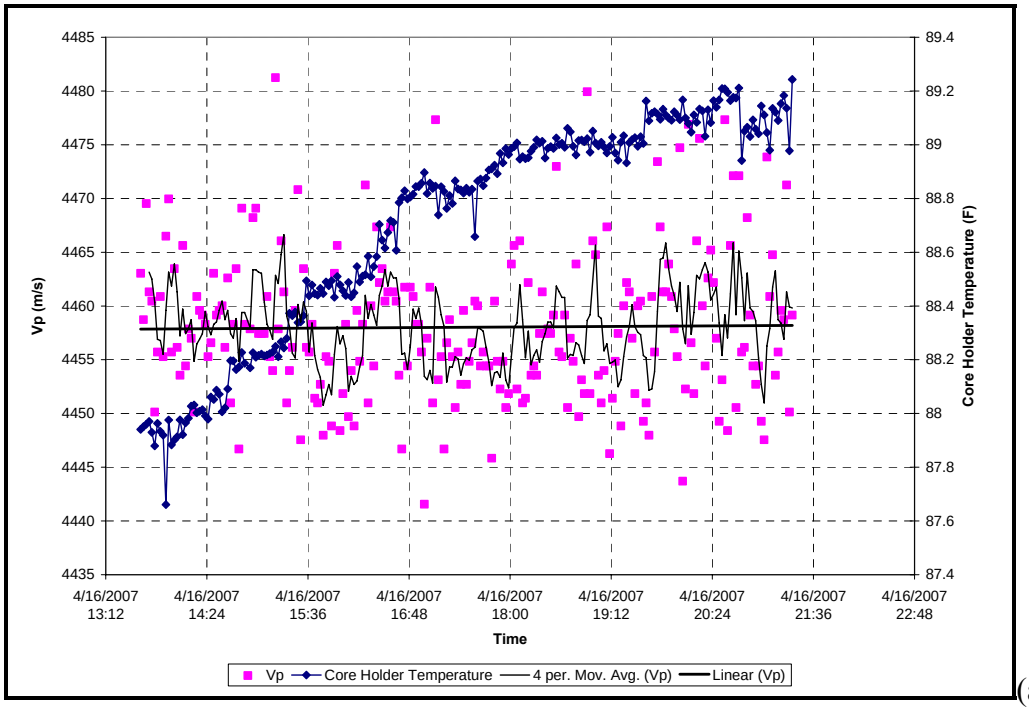

(a)

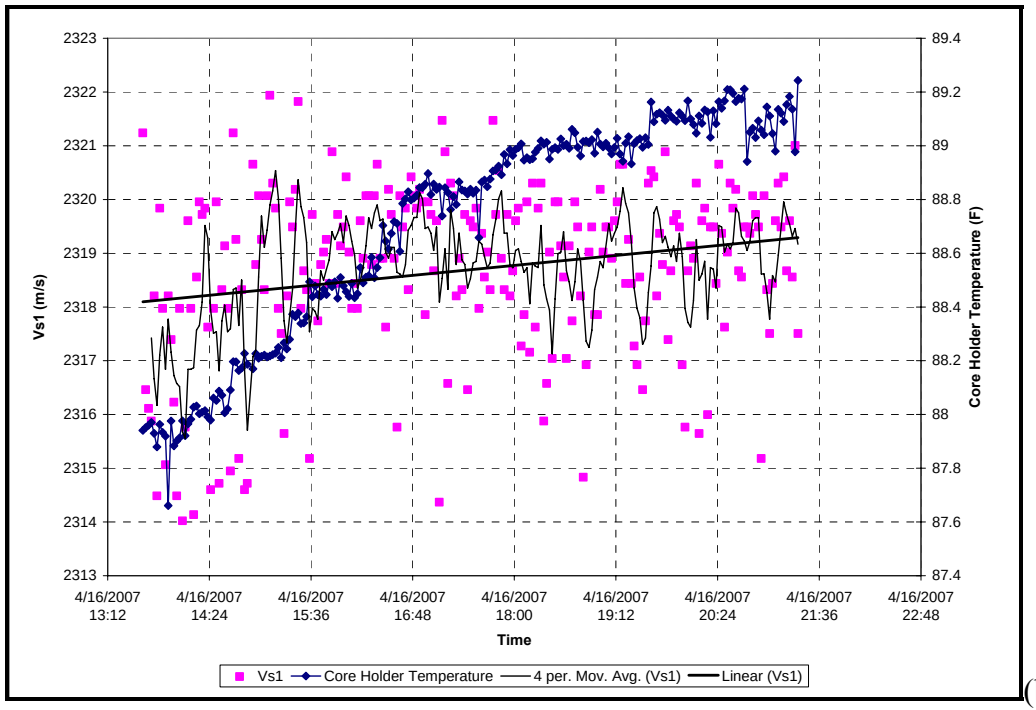

(b)

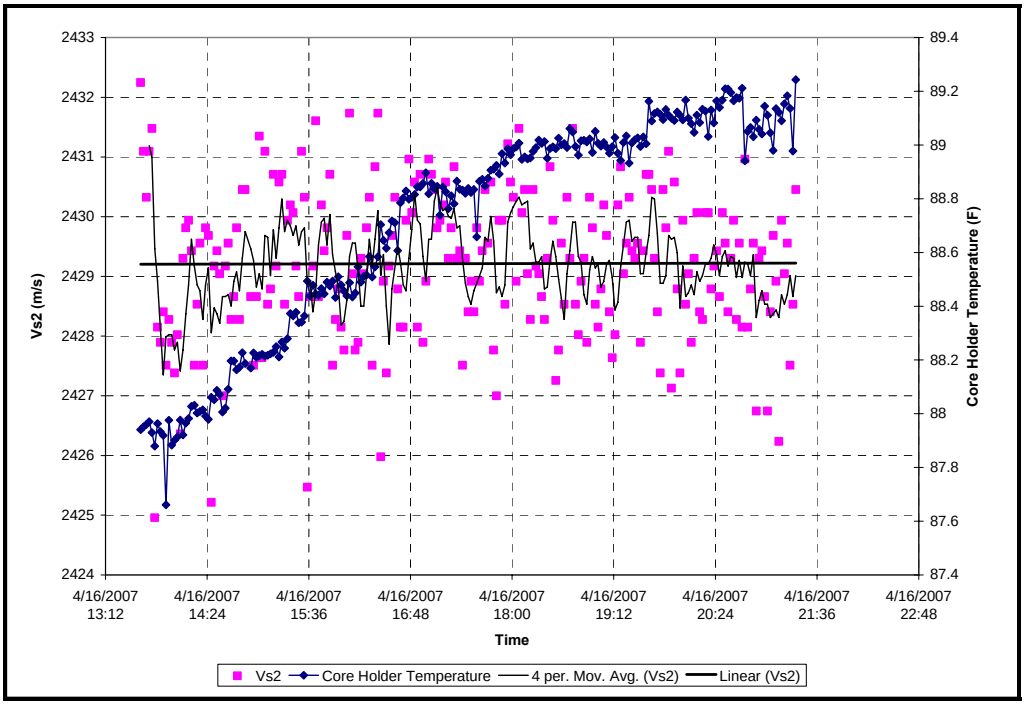

(c)

Fig. 153. Seismic velocities of CO_2 saturated Indiana limestone at critical point. (a) P-wave. (b) SV-wave. (c) SH-wave.

Discussion on CO_2 Phase-Transition Induced Seismic Velocity Changes

Seismic velocity is the speed of propagation of a mechanical perturbation in a medium. In a linear elastic, homogeneous and isotropic media, the P-and S-wave velocities, V_P and V_S, are related to the material properties as follows:[140]

$$\begin{cases} V_P = \sqrt{\dfrac{(1-\nu)}{(1+\nu)(1-2\nu)}\dfrac{E}{\rho}} \\ V_S = \sqrt{\dfrac{\mu}{\rho}} \end{cases}, \qquad 44$$

where E is Young's modulus, μ is shear modulus, v is Poison's ratio, and β is the material density. For rocks, it is found that seismic velocities decrease with temperature increase.[141]

When the rock is saturated with fluid, it is observed that V_P increases while V_S decreases.[142] In conventional log practices, Wyllie's equation is used to correlate P-wave velocity of the saturated rock with that of the fluid and the rock matrix, and the porosity:[143]

$$\frac{1}{V_P} = \frac{\phi}{V_{Pf}} + \frac{1-\phi}{V_{Pm}}, \qquad 45$$

where V_{Pf} and V_{Pm} are P-wave velocities of the fluid and the rock matrix, and φ is the porosity.

Biot found that both P- and S-wave velocities of fluid saturated porous media are frequency dependent.[144]. Each fluid saturated porous media has its characteristic frequency, f_c. When the signal frequency is low than f_c, at the extremely low frequency range, such as those used in seismic exploration, the media's seismic velocity can be approximated by Gassman's equation; in the low-intermediate frequency range below f_c, as used in sonic logging, Geertsma-Smit's approximations are valid; and at the extremely high frequency range above f_c, as used in laboratory research, the P-wave splits into two component: the fast and the slow waves.[145] The characteristic frequency, f_c, of the fluid-porous media can be calculated by:

$$f_c = \frac{\phi\eta}{2\pi\rho_{fl}k}, \qquad 46$$

where φ is the porosity, η is the fluid viscosity, ρ_{fl} is fluid density, and k is the absolute permeability.

In our experiments, the Indiana limestone specimen has a porosity of 0.15 and permeability of 20 mD.[146] At the testing pressure and temperature range, density and viscosity of CO_2 change extensively, from 48 to 14 lb/ft^3, and from 0.02 to 0.041 cP, respectively, as shown

in Figure 154. Applying the above rock and fluid properties to Eq 46, the characteristic frequency of the CO_2 saturated Indiana limestone ranges from 31 to 226 KHz. This value is much lower than that of water and oil saturated Cordova Cream limestone.[147]

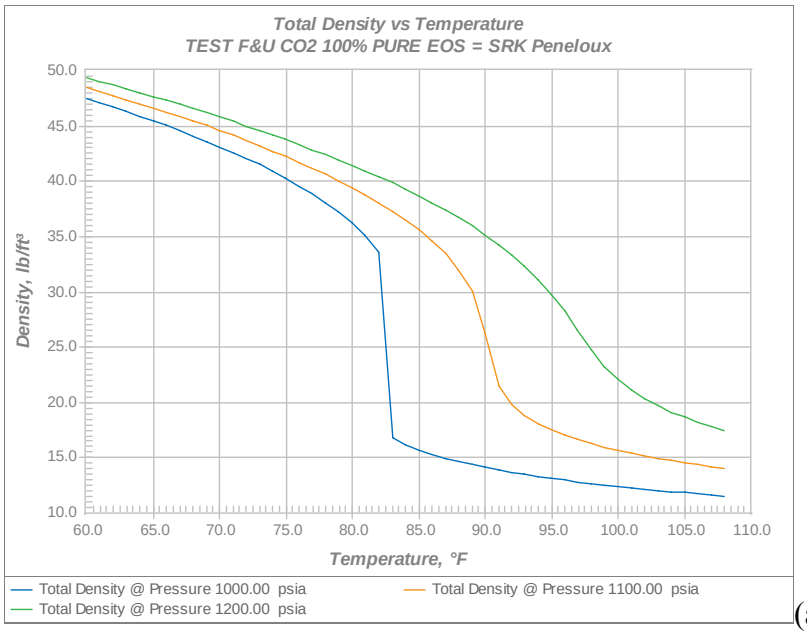

(a)

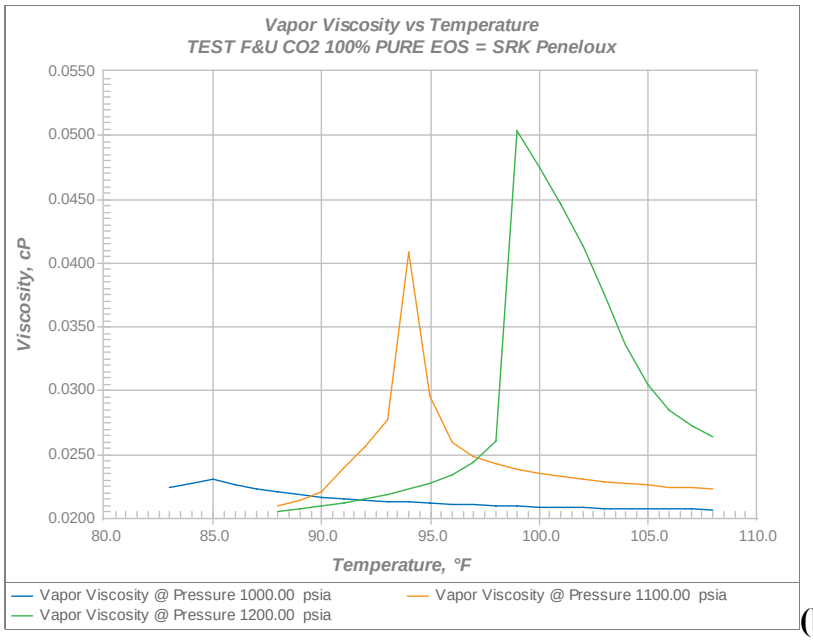

(b)

Fig. 154. Change of CO_2 density and viscosity with temperature under three pressures. (a) CO_2 total density. (b) CO_2 viscosity.

In this study, frequencies of 1 MHz for P-wave and 500 KHz for S-wave were used; both were above the characteristic frequency range. Thus, seismic velocities of this CO_2 saturated Indiana limestone can be described using Biot's theory about high frequency waves. The high frequency wave velocities are calculated by:[145,148]

$$\begin{cases} V_P = \left\{ \dfrac{\Delta \pm \left[\Delta^2 - 4\left(\rho_{11}\rho_{22} - \rho_{12}^2\right)\left(PR - Q^2\right)\right]^{1/2}}{2\left(\rho_{11}\rho_{22} - \rho_{12}^2\right)} \right\}^{1/2} \\ V_S = \left(\dfrac{\mu_{fr}}{\left(\rho - \phi\rho_{fl}\alpha^{-1}\right)} \right)^{1/2} \\ \Delta = P\rho_{22} + R\rho_{11} - 2Q\rho_{12} \\ P = \dfrac{(1-\phi)\left(1-\phi-K_{fr}/K_0\right)K_0 + \phi K_0 K_{fr}/K_{fl}}{\left(1-\phi-K_{fr}/K_0\right) + \phi K_0/K_{fl}} + \dfrac{4}{3}\mu_{fr} \\ Q = \dfrac{\left(1-\phi-K_{fr}/K_0\right)\phi K_0}{1-\phi-K_{fr}/K_0+\phi K_0/K_{fl}} \\ R = \dfrac{\phi^2 K_0}{1-\phi-K_{fr}/K_0+\phi K_0/K_{fl}} \end{cases} \quad 47$$

and

$$\begin{cases} \rho_{11} = (1-\phi)\rho_0 - (1-\alpha)\phi\rho_{fl} \\ \rho_{22} = \alpha\phi\rho_{fl} \\ \rho_{12} = (1-\alpha)\phi\rho_{fl} \\ \rho = (1-\phi)\rho_0 + \phi\rho_{fl} \end{cases} \quad 48$$

where K_{fr} and μ_{fr} are effective bulk and shear moduli of rock frame, K_0 is bulk modulus of mineral material making up the rock, K_{fl} is effective bulk modulus of pore fluid, ρ_0 and ρ_{fl} are densities of mineral and fluid, and α is tortuosity.

From Eqs. 47 and 48 it can be seen that high frequency wave velocities are related to properties of both rock matrix and fluid. Because velocities of dry rock only change linearly and slightly with temperature, as shown in Figs. 149 and 150, the observed nonlinear velocity changes with temperature in Fig. 152 are mainly due to CO_2. In fact, CO_2 properties, especially density and viscosity, are very sensitive to temperature change near the critical point, as shown in Fig. 154. Therefore, it can be concluded that the velocity changes observed in Fig. 152 are induced by CO_2 phase transition.

Summary and Conclusions

(1) A triaxial acoustic core flooding system with the capacity of simulating typical petroleum reservoir conditions was developed.

(2) Using this system, the temperature effect on seismic velocities of stainless steel, Dakota sandstone and Indiana limestone were investigated. It is found that, under confining pressure of 3000 psia, when the samples were heated from 65°F to 150°F, all seismic velocities slightly decrease. The change can be linearly correlated to the temperature.

(3) Using the same system, CO_2 phase transition induced seismic velocity changes were observed. When CO_2-saturated Indiana limestone was heated and cooled across the CO_2 critical temperature while the CO_2 pore pressure was held constant above its critical pressure, all three seismic velocities changed drastically in a non-linear way.

(4) Further experiments revealed that when temperature and pressure are kept constant near the CO_2 critical point, the average seismic velocities keep almost unchanged, which confirms that the above observed seismic velocity change is due to CO_2 phase transition.

(5) More experiments are required to improve our understanding on the phase transition induced seismic behavior, including attenuation and frequency dependency.

C. **MATRIX CHANGE**

C.1. Simulation of Non-Darcy Effect on Gas Flow

Introduction

The reservoir simulator MASTER (Miscible Applied Simulation Techniques for Energy Recovery) is developed based on BOAST (Black Oil Applied Simulation Tool) funded by the U.S. Department of Energy.[149] MASTER is a three-dimensional, three-phase simulator capable of simulating a black-oil reservoir with multiple components including a surfactant and up to four solvent species. In the most recent version, MASTER 3.0, foaming option for water injection alternating with gas (WAG) was incorporated.[149a] In this simulator, fluid behavior is assumed to be governed by Darcy's Law, which, under single-phase, one-dimension form, can be represented by the following equation:[150]

$$-\frac{dp}{dx} = \frac{\mu q}{kk_r A} \qquad 49$$

Generally, this assumption holds when the velocity of fluid is not high. As the flow velocity increases, deviations from Darcy's Law are observed. In low permeability formations, the deviation may be quite significant.[151] In order to make MASTER more comprehensive, therefore, it is necessary to add new features to this simulator so that it can handle situations in which non-Darcy effect should not be ignored. In this study, the non-Darcy feature considered is the Forchheimer correction, which takes into account the inertia effects due to high velocity fluid flow, and this feature is incorporated into the simulator for gas phase only.

Theoretical Formulation

Although there is no agreement on what causes non-Darcy effects, researchers have proposed different explanations and equations to describe non-Darcy flow behavior. Among them, the following equation is a modification to Eq. 49 by adding a quadratic term to account for inertial effect caused by high flow velocity: [152]

$$-\frac{dp}{dx} = \frac{\mu q}{kk_r A} + \beta\rho\left(\frac{q}{A}\right)^2 = \left(\frac{\mu}{kk_r A} + \frac{\beta\rho}{A^2}q\right)q \qquad 50$$

Equation 50 may be rearranged to

$$q = \frac{-\frac{dp}{dx}}{\frac{\mu}{kk_r A} + \frac{\beta\rho}{A^2} q} = \frac{-\frac{kk_r A}{\mu}\frac{dp}{dx}}{1 + \frac{kk_r \beta\rho}{\mu A} q} \qquad 51$$

By denoting

$$F = \frac{1}{1 + \frac{kk_r \beta\rho}{\mu A} q} \qquad 52$$

Equation 51 may be rewritten as

$$q = -F \frac{kk_r A}{\mu}\frac{dp}{dx} \qquad 53$$

Substituting Eq. 53 into Eq. 52 leads to a quadratic equation for F:

$$-\beta\rho\left(\frac{kk_r}{\mu}\right)^2 \frac{dp}{dx} F^2 + F - 1 = 0 \qquad 54$$

Letting

$$a = -\beta\rho\left(\frac{kk_r}{\mu}\right)^2 \frac{dp}{dx} \qquad 55$$

and solving Equation 54 for F give

$$F = \frac{-1 + \sqrt{1 + 4a}}{2a} \qquad 56$$

It should be noted that the flow rate q in Eqs. 50-53 is different from that in Eq. 49. Therefore, it is advisable to distinguish them in an explicit way, that is, to use q_D to represent the rate in Eq. 49, and q_{ND} for the rate in Eqs. 50-53. With these two notations and in view of Eq. 49, we find that Eq. 53 may be expressed as

$$q_{ND} = F q_D \qquad 57$$

The above equation indicates that, as long as factor F is known, the non-Darcy flow rate, q_{ND}, can be calculated based on Darcy flow rate, q_D. This is a shortcut and approximation to obtain the inter-block non-Darcy flow rate, q_{ND}. The actual pressure distribution associated with non-Darcy phenomena is not computed. Other variables, such as saturation and relative permeability, are not accurate either in the sense that non-Darcy effects are not considered when calculating these variables.

Note that Eq. 57 should not be used to calculate production rate at the wellbore block. Instead, the following equation, presented by Su,[153] is used to calculate the production rate at the wellbore:

$$q = \frac{2\pi hkk_r(p_b - p_w)/\mu}{\ln(r_o/r_w) + s + Dq} \qquad 58$$

where for gas flow

$$D = \frac{\beta\rho kk_r}{2\pi h\mu}\left(\frac{1}{r_w} - \frac{1}{r_o}\right) \qquad 59$$

The approach described above, as a shortcut to consider non-Darcy effect, is convenient to implement.[154] If higher precision is desired, however, the Forchheimer correction characterized by Eq. 53 may be incorporated into the pressure equation to get more accurate pressure distribution. The pressure equation incorporated with Forchheimer effect takes the following form[155]:

$$\nabla\cdot\left(\frac{Fkk_r}{B}\right)\nabla p - \frac{q}{\rho} = \frac{\phi c}{B}\frac{\partial p}{\partial t} \qquad 60$$

The difference between Equation (12) and the pressure equation not accounting for non-Darcy effect is that factor F appears in Equation (12). Since F can be considered as a function of pressure p, Equation (12) is nonlinear.

Numerical Solution

Field units are used in simulations. The non-Darcy coefficient, β, can be determined either experimentally,[156] or empirically.[155] In this study, β is calculated for each grid block from the following formula proposed by Jones:[155a]

$$\beta = 1.88\times10^{-10}k^{-1.47}\phi^{-0.53} \qquad 61$$

The rate-dependent skin coefficient, D, is calculated from Eq. 59 with a unit conversion factor of 2.223×10^{-15}. Initially, the non-Darcy flow factor, F, is set to be 1 for every grid block, meaning Darcy flow condition. Iterative method is then used to solve Eq. 60 for pressure and interblock flow rate. Using the calculated well block pressure, the production rate at the well is calculated as follows:

$$q = \frac{\sqrt{\left(\ln\left(r_o / r_w\right) + s\right)^2 + 8\pi hkk_r\left(p_b - p_w\right)D/\mu} - \ln\left(r_o / r_w\right) - s}{2D} \qquad 62$$

Note that Eq. 62 is the quadratic solution of q from Eq. 58. But using Eq. 62 has the benefit to reduce the possibility of instability or more iterations, as indicated by Su.[153] This is because, if Eq. 58 is used, the rate q from a previous time step has to be invoked to obtain the current rate, while using Eq. 62 will not have such a need. Convergence is checked each time F and D are computed. If both of them converge, the simulation proceeds; otherwise, the time step is reduced and another round of iterations start.

Example Results

The example is taken from the SPE First Comparative Solution Project, Case 2.[157] It involves immiscible gas injection into an undersaturated oil reservoir. Gas is injected into a corner injection well at a rate of 100 MMscf/d. In the opposite corner of the rectangular reservoir, the production well is produced at an initial rate of 20,000 STB/d oil. After 1,500 days of production, the control of the production well is switched to a specified bottomhole flow pressure of 1,000 psia. The Cartesian grid system includes 300 (10 by 10 by 3) blocks. Block size in the horizontal directions is 1,000 feet throughout, while the thickness of grid blocks varies from 20 to 50 feet in different layers. The simulation is terminated at 6 years or when the maximum producing gas-oil ratio is exceeded.

Using the results from MASTER 3.0 in which Darcy flow was assumed, some results from simulations considering the non-Darcy effect are presented in Figs. 155–159. Figure 155 shows the pressure distribution in Layer 1, which is the completed layer in the injection well. Pressure in every block is higher when the non-Darcy effect is considered. The variation is from 1.3% to 3.3% in general but is 8.6% in the block with the production well. Figure 156 shows the distribution of the non-Darcy flow factor, F, in Layer 3 which is the completed layer in the production well. It can be seen that the non-Darcy phenomenon is remarkable only in one block where the production well locates. The F value plunges to 0.263 while it is close to 1 in other blocks. Figures 157–159 show the difference of cumulative gas production, cumulative gas injection, and oil production rate caused by considering non-Darcy effect. The difference in cumulative gas production shown in Fig. 157 becomes significant after 1,500 days of production; at 1,815 days, the difference is 7.09%. The difference in cumulative gas injection shown in Fig.

158 becomes significant after 1 year of production; at 1,815 days, the difference is 109%, another indication that the non-Darcy effect should be considered around wellbore. Since non-Darcy effects are not considered for the oil phase, there is essentially no difference for the oil production rate as shown in Fig. 159, except the fluctuations associated with the non-Darcy curve. When non-Darcy effect is considered, the time steps in the simulation must be small enough or remarkable fluctuation will occur and the simulation may end with a very different way.

Conclusions

1. The logic of the non-Darcy effect based on the Forchheimer equation has been successfully incorporated into the reservoir simulator MASTER. Simulation results are reasonable because they demonstrate all expected trends (higher reservoir pressure, significant non-Darcy effect near wellbore, lower gas production and injection rates).
2. Although users of the simulator are provided with the option whether to consider the non-Darcy effect or not, it is clear that, for cases involving high speed gas flow like the one presented in this paper, the non-Darcy effect should be considered.
3. The presented method on how to implement the non-Darcy effect through the use of factor *F* is effective and quite simple.

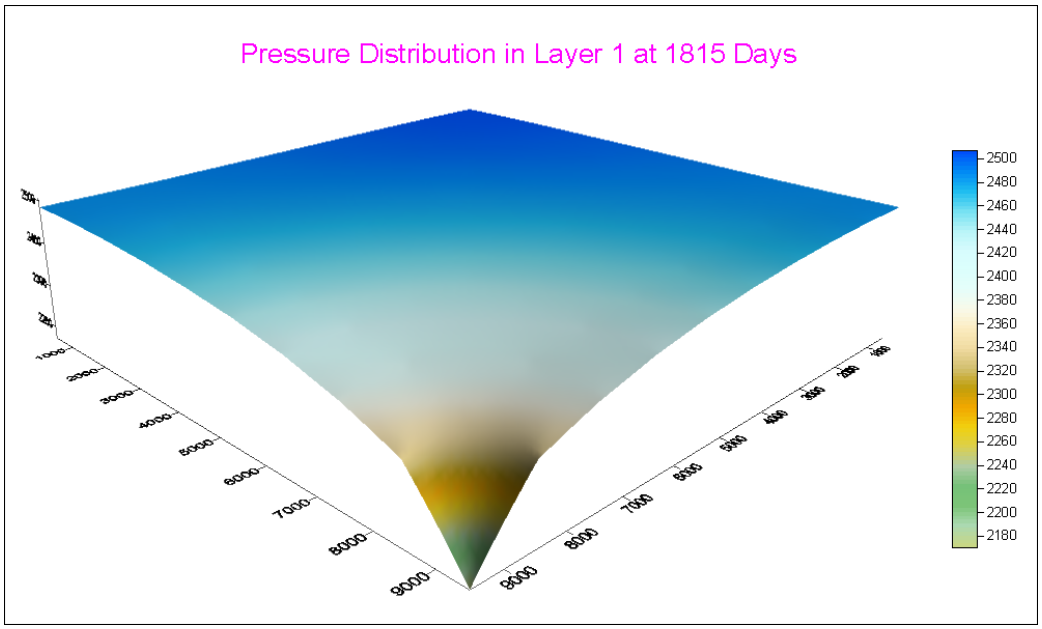

Fig. 155. Pressure distribution.

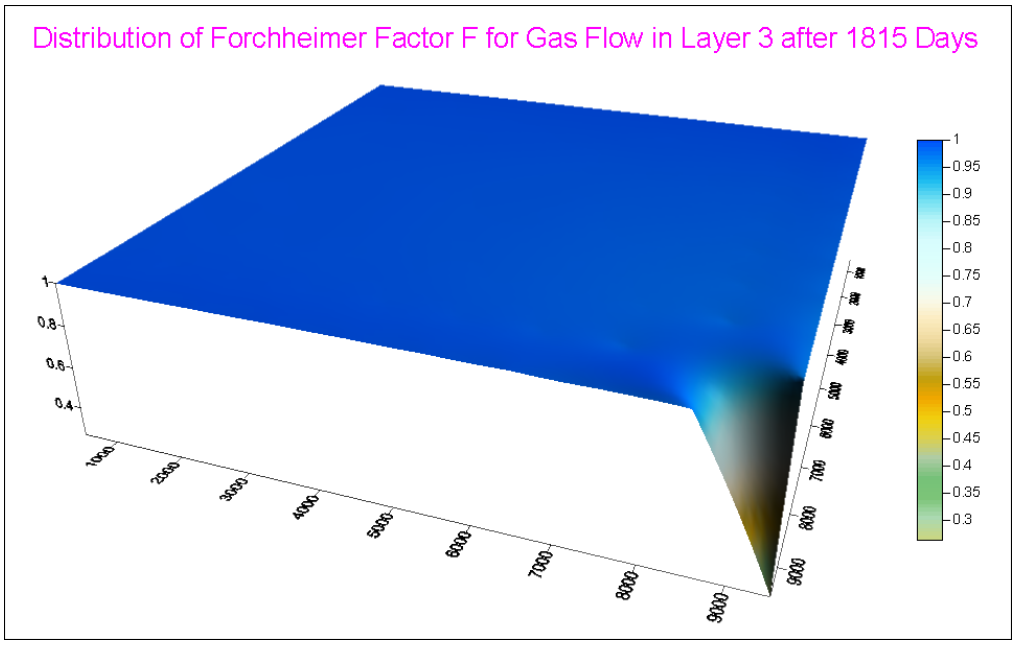

Fig. 156. Distribution of F factor.

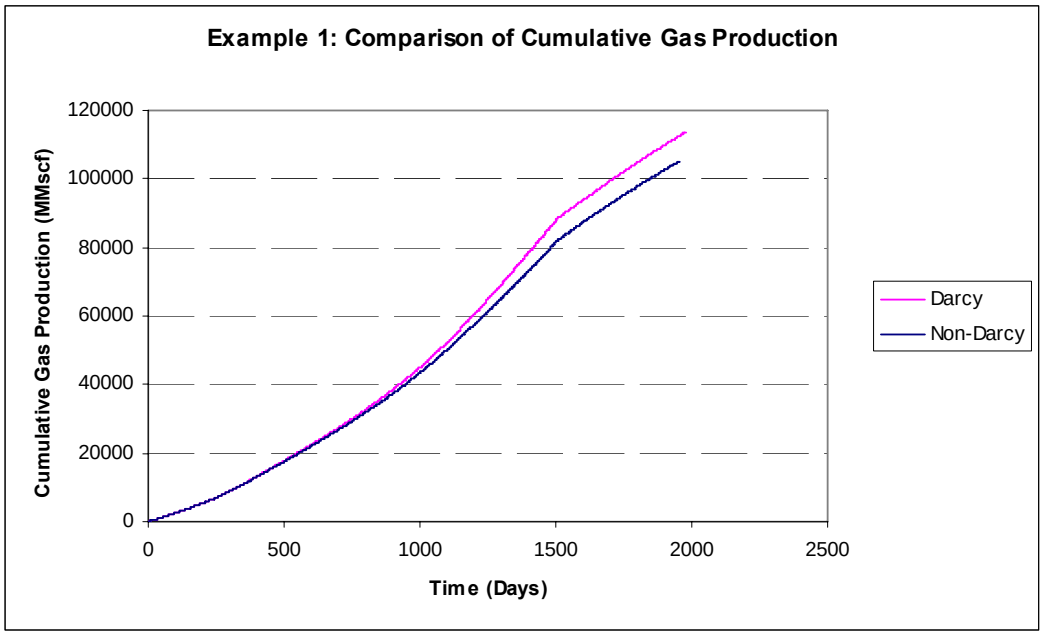

Fig. 157. Comparison of cumulative gas production.

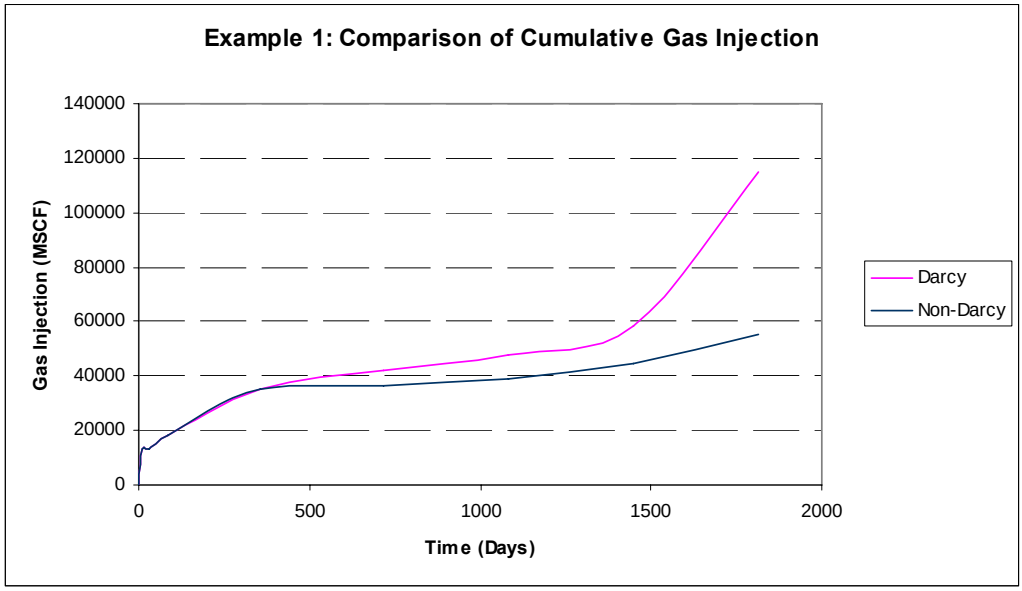

Fig. 158. Comparison of cumulative gas injection.

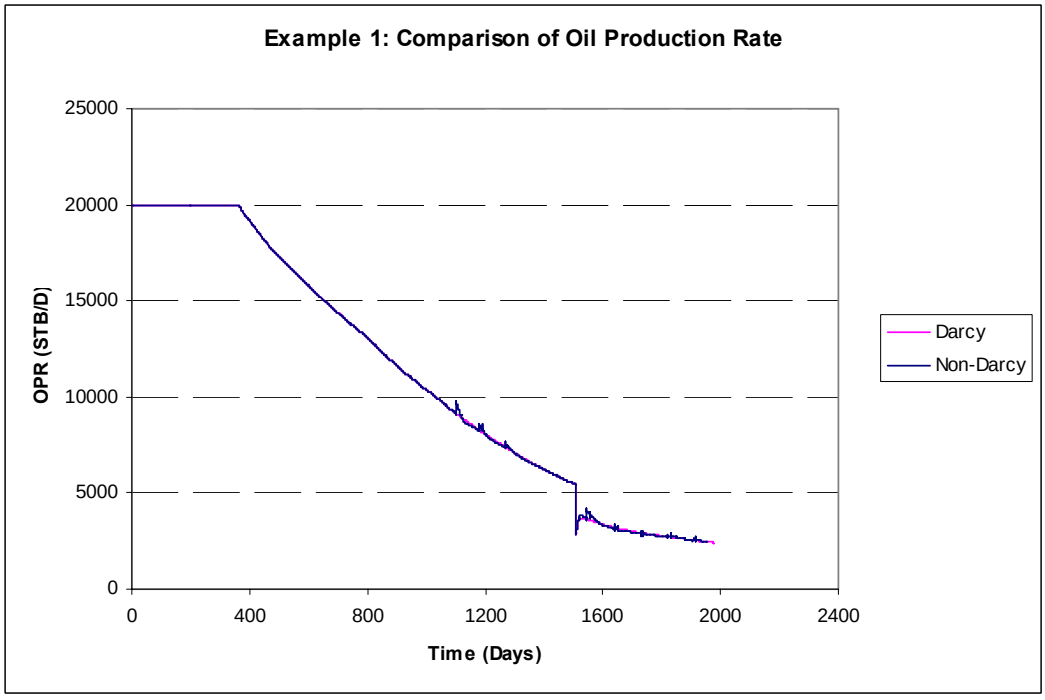

Fig. 159. Comparison of oil production rate.

.

C.2 CO_2/Brine/Carbonate Rock Interactions: Dissolution and Precipitation

Introduction

Determining the injectivity and productivity of CO_2 injection to reservoirs requires detailed knowledge of the complex interactions among CO_2, rock matrix, and pore fluids under reservoir pressure and temperature. Many physical and chemical processes are known to occur both during and after geologic CO_2 injection, including diagenetic chemical reactions and associated permeability changes.

Reported here are findings and comparison of five large coreflooding experimental series performed on quarried and reservoir carbonates (limestone and dolomite) with coinjected or alternating injections of CO_2 and brine at reservoir conditions. Metal chlorides were added as tracer components in injection brines for three tests and appeared in quantities well above natural levels in deposited carbonates in one test. Core segment porosity and permeability are reported to indicate dissolution and deposition. Cores were sectioned and analyzed by chemical and back-scattered electron imaging (BSEI) and chemical titration for compositional changes. In two tests fluid samples taken at reservoir conditions and neutron computed tomography (CT) were used to monitor changes in in-situ fluid compositions and the development of the 3-D porosity structure of the flooded cores, respectively.

Dissolution of carbonates at reservoir conditions during coinjection of CO_2 and brine was confirmed by porosity and permeability increases, neutron CT, and brine compositional analysis performed on effluent brine samples obtained at reservoir conditions. When deposition occurred it was indicated by porosity and permeability reductions in downstream core, BSEI identification, and modeling. The composition and extent of deposits was strongly influenced by the brine composition. Deposition and dissolution were found to occur in close proximity. The

results are being used to calibrate a CO_2 model coupling multiphase flow to chemical reactions that will be used to predict in situ dissolution and deposition related to CO_2 geologic sequestration.

Table 44. **Brine Compositions Used in the Series of Five Large Corefloods**

	Reservoir Brine #1	Reservoir Brine #2	Brine #3 Tracer #1	Brine #4 Tracer #2
NaCl	64700	13531	10000	25000
$CaCl_2$	11000	4330	5000	4040
$MgCl_2$	3810	1914	5000	190
$NaHCO_3$	1850	5645		
Na_2SO_4	5590	4831		
$MnCl_2$			5000	198
$SrCl_2$			5000	
TDS	86950	30251	30000	29428

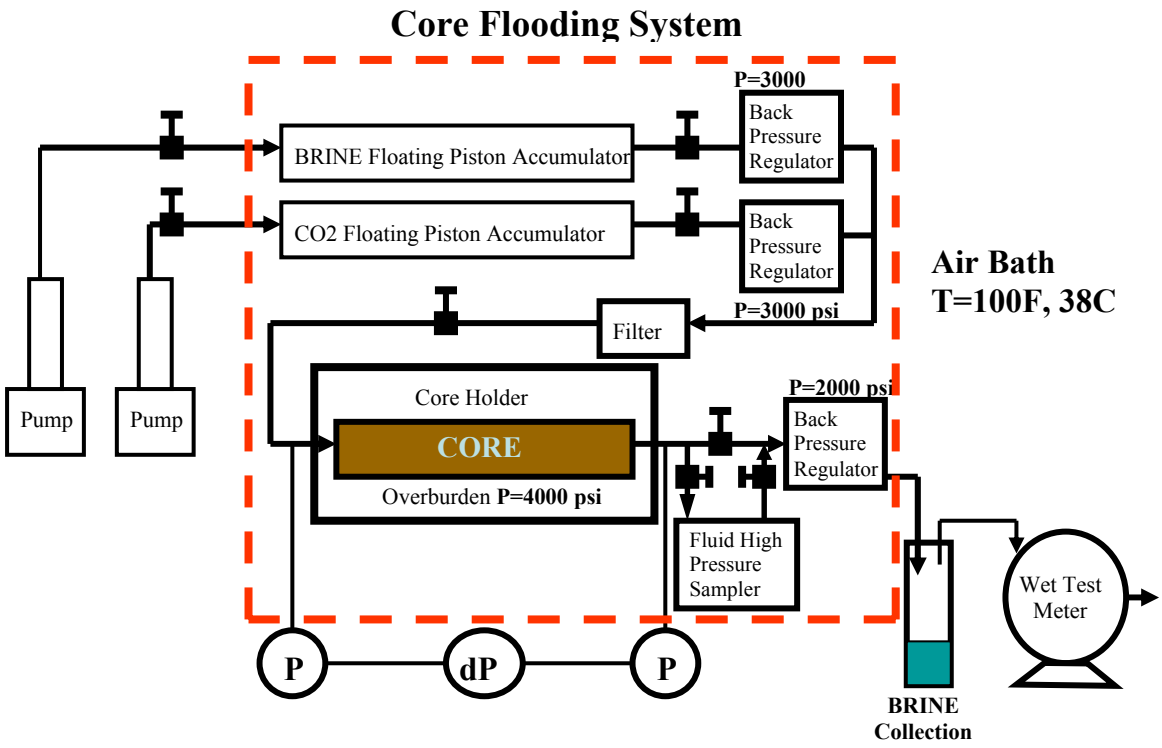

Fig. 160. Coreflood A – Indiana limestone.

The first coreflood was on quarried Indiana limestone at 2000 psig and 100ºF using Reservoir Brine #1 (Table 42). Brine was injected alternating with CO_2 (WAG). After injecting several hundred PV, a 25 cm long solution channel had formed while the permeability of the whole core was essentially the same as the fresh core (Figs. 162 and 163). There was no evidence of plugging though the second half of the core had a permeability reduction by about half, which is an indication of deposition (Fig. 163). Using BSEI and compositional analyses, all possible deposition had the same composition as the fresh core, thus in Coreflood C metal tracers were added to aid in identifying deposition.

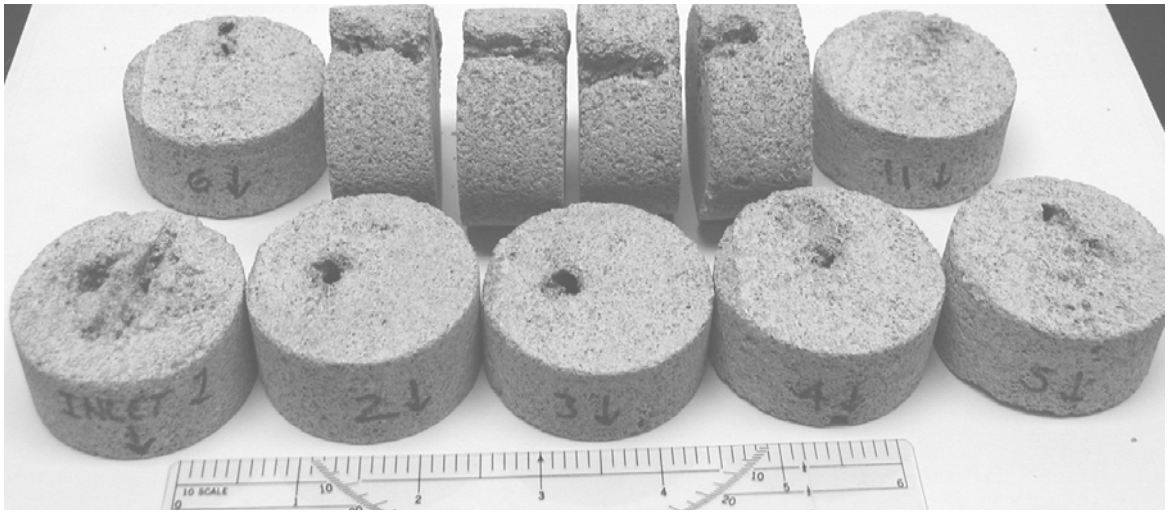

Fig. 161. Post-WAG Indiana limestone dissolution channel.

Fig. 162. Second half of the core did not have a solution channel (last ~ 25 cm). Final permeability of unchannelled core, k=19.5 mD. Initial perm in this same region before WAG ~ 36 mD.

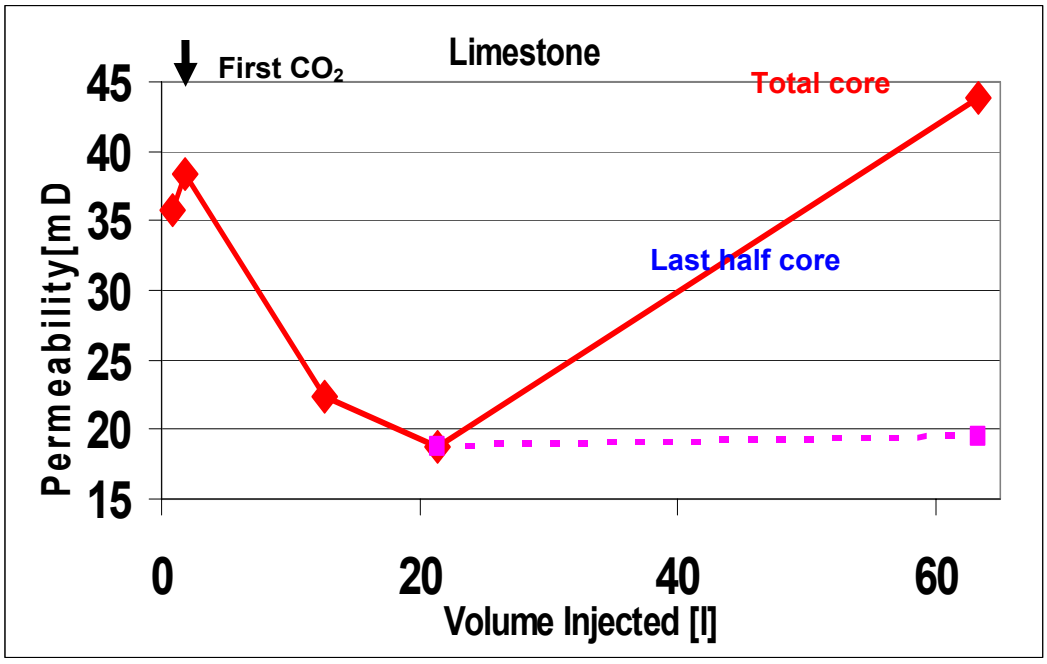

Fig. 163. Limestone permeabilities.

Coreflood B – San Andres

The second coreflood was on San Andres core from the Seminole field in west Texas (Fig. 164). The primary component of the San Andres is dolomite. A significant increase in porosity occurred during the brine flood (Fig. 165) due to anhydrite dissolution. Brine #2 composition was patterned after Seminole produced water (Table 44). Extensive porosity and permeability increases occurred during the WAG portion of the flood with dissolution of dolomite and further dissolution of anhydrites (Figs. 166 and 167).

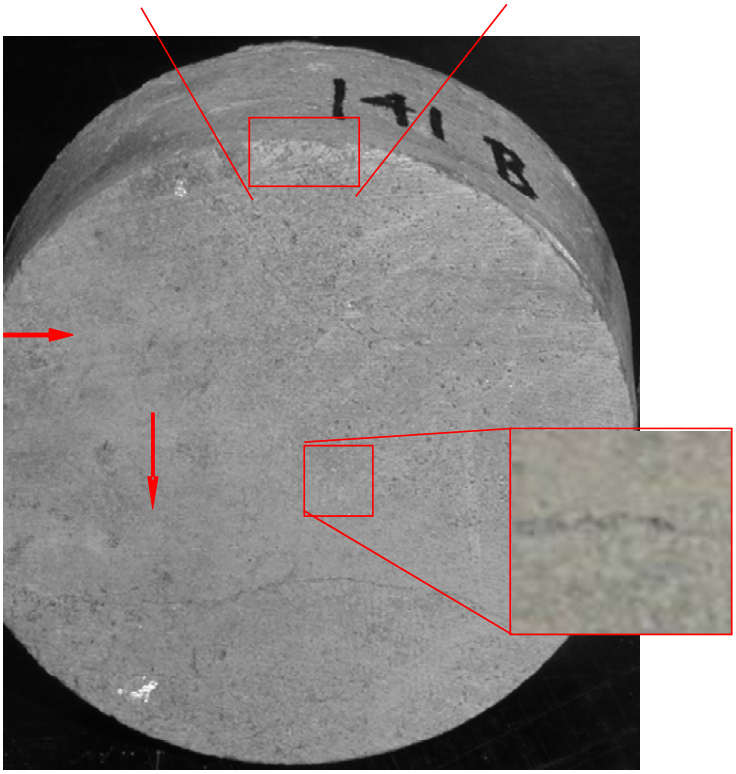

Fig. 164. Pre-flood dolomite, Seminole San Andres, Gaines County TX. Vuggy anhydritic very fine grain dominated packstone, anhydrite nodules, and stylolites.

Fig. 165. Post-waterflood sectioned core after brine flood showing anhydrite dissolution.

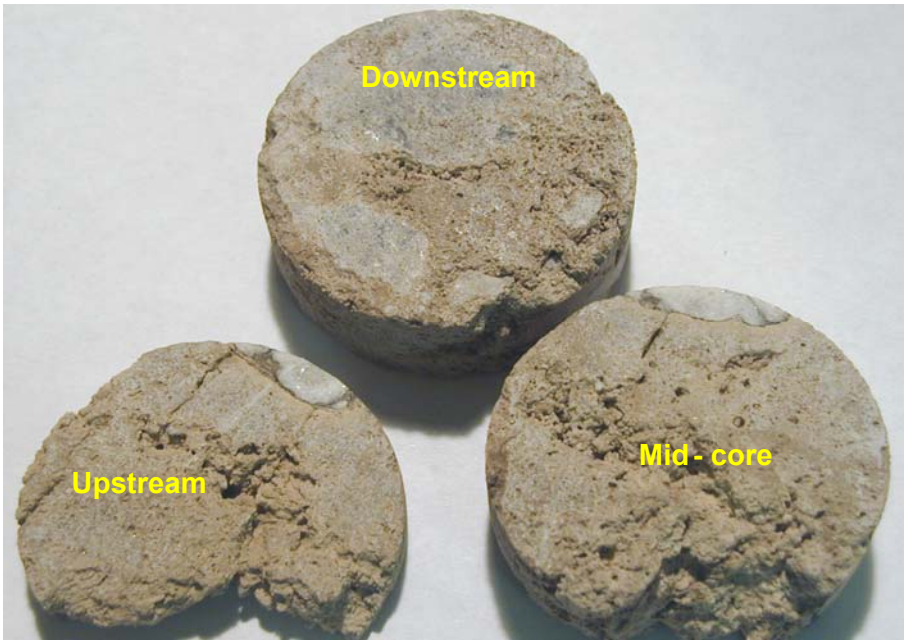

Fig. 166. Post-WAG Seminole San Andres core showing dolomite dissolution with additional anhydrite dissolution.

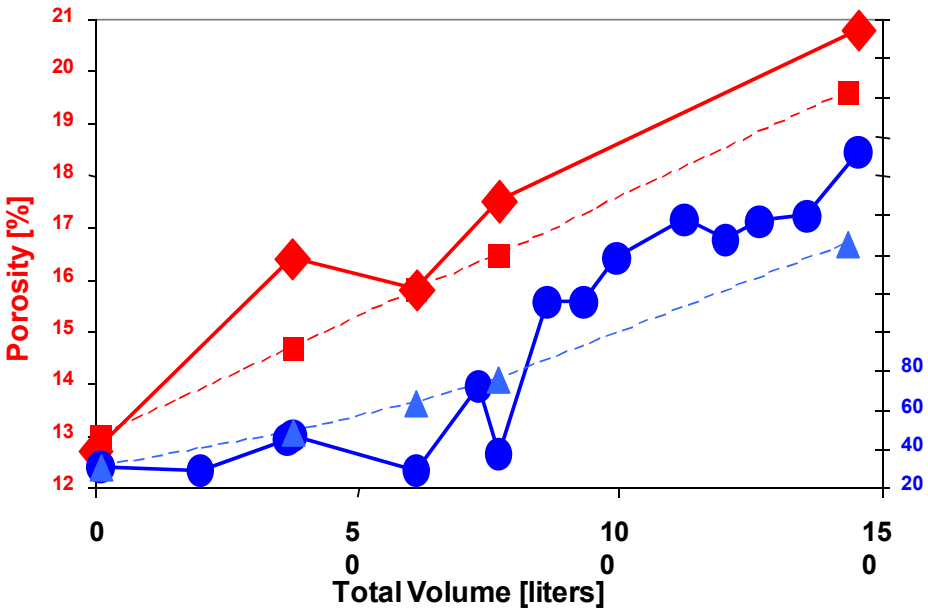

Fig. 167. Measured and calculated porosity and permeability during the flooding of dolomite (San Andres) core.

Coreflood C – Indiana Limestone with Brine #3 Tracer #1

The third coreflood was on quarried Indiana limestone core (Fig. 168) with a coinjection of brine with high levels of metal tracers manganese and strontium added to the brine as chlorides, which are naturally found at very low levels in this limestone. The limestone is over 98% calcite

Table 45. Core Parameters

	Diameter [cm]	Length [cm]	Porosity [%]
Segment A	5.03	17.15	16.91
Segment B	5.03	39.37	17.54
Entire Core	5.03	56.52	17.35

(analysis portion of Figs.173 and 174) in the non-reacted areas. The bright spots are reacted areas and the darker spots non-reacted in Figs 173 and 174. A solution channel formed in the first 15 cm of Segment A (Figs. 169 and 170). Significant deposits of manganese and strontium occurred as carbonates throughout the core; this is shown in the plots in Figs. 171–172 and in the BSE images and quantitative analyses in Figs. 173–174. It was suspected that the system was oversaturated with the tracer carbonates and that in a new system the tracer quantities would be reduced significantly.

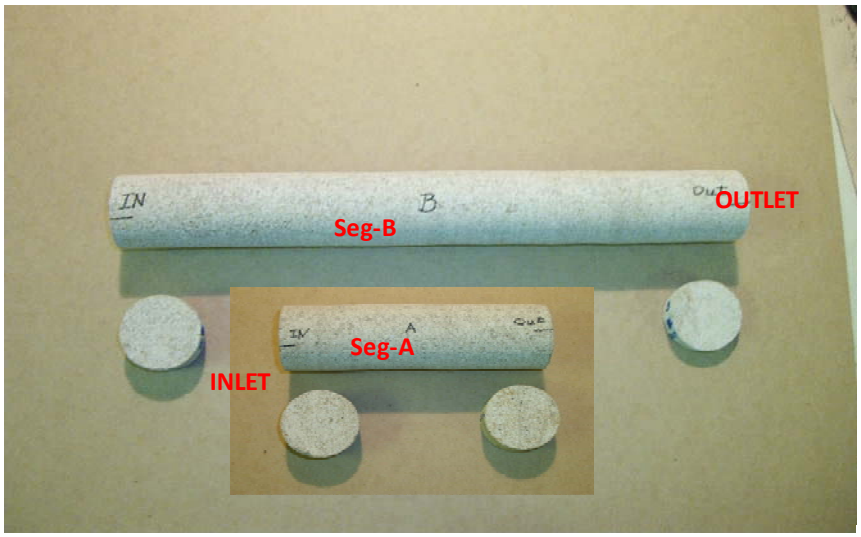

Fig. 168. Pre-flood limestone core.

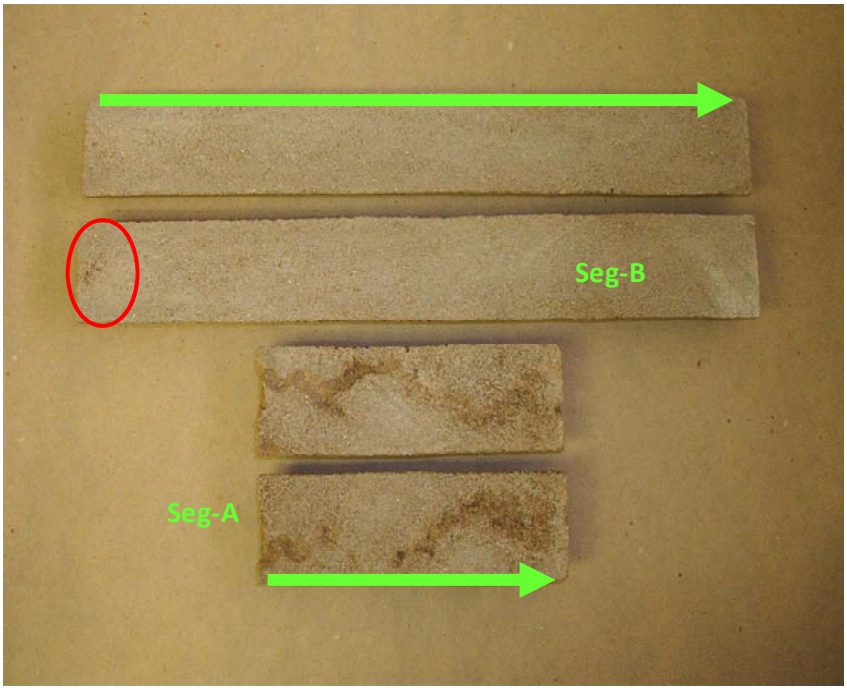

Fig. 169. Post-flood limestone core sectioned.

Fig. 170. End view of Segment A inlet.

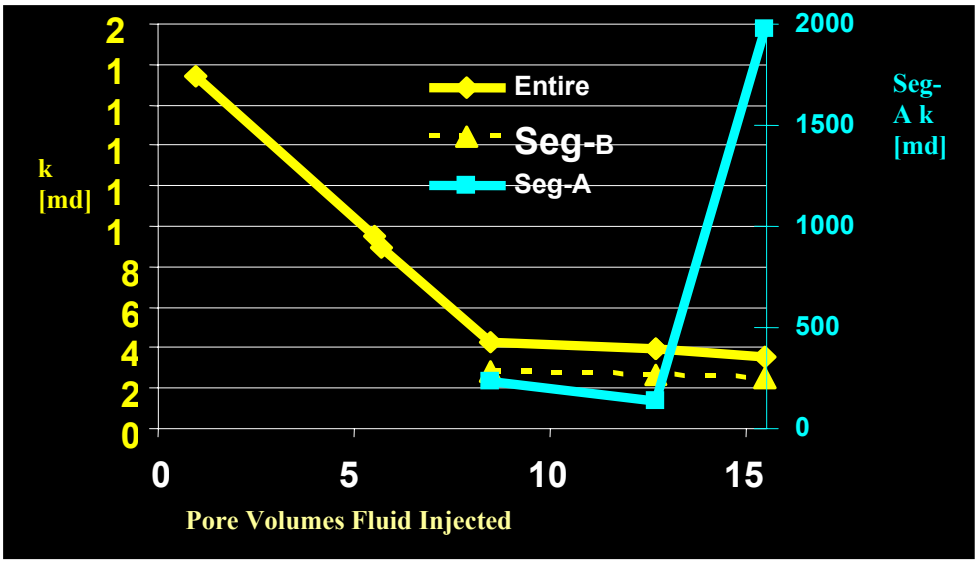

Fig. 171. Permeability results.

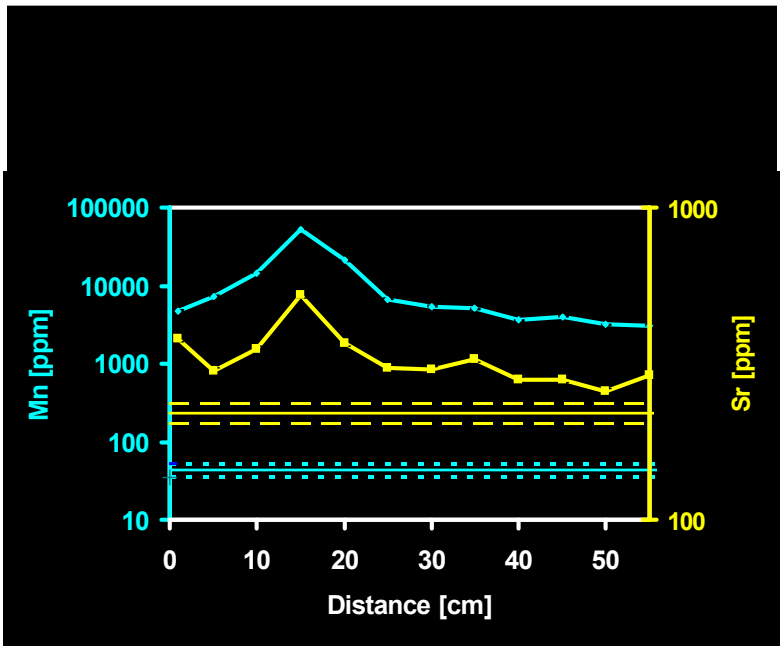

Fig. 172. Cross-section of composition (Mn and Sr) along the length of both segments.

	Ca	Mg	Mn	Sr
1.	98.7	0.65	0.62	0.00
2.	35.2	0.32	64.1	0.20
3.	19.4	0.30	79.7	0.28

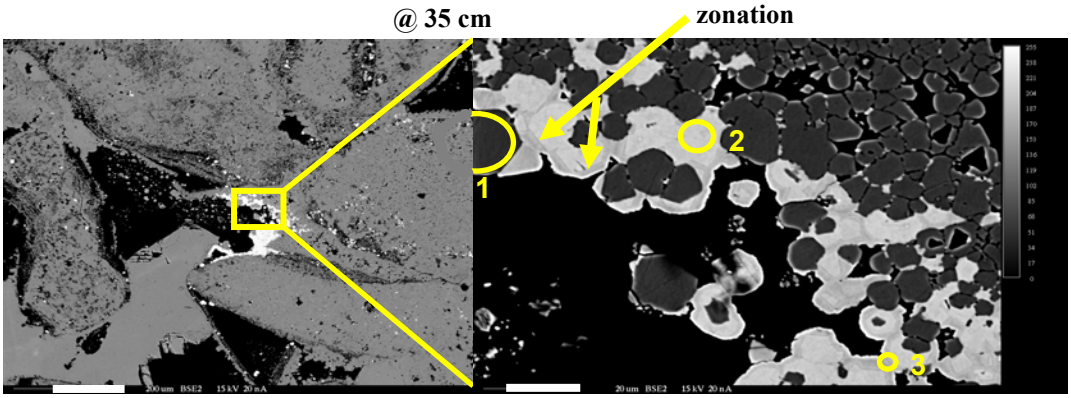

Fig. 173. BSE Quantitative analysis [% as carbonate](above) with BSE images.

	Ca	Mg	Mn	Sr
1.	98.9	0.94	0.05	0.00
2.	30.5	0.47	68.6	0.26

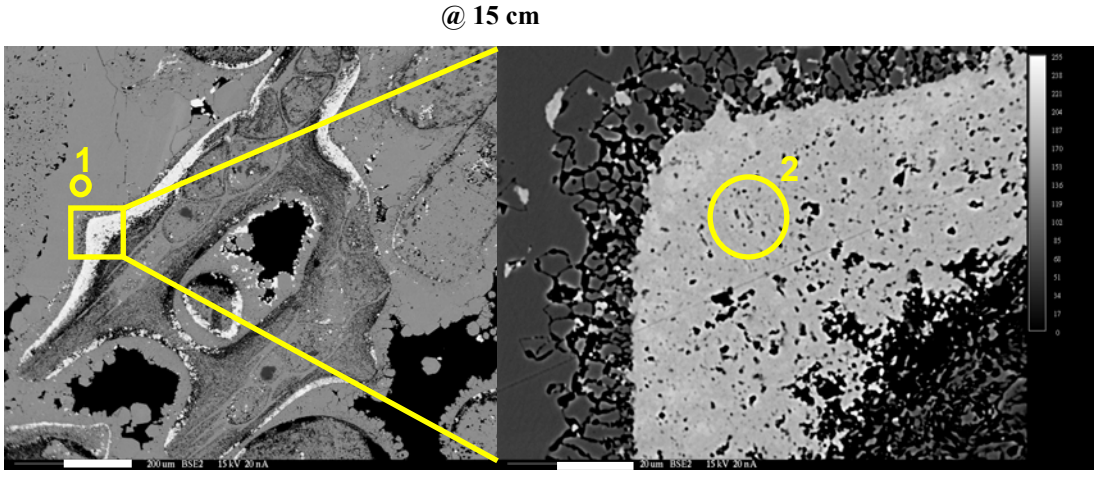

Fig. 174. BSE Quantitative analysis [% as carbonate].

Coreflood D–Indiana Limestone & Coreflood E–Lockport Dolomite (both with Brine #4 Tracer #2)

The fourth (D) coreflood was on quarried Indiana limestone. The fifth (E) coreflood was on quarried Lockport dolomite. Each was performed at 2000 psig and 100ºF with co-injected CO_2 and Brine #4. Brine #4 compared to Brine #3 contained no strontium, less than 4% as much manganese and magnesium, similar calcium concentration, and increased sodium to make up to a similar level of dissolved solids. The intent was to have levels of tracer high enough to detect but not high enough to alter the carbonate dissolution/precipitation behavior, e.g. system undersaturated in manganese. In addition to the tests performed during the earlier test series three CT scans were performed on each core segment: one on the fresh core, one at an interval during the flood, and the final after the last flood period; a bromide tracer diffusivity test for each system (Figs. 179-182 and 188-191), and in situ fluid samples taken for compositional analysis to compare with ambient samples.

Figure 175 is a view of all three limestone sections after the first flood period. The flood had to be stopped because the core sleeve failed due to dissolution creating a cavity near the inlet. In the limestone test injection was interrupted twice due to sleeve failure. After each flood period the core was trimmed. Figure 176 compares the ends after the three flooding periods. Figures 177 and 178 are color enhanced CT images on the fresh core (I), after the first flooding period (II), and following the last flooding period (III) as a cross section at about 6 cm deep (Figure 177) and 90º longitudinal sections (Figure 178) for each of the three times with the location of the cross section indicated. Figures 179-182 are plots of produced compositions taken during the diffusivity test for limestone. Figure 179 shows the produced bromide concentration versus pore volumes injected. The first part is with the bromide spiked Brine #4 displacing unspiked Brine #4. The later stage is a displacement with a coinjection of CO_2 and Brine #4. CO_3 as calcite in solution is also plotted showing an increase of dissolved carbonate with the presence of CO_2. Figures 183-191 are similar figures for dolomite.

In each system there was an increase in porosity and permeability for the three core segments (Fig. 187). Most of the increase was in the first core segment, but there were small increases in porosity and permeability in the two downstream segments. There was not sufficient data in the limestone for a definitive value, but the dolomite had 14% porosity increase in Segment A and 0.8 and 0.4% porosity increases in Segments B and C, respectively, or a system increase of 5% (9.9 cm3). The mass loss calculated using effluent compositions is over 23 g or

over 8.0 cm3. Neither BSEI or chemical analysis detected any tracer precipitation in either core type.

Some observations in comparing the limestone and dolomite results are:

1. Comparing Figs. 179 with 188, it is noted that the flow behavior of the limestone indicates a less homogeneous flow distribution than that of dolomite.
2. Figures 180 and 189 compare the production of manganese that in both cases has a reduction after a soaking period early in the test. There is a spike in produced manganese concentration corresponding to CO_2 breakthrough. There appears to be some manganese precipitation in the early time in the core that is produced after CO_2 breakthrough. At ambient conditions most of the manganese precipitates.
3. Figures 181 and 191 compares the effluent calcium concentrations. In both systems solution calcium increases after CO_2 breakthrough with significant concentrations precipitating at ambient conditions. The higher concentration of calcium is in the limestone that has little magnesium in the solution.
4. Figures 182 and 191 compare magnesium concentration in the effluent. There was little change in either system until CO_2 breakthrough. As might be expected the increase in effluent concentration is small in limestone (~30%) which contains less than 1% magnesium while increases about eight fold in dolomite which contains about equal mole concentrations of magnesium and calcium. Most of the magnesium stays in solution at ambient conditions with little precipitation in either system.

In summary there was no precipitation detected in Corefloods D and E. The primary difference that was noted with earlier floods was a significant change in brine composition. Each of the first three brines (including the reservoir brines) had much high levels of magnesium and the first tracer brine had high levels of manganese and strontium.

Fig. 175. Three limestone core segments after the first flooding period.

Fig. 176. First segment inlet after each flooding period (limestone Coreflood D).

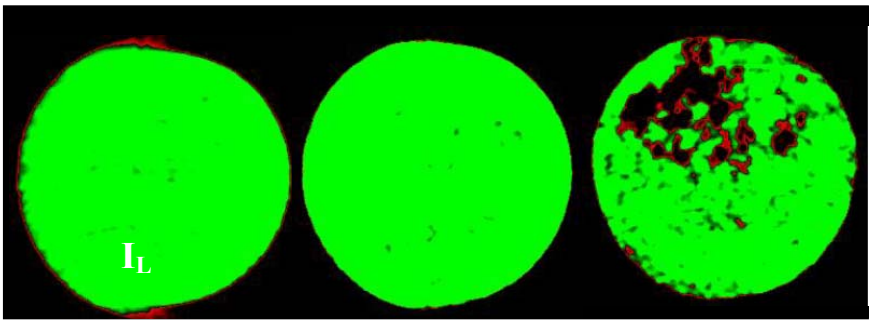

Fig. 177. CT cross section images at ~6 cm from the end of the original limestone Segment A inlet. Pre-flood (IL), after the first flooding period (IIL), and post-flood (IIIL) (limestone Coreflood D).

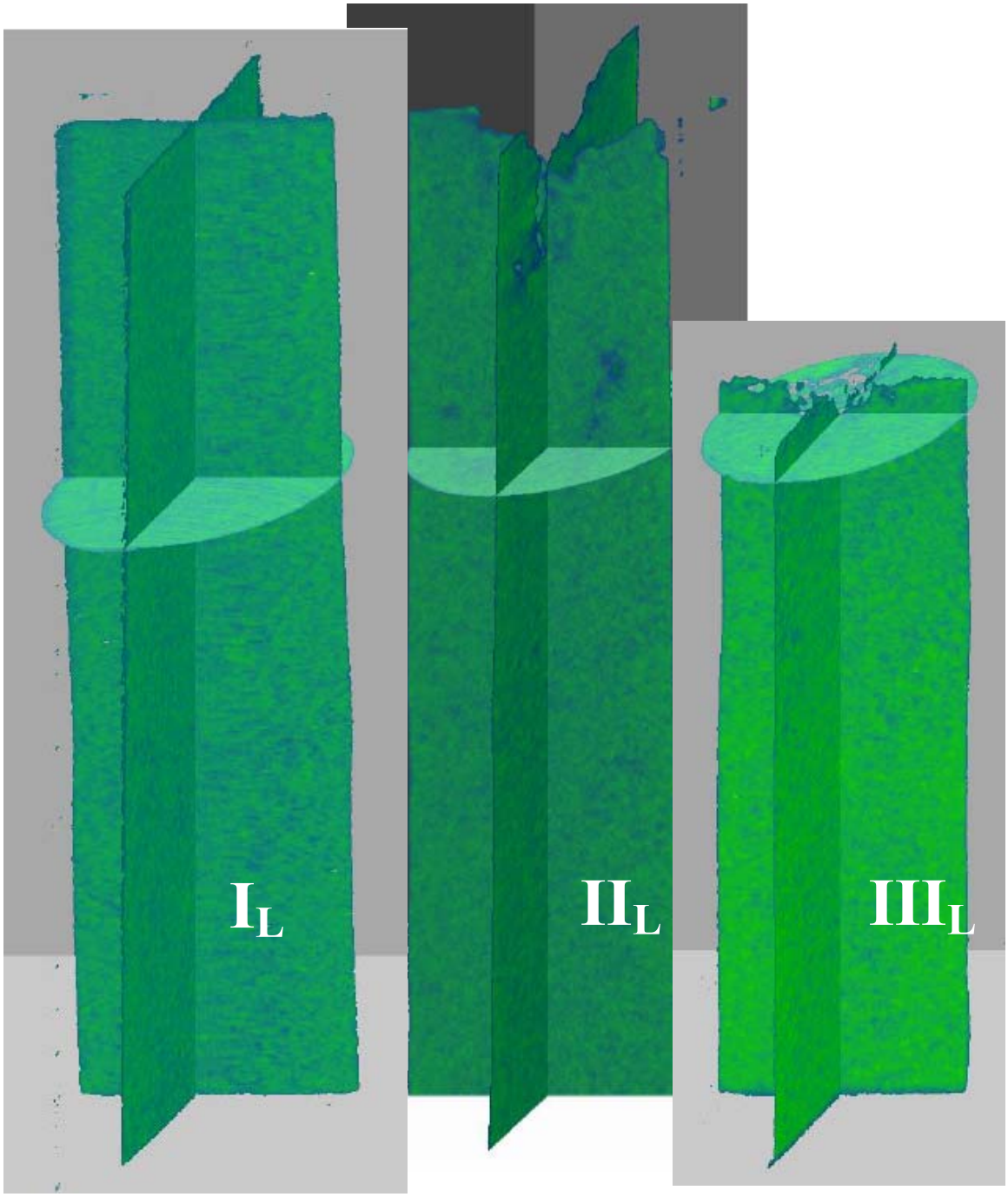

Fig. 178. CT longitudinal sections of core after first flooding period with the Fig. 18 corresponding cross sections marked (limestone Coreflood D).

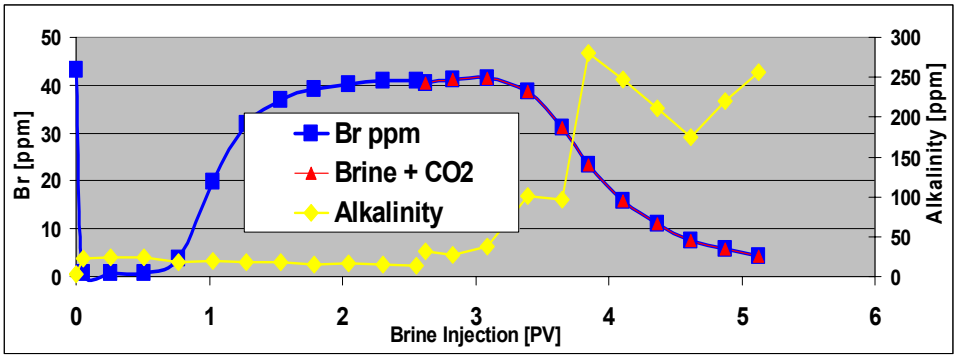

Fig. 179. Bromide diffusivity and alkalinity results (limestone Coreflood D).

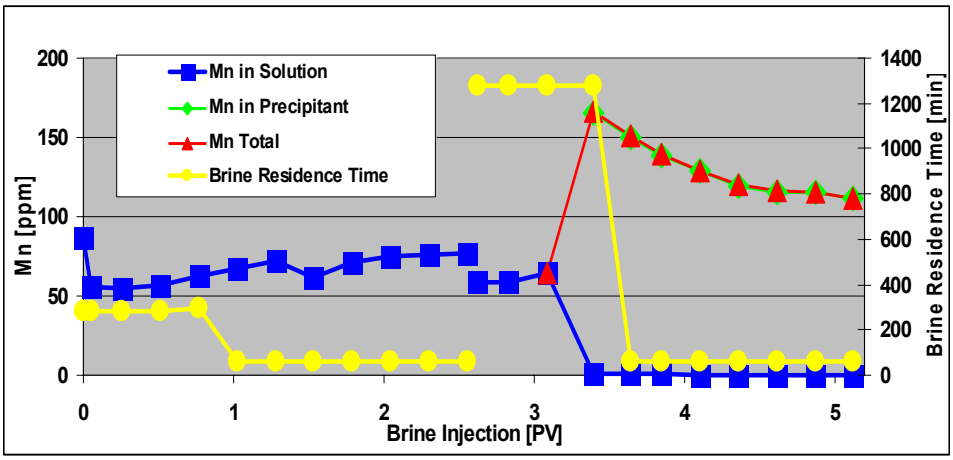

Fig. 180. Manganese concentration in the effluent (limestone Coreflood D).

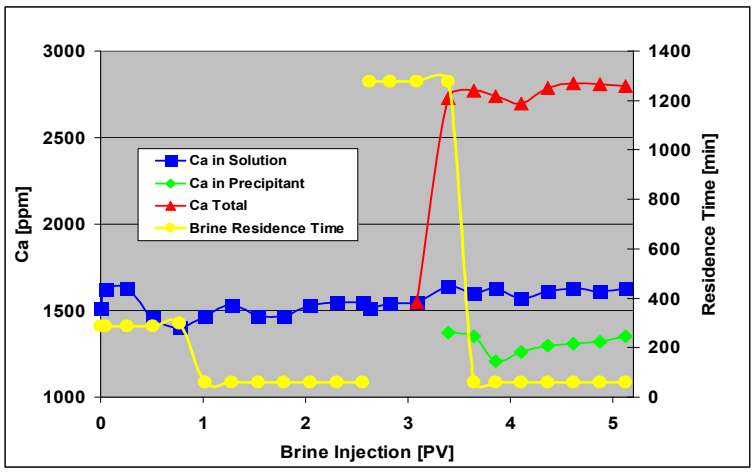

Fig. 181. Calcium concentration in the effluent (limestone Coreflood D).

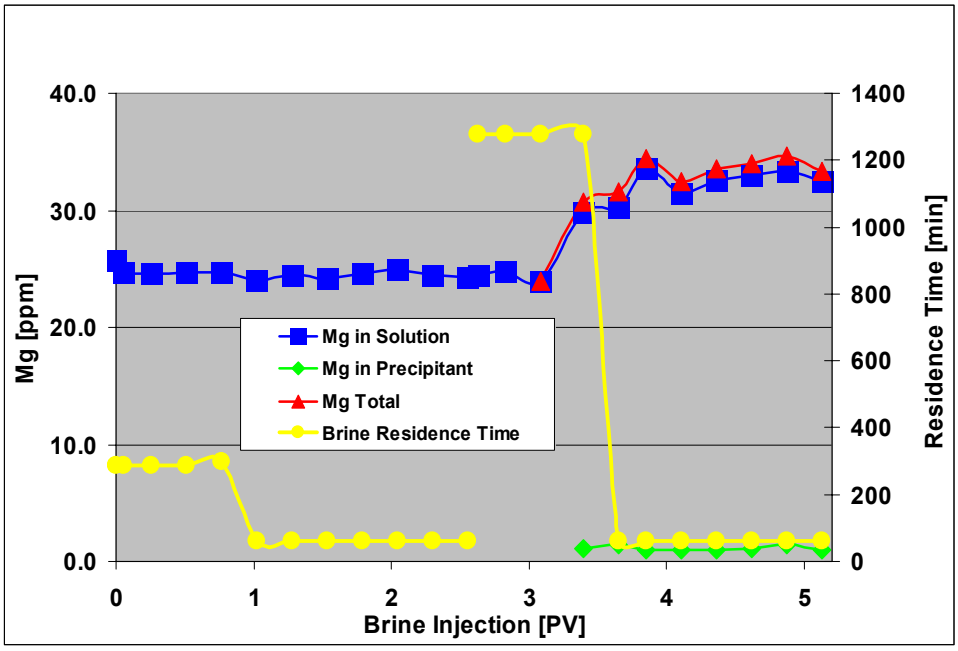

Fig. 182. Magnesium concentration in the effluent (limestone Coreflood D).

Fig. 183. Three dolomite core segments after the first flooding period (Coreflood E).

Fig. 184. Inlet of first segment after each flooding period (dolomite Coreflood E).

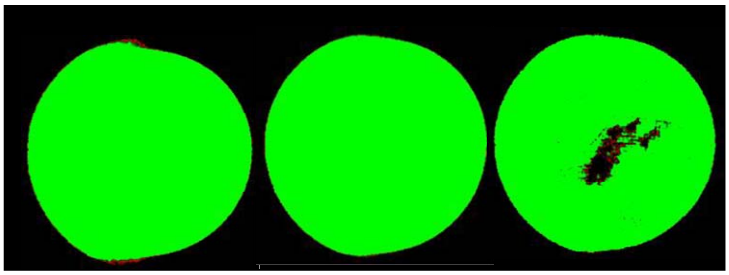

Fig. 185. CT cross section images at ~6 cm from the end of the original dolomite Segment A inlet. Pre-flood (ID), after the first flooding period (IID), and post-flood (IIID) (Coreflood E).

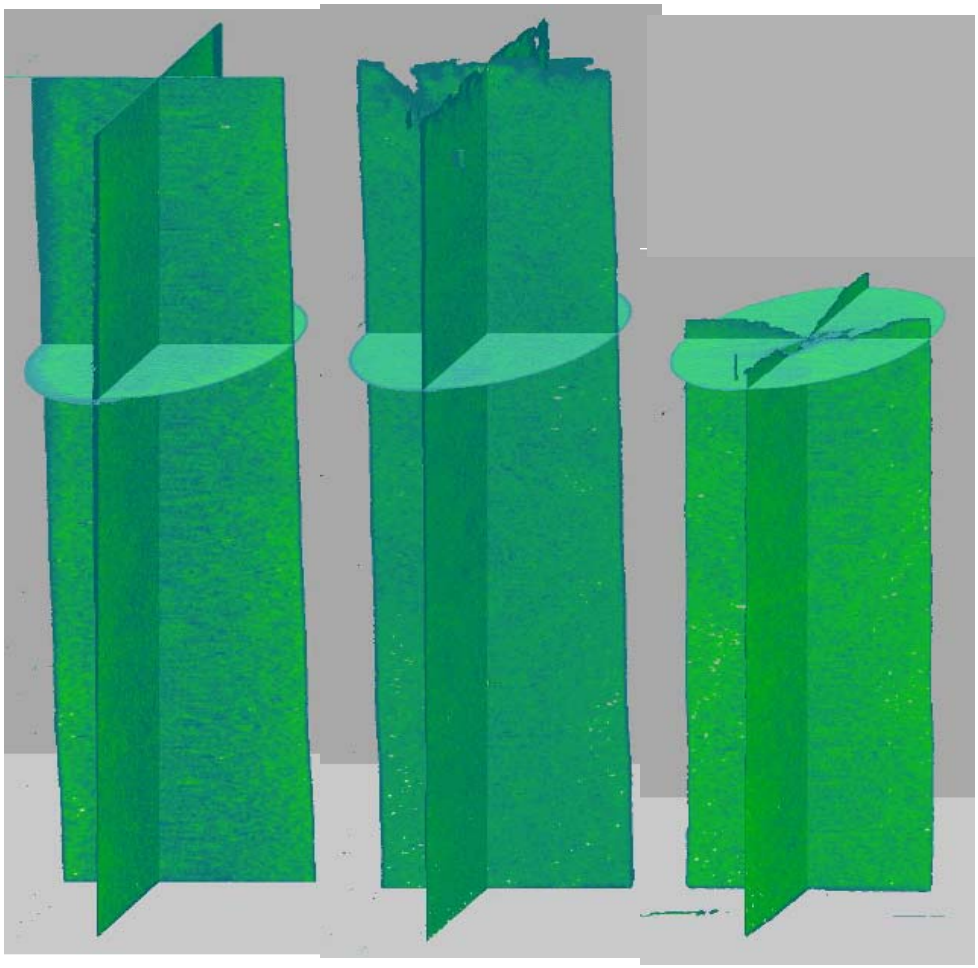

Fig. 186. CT longitudinal sections of core after first flooding period with the Fig. 185 corresponding cross section marked (dolomite Coreflood E).

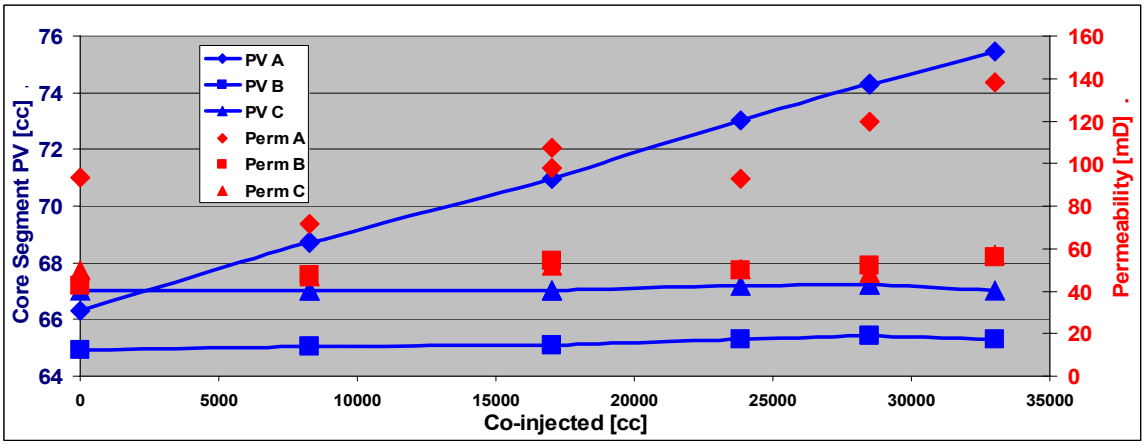

Fig. 187. Dolomite core segment porosity and permeability trends (dolomite Coreflood E).

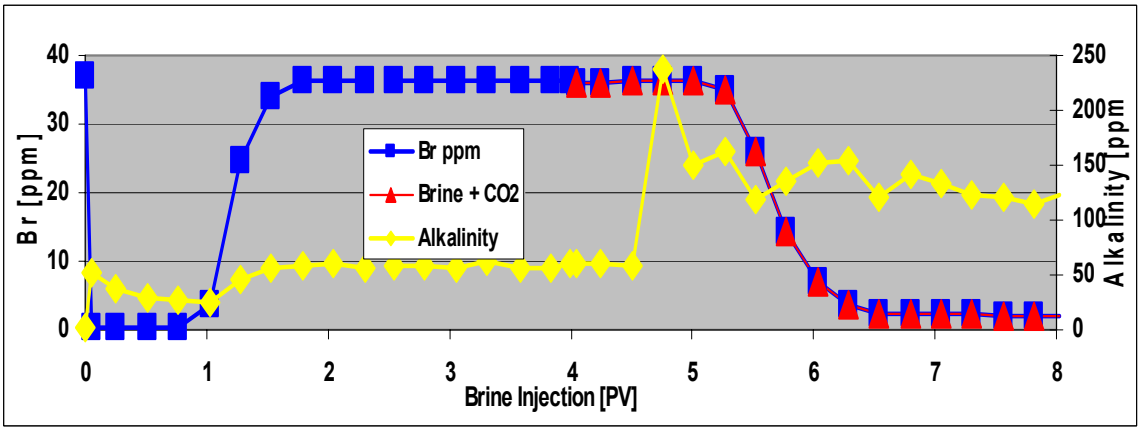

Fig. 188. Bromide diffusivity and alkalinity results (dolomite Coreflood E).

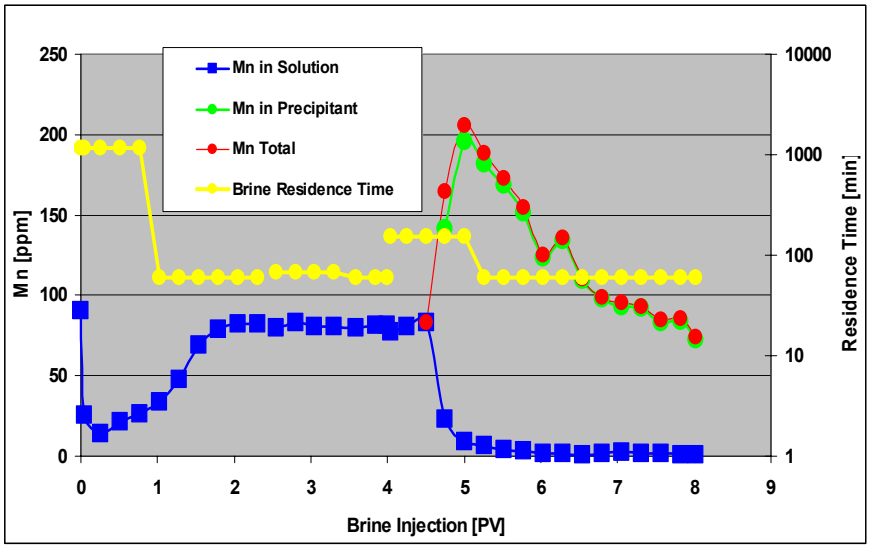

Fig. 189. Manganese concentration in the effluent (dolomite Coreflood E).

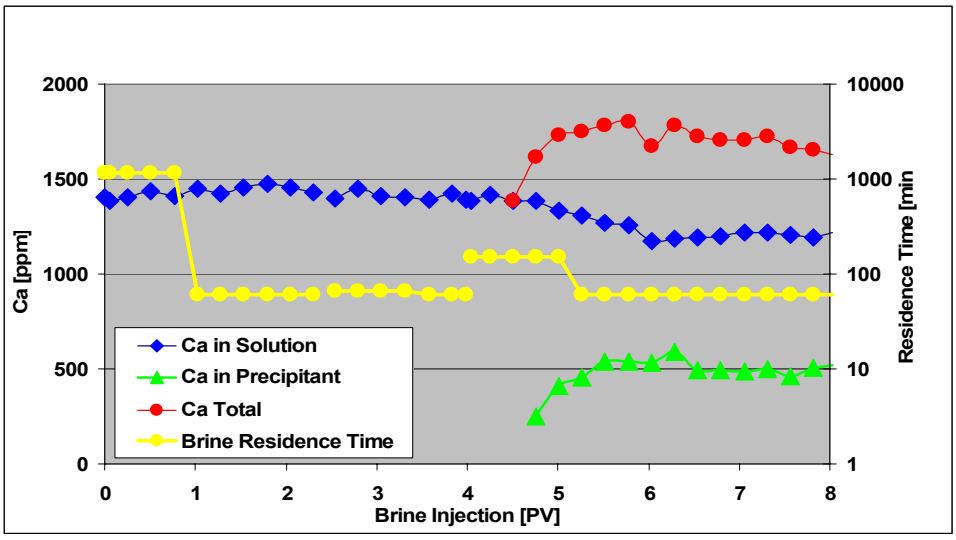

Fig. 190. Calcium concentration in the effluent (dolomite Coreflood E).

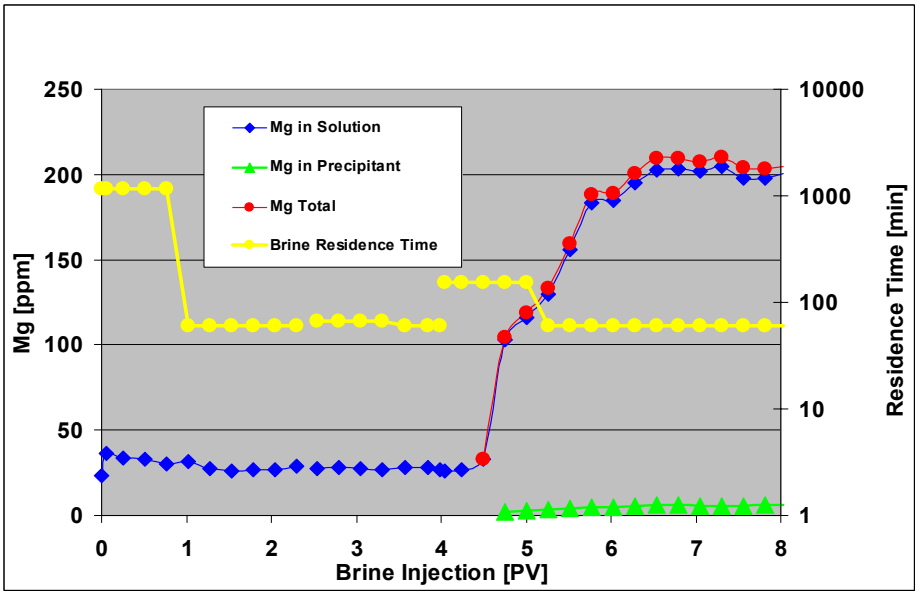

Fig. 191. Magnesium concentration in the effluent (dolomite Coreflood E).

C.4. CO_2 – Indiana Limestone Reaction

Purpose

An experiment was performed to determine the effects of injected deionized water and CO_2 on Indiana limestone. Since dissolving CO_2 into water creates carbonic acid, the lowering of pore fluid pH potentially can change reservoir porosity and permeability. This was the first in a series of experiments designed to identify an optimal injection scheme; measuring porosity and permeability of the reservoir rock during the injection of CO_2 is necessary to determine whether dissolution of reservoir rock or precipitation of minerals are driving factors during the injection process.

To identify the changes in porosity, permeability, and fluid chemistry, deionized water and CO_2 were injected through Indiana limestone (geologically, Mississippian Salem Formation limestone), and the cores were examined for pressure, temperature, and mineralogical changes.

Specimen

Indiana limestone was used since it is homogeneous in texture, structure, and chemistry. The wide availability and previous industry testing of the formation, also makes it an ideal test subject to stand for a clean carbonate reservoir rock. Porosity and density for this rock are about 0.15 and 2.23 g/cm^3, respectively. Individual specimens were measured for porosity, density, length, diameter, and mass prior to testing.

Reservoir Variables

To simulate conditions found in the Williston Basin, the Stadium Field Lodgepole Pool was selected since it is a carbonate reservoir with the potential of CO_2 injection testing (values averaged from NDIC well files for wells 14307, 14212, and 14213). For all laboratory tests the following variables were held constant:

1. Initial Field Fluid Pressure: 4,100 psia
2. Lab Fluid Pressure 3,700 psia (pump limit)
3. Average Depth: 10,500 measured ft (8150 ft MSL)
4. Density: 2.3 to 2.7 g/cm^3
5. Overburden Pressure: 10,400 to 12,300 psia
6. Lab Confining Pressure: 4900 psia (coreholder limit)

7. Temperature: 220° F

Injection Fluids

The fluids to be injected into the specimen were deionized water and CO_2. The first case was simplified to measure the total dissolved solids by evaporation methods without chemical analysis. Later tests required more analysis on the effluent chemistry.

Injection Scheme

The specimen was subjected to Water-Alternating-Gas (WAG) injection, where the injection fluid is alternated between deionized water and CO_2 in a 1 : 1 volumetric ratio. After the specimen was saturated with deionized water, 100 ml of CO_2 was injected, followed by 100 ml of deionized water. A total of five such WAG cycles were injected. This WAG scheme was selected to limit water blocking problems and to increase sweep efficiency in petroleum reservoirs.[158] Because no hydrocarbon component was in the specimen in this test, only the changes among porosity, permeability, and effluent chemistry was observed.

Flow Rate

To simplify the reservoir to be modeled, the following assumptions were made:

(1) The reservoir behaves homogeneously.
(2) The reservoir thickness is constant and is perforated across the entire thickness.
(3) Gravity separation and viscous fingering of the injection fluid does not occur.

The following parameters are required to calculate flow rate for laboratory experimentation.

(1) h: height of reservoir (feet)
(2) r: distance of model from well bore center (feet)
(3) V_{field}: surface injection rate (bbl/month)

The calculation for specimen flow rate ($V_{lab,}$ ml/min) in the laboratory is given by:

$$V_{out}\left(ml/\min\right) = \frac{3.19467\times10^{-3}}{rh} V_{in}\left(bbl/month\right)$$

This formula was scaled to a core specimen 1 in. in diameter; the final unit is ml/min, assuming that the injected fluid expands in all directions in the shape of a cylinder of a constant height, which is equal to the thickness of the formation. Current injection rates for the Stadium field are 175,000 bbl/month of formation water (NDIC well 14212). A range of injection rates is necessary to model possible future conditions that may be encountered.

A height of 50 ft and an injection rate of 175,000 bbl/month were assumed. Table 46 shows the flow rate for different radii:

Table 46. Flow Rate Calculation

Radius (ft)	Flow rate (ml/min)
1	11.18
5	2.24
10	1.12
50	0.22
100	0.11
500	0.022
1000	0.011

The flow rate is sensitive to the rate of injection and the position being modeled in the reservoir. To limit the variables in the experiment, a single flow rate was selected for the injection schemes of 1.0 ml/min to allow for field similarity and probable dissolution observation.

Injection Duration

Carbon dioxide injection into reservoirs is scheduled on the order of years to tens of years, but in the laboratory it is not possible to reproduce this time frame is not possible. For the preliminary experiment the length of injection was the total time for five WAG cycles at 1.0 ml/min (1000 min). To facilitate the extrapolation of time from laboratory scaled experiments, future experiments will be required. Several durations will be needed to be used and then reevaluated to determine if longer durations are necessary to provide predictive results. Future injection periods will be 1, 2, and 4 weeks for each experimental set of conditions.

Effluent Fluid

The fluid discharged from the BPR was collected and evaporated to measure for TDS.

Equipment and Materials

Acoustic Velocity Coreholder and Injection setup

(1) Effluent Collection
(2) Indiana Limestone
(3) Deionized water
(4) Carbon dioxide

Procedures

(1) Load specimen into acoustic velocity core holder.
(2) Set back pressure regulator to reservoir fluid pressure.
(3) Load confining and fluid pressures.
(4) Start data acquisition program and follow steps to set temperature and monitoring interval.
(5) Allow temperature to stabilize (about 19 hours).
(6) Start injection fluid at specified flow rate.
(7) Monitor system and refill injection pump as needed.
(8) Monitor effluent collection and take 25 ml samples as available.
(9) Allow specified time to elapse.
(10) Stop injection pump and confining pressure pump.
(11) Release pressure from system.
(12) Make final measurements of effluent water.
(13) Remove specimen from core holder.
(14) Flush system with deionized water to remove carbon dioxide.
(15) Measure mass, porosity, density, length, and diameter of specimen.

Experimental Runs

Indiana limestone with WAG 1:1 injection at 1.0 ml/min for 1000 ml

Total injection time: 17 hours

Observed Results

Sample: ILA0507

(1) Length: 42.48 mm

(2) Diameter: 24.73 mm

(3) Starting Mass: 46.437 g

(4) Starting Bulk Density: 2.276 g/cm^3

(5) Ending Mass: 46.052* g

(6) Ending Bulk Density: 2.257* g/cm^3

*The edges of the sample were damaged under confining pressure, not all of the mass difference can be attributed to dissolution.

Table 47. Total Dissolved Solids

	Time	Beaker Empty	Beaker and H2O	Beaker Dried	ml H2O	Concentration mg/L
1	03/10/2008 13:01:47	101.398	125.020	101.408	25	400.0
2	03/10/2008 15:46:22	100.809	125.678	100.833	25	960.0
3	03/10/2008 16:13:22	102.453	127.316	102.465	25	480.0
4	03/10/2008 17:37:22	100.815		100.821	25	240.0
5	03/10/2008 19:11:26	97.234	122.147	97.250	25	640.0
6	03/10/2008 20:06:12	99.605	124.477	99.610	25	200.0
7	03/10/2008 20:21:15	100.811	125.718	100.819	25	320.0
8	03/10/2008 21:35:52	101.401	126.250	101.412	25	440.0
9	03/10/2008 22:36:52	100.809	125.698	100.832	25	920.0
10	03/10/2008 23:16:22	102.451	127.354	102.464	25	520.0
11	03/10/2008 23:53:22	99.603	124.505	99.611	25	320.0
12	03/11/2008 00:30:22	100.813	125.705	100.822	25	360.0
13	03/11/2008 02:00:52	101.422	126.330	101.422	25	0.0
14	03/11/2008 02:31:22	100.807	125.712	100.821	25	560.0
15	03/11/2008 03:15:22	99.595	124.375	99.609	25	560.0
16	03/11/2008 03:38:37	102.449	127.322	102.464	25	600.0
17	03/11/2008 05:29:28	100.812	125.727	100.835	25	920.0
18	03/11/2008 05:54:02	101.399	126.318	101.416	25	680.0
19	03/11/2008 06:15:22	97.231	122.143	97.243	25	480.0

The color-blocked lines are suspect. The actual time of line 4 is estimated, due to a clerical error. Line 13 is attributed to heat effect and that the salts found in the beaker were not properly measured.

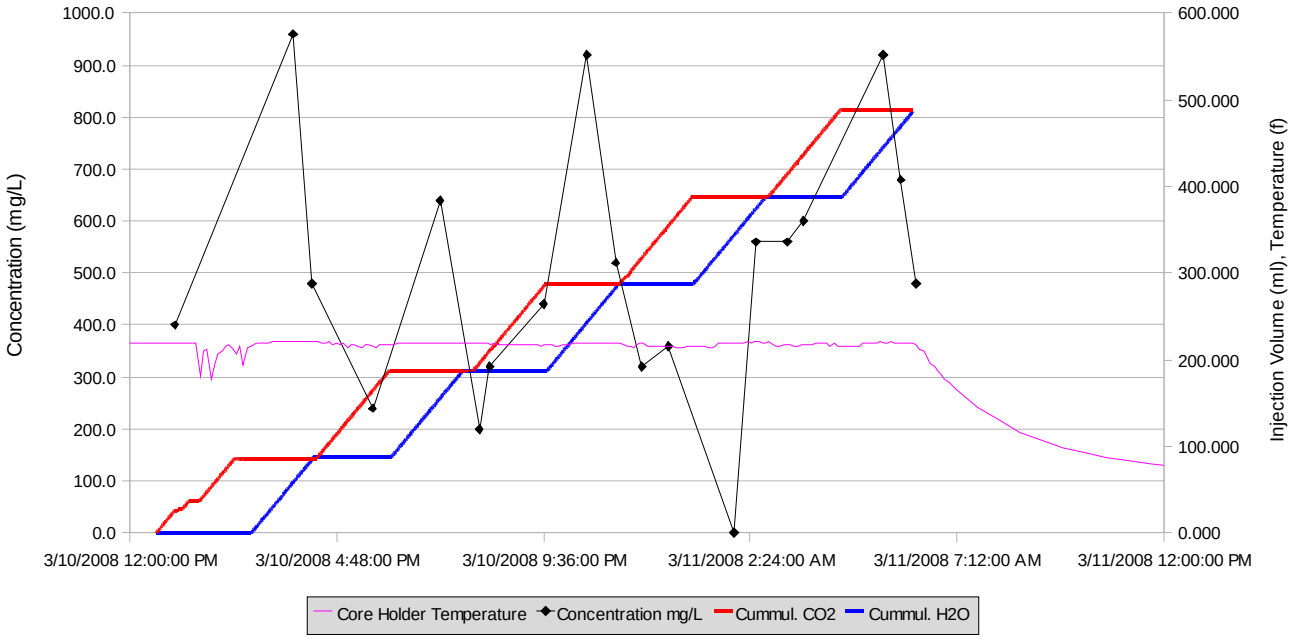

Fig. 192. Graph of TDS concentrations, WAG cycles, and temperature. Suspect points are circled. Temperature is most variable during carbon dioxide injection. This may be caused by the carbon dioxide expanding into the core plug, which would cause a cooling effect.

Acoustic Wave Propagation during Injection

During the experiment the velocity of P, S1, and S2 waves were measured. The following is a graph of the results during the injection. Higher variability is observed when carbon dioxide saturation and flooding occur. More stability is observed when deionized water saturation and flooding occur. Some of this may be attributed to the temperature effect of the expanding carbon dioxide in to the core sample causing cooling as also seen in the temperature log.

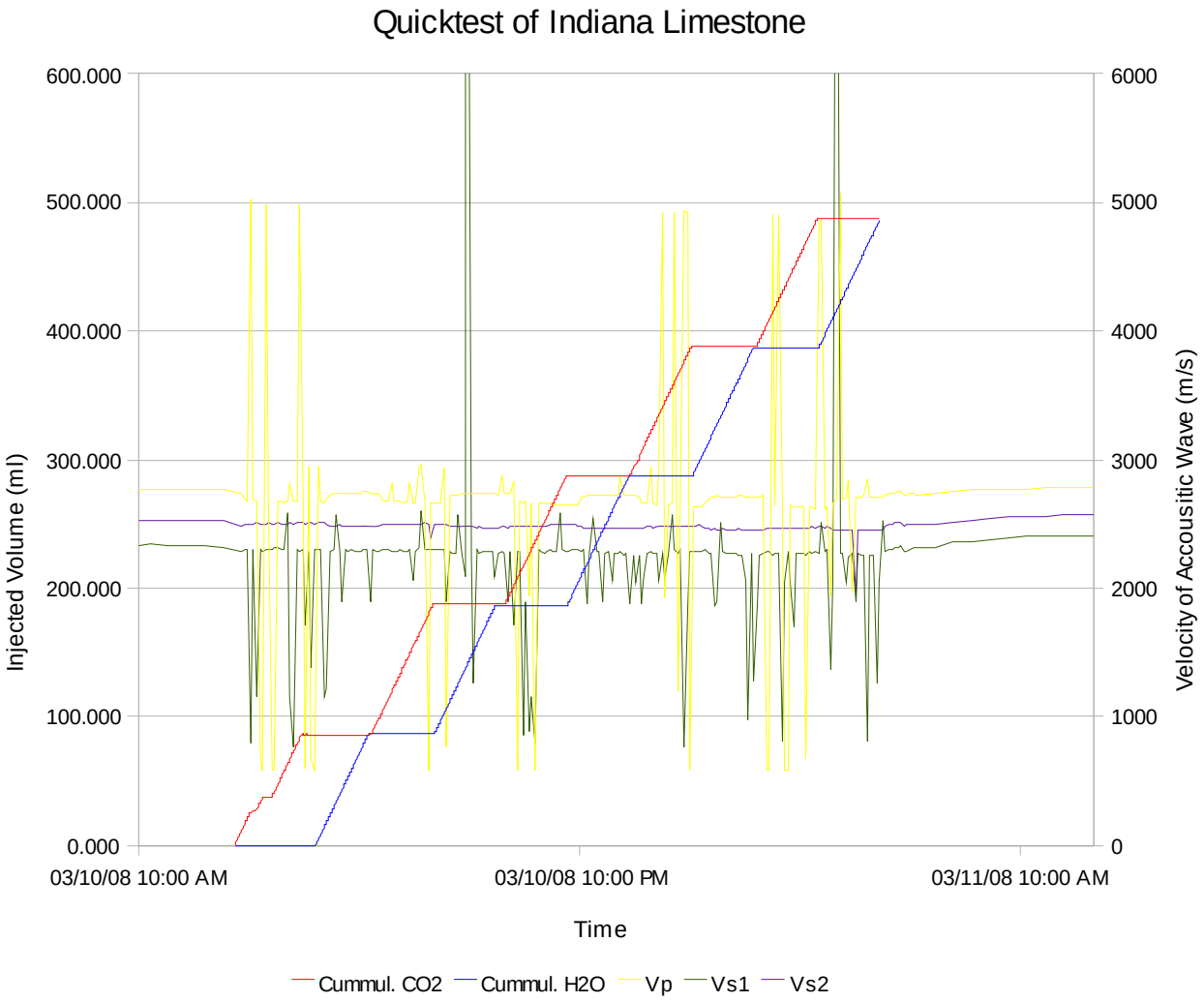

Fig. 193. Pressure, temperature graph for experiment.

The variability in the green and gray lines represent the times when the pressure was maintained manually during water injection. Future experiments will not require manual control and should result in a more constant line. The pressure is shown higher than 4900 psi due to calibration error with pressure transducers. Pump controls were corrected for temperature fluctuation in the room and are deemed more reliable. Temperature fluctuations correspond to CO_2 injection and were discussed previously. Injection, core in, and core out correspond well

and large fluctuations are due to line icing or back-pressure-regulator temperature change. This will need to be controlled better in the future to remove the possibility of pressure change to affect injection experiments.

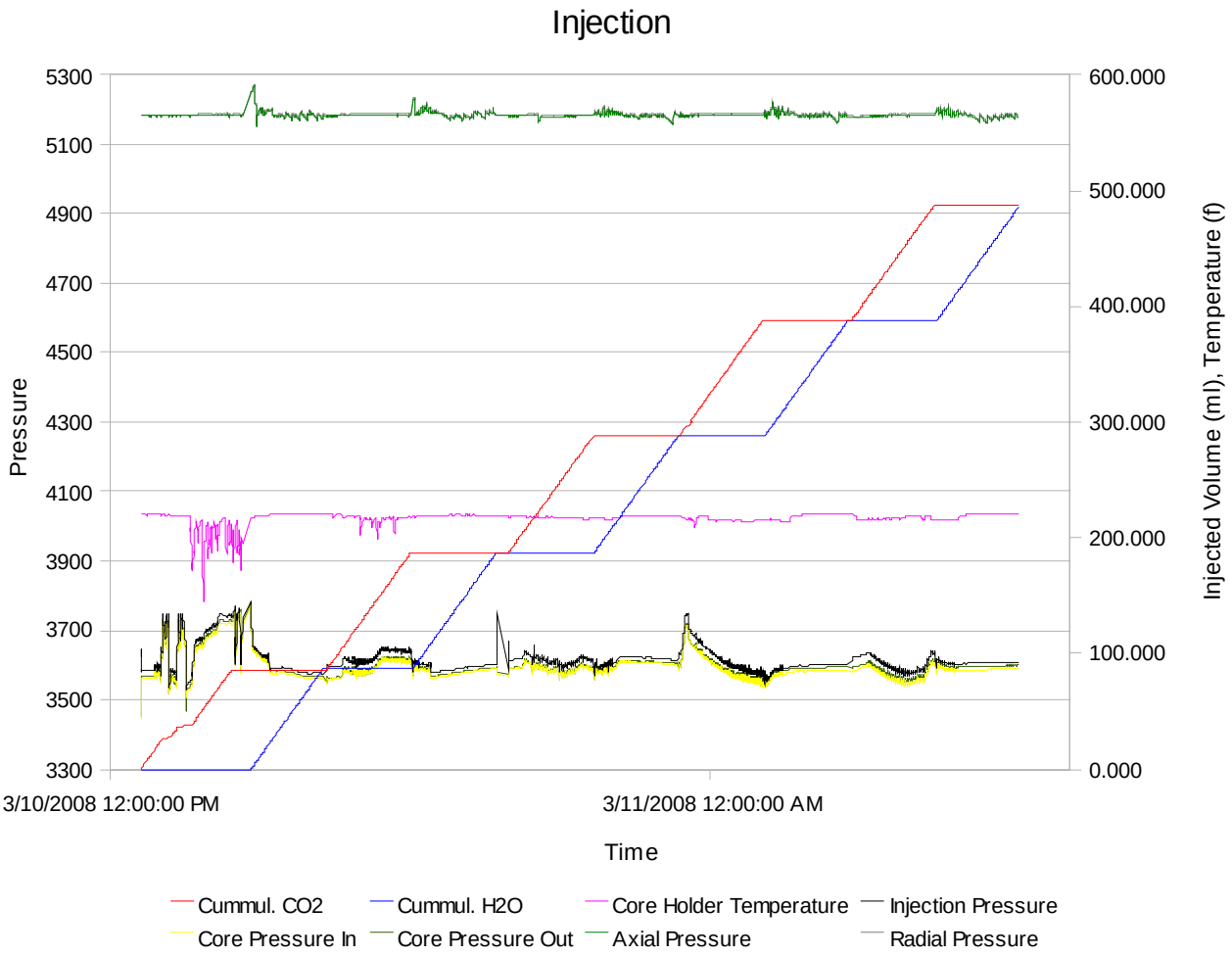

Fig. 194. Positron emission tomography before injection.

Photon Emission Tomography (PET) uses photons from a radioactive germanium source to scan a sample. The detectors pick up the original signal as well as refracted or reflected signals. Brighter colors denote less dense material by a stronger radioactive signal passing through the sample. The before and after images presented are longitudinal slices of the core sample. The core sample shows up in frames 48 through 81 on each picture. After the injection

of the fluid, the PET scanner found the sample to be less dense, but the resolution does not allow for the identification of a preferential flow path.

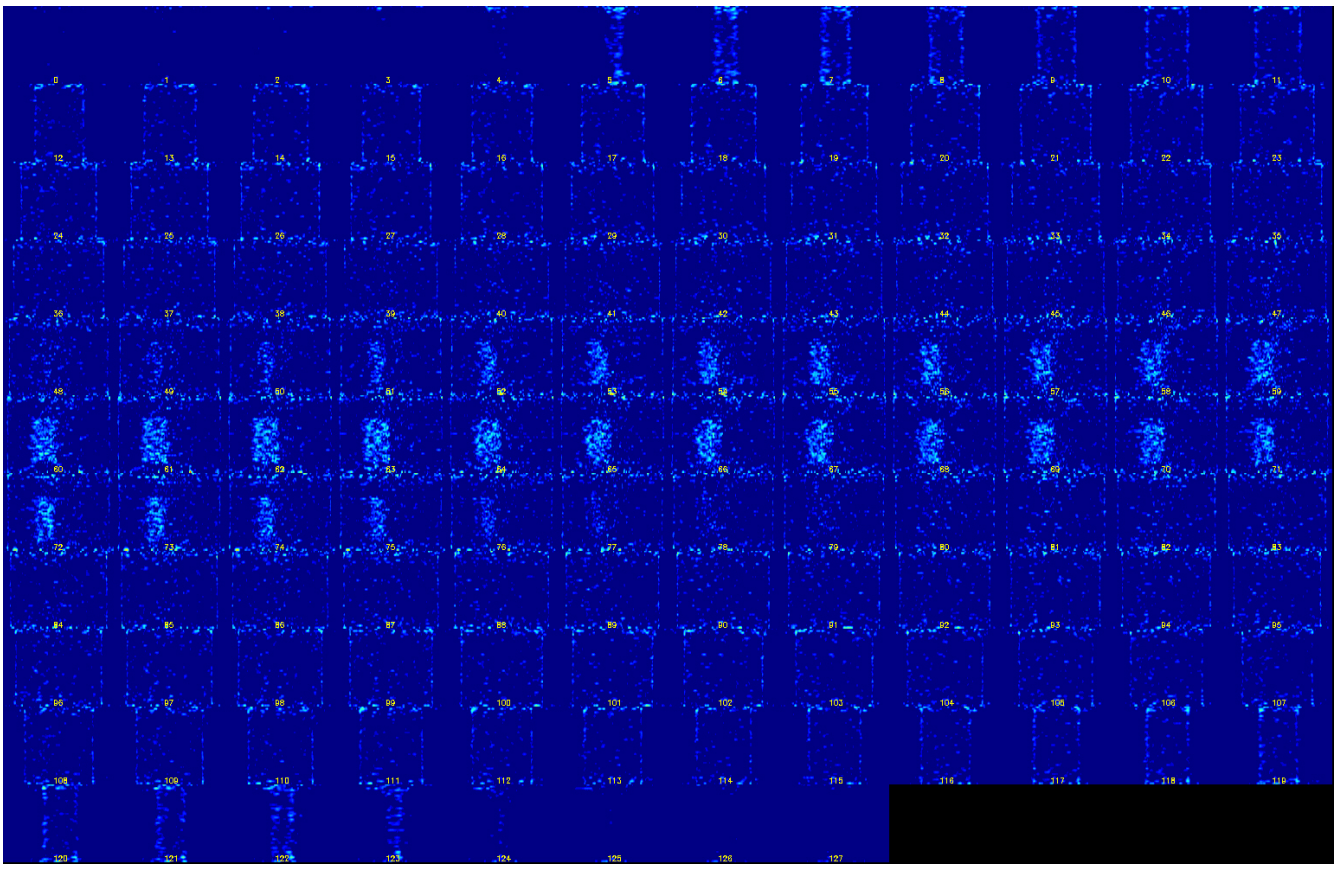

Fig. 195. After injection.

Conclusions and Recommendations

After completing this preliminary experiment, the sample had portions of visibly dissolved areas on the injection side of the specimen. This is a strong evidence of CO_2-rock reaction for a WAG experiment of such short duration. The most reactive periods, as shown by the TDS, were during the switch between the CO_2 and deionized water. Changing the injection scheme to larger

quantities to mimic field scale dimensions may not allow for great changes to be observed in a short time frame, but this exploratory experiment proves that dissolution takes place in the Indiana limestone and it can be observed with petroleum engineering laboratory equipment. More experimentation is required to make any further conclusions on the change in porosity and permeability in Indiana limestone due to CO_2 injection.

Future Recommendations

(1) Use a heating mechanism to reduce line icing.
(2) Use a larger pressure vessel to preload pressurized CO_2 into the injection pump.
(3) Use a larger pressure reservoir to limit fluctuations to back-pressure-regulator temperature changes.
(4) Use a mass viton sleeve and sample together to reduce mass loss due to specimen corner breakage.
(5) Use a conductivity/TDS/ion/pH meter to measure effluent in real time.

C.4. Experimental Investigation of Stress- and Phase-Sensitivities of Non-Darcy Flow Parameters

Introduction

Reservoir performance is influenced by reservoir pressure change. This performance change is attributed to effective permeability alteration and fluid phase transition. Effective permeability changes significantly in stress-sensitive reservoirs. Fluid phase transition occurs when reservoir pressure and temperature change near the critical point of the fluid. Non-Darcy flow behavior occurs at high flow rates, which normally only occur in the near-wellbore region, in gas wells. A way to quantify the effects of stress- and phase-sensitivities on reservoir performance under non-Darcy flow conditions requires additional investigation.

This section presents experimental results of non-Darcy flow parameters, i.e. permeability, k, and non-Darcy coefficient, β, in several representative rock samples under typical reservoir pressure and temperature conditions. Based on these experimental measurements and calculations, the following are investigated: (1) changes of non-Darcy flow parameters with average effective stress, (2) development of general stress sensitivity functions for non-Darcy flow parameters, and (3) comparison of non-Darcy flow parameters of nitrogen (N_2) and carbon dioxide (CO_2) to address the phase sensitivity phenomena.

Background

Petroleum reservoir formations are subject to tectonic, structural, gravitational and geothermal activities. Total in-situ stress is the combination of all these components, and is usually considered as constant during the time period of reservoir production. It is distributed onto both rock matrix and pore fluids. Stress on the matrix is effective stress and stress on the fluids is pore pressure. When fluids are produced from or injected into the reservoir, the pore pressure changes. This causes the effective stress to change in the opposite direction. Change in the effective stress will modify the rock matrix and pore structures, and thereby the porosity and effective permeability.

Previous studies indicate that the change in effective permeability is dependent on a number of factors. McLatchie et al.[159] found that effective compressibility is rock-dependent: sandstones with high clay and fine mineral content have much higher compressibility than limestone. Gray et al.[160] experimentally showed that permeability reduction is a function of the ratio of radial to

axial stresses. Wyble[161] proposed a general exponential equation to relate the change of rock properties to the change of stress; Evers and Soeiinah[162] modified this equation by substituting stress with pressure. Based on results of compressibility and flow tests of more than 100 tight gas sandstone samples from five different formations, Jones and Owens[163] found that confining pressure can reduce permeability at varied scales, depending on the permeability and rock type. Holt[164] investigated the permeability reduction of high porosity/high permeability sandstone under both hydrostatic and non-hydrostatic in-situ stress conditions, and found that non-hydrostatic stresses cause a greater change in permeability; Rhett and Teufel[165] further found that the reduction of permeability and porosity are loading path-dependent. It has been observed that some formations, such as the tight Mesa Verde formation in northwestern Colorado,[166] the naturally fractured Spraberry formation of west Texas,[167] and the high-porosity, high-permeability Ekofisk reservoirs of the North Sea,[168] are more sensitive to stress change than are others. Lorenz [169]provided a good review of these types of stress-sensitive reservoirs. Numerical simulation of these reservoirs needs generally defined stress sensitivity functions to describe permeability change with reservoir conditions,[170]

Stress sensitivity is conventionally investigated under Darcy flow conditions.[160,171] But non-Darcy behavior has significant influences on well performance, especially at the near-wellbore region in both production and injection gas wells,[172] Example field data show superficial velocity of CO_2 at the near-wellbore region varying from 21 ft/day to 1170 ft/day,[173] For a typical low permeability Indiana limestone at 100°F and 1500 psig, this velocity corresponds to a Forchheimer number of 3.11, much higher than the proposed critical value of 0.1 for significant non-Darcy effect,[174] Many studies have addressed the determination of non-Darcy flow parameters, the physical meaning of non-Darcy coefficient, and possible correlations between permeability and non-Darcy coefficient,[175,176] Some numerical simulations have included the non-Darcy effect,[177] In fact, non-Darcy flow parameters are also stress-sensitive. Ramey[178] and Wattenbarger and Ramey[179] proved that non-Darcy flow has significant effect on gas flow behavior, and is loading-path dependent. Vairogs and Rhoades[180] confirmed the differences of the permeability derived from drawdown and buildup tests, and showed that the stress sensitivity effect is higher in low permeability formations. Several studies have investigated the influence of overburden stress on the non-Darcy coefficient,[181,182] In a recent study, Zeng et al,[183] found linear correlations between non-Darcy flow parameters and octahedral, i.e., average effective stress

based on experimental results from a Dakota sandstone under hydrostatic in-situ stress state at 100°F and core outlet at 500 psig. Whether similar correlations exist in other rocks and other reservoir conditions deserves further investigation.

Theoretically, permeability can be measured using any nonreactive fluid. However, the flow behaviors of hydrogen, nitrogen and carbon dioxide are different under intermediate pressures, while at high pressure they merge to the same permeability, i.e., the same liquid permeability, by the Klinkenberg method,[184] Wei et al.[185] found marked reduction in permeability of tight-gas sandstones with the change of fluids from gas to liquid. This phase-dependent behavior deserves further investigation under non-Darcy flow conditions.

Experimental

In order to represent typical reservoir conditions in the experiment, a survey was conducted concerning the status of active CO_2 flooding projects.[173,186] Based on the survey and laboratory capabilities, five different rocks were selected: low permeability Dakota sandstone (DS), low permeability Indiana limestone (ILL), high permeability Indiana limestone (ILH), low permeability Berea sandstone (BSL), and high permeability Berea sandstone (BSH). These were tested under the experimental conditions shown in Table 48.[173,187] In total, 193 series of high pressure, high temperature, high velocity (HP/HT/HV) fluid flow experiments were conducted at different combinations of in-situ stress, temperature, pore pressure, core sample and injected fluid, as summarized in Table 49. Additional details of the experiments have been given elsewhere. [173,187,188]

Table 48. Selected Experimental Conditions

Parameter	Value
Overburden pressure	2000 ~10000 psig
Axial stress	2000 ~10000 psig
Radial stress	2000 ~10000 psig
Inlet back pressure	2000 ~ 2500 psig
Outlet back pressure	500 ~ 1500 psig
Temperature	100 ~ 200° F
Flow rate at pump (80°F, 2000 psig)	25 ~10000 cc/hour
Superficial velocity in core	4 ~ 6775 ft/day
Sample size	1-in diameter by 2-in length
Sample permeability	1~1000 mD

Table 49. Test Conditions for Each Sample

Rock Type	Fluid	Temperature, °F	Stress, psig	Core effluent pressure, p_2 psig	Tests
DS	N_2	100, 150 200	2000~10000	500	78
BSL	N_2	100, 150 200	2000~10000	500	15
BSH	N_2	100, 150 200	2000~10000	500	15
ILL	N_2	100, 150, 200	2000~10000	500	15
ILH	N_2	100	2000~10000	1500	36
ILL	CO_2	100, 150, 200	2000~10000	500, 1000, 1500	34
Total					193

Theory and Formulas for Data Process

Forchheimer's theory[189] is used to calculate the non-Darcy flow parameters k and β. According to Green et al.,[190] the modified Forchheimer's equation can be expressed as:

$$\left(-\frac{dp}{dl}\right)=\frac{\mu}{k}v+\beta\rho v^2 \qquad 63$$

where k is permeability, β is the non-Darcy coefficient, ($-dp/dl$) is the pressure gradient, μ is fluid viscosity, v is superficial fluid velocity, and ρ is fluid density. Using the PVT relationships of a real gas, Eq. 63 can be rewritten as[191]:

$$\frac{M\left(p_1^{\,2}-p_2^{\,2}\right)}{2zRT\mu\, l\left(\frac{W}{A}\right)}=\frac{1}{k}+\beta\left(\frac{W}{\mu A}\right) \qquad 64$$

where M is the molecular weight of the fluid, R is the universal gas constant, l and A are the sample length and cross sectional area, p_1 and p_2 are the pressures at the inlet and outlet of the core sample, T is the sample temperature, W is the mass flow rate, which is the product of the pump volumetric flow rate Q and the fluid density in the accumulator ρ_a obtained from a commercial PVT simulator by inputting the measured pump pressure and temperature, and z and μ are the gas deviation factor and viscosity, respectively. For N_2 experiments, z and μ were calculated using the following correlations:

$$\begin{cases} z_{100}=3\times10^{-5}p+0.9953 & (\mathrm{R}^2=1.00) \\ z_{150}=3\times10^{-5}p+0.9932 & (\mathrm{R}^2=0.99) \\ z_{200}=2\times10^{-5}p+0.9913 & (\mathrm{R}^2=0.98) \end{cases} \qquad 65$$

and

$$\begin{cases} \mu_{100} = 5\times10^{-5}\, p + 0.5928 & (\mathrm{R}^2 = 1.00) \\ \mu_{150} = 5\times10^{-5}\, p + 0.5858 & (\mathrm{R}^2 = 1.00) \\ \mu_{200} = 4\times10^{-5}\, p + 0.5867 & (\mathrm{R}^2 = 1.00) \end{cases} \qquad 66$$

These correlations were based on data generated from a PVT simulator using the Peng-Robinson Equation of State option at temperatures of ı̃°F, 150°F and 200°F, respectively.[173] Using Eqs. 65 and 66, z and μ are calculated at each corresponding pressure and temperature. Values of viscosity were checked against experimental results,[192] and were found to be generally 2 to 4% higher. For CO_2 flow experiments, z and μ were obtained using the PVT simulator with preset sample temperature and measured average pressure, $(p_1 + p_2)/2$. Using the calculated values of z and μ, Eq. 64 has two unknowns, k and β. Thus k and β can be determined using linear regression on a number of tests at various flow rates. Table 50 is an example of the measured and calculated values for a test series on Dakota sandstone at 100°F. The accumulator was 2000 psig, outlet or end pore pressure was 500 psig, and gas density in the accumulator was 0.144 g/cm^3. The plot of "y" (the left hand side of Eq. 64) versus "x" (the multiplier of β) is used to determine k (one over the intercept of y), and β (the slope), as shown in Fig. 196. Following the same procedure, permeability and the non-Darcy coefficient of all the 193 experiments have been determined.[187,188] Table 51 summarizes the k and β with fluid, sample, and temperature as indicated before each group of tests, in which, unless indicated otherwise, the accumulator pressure and outlet pore pressure were 2000 and 500 psig, respectively.

Table 50. Measured and Calculated Values of a DS Test

Q	Δp	W	ρ @ $(p_1+P_2)/2$	z	μ	x	y
cc/hr	psig	g/hr	g/cm^3		cP	100/cm	1/Darcy
25	2	3.6	0.0364	1.0026	0.0186	0.01	294
100	9	14.4	0.0367	1.0026	0.0186	0.04	287
400	37	57.6	0.0381	1.0028	0.0186	0.17	318
600	58	86.5	0.0390	1.0029	0.0186	0.25	341
1000	103	144	0.0408	1.0032	0.0187	0.42	381
2000	227	288	0.0457	1.0039	0.0187	0.84	468
4000	500	576	0.0560	1.0054	0.0189	1.67	628
5000	635	720	0.0610	1.0061	0.0190	2.08	692
6000	771	864	0.0661	1.0068	0.0191	2.48	755
7000	905	1008	0.0711	1.0076	0.0191	2.89	814
8000	1040	1152	0.0760	1.0083	0.0192	3.28	872
9000	1171	1296	0.0809	1.0090	0.0193	3.68	925
10000	1201	1440	0.0856	1.0097	0.0194	4.07	975

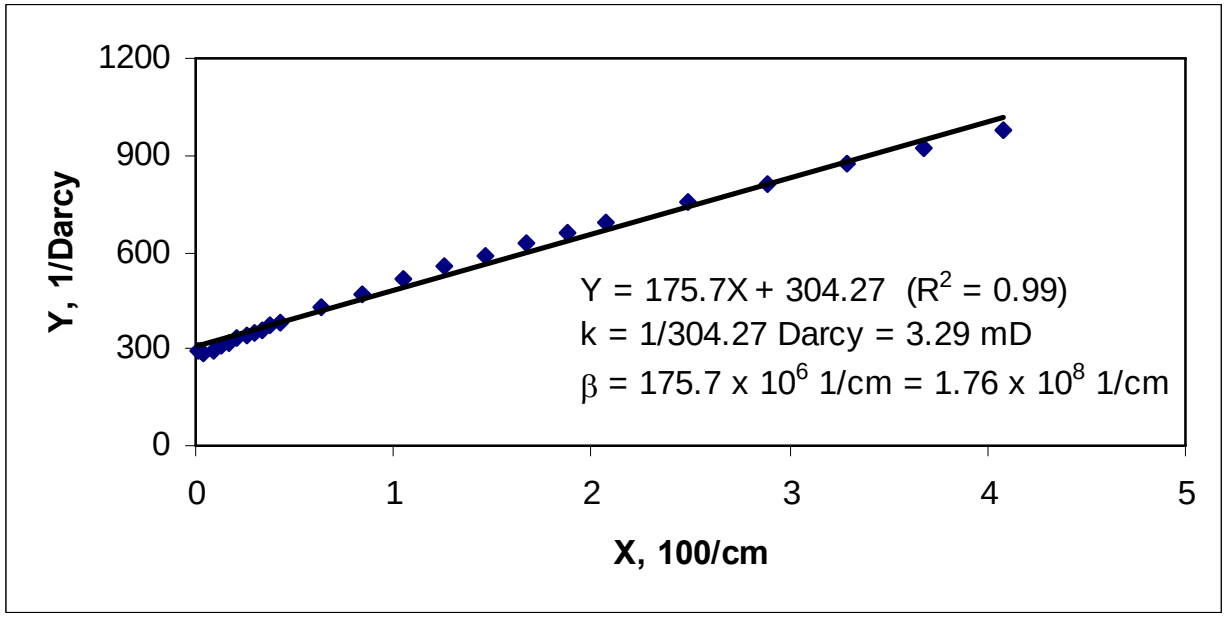

Fig. 196. Determining k and β of the test shown in Table 48.

Table 51. Summary of k and β for All 193 Series of Tests

Tests	σ_a	σ_r	σ_{eff}	τ	k	β
	Psig	psig	psig	psig	mD	10^6/cm
N_2, DS, 100˚F						
1~9	2000~10000	2000~10000	1193~9161	0	3.07~3.44	155.51~195.94
10~33	2000~10000	2000~10000	1847~7856	471~3771	3.07~3.33	162.91~198.00
N_2, DS, 150˚F						
34~42	2000~10000	2000~10000	1179~9126	0	3.01~3.25	177.87~226.72
N_2, DS, 150˚F						
43~62	2000~10000	2000~10000	1831~8462	943~3771	3.03~3.34	103.28~231.87
N_2, DS, 200˚F						
63~66	2000~10000	2000~10000	986~9080	0	2.93~3.21	202.25~245.98
67~78	2000~10000	2000~10000	1756~8395	942~3771	2.95~3.14	213.11~260.76
N_2, BSL, 100˚F						
79~83	2000~10000	2000~10000	1450~9453	0	198.85~215.55	2.67~2.88
N_2, BSL, 150˚F						
84~88	2000~10000	2000~10000	1449~9446	0	173.97~196.49	2.95~3.20
N_2, BSL, 200˚F						
89~93	2000~10000	2000~10000	1420~9404	0	154.15~176.43	3.29~3.49
N_2, BSH, 100˚F						
94~98	2000~10000	2000~10000	1463~9463	0	879.28~1133.79	1.02~1.34
N_2, BSH, 150˚F						
99~103	2000~10000	2000~10000	1451~9448	0	666.40~834.10	1.67~1.91
N_2, BSH, 200˚F						
104~108	2000~10000	2000~10000	1454~9455	0	529.38~682.31	1.57~2.55
N_2, ILL, 100˚F						
109~113	2000~10000	2000~10000	1342~9328	0	20.34~22.14	36.00~40.50
N_2, ILL, 150˚F						
114~118	2000~10000	2000~10000	1377~9345	0	17.91~19.71	40.84~47.04
N_2, ILL, 200˚F						
119~123	2000~10000	2000~10000	1333~9315	0	15.42~17.20	43.74~48.71
N_2, ILH, 100˚F						
124~144	1000~6000	2000~10000	1074~8045	236~4243	56.23~93.91	18.48~42.14
N_2, ILH, 100˚F, 2500 psig, 1500 psig						
145~159	2000~6000	6000~10000	3085~7086	942~3771	63.67~81.49	21.93~25.38
CO_2, ILL, 100˚F, 2500 psig, 1500 psig						
160~169	6000~10000	2000~8000	1690~6928	942~3771	22.01~25.01	33.19~44.06
CO_2, ILH, 100˚F						
170~179	4000~10000	2000~6000	2034~6696	943~3771	12.17~13.77	36.82~41.95
CO_2, ILL, 150˚F						
180~185	6000~8000	2000~6000	2675~6001	943~2828	12.50~14.61	37.06~46.04
CO_2, ILL, 200˚F						
186~191	6000~8000	2000~6000	2666~5997	943~2828	12.66~15.43	45.27~50.74
CO_2, ILL, 100˚F, 2000 psig, 1000 psig						
192~193	4000~6000	2000~4000	Incomplete due to cooling effect.			

Analysis of Stress Sensitivity

Calculation of Stresses

Stress sensitivity of non-Darcy flow parameters results from a change in rock matrix and pore structure. The pore structure changes via two mechanisms of deformation: compression (or dilatation) and distortion. Compression and dilatation refers to uniform expansion and shrinkage where the bulk volume is changed while the shape is unchanged; in contrast, distortion refers to deformations that result in shape change while the volume is constant. According to solid mechanics, compression and dilatation are proportional to average normal stress, which is equal to octahedral normal stress; similarly, distortion depends on octahedral shear stress.[193,194]

In a petroleum reservoir, formations are subjected to three-dimensional, compressive in-situ stresses coupled with pore pressure generated from fluids in the void spaces. In this case, the compressive or dilatational deformation is proportional to the octahedral effective normal stress, which equals the difference between the octahedral normal stress and the pore pressure. The distortion is proportional to the octahedral shear stresses.[195]

Using the same equations defined in a previous paper,[183] octahedral effective normal stress (effective stress hereafter unless otherwise specified), σ_{eff}, and octahedral shear stress (shear stress hereafter unless otherwise specified), τ, are calculated as:

$$\begin{cases} \sigma_{eff} = \dfrac{1}{3}(\sigma_{1eff} + \sigma_{2eff} + \sigma_{3eff}) \\ \tau = \dfrac{\sqrt{(\sigma_{1eff} - \sigma_{2eff})^2 + (\sigma_{2eff} - \sigma_{3eff})^2 + (\sigma_{3eff} - \sigma_{1eff})^2}}{3} \end{cases} \qquad 67$$

where σ_{1eff}, σ_{2eff}, and σ_{3eff} are the maximum, intermediate, and minimum effective principal stresses. Under the triaxial experimental conditions in this study, σ_{1eff}, σ_{2eff}, and σ_{3eff} are calculated as follows:

$$\begin{cases} \sigma_{1eff} = \max\{\sigma_a - p, \sigma_r - p\} \\ \sigma_{2eff} = \sigma_r - p \\ \sigma_{3eff} = \min\{\sigma_a - p, \sigma_r - p\} \end{cases} \qquad 68$$

where p is the average pore pressure that equals the average of the pore pressures corresponding to the lowest and the highest flow rates in the same series of experiments. Values of the effective stress and shear stress for each series of experiments were calculated and summarized in Table 51.

Sensitivity to Effective Stress

Based on the results shown in Table 49 and elsewhere,[187,188] stress sensitivity of k and β is analyzed as follows. First is the sensitivity of non-Darcy flow parameters to effective stresses.

In Hydrostatic In-Situ Stress Fields

Experiments conducted under hydrostatic in-situ stress fields are those performed under conditions where the radial stress equals the axial stress. Figures 197 and 198 show the influence of effective stress on permeability, $k(\sigma_{eff})$, and non-Darcy coefficient, $\beta(\sigma_{eff})$ at three temperatures: 100°F, 150°F and 200°F in four different rock samples (Table 51: Tests 1–9, 34–42, 63–66 for DS; Tests 79–93 for BSL; Tests 94–108 for BSH; and Tests 109–123 for ILL).

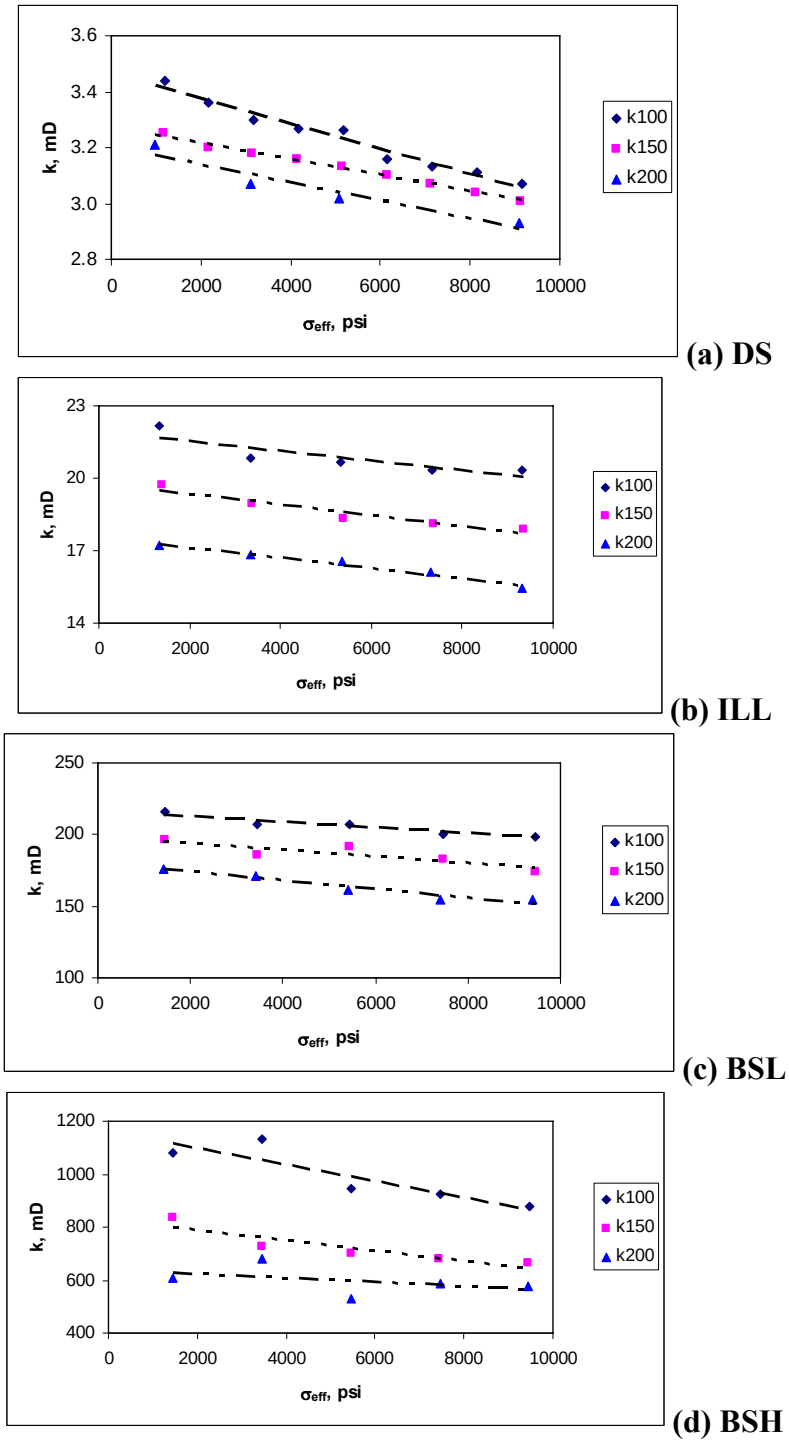

Fig. 197. Comparison of σ_{eff} vs. k under hydrostatic in-situ stress fields at 100°F, 150°F and 200°F in four different rocks.

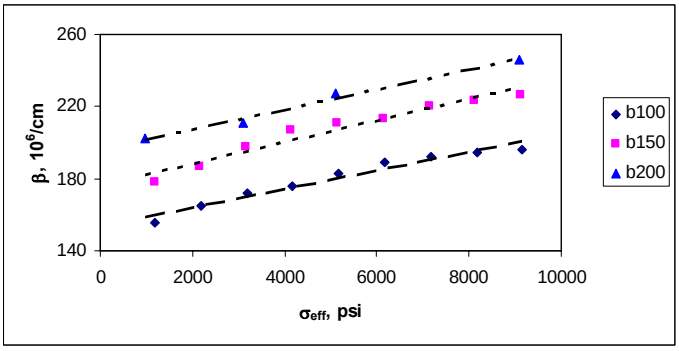

(a) DS

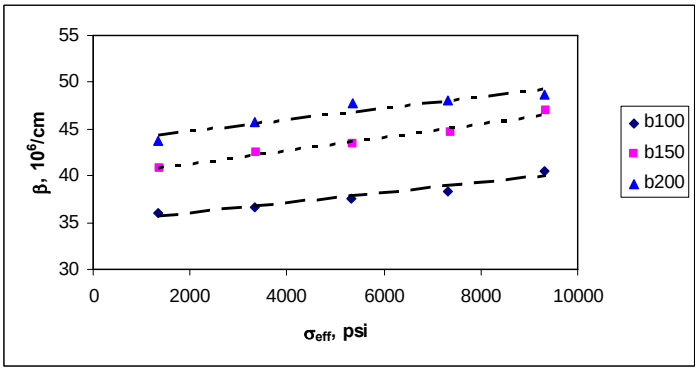

(b) ILL

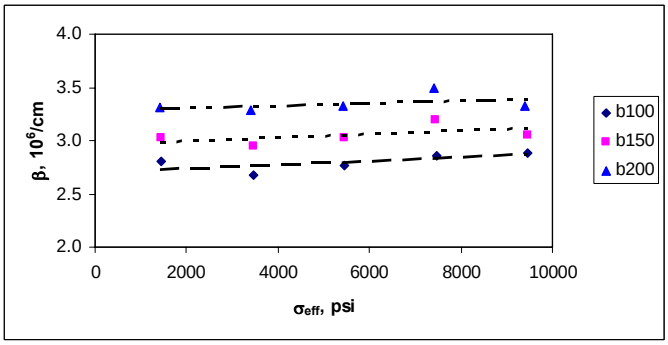

(c) BSL

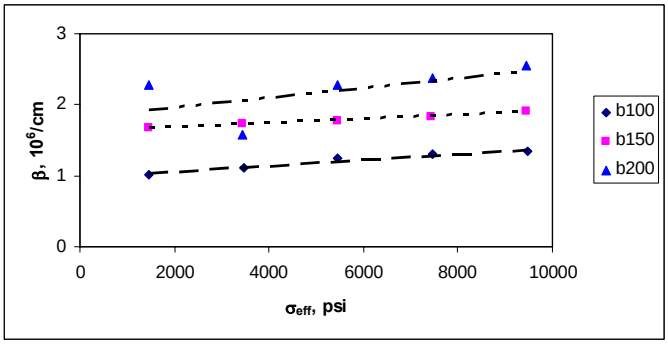

(d) BSH

Fig. 198. Comparison of σeff vs. β under hydrostatic in-situ stress fields at 100°F, 150°F and 200°F in four different rock samples.

The permeability decreased while the non-Darcy coefficient increased linearly with the effective stresses for all three temperatures and four rock samples. Also, under the same effective stress, permeability decreased while the non-Darcy coefficient increased with temperature. The above linear change of k and β with σ_{eff} are quantitatively correlated as follows:

(1) Dakota sandstone, DS:

$$\begin{cases} k_{100} = -4.48\times10^{-5}\sigma_{eff} + 3.47 & (R^2 = 0.97) \\ k_{150} = -2.88\times10^{-5}\sigma_{eff} + 3.27 & (R^2 = 0.99) \\ k_{200} = -3.26\times10^{-5}\sigma_{eff} + 3.21 & (R^2 = 0.92) \end{cases} \quad 69$$

$$\begin{cases} \beta_{100} = 5.10\times10^{-3}\sigma_{eff} + 154.06 & (R^2 = 0.95) \\ \beta_{150} = 5.96\times10^{-3}\sigma_{eff} + 176.41 & (R^2 = 0.95) \\ \beta_{200} = 5.57\times10^{-3}\sigma_{eff} + 196.12 & (R^2 = 0.99) \end{cases} \quad 70$$

(2) Low permeability Indiana limestone, ILL:

$$\begin{cases} k_{100} = -2.03\times10^{-4}\sigma_{eff} + 21.95 & (R^2 = 0.75) \\ k_{150} = -2.22\times10^{-4}\sigma_{eff} + 19.80 & (R^2 = 0.92) \\ k_{200} = -2.13\times10^{-4}\sigma_{eff} + 17.56 & (R^2 = 0.96) \end{cases} \quad 71$$

$$\begin{cases} \beta_{100} = 5.39\times10^{-4}\sigma_{eff} + 34.93 & (R^2 = 0.94) \\ \beta_{150} = 7.29\times10^{-4}\sigma_{eff} + 39.76 & (R^2 = 0.97) \\ \beta_{200} = 6.14\times10^{-4}\sigma_{eff} + 43.54 & (R^2 = 0.91) \end{cases} \quad 72$$

(3) Low permeability Berea sandstone, BSL:

$$\begin{cases} k_{100} = -1.99\times10^{-3}\sigma_{eff} + 216.77 & (R^2 = 0.92) \\ k_{150} = -2.40\times10^{-3}\sigma_{eff} + 199.25 & (R^2 = 0.78) \\ k_{200} = -3.08\times10^{-3}\sigma_{eff} + 180.25 & (R^2 = 0.94) \end{cases} \quad 73$$

$$\begin{cases} \beta_{100} = 1.75\times10^{-5}\sigma_{eff} + 2.70 & (R^2 = 0.43) \\ \beta_{150} = 1.55\times10^{-5}\sigma_{eff} + 2.97 & (R^2 = 0.28) \\ \beta_{200} = 1.10\times10^{-5}\sigma_{eff} + 3.29 & (R^2 = 0.19) \end{cases} \quad 74$$

(4) High permeability Berea sandstone, BSH:

$$\begin{cases} k_{100} = -3.05\times10^{-2}\sigma_{eff} + 1158.64 & (R^2 = 0.78) \\ k_{150} = -1.91\times10^{-2}\sigma_{eff} + 826.13 & (R^2 = 0.82) \\ k_{200} = -0.78\times10^{-2}\sigma_{eff} + 639.52 & (R^2 = 0.20) \end{cases} \quad 75$$

$$\begin{cases} \beta_{100} = 4.10\times10^{-5}\sigma_{eff} + 0.98 \quad (R^2 = 0.95) \\ \beta_{150} = 2.90\times10^{-5}\sigma_{eff} + 1.63 \quad (R^2 = 0.99) \\ \beta_{200} = 6.85\times10^{-5}\sigma_{eff} + 1.83 \quad (R^2 = 0.33) \end{cases} \qquad 76$$

From Eqs. 69, 71, 73 and 75, k-σ_{eff} correlations can be represented by the following general $k(\sigma_{eff})$ function:

$$k = -s_k\sigma_{eff} + k_0 \qquad 77$$

where s_k is the sensitivity of permeability to effective stress and k_0 is the unconfined permeability corresponding to zero effective stress. Similarly, a general $\beta(\sigma_{eff})$ function can be expressed as:

$$\beta = s_\beta\sigma_{eff} + \beta_0 \qquad 78$$

where s_β is the sensitivity of the non-Darcy coefficient to effective stress and β_0 is the unconfined non-Darcy coefficient corresponding to zero effective stress.

In Non-Hydraulic In-Situ Stress Fields

Generally, reservoir formations are under differential in-situ stresses. Thus, it was imperative to verify whether or not, if under differential in-situ stress fields where the radial and the axial stresses differ, the above results are valid. Experiments were designed to measure non-Darcy flow parameters, k and β, at three temperatures: 100°F, 150°F and 200°F, and varying stress fields in Dakota sandstone (Table 51: Tests 10–33, 43–62, and 67–78). Figure 199 shows the k-σ_{eff} and β-σ_{eff} relationships.

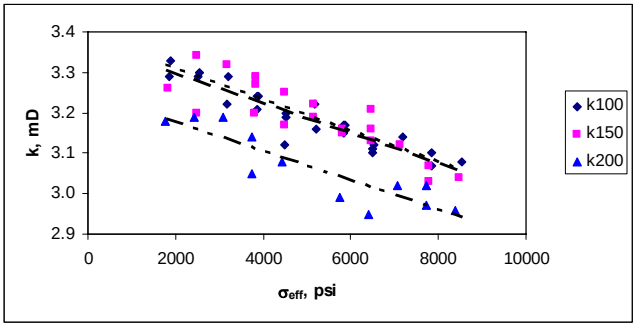

(a) σ_{eff} vs. k

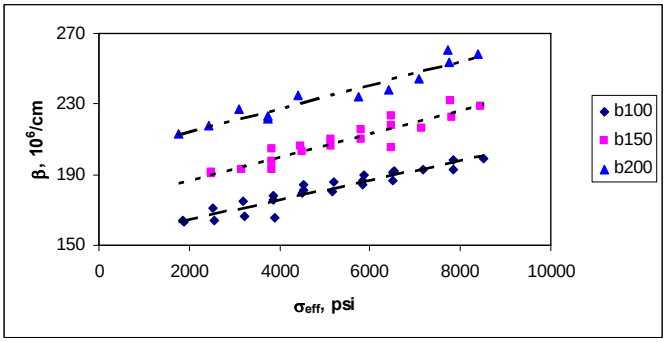

(b) σ_{eff} vs. β

Fig. 199. k(σeff) and β(σeff) relationships versus in-situ stress fields at three temperatures in DS.

The quantitative correlations for Dakota sandstone are:

$$\begin{cases} k_{100} = -3.67\times10^{-5}\sigma_{eff} + 3.37 & (R^2 = 0.86) \\ k_{150} = -3.85\times10^{-5}\sigma_{eff} + 3.39 & (R^2 = 0.74) \\ k_{200} = -3.61\times10^{-5}\sigma_{eff} + 3.25 & (R^2 = 0.80) \end{cases} \qquad 79$$

and

$$\begin{cases} \beta_{100} = 5.48\times10^{-3}\sigma_{eff} + 153.97 & (R^2 = 0.90) \\ \beta_{150} = 6.53\times10^{-3}\sigma_{eff} + 173.93 & (R^2 = 0.88) \\ \beta_{200} = 6.68\times10^{-3}\sigma_{eff} + 200.90 & (R^2 = 0.92) \end{cases} \qquad 80$$

Comparing Eq. 79 to its counterpart under hydrostatic in-situ stress fields, Eq. 69, k has similar correlations with σ_{eff} under both hydrostatic and differential in-situ stress fields. The same is true for the β-σ_{eff} correlation under these two in-situ stress fields.

Under Different Pore Pressures

The previous two sets of experiments were performed at a constant outlet pore pressure of 500 psig. The effects of pore pressure on the above observations were further investigated with experiments at outlet pore pressures of 1500 psig. Figure 200 compares experimental results under outlet pore pressures of 500 psig and 1500 psig at 100°F (Table 51: Tests 124–144 for 500 psig, and Tests 145–159 for 1500 psig).

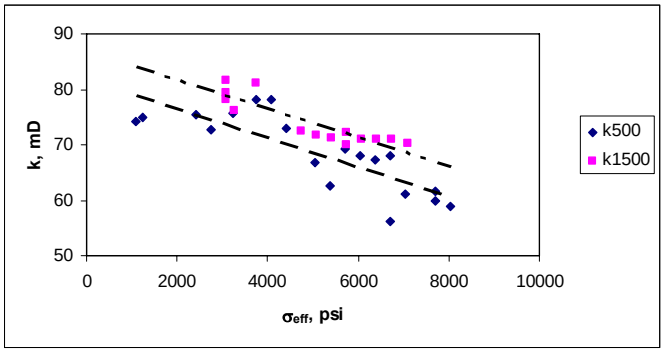

(a) σ_{eff} vs. k

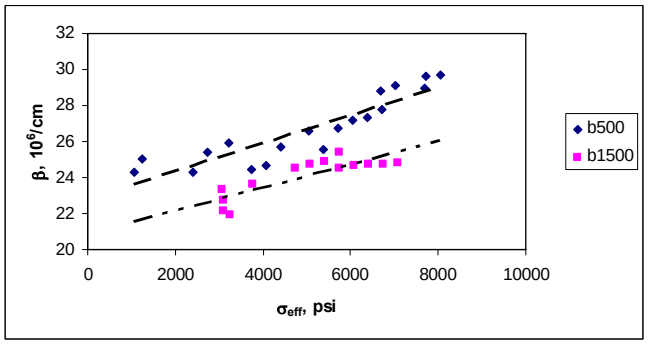

(b) σ_{eff} vs. β

Fig. 200. σeff –k and σeff -β relations under different pore pressures at 100°F in ILH.

The results indicate that at different pore pressures the linear trends for the change of k and β with σ_{eff} are similar. Equations 81 and 82 show the quantitative correlations:

$$\begin{cases} k_{500} = -2.62\times10^{-3}\,\sigma_{eff} + 81.70 \quad (R^2 = 0.68) \\ k_{1500} = -2.58\times10^{-3}\,\sigma_{eff} + 86.89 \quad (R^2 = 0.78) \end{cases} \qquad 81$$

and

$$\begin{cases} \beta_{500} = 7.77\times10^{-4}\sigma_{eff} + 22.79 \quad (R^2 = 0.81) \\ \beta_{1500} = 6.45\times10^{-4}\sigma_{eff} + 20.86 \quad (R^2 = 0.73) \end{cases} \qquad 82$$

Figure 200 also indicates that under the same effective stress, k increases, while β decreases, with increasing reservoir pore pressure. Comparing temperature influence on k and β under the same effective stress, it is observed that the influence of increasing reservoir pressure versus temperature on k and β has the opposite effect.

General Formulas of Effective Stress Sensitivity

Equations 69, 71, 73 and 75 show that stress sensitivity s_k increases with k_0, and the trend is similar between s_β and β_0, as shown in Eqs. 70, 72, 84 and 86. The relationship between k_0-s_k and β_0-s_b at different temperatures in different rock samples is shown in Fig. 201. It is obvious that, regardless of the rock type and temperatures examined, the distribution of all the (k_0, s_k) and (β_0, $s_\square$) points follows an orderly trend.

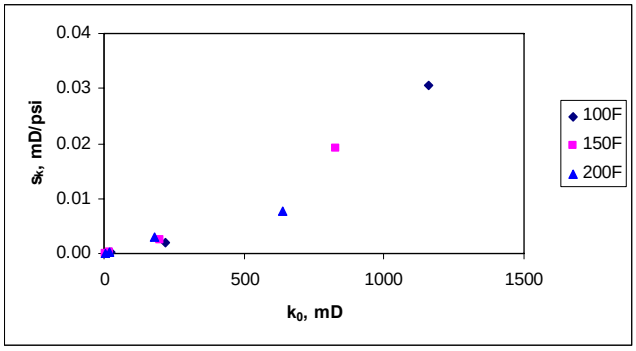

(a) k_0 vs. s_k

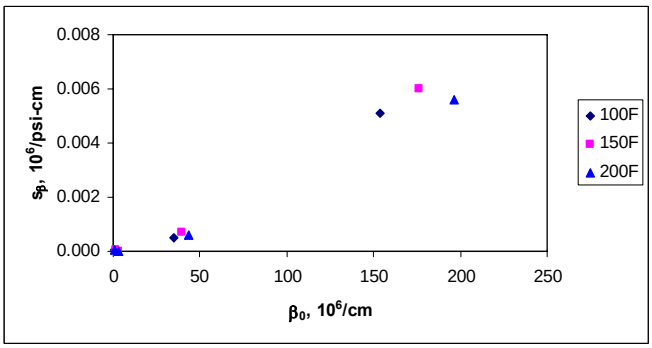

(b) β_0 vs. s_β

Fig. 201. Comparison of stress sensitivities with unconfined non-Darcy flow parameters.

From these distributions, the general equations of stress sensitivity of non-Darcy flow parameters are obtained as follows:

$$s_k = 2\times10^{-8} k_0^2 + 5\times10^{-6} k_0 \qquad (\mathrm{R}^2 = 0.98) \qquad 83$$

and

$$s_\beta = 3\times10^{-5} \beta_0 \qquad (\mathrm{R}^2 = 0.97) \qquad 84$$

Using these two general equations, the stress sensitivity of a formation rock can be estimated when k_0 and β_0 are known. Furthermore, with s_k and s_β from Eqs. 83 and 84, the change of the non-Darcy flow parameters due to change in reservoir pressure can be predicted using Eqs. 77 and 78.

Sensitivity to Shear Stress

At Different Temperatures

Previous work indicated that k and β are independent of shear stress, τ, at 100°F.[183] More experiments were conducted on the same Dakota sandstone (DS) sample under similar axial and radial stresses, but at higher temperatures: 150°F and 200°F (Table 51: Tests 10–33 at 100°F, Tests 43–62 at 150°F and Tests 67–78 at 200°F). Figure 202 shows all the τ-k and τ-β results at all three temperatures. Equations 85 and 86 are the linear best fit of these data.

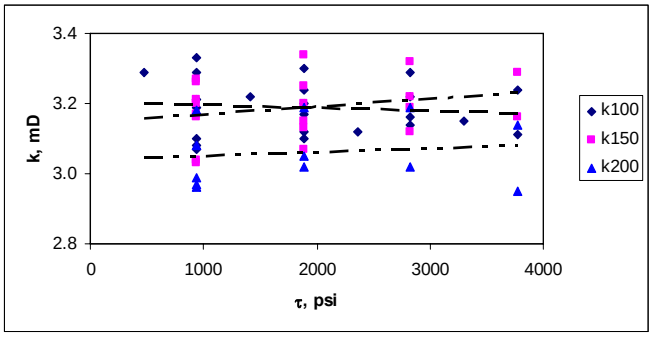

(a) τ vs. k

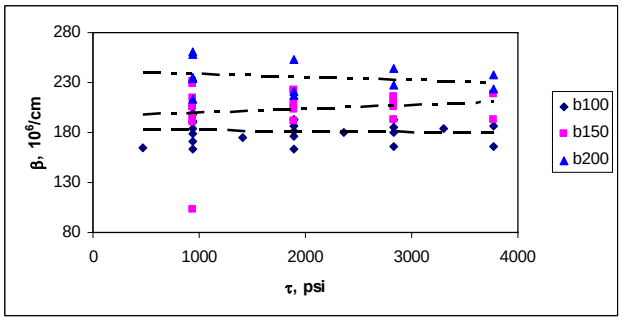

(b) τ vs. β

Fig. 202. τ-k and τ-β curves at 100°F, 150°F and 200°F in DS: widely scattered points indicate poor correlation.

$$\begin{cases} k_{100} = -8.06\times10^{-6}\,\tau + 3.20 & (R^2 = 0.01) \\ k_{150} = 2.17\times10^{-5}\,\tau + 3.15 & (R^2 = 0.06) \\ k_{200} = 1.05\times10^{-5}\,\tau + 3.04 & (R^2 = 0.02) \end{cases} \qquad 85$$

$$\begin{cases} \beta_{100} = -5.22\times10^{-4}\,\tau + 182.18 & (R^2 = 0.00) \\ \beta_{150} = 3.61\times10^{-3}\,\tau + 196.59 & (R^2 = 0.02) \\ \beta_{200} = -3.01\times10^{-3}\,\tau + 241.47 & (R^2 = 0.04) \end{cases} \qquad 86$$

The results shown in Fig. 202 appear to be randomly scattered in the (τ, k) and (τ, β) coordinate systems with correlation coefficients, R, extremely low for Eqs. 85 and 86. These two facts make it evident that k and β are relatively insensitive to τ.

5.3.2 Under Different Pore Pressures

The independence of k and β on shear stress, τ, is further examined with, and confirmed by, the N_2 flow experimental results on a Indiana limestone (ILH) under two different pore pressure ranges, 500 psig and 1500 psig (Table 51: Tests 124–144 at 500 psig and Tests 145–159 at 1500 psig). Figure 203 shows the results in the (τ, k) and (τ, β) coordinate systems with their quantitative correlations expressed in Eqs. (25) and (26). Similar to the results shown in Fig. 202 and Eqs. 85 and 86, Fig. 203 and Eqs. 87 and 88 suggest that the non-Darcy flow parameters in Indian limestone under different pore pressures are also independent of shear stress.

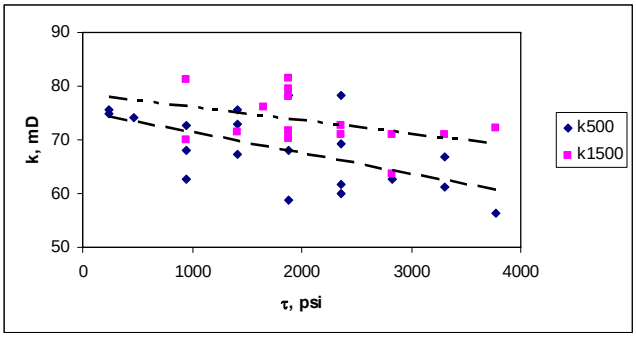

(a) τ vs. k

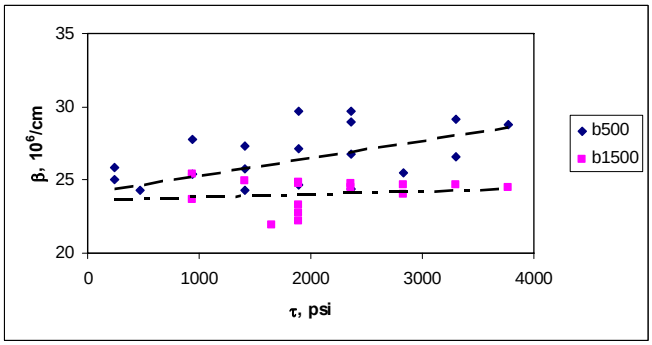

(b) τ vs. β

Fig. 203. τ-k and τ-β curves for outlet pore pressures of 500 psig and 1500 psig in ILH: widely scattered points indicate poor correlation.

$$\begin{cases} k_{500} = -3.86\times10^{-3}\tau + 75.27 \quad (R^2 = 0.34) \\ k_{1500} = -2.47\times10^{-3}\tau + 78.65 \quad (R^2 = 0.16) \end{cases} \quad 87$$

$$\begin{cases} \beta_{500} = 1.18\times10^{-3}\tau + 24.13 \quad (R^2 = 0.22) \\ \beta_{1500} = 2.30\times10^{-4}\tau + 23.56 \quad (R^2 = 0.03) \end{cases} \quad 88$$

General Comments on Shear Stress Sensitivity

The results of $k(\tau)$ and $\beta(\tau)$ at different temperatures and different pore pressures in different rock samples consistently confirm that non-Darcy flow parameters k and β are independent of shear stresses under 3-dimensional, compressive in-situ stress fields. These results are consistent with previously mentioned observations.

Analysis of Phase Sensitivity

A phase is normally defined as any chemically (compositionally) homogeneous and physically distinct part of a system.[157] The phase of a fluid can be solid, liquid, vapor or supercritical, depending on the pressure and temperature and the fluid composition (Fig. 204). The triple point is where the three phases (solid, liquid and vapor) are in equilibrium for a single component system. The critical point is where the liquid and vapor become indistinguishable and the phase boundary disappears. The system at pressures and temperatures above the critical point is commonly referred to as the supercritical region. Unlike the other phases, the supercritical region is not separated from other phase by a common, distinct boundary or phase transition. It is an artificial distinction attributed to a region that is both above the critical pressure and critical temperature. This section of the study focuses on the non-Darcy flow behavior of a fluid in the vapor, supercritical fluid, and liquid regions.

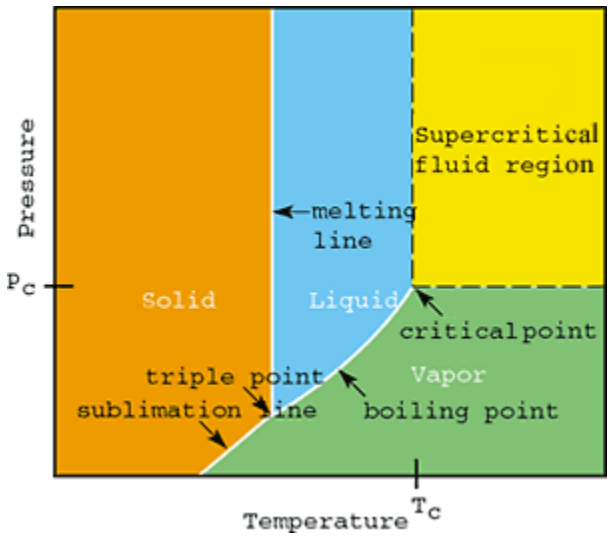

Fig. 204. Phase diagram of a typical fluid.[200]

The critical points of N_2 and CO_2 are as follows: N_2 P_c is 493 psia and T_c is -233°F; CO_2 P_c is 1071 psia and T_c is 88°F.[196] Under typical reservoir conditions N_2 is in the supercritical region while CO_2 can be a vapor, liquid, or supercritical fluid; more often than not, it is in the supercritical region. The various phase conditions are obtained in core tests by varying the outlet pore pressure and core temperature. Based on the above phase definition, we further classify phase sensitivity into two categories: (1) compositional phase sensitivity, and (2) physical phase sensitivity. Compositional phase sensitivity is due to physical property differences from fluid composition, such as N_2 versus CO_2. In contrast, physical phase sensitivity is due to different fluid states arising from differences in pressure and temperature while the composition remains the same.

In order to emphasize phase sensitivity of non-Darcy flow parameters, the stress sensitivity discussed in the previous section is excluded. This is achieved through two steps: (1) the effect of shear stress on CO_2 non-Darcy flow parameters was proved trivial, as was done for N_2; and (2) the effect of the effective stress is eliminated by comparing results from experiments under similar effective stresses.

Sensitivity of CO_2 non-Darcy Flow Parameters to Shear Stress

As with N_2 (Figs. 201 and 202), the CO_2 non-Darcy flow parameters were found to be insensitive to shear stress. Using the shear stress and the calculated non-Darcy parameters of CO_2 flow at 100°F in the ILL sample (Table 51: Tests 170–179), the shear stress influences on k_{CO2} and β_{CO2} are shown in Fig. 205 and Eq. 89. The scattered distribution of the (τ, k_{CO2}) and (τ, β_{CO2}) data in Fig. 205 indicates poor τ-k_{CO2} and τ-β_{CO2} correlations. The extremely low correlation coefficient in Eq. 89 suggests that k_{CO2} and β_{CO2} are independent of τ.

$$\begin{cases} k_{CO2} = 0.0002\tau + 12.49 & (R^2 = 0.13) \\ \beta_{CO2} = -0.0002\tau + 40.28 & (R^2 = 0.01) \end{cases} \qquad 89$$

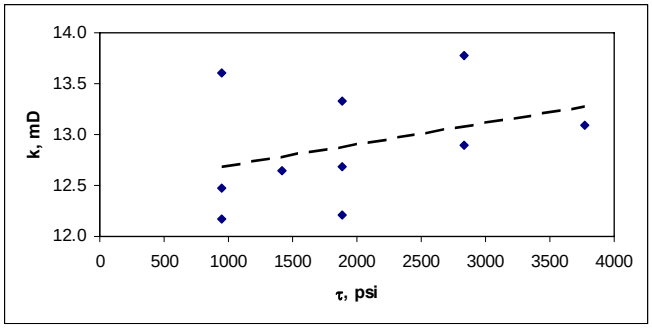

(a). τ vs. k

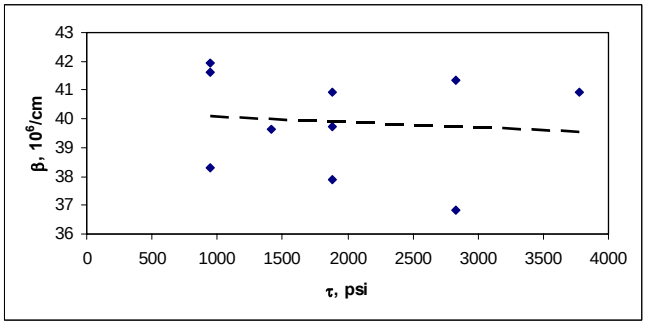

(b). τ vs. β

Fig. 205. Relationship between shear stress and CO_2 non-Darcy flow parameters in ILL at temperature of 100°F: (a) permeability, (b) non-Darcy coefficient.

Compositional Phase Sensitivity: Supercritical N_2 vs. Supercritical CO_2

In order to identify compositional phase sensitivity, supercritical N_2 and supercritical CO_2 were injected separately through the same rock (ILL). Because of the difference in critical points, the

outlet BPR pressure was set at 500 psig for supercritical N_2 non-Darcy flow, and at 1500 psig for supercritical CO_2 non-Darcy flow; the temperature was set at 100°F for both. Results of these experiments are shown in Table 51 (Tests 109–113 for N_2, and Tests 160–169 for CO_2) and Fig. 206. It is clear that k_{CO2} is systematically higher than k_{N2} at all levels of effective stresses, with no consistent relationships between β_{CO2} and β_{N2} identified because of data scatter.

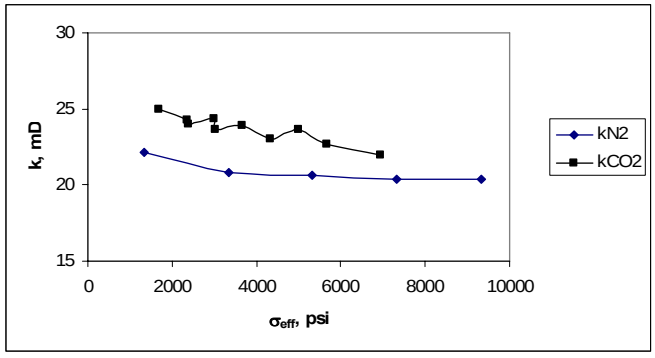

(a)

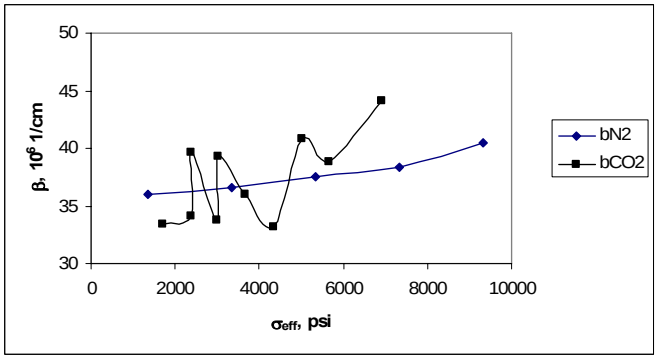

(b)

Fig. 206. Compositional phase sensitivity of non-Darcy flow parameters for supercritical fluids in Indiana limestone: (a) k_{N2} vs. k_{CO2}, (b)β_{N2} vs. β_{CO2}.

The quantitative relations between k, β and σ_{eff} are:

$$\begin{cases} k_{N2} = -0.0002\sigma_{eff} + 21.95 & (R^2 = 0.75) \\ k_{CO2} = -0.0005\sigma_{eff} + 25.51 & (R^2 = 0.85) \end{cases} \qquad 90$$

and

$$\begin{cases} \beta_{N2} = 0.0005\sigma_{eff} + 34.93 \quad (\mathrm{R}^2 = 0.94) \\ \beta_{CO2} = 0.0015\sigma_{eff} + 31.67 \quad (\mathrm{R}^2 = 0.43) \end{cases} \qquad 91$$

The constant terms in the right-hand-side of Eqs. 90 and 91 are the unconfined permeability, k_0, and the unconfined non-Darcy coefficient, β_0, for the flow of two supercritical fluids through the ILL sample. Using the supercritical CO_2 unconfined non-Darcy flow parameters as references, the compositional phase sensitivity can be quantified as follows:

$$\begin{cases} \Delta k_C = \left| \dfrac{k_{0\_CO_2} - k_{0\_N_2}}{k_{0\_CO_2}} \right| \times 100\% \\ \Delta \beta_C = \left| \dfrac{\beta_{0\_CO_2} - \beta_{0\_N_2}}{\beta_{0\_CO_2}} \right| \times 100\% \end{cases} \qquad 92$$

where Δk_C is the compositional phase sensitivity for permeability, $\Delta \beta_C$ is the compositional phase-sensitivity for the non-Darcy coefficient, k_{0_CO2} and k_{0_N2} are the unconfined permeability of supercritical CO_2 and N_2, and β_{0_CO2} and β_{0_N2} are the unconfined non-Darcy coefficient of supercritical CO_2 and N_2, respectively. Using Eq. 92, the compositional phase sensitivity of unconfined permeability is Δk_C=13.96%, and the compositional phase-sensitivity of unconfined non-Darcy coefficient is $\Delta \beta_C$=10.29%.

Physical Phase Sensitivity: Vapor CO_2 vs. Supercritical CO_2

The above mentioned supercritical CO_2 flow experimental results (Tests 160-169) were compared with vapor CO_2 flow experimental results measured in the same rock sample. The vapor CO_2 flow experiments were conducted at an outlet BPR pressure (outlet pore pressure) of 500 psig. The temperature was 100°F, the same as that in the supercritical CO_2 experiments. A summary of the vapor CO_2 experiments are shown in Table 51 (Tests 170–179). Comparison of the two series of experiments is shown in Fig. 207.

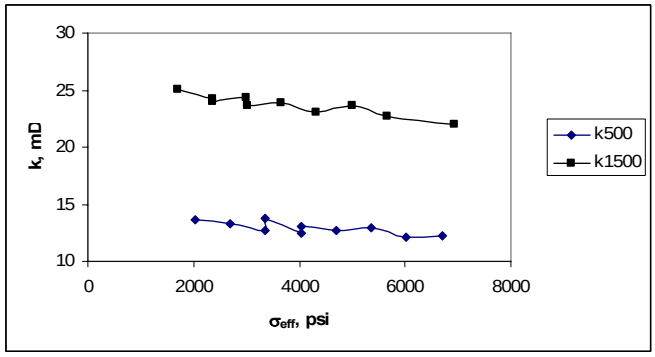

(a)

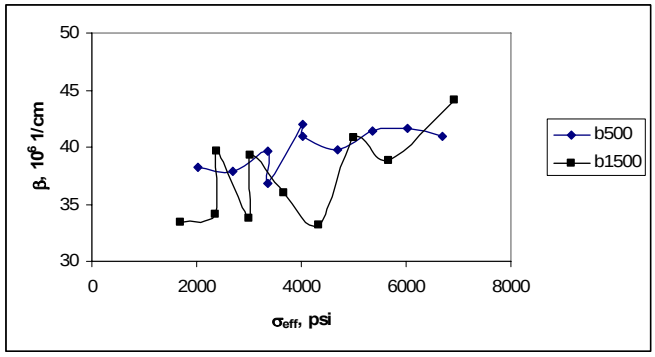

(b)

Fig. 207. Physical phase sensitivity of non-Darcy flow parameters for CO_2 in Indiana limestone. Outlet pore pressure is 1500 psig for supercritical CO_2, and 500 psig for vapor CO_2: (a) k_{1500} vs. k_{500}, (b)β_{1500} vs. β_{500}.

The physical phase sensitivity is analyzed in the same way as compositional phase sensitivity. Correlations between k, β and σ_{eff} are as follow:

$$\begin{cases} k_{500} = -0.0003\sigma_{eff} + 14.15 & (R^2 = 0.62) \\ k_{1500} = -0.0005\sigma_{eff} + 25.51 & (R^2 = 0.85) \end{cases} \quad 93$$

and

$$\begin{cases} \beta_{500} = 0.0008\sigma_{eff} + 36.45 & (R^2 = 0.48) \\ \beta_{1500} = 0.0015\sigma_{eff} + 31.67 & (R^2 = 0.43) \end{cases} \quad 94$$

Similar to Eq. 92, the physical phase-sensitivity of k and β are defined as:

$$\begin{cases} \Delta k_P = \left| \dfrac{k_{0\_1500} - k_{0\_500}}{k_{0\_1500}} \right| \times 100\% \\ \Delta \beta_P = \left| \dfrac{\beta_{0\_1500} - \beta_{0\_500}}{\beta_{0\_1500}} \right| \times 100\% \end{cases} \quad 95$$

where Δk_P is the physical phase sensitivity of permeability, $\Delta \beta_P$ is the physical phase sensitivity of the non-Darcy coefficient, k_{0_1500}, k_{0_500},β_{0_1500}, and β_{0_500} are the unconfined permeability and non-Darcy coefficient of supercritical CO_2 and vapor CO_2, respectively. From Eqs. 93-94, Δk_P=44.53%, and $\Delta \beta_P$=15.09%. Table 50 compares the compositional and physical phase sensitivities of unconfined permeability k_0 and unconfined non-Darcy coefficient β. This shows k_0 has a higher phase sensitivity than β_0 in each category. Both parameters show higher physical phase sensitivities than their counterparts of compositional phase sensitivities; specifically, the physical phase-sensitivity of k_0 is about three times of its compositional phase sensitivity.

Table 52. Compositional vs. Physical Phase Sensitivity in Indiana Limestone

Parameter	Compositional phase-sensitivity	Physical phase-sensitivity
k_0	13.96%	44.53%
β	10.29%	15.09%

Temperature Effect on Phase Sensitivity for Vapor CO_2

Parallel to the above experiments of constant temperature under varied outlet pore pressures, three series of experiments of constant outlet pore pressure at varied temperatures were conducted to investigate the temperature effect on vapor CO_2 phase sensitivity. The outlet pore pressure was 500 psig, and the temperatures were 100°F, 150°F and 200°F (Table 51: Tests 170–191). The results are shown in Fig. 208. In contrast to the consistent change of k_{N2} and β_{N2} with temperature in N_2 flow (Figs. 197–199), k_{CO2} and β_{CO2} are less sensitive to the temperature change.

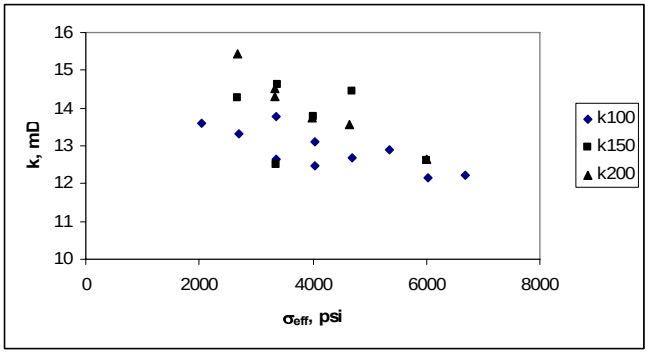

(a)

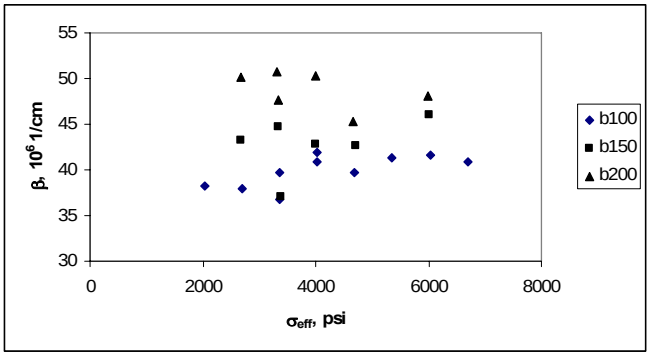

(b)

Fig. 208. **Temperature effect on non-Darcy coefficient in CO_2 flow.**

Phase Sensitivity for CO_2 at Near-Critical Conditions

To investigate the phase sensitivity at near-critical conditions for CO_2, several experiments were performed at 100°F with an outlet pore pressure of 1000 psig (Table 51: Tests 192–193). The experiments were incomplete due to failure to establish flow equilibrium. However, the change of the pressures and temperatures with flow rate, Q, at the inlet and outlet of the sample confirmed phase sensitivity (Fig. 209). When the inlet pressure was close to CO_2 critical conditions (1071 psia and 88°F), the inlet and outlet temperatures dropped drastically. However, when the pressure at the inlet was increased to higher than the critical pressure, the inlet temperature increased, though still below the air bath control temperature; but the outlet pressure and temperature continued to decrease.

This process can be interpreted as the result of phase change. When the core inlet pressure approaches the critical point for CO_2, it rapidly changes density with relatively small changes in pressure or temperature, as shown in Fig. 210. Supercritical CO_2 can have a much higher density than CO_2 vapor. Therefore, at the same mass flow rate, the density and thus the volume flow rate in the case of CO_2 can change rapidly and significantly. The expansion of gas will cause what is referred to as Joule-Thomson cooling. In this case, with significant changes in volume, the constant temperature bath could not keep up with the resulting cooling. Thus, the cooling shown in Fig. 209 results from the rapid changes in volume flow rates, temperature, and local pressure gradients. With all these changes the system was unstable. In the case of N_2 flow in ILL, such as Test 110 plotted in Fig. 211, the change in density may drop 50% at the high flow rate; it is in the supercritical region but far from the critical point and thus the transition is smooth, and extends over the entire core. For CO_2, however, it is at near–critical conditions and the fluid density can change fourfold over relatively small pressure and temperature changes with a Joule-Thomson coefficient about five times that of N_2.[197]

Figure 212 shows the inlet and outlet pressures and temperatures, respectively, for CO_2 flow in ILL (Test 170). The core inlet temperature, T_1, which was measured with a sensor external to the core and thus probably at least a few degrees higher, cooled to 88°F while the inlet pressure, P_1, increased to almost 900 psig; T_1 continued fluctuating but less significantly as P_1 continued to increase; the core outlet temperature, T_2, dropped rapidly when P_1 reached 940 psig and P_2 decreased slowly during this process. This experiment terminated at Q = 5000 cc/hr, due to failure in reestablishing flow equilibrium after T_2 reached the CO_2 critical temperature, 88°F.

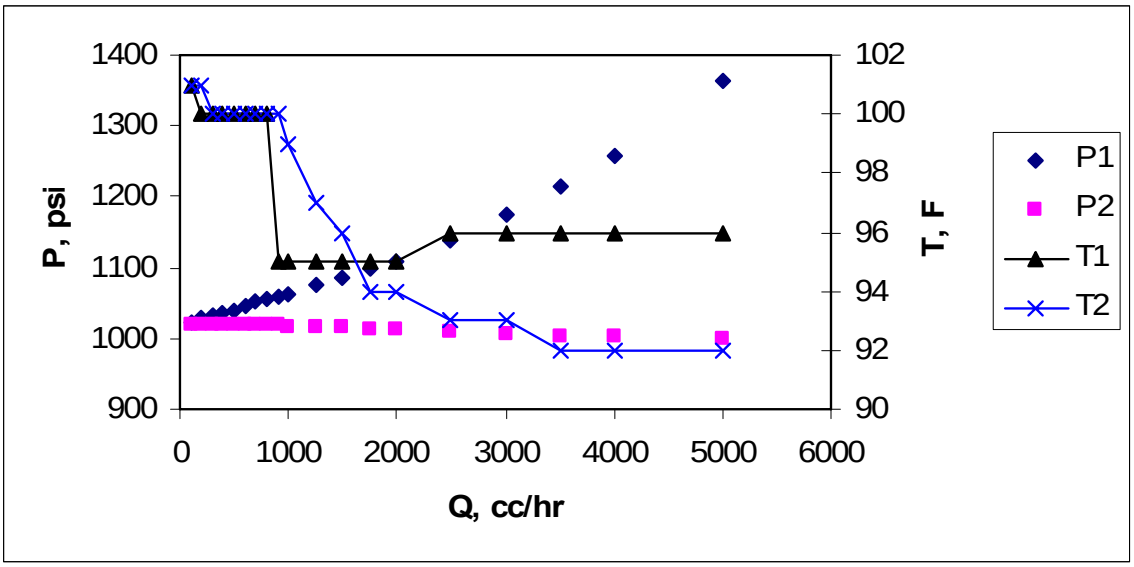

Fig. 209. Change of pressure and temperature at the inlet and outlet of sample in a CO_2 flow experiment (Test 193). Drastic cooling occurred as the inlet conditions approached CO_2 critical point.

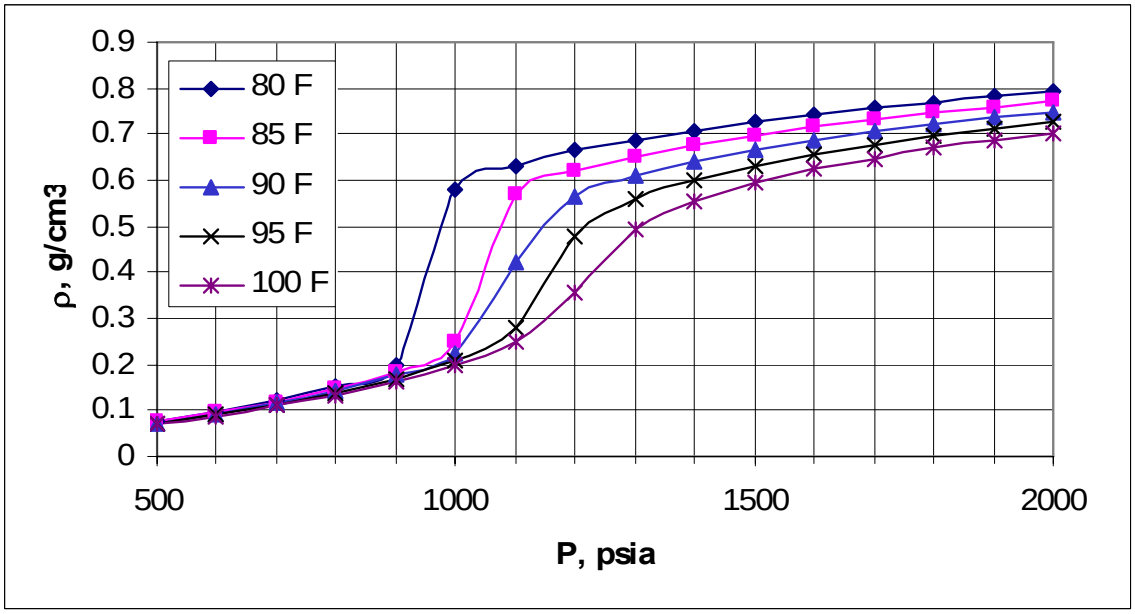

Fig. 210. Change of CO_2 density with pressure at several temperatures near the critical point.

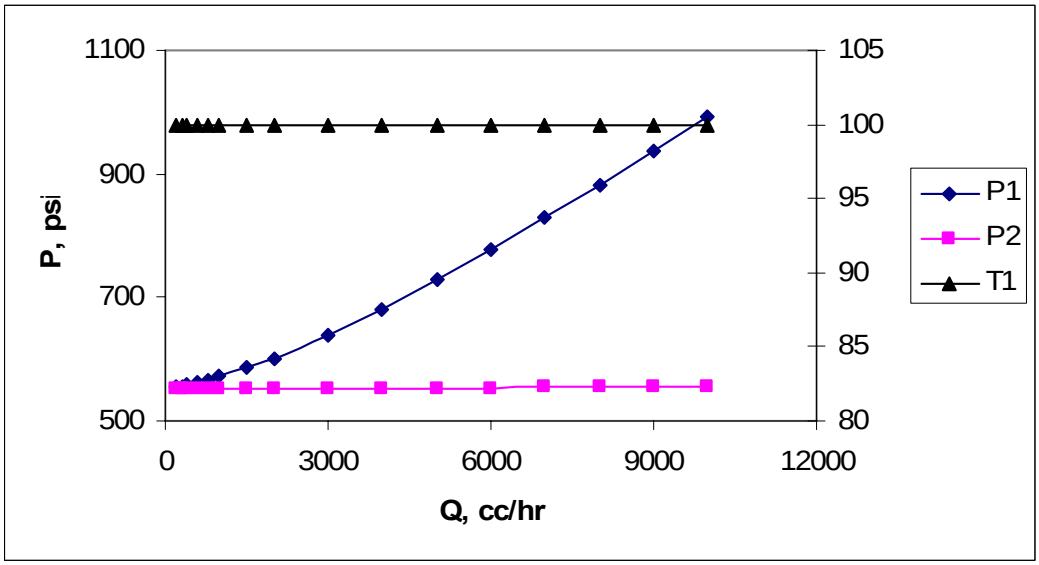

Fig. 211. Stable N_2 flow in ILL (Test 110): no change of temperature with the increase of flow rate and inlet pressure.

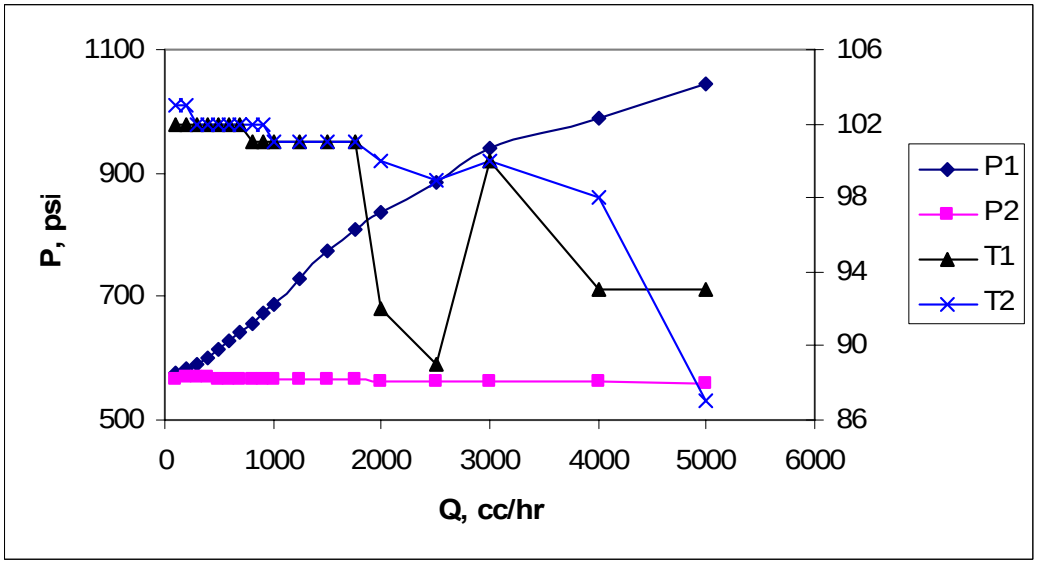

Fig. 212. Unstable CO_2 flow in ILL (Test 170): temperature decreases rapidly with increase of flow rate and inlet pressure.

The West Pearl Queen field test[198] yielded a similar observation and interpretation of CO_2 flow behavior. Figure 213 shows the bottomhole pressure, P_{BH}, and temperature, T_{BH}, during the huff cycle of a Huff'n'Puff CO_2 flooding project. When the bottomhole conditions approached CO_2 critical conditions, the pressure and temperature decreased rapidly. The production was about 95% CO_2 with a few percent light hydrocarbons and a relatively small volume of free water. The cooling effect enhanced the reduction of the bottomhole pressure. As production proceeded, the pressure and temperature conditions near the critical point moved into the reservoir away from the wellbore. Thus the reservoir temperature increased toward the reservoir temperature of 95°F with the pressure remaining in the low pressure (CO_2 vapor) region ahead of the phase change zone that had moved into the reservoir formation away from the wellbore.

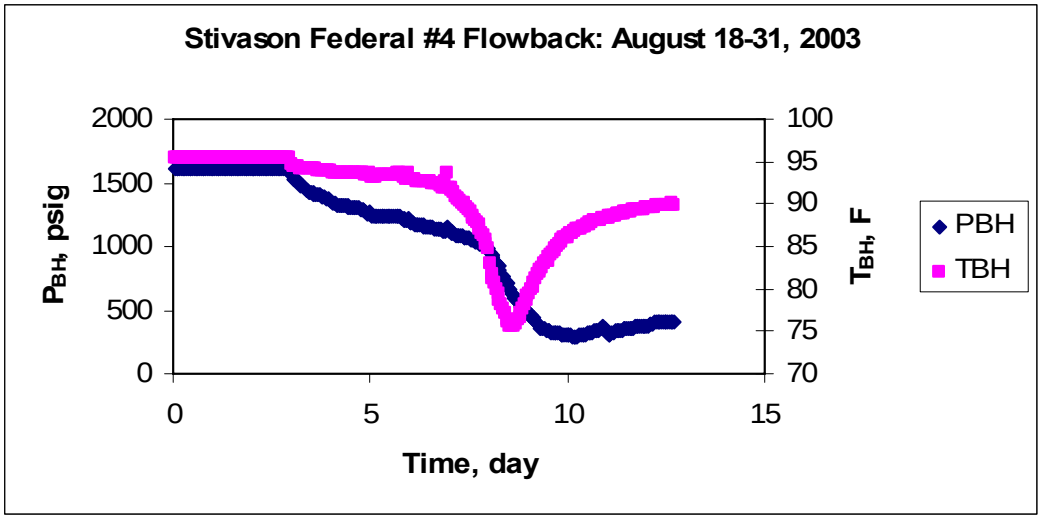

Fig. 213. Wellbore cooling effect when bottomhole conditions approached the critical point of CO_2.

These laboratory and field cases indicate that when reservoir conditions approach CO_2 critical conditions, the flow conditions will be changing rapidly and thus create an unsteady state. If the temperature is not far above the critical temperature, the non-equilibrium of the flow will be more severe until the interruption of the flow.

Discussion

Forchheimer Number and Non-Darcy Effect

While non-Darcy flow behavior is very important, an equally important issue is how to quantify this effect using a definable parameter. A criterion was recommended[174] using the Forchheimer number, *Fo*, which is defined as:

$$Fo = \frac{k\beta\rho v}{\mu} \qquad 96$$

where k is the permeability, β is the non-Darcy flow coefficient, ρ is the fluid density, v is the fluid velocity, and μ is the fluid viscosity.

By defining the non-Darcy effect, *E*, as the ratio of the energy consumed by the non-Darcy effect to the total energy consumed by the whole flow system, the Forchheimer number can be used to quantify the non-Darcy effect as follows:

$$E = \frac{Fo}{1+Fo} \qquad 97$$

Given E_c as the limit of the non-Darcy effect, above which it becomes severe, the corresponding critical Forchheimer number, Fo_c, can be determined from Eq 97:

$$Fo_c = \frac{E_c}{1-E_c} \qquad 98$$

For example, for a 10% limit of *Ec*, the corresponding Fo_c is 0.11. By calculating k, β, μ, v and ρ through analytical, numerical or experimental method,[199] the Forchheimer number at a specific location can be determined. Comparison of the actual Forchheimer number with the critical Forchheimer number can help decide if the non-Darcy effect needs to be considered.

Adding the stress-sensitivities of non-Darcy flow parameters, k and β, would improve the accuracy for the calculation of Forchheimer number, which can be very significant in cases of gas production or injection fields.

Application of the Stress-Sensitivity Correlations

The application of stress-sensitivity correlations involves the following four steps:

Step 1: Calculation of s_k and s_β using Eqs. 83 and 84, and unconfined non-Darcy parameters k_0 and β_0, which can be determined from experimental, empirical, or analytical methods,[199] the stress-sensitivities of s_k and s_β can be calculated.

Step 2: Derivation of the $k(\sigma_{eff})$ and $\beta(\sigma_{eff})$ functions. By applying k_0, β_0, s_k and s_β to Eqs. 77 and 78, the $k(\sigma_{eff})$ and $\beta(\sigma_{eff})$ functions can be determined.

Step 3: Calculation of σ_{eff}. The in-situ stress field, represented by its principal components (σ_1, σ_2, σ_3) in the reservoir formation, can be measured using rock mechanics techniques,[200,201] or estimated using empirical equations.[202] Assuming the reservoir pressure, p, updated due to petroleum production or fluid injection, is known, then the effective principal stresses (σ_{1eff}, σ_{2eff}, σ_{3eff}) will be (σ_1-p, σ_2-p, σ_3-p). Applying the effective principal stresses (σ_{1eff}, σ_{2eff}, σ_{3eff}) to Eq. 67, the average effective stress σ_{eff} can be obtained.

Step 4: Determination of k and β at current reservoir pressure. Inputting σ_{eff} from Step 3 to $k(\sigma_{eff})$ and $\beta(\sigma_{eff})$ functions obtained in Step 2, the non-Darcy parameters at the current reservoir pressure, p, can be obtained.

By repeating Steps 3 and 4, non-Darcy parameters, k and β, can be updated as often as needed.

Conclusions

In this part of the Project, sensitivities of non-Darcy flow parameters (i.e., permeability, k, and non-Darcy coefficient, β) to the change of effective stress, shear stress, pore pressure, temperature, fluid compositional composition and fluid physical state, under representative petroleum reservoir conditions, were experimentally studied. From this investigation, the following conclusions are derived:

1. N_2 non-Darcy flow parameters are sensitive to the change of effective stress, and insensitive to the change of shear stress. Permeability, k, decreases while the non-Darcy coefficient, β, increases linearly with increasing effective stresses.
2. General functions of stress sensitivities of N_2 non-Darcy flow parameters, s_k and s_β, can be expressed in terms of unconfined non-Darcy flow parameters k_0 and β_0 corresponding to zero effective stress conditions, regardless of rock properties, in-situ stress fields, and temperatures.
3. General functions, $k(\sigma_{eff})$ and $\beta(\sigma_{eff})$ are derived in terms of stress sensitivities, s_k and s_β, and unconfined non-Darcy flow parameters, k_0 and β_0. Influence of reservoir pressure change on k and β can be predicted using these functions.

4. Non-Darcy parameters are sensitive to the compositional and physical phase changes of the fluids. However, comparing to non-Darcy coefficients, permeability is more sensitive to both compositional and physical phase changes. For the same parameter, physical phase sensitivity is higher than compositional phase sensitivity.
5. For fluid flow at near-critical conditions, localized cooling may cause phase changes, which further influence the non-Darcy flow behavior.

The above conclusions were developed under regular compaction conditions. In case of dilatation, more experiments need to be conducted to verify their validation. In addition, the phenomenon of phase sensitivity deserves more experimental investigations, due to the complexity of the problem.

CONCLUSIONS and SUMMARY

A. SORPTION

1. For CD, IFT has been determined to decrease with surfactant concentration below the CMC and to be essentially constant above the CMC, to increase with the increase of temperature and decrease of pressure, to remain essentially constant over the initial pH range from 1 to 12, and to be insensitive to brine concentration over a wide range with a minimum around 10%.
2. CD foam in 2% brine is stable at 60ºC and below, at all tested temperatures and CD concentrations, except at the lowest CD concentration (0.005 wt%) tested. However, foam stability is lower at 75ºC and increases with CD concentration.
3. Foam is stable under all tested pressures at surfactant concentrations of 0.025 wt% and above, and foam stability decreases with increasing temperature at the surfactant CD concentration of 0.005 wt%.
4. Interfacial tension (IFT) does not directly correlate to foam stability and foam stability cannot be predicted solely by the value of IFT.
5. At a constant gas flow rate, gas mobility slightly decreases with increasing foam quality when below the critical foam quality (fg*) and increases with increasing foam quality above f_g*.
6. Low gas mobility can be found over a wide range of foam qualities.
7. Increased surfactant concentration leads to the decrease of gas mobility. Comparing coinjected surfactant and gas (CSG) with coinjected water and gas (CWG) shows that the gas mobility of CSG is an order of magnitude lower than that of CWG.
8. Surfactant adsorption with gas present can be determined using surfactant solution alone, which lowers the expense due to simpler experimental setup and less time required.
9. Coreflood circulation tests indicated that surfactant adsorption density was higher in sandstone than for limestone under the same conditions such surfactant concentration, temperature, salinity, and pressure.
10. The adsorption density of both the sandstone and limestone reached a plateau region where there was little or no increase at all after a certain period of time. The concentration of the surfactant in the flask also did not change after the adsorption density reached the plateau

region.

11. In the waterflood experiments, the 2.0 wt% brine was found to bypass zones and reached breakthrough at the outlet before some of the taps in the third (last) section of the core, taps nearer the input broke through earlier, suggesting that the core was not as homogeneous as previously thought.
12. In the waterflood experiments, earlier breakthroughs were recorded in the lower side of the core than in the upper side of the core. The taps at the bottom registered early breakthrough and salinity peaks faster than their counterparts on the top side, which means brine flow was preferentially faster in the bottom side. Test show that this was due to gravity.
13. In the multi-taps dynamic experiments, boundary layer effect was found to be influencing flow fluid along the edges of the core where samples were taken. Thus the sampling port holes were drilled into the core about one forth of the distance.
14. An anisotropic permeability was found to influence brine displacement profile.
15. Surfactant adsorption was greatest in the zones closest to the injection port.
16. Surfactant adsorption was found to be higher in the bottom side of the core than in the top side of the core due to gravity.
17. Surfactant adsorption isotherm of CD 1045 on sandstone was found to depict the highly regarded four-region adsorption isotherm model.
18. Surfactant desorption was greatest in the section nearest the injection port.
19. Surfactant desorption (depletion) was found to be higher in the bottom side of the core than in the top side due to gravity as in the adsorption.
20. Values of CD adsorption density on crushed and non-flow solid limestone cubes were found to be the same and best described as a function of surfactant availability (mass of surfactant available per mass of solid) in the system.
21. The shape of the adsorption isotherms on crushed sandstone comparing surfactant availability with adsorption density, suggests the slopes and possibly the density plateau depend on surfactant concentration and availability.
22. Adsorption time dynamic depends on the state of solid and flow conditions. Time to reach equilibrium in nonflow core volumes was an order of magnitude greater compared to circulation experiment, and 3 orders of magnitude greater compared to the crushed rock. Thus the rate of adsorption is dependent on the availability of surfactant with the kinetics and

equilibrium being comparably very rapid.

23. When comparing flow versus nonflow systems in cube or core samples, the adsorption density on limestone underwent a significant decrease due to the flow in porous media while adsorption density on sandstone remained the same. This might be an indication of different adsorption mechanisms and/or energy levels that occur on limestone and sandstone surfaces. Tests such as heats of adsorption that are planned for the future should shed some light the cause of these differences.
24. The results should be considered when determining reservoir adsorption requirements.
25. Eight systems were tested for N_2 at immiscible conditions. As with CO_2 IFT is an aid in screening, but is not definitive in determining foam durability nor displacement efficiency.
26. A mixed surfactant was the best system for foam stability and mobility reduction, but the resistance factor was so high it would probably not propagate through a reservoir at appreciable rates.
27. The pseudo first and second order kinetic models for adsorption and desorption were derived in a mathematically complete format. These models are nonlinear. The adsorption models have two unknown parameters, and the desorption models have three unknown parameters.
28. A simplex nonlinear optimization method was adapted for the determination of the unknown parameters for these kinetics models. This algorithm can be applied to determine not only the parameters of these nonlinear models, but also the absolute error between the model and the measured results.
29. The adsorption and desorption processes of surfactant CD1045 onto and from Berea sandstone were found to obey pseudo second order adsorption model and the pseudo first order desorption models, respectively. More experimental work under different conditions will be carried out to better understand the influences of different factors on the sorption processes.

.

B. RELATIVE PERMEABILITY and PHASE BEHAVIOR

1. Using relatively short cores (5.71 to 8.17 cm), about 3.8 cm in diameter, in the range of 0.2 to 0.3 PV fraction of CO_2 saturation was required to establish a CO_2 flow path, after which

there was little brine production except through evaporation, which is a slow process. The CO_2 saturation can be increased by increasing the flow rate and by water evaporation.

2. At the end of CO_2 injection there was a relatively low CO_2 saturation and high brine saturation in the core; thus no reduction in CO_2 saturation was required to return to brine flow. Only in the Queen sandstone was there free flowing CO_2 with subsequent free CO_2 produced during brine injection.
3. Brine is equilibrated with CO_2 in a short time frame over a relatively short distance. Only when a solution channel was formed was brine produced that was not saturated with CO_2, while a significant residual CO_2 remained in the core.
4. The injection of brine into a 100% CO_2 phase required 0.2 to 0.3 PV fraction saturation to establish a brine flow path.
5. The sandstone and carbonate systems initially performed similarly. This changed when, through dissolution of the rock matrix, a solution channel was formed in the limestone, creating a dominant flow path that significantly altered the flow behavior of the core.
6. This work estimates that the removal of CO_2 saturation near a wellbore will take ten times as long as it took to establish it.
7. A triaxial acoustic core flooding system with the capacity of simulating typical petroleum reservoir conditions was developed.
8. Using this system, the temperature effect on seismic velocities of stainless steel, Dakota sandstone and Indiana limestone were investigated. It is found that, under confining pressure of 3000 psia, when the samples were heated from 65°F to 150°F, all seismic velocities slightly decrease. The change can be linearly correlated to the temperature.
9. Using the same system, CO_2 phase transition induced seismic velocity changes were observed. When CO_2-saturated Indiana limestone was heated and cooled across the CO_2 critical temperature while the CO_2 pore pressure was held constant above its critical pressure, all three seismic velocities changed drastically in a non-linear way.
10. Further experiments revealed that when temperature and pressure are kept constant near the CO_2 critical point, the average seismic velocities keep almost unchanged, which confirms that the above observed seismic velocity change is due to CO_2 phase transition.
11. More experiments are required to improve our understanding on the phase transition induced seismic behavior, including attenuation and frequency dependency.

C. MATRIX

1. The logic of non-Darcy effect based on the Forchheimer equation has been successfully incorporated in the reservoir simulator MASTER. Simulation results are reasonable because they demonstrate all expected trends (higher reservoir pressure, significant non-Darcy effect near wellbore, lower gas production and injection rates).
2. Although users of the simulator are provided with the option whether to consider non-Darcy effect or not, it is clear that, for cases involving high speed gas flow like the one presented in this paper, non-Darcy effect should be considered.
3. The presented method on how to implement non-Darcy effect through the use of factor *F* is effective and quite simple.
4. The flow behavior of the limestone indicates a less homogeneous flow distribution than that of dolomite.
5. The production of manganese in both cases has a reduction after a soaking period early in the test. There is a spike in produced manganese concentration corresponding to CO_2 breakthrough. There appears to be some manganese precipitation in the early time in the core that is produced after CO_2 breakthrough. At ambient conditions most of the manganese precipitates.
6. Regarding effluent calcium concentrations: in both systems solution calcium increases after CO_2 breakthrough with significant concentrations precipitating at ambient conditions. The higher concentration of calcium is in the limestone that has little magnesium in the solution.
7. There was little change manganese concentration in until CO_2 breakthrough. As might be expected the increase in effluent concentration is small in limestone (~30%) which contains less than 1% magnesium, while it increases about eightfold in dolomite which contains about equal mole concentrations of magnesium and calcium. Most of the magnesium stays in solution at ambient conditions with little precipitation in either system.
8. There was no precipitation detected in Corefloods D and E. The primary difference that was noted with earlier floods was a significant change in brine composition. Each of the first three brines (including the reservoir brines) had much high levels of magnesium and the first tracer brine had high levels of manganese and strontium.

9. Preliminary experiments on WAG using acoustic equipment verify that samples have areas of visibly dissolved portions on the injection side of the specimen. This is a strong evidence of CO_2-rock reaction for such a short duration of WAG experiment. The most reactive periods, as shown by the TDS, are during the switch between CO_2 and deionized water. Changing the injection scheme to larger quantities to mimic field scale dimensions may not allow for large changes to be observed in a short time frame, but this exploratory experiment proves that dissolution takes place in the Indiana limestone and it can be observed with petroleum engineering laboratory equipment. More experimentation is required to make any further conclusions on the change in porosity and permeability in Indiana limestone due to carbon dioxide injection.
10. N_2 non-Darcy flow parameters are sensitive to the change of effective stress, and insensitive to the change of shear stress. Permeability, k, decreases while the non-Darcy coefficient, β, increases linearly with increasing effective stresses.
11. General functions of stress sensitivities of N_2 non-Darcy flow parameters, s_k and s_β, can be expressed in terms of unconfined non-Darcy flow parameters k_0 and β_0 corresponding to zero effective stress conditions, regardless of rock properties, in-situ stress fields, and temperatures.
12. General functions, $k(\sigma_{eff})$ and $\beta(\sigma_{eff})$ are derived in terms of stress sensitivities, s_k and s_β, and unconfined non-Darcy flow parameters, k_0 and β_0. Influence of reservoir pressure change on k and β can be predicted using these functions.
13. Non-Darcy parameters are sensitive to the compositional and physical phase changes of the fluids. However, comparing to non-Darcy coefficients, permeability is more sensitive to both compositional and physical phase changes. For the same parameter, physical phase sensitivity is higher than compositional phase sensitivity.
14. For fluid flow at near-critical conditions, localized cooling may cause phase changes, which further influence the non-Darcy flow behavior.
15. The above conclusions were developed under regular compaction conditions. In case of dilatation, more experiments need to be conducted to verify their validation. In addition, the phenomenon of phase sensitivity deserves more experimental investigations, due to the complexity of the problem.

ACKNOWLEDGMENTS

Appreciation is expressed to the Department of Energy and the State of New Mexico for funding this work. Thanks to members of the New Mexico Petroleum Recovery Research center: Reid B. Grigg, Robert K. Svec, Zhengwen Zeng, Baojun Bai, Yi Liu, Alexander Mikhalin, Guoqiang Yin, Ghislain E. Fai-Yengo, Yusif Oni, Guoqiang Yin, Alexander Mikhalin, Peter Empey, Alvaro Nunez, Vignesh Proddaturi, Solomon Ampin, Rashid Kassim, and Pinyok Kovisuith who have contributed to this work. Also we would like to acknowledge Ms. Liz Bustamante for her assistance in editing this manuscript. For contributions from outside the PRRC we would like to acknowledge George Hirasaki at Rice University for his very helpful suggestions, and Shinichi Sakurai, an Associate at the Bureau of Economic Geology at the University of Texas at Austin, for the core samples.

REFERENCES

1. Taber, J.J.: "Environmental Improvements and Better Economics in EOR Operations," *In Situ* (1990) 14(4), 345-404.
2. Stalkup, F. I.: "Miscible Displacement," SPE Monograph No. 8, New York (1983).
3. Grigg, R. B., et al.: "Cost Reduction and Injectivity Improvements for CO_2 Foams for Mobility Control," paper SPE 75178 presented at the 2002 SPE/DOE IOR, Tulsa, April 13-17.
4. Cheng, L., et al.: "Simulating Foam Processes at High and Low Foam Qualities," paper SPE 59287 presented at the 2000 SPE/DOE IOR. Tulsa, April 2-5.
5. Shan, D. and Rossen, W.R.: "Optimal Injection Strategies for Foam IOR," paper SPE 75180 presented at the 2002 SPE/DOE IOR. Tulsa, April 13-17.
6. Grigg, R.B., et al.: "Improving CO_2 Efficiency for Recovering Oil In Heterogeneous Reservoirs," First Annual Technical Report, US DOE Contract No. DE-FG26-01BC15364 (2003).
7. Grigg, R.B., et al.: "Improved CO_2 Efficiency for Recovering Oil in Heterogeneous Reservoirs," Second Annual Technical Report, DOE Contract No. DE-FG26-01BC15364 (2003).
8. Grigg, R.B. and Bai, B.: "Calcium Lignosulfonate Adsorption and Desorption on Berea Sandstone," Journal *of Colloid and Interface Science*, 279 (2004) 36-45.
9. Grigg, R.B. and Bai, B.: "Sorption of Surfactant Used in CO_2 Flooding onto Five Minerals and Three Porous Media," paper 93100 presented at the 2005 SPE International Symposium on Oilfield Chemistry, Houston, Feb. 2-4.
10. Bai, B. and Grigg, R.B.: "Kinetics and Equilibria of Calcium Lignosulfonate Adsorption and Desorption onto Limestone," paper 93098 presented at the 2005 SPE International Symposium on Oilfield Chemistry, Houston, Feb. 2–4.
11. Grigg, R.B., Bai, B., and Liu, Y.: "Competitive Adsorption of Hybrid Surfactant System onto Five Minerals, Berea Sandstone, and Limestone," paper SPE 90612 presented at the 2004 SPE ATCE, Houston, Sep. 26-29.
12. blank
13. Rogers, J.D. and Grigg, R.B.: *SPE Reservoir Eval. & Eng.*, Vol. 5, No. 5.

14. Tsau, J.-S. and Heller, J.P.: "Evaluation of Surfactants for CO_2-Foam Mobility Control," paper SPE 24013, 1992 PBOGR, Midland, March 18-20.
15. Tsau, J.-S., et al.: "Use of Mixed Surfactants to Improve Mobility Control in CO Flooding," paper SPE 39792 presented at the 1998 PBOGR, Midland, March 23–26.
16. Tsau, J.S. and Heller, J.P.: "Evaluation of Surfactants for CO_2-Foam Mobility Control," paper SPE 24013 presented at the 1992 Permian Basin Oil and Gas Recovery Conference, Midland, March 18-20.
17. Tsau, J-S., et al.: "Smart Foam to Improve Oil Recovery in Heterogeneous Porous Media," paper SPE 39677 presented at the 1998 SPE/DOE IOR, Tulsa, April 19–22.
18. Martin, F.D., et al.: "CO_2-Foam Field Verification Pilot Test at EVGSAU Injection Project Phase I: Project Planning and Initial Results," paper SPE 24176 presented at the 1992 SPE/DOE IOR, Tulsa, April 22-24.
19. Tsau, J.S., et al.: "CO_2 Foam Field Verification Pilot Test at EVGSAU: Phase IIIA—Surfactant Performance Characterization and Quality Assurance," paper SPE 27785, presented at the 1994 SPE/DOE IOR, Tulsa, April 17-20.
20. Stevens, J. E., and Martin, F. D.: "CO_2 Foam Field Verification Pilot Test at EVGSAU: Phase IIIB—Project Operations and Performance Review," paper SPE 27786 presented at the 1994 SPE/DOE IOR, Tulsa, April 17-20.
21. Harpole, K.J., et al.: "CO_2 Foam Field Verification Pilot Test at EVGSAU: Phase IIIC—Reservoir Characterization and Response to Foam Injection," paper SPE 27798 presented at the 1994 SPE/DOE IOR, Tulsa, April 17-20.
22. Martin, F.D., et al.: "CO_2-Foam Field Test at the East Vacuum Grayburg/San Andres Unit," *SPERE* (November 1995) 10(4), 266-272.
23. Heller, J.P., et al.: "Field Test of CO_2 Mobility Control at Rock Creek," paper SPE 14395 presented at the 1985 SPE ATCE, Las Vegas, Sept.22-25.
24. Jonas, T. M., et al.: "Evaluation of a CO_2 Foam Field Trial: Rangely Weber Sand Unit," paper SPE 20468 presented at the 1990 SPE ATCE, New Orleans, Sept. 23-26.
25. Chou, S. I., et al.: "CO_2 Foam Field Trial at North Ward-Estes," paper SPE 24643 presented at the 1992 SPE ATCE, Washington, DC, Oct. 4-7.
26. Hoefner, M. L., et al.: "CO_2 Foam: Results From Four Developmental Field Trials," paper SPE/DOE 27787 presented at the 1994 SPE/DOE IOR, Tulsa, April 17-20.

27. Holm, L.W. and Garrison, W.H.: "CO_2 Diversion with Foam in an Immiscible CO_2 Field Project," *SPERE* (February 1988), Vol. 3, No. 1, 112-118.
28. Moritis, G.: "EOR/Heavy Oil Survey—Special Report" and "2006 Worldwide EOR Survey," *Oil & Gas Journal*, (April 17, 2006) 104:15, 37-57.
29. Zeng, Z., Jakupi, A., Bigelow, T., Grigg, R.B., Kringstad, J. Belobraydic, M., and Zhou, X.: "Laboratory Observation of CO_2 Phase Transition Induced Seismic Velocity Change", This paper was prepared for presentation at the 42nd US Rock Mechanics Symposium and 2nd U.S.-Canada Rock Mechanics Symposium, San Francisco, June 29-July 2, 2008.
30. Zeng, Z.W and Grigg, R.B.: "TOPICAL REPORT: MASTER 2008 Manual (Miscible Applied Simulation Techniques for Energy Recovery)",for the project "IMPROVING GAS FLOODING EFFICIENCY" DOE CONTRACT NO. DE-FC26-04NT15532, July 2008
31. Grigg, R.B. and Svec, R.K.: "Injectivity Changes and CO2 Retention for EOR and Sequestration Projects," paper SPE 110760 presented at the 2008 SPE Improved Oil Recovery Symposium, Tulsa, 19-23 April.
32. Zeng, Z.W, Grigg, R.B., Gupta, D.B., and Bethapudi, L.V.: "Experimental Investigation of Stress- and Phase-Sensitivities of Non-Darcy Flow Parameters" *SPEREE in press.*
33. Grigg, R.B.: Second Annual Report for "IMPROVING GAS FLOODING EFFICIENCY" DOE CONTRACT NO. DE-FG26-04NT15532, June 2007
34. Grigg, R.B. and Svec, R.K.: "CO_2 Retention and Injectivity Changes: Laboratory Tests," Paper 145 presented at the Sixth Annual Conference on Carbon Capture and Sequestration – DOE/NETL, Pittsburgh, 7-19 May 2007.
35. Grigg, R.B. and Mikhalin, A.A.: "Effects of Flow Conditions and Surfactant Availability on Adsorption," paper SPE 106205 presented at the 2007 SPE International Symposium on Oilfield Chemistry, Houston, Feb. 28 – March 2.
36. Grigg, R.B.: "Technologies Hold Key to Improving Recovery Efficiency," *The American Oil & Gas Reporter*, February 2007, 106.
37. Grigg, R.B. and Svec, R.K.: "CO_2 Transport Mechanisms in CO_2/Brine Coreflooding," paper SPE 103228 presented at the 2006 SPE Annual Technical Conference and Exhibition, San Antonio, Sep. 24-27.

38. Zeng, Z-W., Grigg, R.B., and Bai, B.: "Experimental Development of Adsorption and Desorption Kinetics of CO_2-Foaming Surfactant onto Berea Sandstone," paper SPE 103117 presented at the 2006 SPE Annual Technical Conference and Exhibition, San Antonio, Sep. 24-27.
39. Pawar, R.J., Warpinski, N.R., Lorenz, J.C. Benson, R.D., Grigg, R.B., Stubbs, B.A., Stauffer, P.H., Krumhansl, J.L., Cooper, S.P., and Svec, R.K.: "Overview of a CO2 Sequestration Field Test in the West Pearl Queen Reservoir, New Mexico," *Environmental Geosciences,* V.13, No. 3 (September 2006), pp. 163-180.
40. Grigg, R.B. and Svec, R.K.: "CO_2 Saturations and Transport Mechanisms in Frio Sandstone," Paper 157 presented at the Fifth Annual Conference on Carbon Capture and Sequestration – DOE/NETL, Washington, D.C., 8-11 May 2006.
41. Grigg, R.B. and Svec, R.K.: "Laboratory and Model Tests at Reservoir Conditions for CO_2-Brine-Carbonate Rock Systems Interactions," prepared and presented at The Fifth Annual DOE Carbon Sequestration Conference, Washington, D.C., 8-11 May 2006.
42. Zeng, Z-W. and Grigg, R.: "A Criterion for Non-Darcy Flow in Porous Media," *Transport in Porous Media,* (2006) 63: 57-69.
43. Grigg, R.B.: First Annual Report for "IMPROVING GAS FLOODING EFFICIENCY" DOE CONTRACT NO. DE-FG26-04NT15532, May 2006
44. Liu. Y., Grigg, R.B., and Svec, R.K..: "Foam Mobility and Adsorption in Carbonate Core," paper SPE 99756 presented at the 2006 SPE/DOE Symposium on Improved Oil Recovery, Tulsa, 22–26 April.
45. Bai, B., Grigg, R.B., Liu, Y., and Zeng, Z-W.: "Adsorption and Desorption of a CO_2-Foam-Forming Surfactant onto Berea Sandstone," paper SPE 95920 presented at the 2005 SPE Annual Technical Conference and Exhibition, Dallas, 9 – 12 October.
46. Grigg, R.B.: "Improved CO_2 Efficiency for Recovering Oil in Heterogeneous Reservoirs," Final Report for DOE contract no. DE-FC26-01BC15364, June 2005
47. Grigg, R.B., Svec, R.K., Peter C. Lichtner, P.C., Carey, W., and Lesher, C.E.: "CO_2/Brine/Carbonate Rock Interactions: Dissolution and Precipitation," prepared and presented at the Fourth Annual Conference on Carbon Capture & Sequestration, Alexandria, 2-5 May 2005.

48. Liu, Y., Grigg, R.B., and Svec, R.K.: "CO_2 Foam Behavior: Influence of Temperature, Pressure, and Concentration of Surfactant," paper 94307 presented at the 2005 SPE Production and Operations Symposium, Oklahoma City, 17-19 April.
49. Pariani, G.J. et al.: "An Approach to Optimize Economics in a West Texas CO_2 Flood," *JPT* (September 1992) 984; Trans., AIME, 293.
50. Schramm, L.L.: "Foams: Fundamentals and Applications in the Petroleum Industry," American Chemical Society, Washington, DC (1994).
51. Harkins, W.D. and Brown, F.E., "The Determination of Surface Tension (Free Surface Energy), and the Weight of Falling Drops: the Surface Tension of Water and Benzene by the Capillary Height Method," *Amer.Chem. Soc* (1919) 41, 499-524.
52. Adamson, A.W.: *Physical Chemistry of Surfaces*. New York, John Wiley & Sons (1982).
53. Syahputra, A.E.: "Experimental Evaluation of Lignosulfonate as a Sacrificial Agent in CO_2-Foam Flooding," Thesis, New Mexico Tech, Socorro, NM (Aug. 1999).
54. Lee, H.O., Heller, J.P., and Hoefer, A.M.W.: "Change in. Apparent Viscosity of CO_2 Foam with Rock Permeability," *SPERE* (Nov. 1991) 421-428.
55. Liu, Y., Grigg, R.B., and Bai, B.: "Salinity, pH, and Surfactant Concentration Effects on CO_2-Foam," paper SPE 93095 presented at the 2005 SPE International Symposium on Oilfield Chemistry, Houston, Feb. 2 – 4.
56. Grigg, R.B., Bai, B., and Liu, Y.: "Competitive Adsorption of a Hybrid Surfactant System onto Five Minerals, Berea Sandstone, and Limestone," paper SPE 90612 presented at the 2004 SPE Annual Technical Conference and Exhibition, Houston, Sep. 26-29.
57. Israelachvili, J. N.: Intermolecular and Surface Forces. Harcourt Brace & Company, (1991).
58. Fones, J.B. and Adamson, A.W.: "Temperature Dependence of Contact Angle and of Interfacial Free Energies in the Aaphthalene-Water-Air System," *Journal of Physical Chemistry,* (Feb. 1968). 72 **(**2), 646-650.
59. Poston. S. W.; Ysrael, S., Hossain, A. K.M. S., Montgomery. E. F., and Ramey, H. J.: "The Effect of Temperature on Irreducible Water Saturation and Relative Permeability of Unconsolidated Sands," *SPEJ* (June 1970) 171-180.

60. Schramm, L.L., Fisher, D.B., Schurch, S., and Cameron, A.: "A Captive Drop Instrument for Surface or Interracial Tension Measurements at Elevated Temperatures and Pressures," *Colloids and Surfaces A: Physical and Engineering Aspects* 94, 145-159 (1995).
61. Wang, W. and Gupta, A.: "Investigation of the Effect of Temperature and Pressure on Wettability Using Modified Pendant Drop Method," paper SPE 30544 presented at the 1995 SPE Annual Technical Conference & Exhibition, Dallas, Oct. 22-25.
62. McCaffery, F.G.: "Measurement of Interfacial Tensions and Contact Angles at High Temperature and Pressure," *JCPT*, (July-Sept. 1972), 26-32.
63. Hjelmeland, O. S.: "Experimental Investigation of the Effects of Temperature, Pressure, and Crude Oil Composition on Interfacial Properties," paper SPE 12124 presented at the 1983 SPE Annual Technical Conference and Exhibition, San Francisco, Oct. 5-8.
64. Nikolov, A. D.et al.: "Drainage of foam films in the presence of nonionic micelles," *Progress in Colloid and Polymer Science.* 82, 87 (1990).
65. Maini, B. and Ma, V.; " Relationship Between Foam Stability Measured in Static Tests and Flow Behavior of Foams in Porous Media," paper SPE 13073 presented at the 59th Annual Technical Conference and Exhibition, Houston, Sept. 16-19 (1984).
66. Wang, G. C.: " A Laboratory study of CO_2 Foam Properties and Displacement Mechanism," paper SPE/DOE 12645 presented at the 1984 SPE/DOE Symposium on Enhanced Oil Recovery, Tulsa, April 15-18.
67. Mackay, E.J., Henderson, D.H., Tehrani, D.H., and Danesh, A.: "The Importance of Interfacial Tension on Fluid Distribution During Depressurization," paper SPE 38919 presented at the 1997 SPE Annual Technical Conference and Exhibition, San Antonio, 5-8 October.
68. Lakatos, I.; Bauer. K.; Lakatos-Szabo, J.: "Injection of Lean Gases into Light Oil Reservoirs: Interfacial Aspects," paper SPE 56605 presented at the 1999 SPE Annual Technical Conference and Exhibition, Houston, Oct. 3–6.
69. Zhang, H.R.; Bjorkvik, B.J.A.: "Measurement of Flow Properties and Interfacial Tensions for Gas Condensate," paper SPE 59774 presented at the 2000 SPE/CERI Gas Technology Symposium, Calgary, April 3-5.

70. Holt, T.; Vassenden, F.: "Effects of Pressure on Foam Stability; Implications for Foam Screening," paper SPE 35398 presented at the 1996 SPE/DOE Symposium on Improved Oil Recovery, Tulsa, April 21-24 .
71. Grigg, R.B., Tsau, J.-S., and Martin, F.D.: "Cost Reduction and Injectivity improvements for CO_2 Foam for Mobility Control," paper SPE 75178 presented at the 2002 SPE/DPE Symposium on Improved Oil Recovery, Tulsa, April 13-17.
72. Svec R.K. and Grigg, R.B.: "Physical Effects of WAG Fluids on Carbonate Core Plugs," paper SPE 71496 presented at the 2001 SPE Annual Technical Conference and Exhibition held in New Orleans, Louisiana, Sep. 30–Oct. 3.
73. Liu, Y., Grigg, R.B., and Bai, B.: "Salinity, pH, and Surfactant Concentration Effects on CO_2-Foam," paper SPE 93095 presented at the 2005 SPE International Symposium on Oilfield Chemistry, Houston, Feb. 2 – 4.
74. Liu, Y., Grigg, R. B., and Svec, R. K.: "CO_2 Behavior: Influence of Temperature, Pressure, and Concentration of Surfactant," paper SPE 94307 presented at the 2005 SPE Production and Operation Symposium, April 16-19.
75. Tsau, J.-S., Syahputra, A.E., and Grigg, R.B.: "Economic Evaluation of Surfactant Adsorption in CO_2 Foam Application," paper SPE 59365 presented at the 2000 SPE/DOE Improved Oil Recovery Symposium, Tulsa, April 3-5.
76. Bernard, G. G., Holm, L. W., and Jacobs, W. A.: "Effect of Foam on Trapped Gas Situation and on Permeability of Porous Media to Water," *SPEJ* (Dec. 1965) 295-300; *Trans.*, AIME, 234.
77. Holm, L.W.: "The Mechanism of Gas and Liquid Flow Through Porous Media in the Presence of Foam," *SPEJ*. (1968) 8(4), 359-369.
78. Friedmann, F.: "Some Parameters Influencing the Formation and Propagation of Foams in Porous Media," paper SPE 15087 presented at the SPE 1986 California Regional Meeting, Oakland, April 2–4.
79. Sanchez, J.M., Schechter, R. S.; Monsalve, A.: "The Effect of Trace Quantities of Surfactant on Nitrogen/Water Relative Permeabilities," paper SPE 15446 presented at the 1986 SPE Annual Technical Conference and Exhibition, New Orleans Oct. 5–8.
80. Huh, D.G., Handy, L. L.: "Comparison of Steady- and Unsteady-State Flow of Gas and Foaming Solution in Porous Media," *SPEJ*, (1989) 4(1), 77-84.

81. De Vries, A.S., Wit, K.: "Rheology of Gas/Water Foam in the Quality Range Relevant to Steam Foam," *SPEJ*, (1990), 5 (2), 185-192.
82. Osterloh, W.T. and Jante, M. J.: "Effects of Gas and liquid Velocity on Steady-State Foam Flow at High Temperature," paper SPE 24179 presented at the 1992 SPE/DOE Enhanced Oil Recovery Symposium, Tulsa, Oklahoma, April 22-24.
83. Alvarez, J. M., Rivas, H. J. and Rossen, W. R.: "Unified Model for Steady-State Foam Behavior at High and Low Foam Qualities," SPEJ (September 2001) 325-333.
84. Khatib, Z.I., Ekserova, D.R., and Kruglyakov, P.M.: "Influence of Film Type on Foam Stability," *Colloid J. USSR* (1981)43, 80-84.
85. Khatib, Z.I., Hirasaki, G.J., Falls, A.H.: "Effects of Capillary Pressure on Coalescence and Phase Mobilities in Foams Flowing Through Porous Media," *SPERE*, (August 1988) 919-926.
86. Grigg, R.B. and Bai, B.: "Sorption of Surfactant Used in CO_2 Flooding onto Five Minerals and Three Porous Media," SPE 93100 presented at the 2005 SPE International Symposium on Oilfield Chemistry, Houston, 2-4 February.
87. Fried, A.N: "The Foam Drive Process for Increasing the Recovery of Oil," Report RI-5866, U.S. Bureau of Mines, Washington, DC (1961).
88. Heller, J.P. and Taber, J.J: "Mobility Control for CO_2 Floods-A Literature Survey," topical report, Contract No. DE-AC21-79MC10689 U.S. DOE, Washington, DC (October 1980).
89. Heller, J.P., Lien, C.L, and Kuntamukkula, M.S.: "Foamlike Dispersions for Mobility Control in CO_2 Floods," *SPE*J (August 1985) 603; *Trans*., AIME 279.
90. Marsden, S.S et al.: "Use of Foam in Petroleum Operations," *Proc*., Seventh World Pet. Cong., Mexico City (1966); Elsevier Press, Essex, England, 3, 235-242.
91. Marsden, S.S: "Foam in Porous Media," topical report, Contract No. DE-AC03-81SF11564 (SUPRI TR-49) U.S. DOE, Washington, DC (May 1986)
92. Lee, H.O., Heller, J.P.; "Laboratory Measurements of CO_2-Foam Mobility," *SPER*E (May 1990) 193-197.
93. Hirasaki, G.J.: "The Steam-Foam Process," *JPT* (May 1989) 449.
94. Hirasaki, G.J.: "Supplement to SPE 19505, The Steam-Foam Process-Review of Steam-Foam Process Mechanisms," paper SPE 19518 available from SPE Book order Dept., Richardson, TX (1989).

95. Kate Wavrik, "Manual for Constructing PVC pipe Core-holders," PRRC 2006
96. Bai, B.: "Sorption of Surfactant and Sacrificial Agent Used in CO2 Foam Flooding," Ph.D. dissertation, New Mexico Tech, (June 2005).
97. Turns, S.R.: *Thermal-Fluid Science*, Cambridge university Press, 2006.
98. Enick, R.M., et al.: "Direct Thickeners for Carbon Dioxide," paper SPE 59325 presented at the 2000 SPE/DOE Improved Oil Recovery Symposium, Tulsa, 3-5 April.
99. Schramm L.L. Ed.: *Surfactants: Fundamentals and Applications in the Petroleum Industry*, Cambridge University Press, 2000.
100. Grigg, R.B., Tsau, J.S., and Martin, F.D.: "Cost reduction and Injectivity Improvements for CO_2 Foams for Mobility Control," paper SPE 75178 presented at the 2002 SPE/DOE Improvement Oil Recovery Symposium, Tulsa, 13-17 April.
101. Mannhardt, K.; Schramm, L.L.; Novosad, J.J.: "Colloids and Surfaces," 1992, 68, 37.
102. Schramm, L.L. Ed.: *Foams: Fundamentals and Applications in the Petroleum Industry*, American Chemistry Society, 1994, 259-316.
103. Ogden, P.H. Ed.: *Chemicals in the Oil Industry: Developments and Applications*, Special Publication 97, Royal Society of Chemistry: Cambridge, 1991, 159-173.
104. Tsau, J.S., and Grigg, R.B.: "Assessment of Foam Properties and Effectiveness in Mobility Reduction for CO_2 Foam floods", paper 37221 presented at the 1997 SPE International Symposium on Oilfield Chemistry, Houston, 18-21 February.
105. Tsau, J.S., at al.: "CO_2 Foam Flood Verification Pilot Test at EVGSAU: Phase IIIA: Surfactant Performance Characterization and Quality Assurance," paper SPE 27785 presented at the 1994 SPE/DOE Ninth Symposium on Improved Oil Recovery, Tulsa, 17-21 April.
106. Kuehne, D.L. at al.: "Evaluation of Surfactants for CO_2 Mobility in Dolomite Reservoirs," paper SPE 24177 presented at the 1992 SPE/DOE Symposium on Enhanced Oil Recovery, Tulsa, 22-24 April.
107. Tsau, J.S., Syahputra, A.E., and Grigg, R.B.: "Economic Evaluation of Surfactants Adsorption in CO_2 Foam Application," paper SPE 59365 presented at the 2000 SPE/DOE Symposium on Improved Oil Recovery, Tulsa, 3-5 April.

108. Grigg, R.B., Bai, B., and Liu,Y.: "Competitive Adsorption of a Hybrid Surfactant System onto Five Minerals, Berea Sandstone, and Limestone," paper SPE 90612 presented at the 2004 SPE Annual Technical Conference and Exhibition, Houston, 26-29 September.
109. Grigg, R.B. and Bai, B.: "Sorption of Surfactant Used in CO_2 Flooding onto Five Minerals and Three Porous Media," paper SPE 93100 presented at the 2005 SPE International Symposium on Oilfield Chemistry, Houston, 2-4 February.
110. Grigg, R.B., and Bai, B.: "Calcium Lignosulfonate Adsorption and Desorption on Berea Sandstone," *Journal of Colloid and Interface Science*, 2004, **279**, 36.
111. Somasundaram, P., Shrotri, S. and Huang, L.: "Thermodynamics of adsorption of surfactants at solid-liquid interface," 1998, **70**, 621.
112. Wei Y. et al., IFT of (Methane + Nitrogen) + Water and (Carbon Dioxide + Nitrogen) + Water System, J Chem Eng. Data, 2001, 46, 1544 - 1548
113. Schramm, L.L., Ed., F.: "Surfactants, *Fundamentals and Applications in the Petroleum Industry*; American Chemical Society, Washington, DC, 2000
114. Heller, J. P.; Martin, F.D. "Improvements of CO_2 Flood Performance," Fifth Annual Report, New Mexico Petroleum Recovery Research Center, Oct. 1 1988 – Sept. 30 1989.
115. Israelachbvili, J.N.: *Intermolecular and surface Forces.* New York, Harcourt Brace & Company (1991).
116. Bai B, "Sorption of Surfactants and Sacrificial Agent Used in CO_2 Foam Flooding," PhD Dissertation, New Mexico Institute of Mining and Technology, Socorro, NM (2005).
117. Fernandez, M., El Emary, M., Wade, W.H., Schechter, R.S., and Trogus, F.J.: "Rate Effects Attending the Flow of Surfactant Solutions through Porous Media," paper SPE 7058 presented at the 1978 SPE Fifth Symposium on Improved Oil Recovery, Tulsa, Oklahoma, April 16-19.
118. Harwell, J.H.; Scamehorn, J.F. In mixed surfactant systems; Ogino, K.; Abe, M., Eds.; Marcel Dekker: New York; pp 263-81.
119. Chang, S., Grigg, R.B., "Effects of Foam Quality and Flow Rate on CO_2 – foam Behavior at Reservoir Temperature and Pressure," paper SPE 56856 presented at the 1998 SPE/DOE Improved Oil Recovery Symposium, Tulsa, Oklahoma, April 19-22.

120. Tsau, J., Grigg, R.B., and Yaghoobi, H.: "Use of Mixed Surfactants to Improve Mobility Control in CO_2 Flooding," paper SPE 39792 presented at the 1998 SPE Permian Basin Oil & Gas Recovery Conference, Midland, Texas, March 25-27.
121. Azizian, S.: "Kinetics Models of Sorption: A Theoretical Analysis," *Journal of Colloid and Interface Science*, Vol. 276(August 2004) 47-52.
122. Dantzig, G. B.: "*Linear Programming and Extensions"*, Prentice-Hall, Englewood Cliffs, New Jersey (1961).
123. Nelder, J.A. and Mead, R.: "A simplex method for function minimization," *Computer Journal*, Vol. 7(1965) 308-313.
124. Jacoby, S.L.S., Kowalik, J.S., and Pizzo, J.T.: *"Iterative Method for Nonlinear Optimization Problems"*, Prentice-Hall Inc., Englewood Cliffs, New Jersey (1972).
125. Rogers, J.D. and Reid B. Grigg, R.B.: "A Literature Analysis of the WAG Injectivity Abnormalities in the CO_2 Process," *SPE Reservoir Eval. & Eng.*, Vol. 5, No. 5, October 2001
126. Pawar, R.J., Warpinski, N.R., Lorenz, J.C. et al. 2006. Overview of a CO_2 Sequestration Field Test in the West Pearl Queen Reservoir, New Mexico. *Environmental Geosciences* **13**(3), 163–180.
127. Benson, S.M.: "Overview of Geologic Storage of CO_2," *Carbon Dioxide Capture for Storage in Deep Geologic Formations*, Volume 2, Introduction, C.C. Thomas and S.M. Benson (Eds.), 2005 Elsevier Ltd.
128. Grigg, R.B. and Svec, R.K.: "CO_2 Transport Mechanisms in CO_2/Brine Coreflooding," paper SPE 103228 presented at the 2006 SPE Annual Technical Conference and Exhibition, San Antonio, 24–27 September 2006.
129. Wiebe R. and Gaddy, V.L.: "The Solubility for Carbon Dioxide in Water at Various Temperatures from 12 to 40°C and at Pressure to 500 Atmospheres. Critical Phenomena," *J Amer. Chem. Soc.*, Vol. 62, 815-817, (April 1940).
130. Enick, R.M.: "CO_2 Solubility in Water and Brine under Reservoir Conditions," *Chem. Eng. Comm.* (1990), Vol. 90, pp 23-33.
131. Grigg, R.B. and Svec, R.K.: "Co-Injected CO_2-Brine Interactions with Indiana Limestone," SCA2003-19, presented at the Society of Core Analysts Convention SCA 2003 Pau, France, 21-24 September 2003.

132. Wellman, T.P, Grigg, R.B., McPherson, B.J., Svec, R.K., and Lichtner, P.C.: "Evaluation of CO_2-Brine-Reservoir Rock Interaction with Laboratory Flow Tests and Reactive Transport Modeling," paper 80228 presented at the 2003 SPE International Symposium on Oilfield Chemistry, Houston, Feb. 5–8.
133. Pawar, R.J., Warpinski, M.R., Benson, R.D., Grigg, R.B., Krumhansl, J.L., and Stubbs, B.A.: "Geologic Sequestration of CO_2 in a Depleted oil Reservoir: An Overview of a Field Demonstration Project," paper SPE 90936 presented at the 2004 SPE Annual Technical Conference and Exhibition, Houston, 26-29 September 2004.
134. Pawar, R., Warpinski, N., Byrer, C, Benson, R, Grigg, R, Stubbs, B, Krumhansl, J., Lorenz, J., Svec, R., Stauffer, P., Zhang, D., and Westrich, H.: "Geologic Sequestration of CO_2 in West Pearl Queen Field: Results of a Field Demonstration Project," Third Annual Conference on Carbon Sequestration, Washington, DC, May 2004.
135. Bennion
136. Fanchi, J.R. 2001. Feasibility of monitoring CO_2 sequestration in a mature oil field using time-lapse seismic analysis. Paper SPE 66569. In *Proc. SPE/EPA/DOE Exploration and Production Envir. Conf.*, 26-28 February, San Antonio, Texas, USA.
137. Zeng, Z. 2002. *Laboratory Imaging of Hydraulic Fracturing Using Microseismicity*. PhD Dissertation, University of Oklahoma, Norman, Oklahoma, USA.
138. Zeng, Z. 2006. *Multipurpose Tri-axial Core Flooding System*. Research Report, University of North Dakota, Grand Forks, North Dakota, USA.
139. Jakupi, A. *Seismic Waveform-based Criteria for Phase Transition of CO_2 in Sample Rocks*. MS Thesis, University of North Dakota, Grand Forks, North Dakota, USA.
140. Jaeger, J.C., and N.G.W. Cook. 1979. *Fundamentals of Rock Mechanics*, Chapman and Hall, London.
141. Lama, R.D., and V.S. Vutukuri. 1978. *Handbook on Mechanical Properties of Rocks (Volume II)*, Trans Tech Publications, Clausthal, Germany.
142. Fjaer, E., R.M. Holt, P. Horsrud, A.M. Raaen, and R. Risnes. 1992. *Petroleum Related Rock Mechanics*. Amsterdam: ELSEVIER.
143. Wyllie, M.R.J., A.R. Gregory, and G.H.F. Gardner. 1958. An experimental investigation of factors affecting elastic wave velocities in porous media. *Geophysics*, 23: 459-493.

144. Biot, M.A. 1956. Theory of propagation of elastic waves in fluid saturated porous solid. I. Low frequency range and II. Higher frequency range. *J. Acoust. Soc. Am.*, 28, 168-191.
145. Mavko, G., T. Mukerji, and J. Dvorkin. 1998. *The rock physics handbook - tools for seismic analysis in porous media*. Cambridge University Press, UK.
146. Zeng, Z., R.B. Grigg, and D.B. Gupta. 2004. Laboratory investigation of stress-sensitivity of non-Darcy gas flow parameters, paper SPE 89431, *Proc. SPE/DOE 14th Symp. Improved Oil Recovery*, Tulsa, Oklahoma, USA, April 17–21.
147. Bourbie, T., O. Coussy, and B. Zinszner. 1986. *Acoustics of porous media*. Paris: Editions Technip.
148. Johnson, D.L., and T.J. Plona. 1982. Acoustic slow waves and the consolidation transition. *J. Acoust. Soc. Am.*, 72, 556-565
149. Ammer, J. R., Brumert, A. C. and Sams, W. N. 1991. Miscible Applied Simulation Techniques for Energy Recovery (Version 2.0), DOE/BC-1/2/SP, Morgantown Energy Technology Center, WV.
150. Bass, D.M., Jr. 1987. Chapter 26 Properties of reservoir Rocks, in Petroleum Engineering Handbook (Bradley et al, eds), Society of Petroleum Engineers, Richardson, Texas, USA.
151. Zeng, Z., Grigg, R.B, and Gupta, D.B., 2004. Laboratory Investigation of Stress-Sensitivity of Non-Darcy Gas Flow Parameters, SPE 89431 presented at SPE/DOE Fourteenth Symposium on Improved Oil Recovery, Tulsa, Oklahoma, USA, April 17–21.
152. Forchheimer, P. 1901, Wasserbewegung durch Boden, *Zeit. Ver. Deutsch. Ing.*, Vol. 45, 1781-1788.
153. Su, H. 2004. A Three-Phase Non-Darcy Flow Formulation in Reservoir Simulation, SPE 88536 presented at SPE Asia Pacific Oil and Gas Conference and Exhibition, 18-20 October, Perth, Australia.
154. Schlumberger, 2006. Chapter 42 Non-Darcy Flow, ECLIPSE Version 2006.1 Technical Description.
155. Li, D., Svec, R.K., Engler, T.W. and Grigg, R.B. 2001. Modeling and Simulation of The Wafer Non-Darcy Flow Experiments, SPE 68822 presented at SPE Western Regional Meeting, 26-30 March, Bakersfield, California, USA.

155a. Jones, S.C. 1987. Using the Inertial Coefficient, □, to Characterize Heterogeneity in Reservoir Rock, SPE 16949, presented at SPE Annual Technical Conference and Exhibition, 27-30 September, Dallas, Texas, USA.

156. Zeng, Z. and Grigg, R. 2006. A Criterion for Non-Darcy Flow in Porous Media. Transport in Porous Media. 63: 57-69.

157. Odeh, A.S. 1981. Comparison of Solutions to a Three-Dimensional Black-Oil Reservoir Simulation Problem, Journal of Petroleum Technology 33(1) pp13-25.

158. Jarrell, P.M., C.E. Fox, et al. (2002), *Practical Aspects of CO2 Flooding*, 1st ed., edited by R. Johns, Society of Petroleum Engineers, Richardson, Texas.

146. McLatchie, A.S., Hemstock, R.A., and Young, J.W.: "The Effective Compressibility of Reservoir Rock and Its Effects on Permeability," *JPT* (June 1958) 49.

147. Gray, D.H., Fatt, I. and Bergamini, G.: "The Effect of Stress on Permeability of Sandstone Cores," *SPEJ* (June 1963) 95-100.

148. Wyble, D.O.: "Effect of Applied Pressure on the Conductivity, Porosity and Permeability of Sandstones," *JPT* (November 1958) 57

149. Evers, J.F. and Soeiinah, E.: "Transient Tests and Long-Range Performance Predictions in Stress-Sensitive Gas Reservoirs," *JPT* (August 1977) 1025.

150. Jones, F.O. and Owens, W.W.: "A Laboratory Study of Low-Permeability Gas Sands," *JPT* (September 1980) 1631.

151. Holt, R.M.: "Permeability Reduction Induced by a Nonhydrostatic Stress Field," *SPEFE* (December 1990) 444.

152. Rhett, D.W. and Teufel, L.W.: "Effect of Reservoir Stress Path on Compressibility and Permeability of Sandstones," paper SPE 24756 presented at the 1992 SPE Annual Technical Conference and Exhibition, Washington, DC, 4-7 October.

153. Warpinski, N,R.: "Hydraulic Fracturing in Tight, Fissured Media," *J. Pet. Tech.*(Feb. 1991)146-152.

154. Schechter, D.S., McDonald, P., Sheffield, T., Baker, R.: "Reservoir Characterization and CO_2 Pilot Design in the Naturally Fractured Spraberry Trend Area," paper SPE 35469 presented at the 1996 SPE Permian Basin Oil and Gas Recovery Conference, Midland, Texas, 27-29 March.

155. Teufel, L.E. and Farrell, H.E.: "Interrelationship between In-Situ Stresses, Natural Fractures, and Reservoir Permeability Anisotropy: A Case Study of the Ekofisk Field, North Sea," *Proc.*, ISRM Conference on Fractured and Jointed Rock, Lake Tahoe (1992).
156. Lorenz, J.C.: "Stress-Sensitive Reservoirs," *J. Pet. Tech.*, (Jan. 1999) 61-63.
157. Chin, L.Y., Raghavan, R., Thomas, L.K.: "Fully Coupled Geomechanics and Fluid-Flow Analysis of Wells with Stress-Dependent Permeability," paper SPE 58968 presented at the 1998 SPE International Conference and Exhibition, Beijing, 2-6 November.
158. Bai, M., Meng, F. Roegiers, J.-C., and Green, S.: "Improved Determination of Stress-Dependent Permeability for Anisotropic Formations," paper SPE/ISRM 78188 presented at the 2002 SPE/ISRM Rock Mechanics Conference, Irving, Texas, 20-23 October.
159. Wattenbarger, R.A. and Ramey, H.J., Jr.: "Gas Well Testing With Turbulence, Damage and Wellbore Storage," *JPT* (August 1968) 877.
160. Grigg, R.B.: "Improving CO_2 Efficiency for Recovering Oil in Heterogeneous Reservoirs," annual technical progress report, DOE Contract No. DE-FG26-01BC15364, (Oct. 2003).
161. Zeng, Z. and Grigg, R. B.: "A Criterion for Non-Darcy Flow in Porous Media," *Transport in Porous Media* (2006) 63, 57-69.
162. Firoozabadi, A. and Katz, D.L.: "An Analysis of High-Velocity Gas Flow through Porous Media," *J. Pet. Tech.* (Feb. 1979).
163. Grigg, R.B. and Hwang, M.K.: "High Velocity Gas Flow Effects in Porous Gas-Water System," paper SPE 39978 presented at the 1998 SPE Gas Technology Symposium, Calgary, March 15-18.
164. Ewing, R. E., Lazarov, R.D., Lyons, S.L., Papavassiliou, D.V., Pasciak, J. and Qin, G.: "Numerical Well Model for Non-Darcy Flow through Isotropic Porous Media," *Computational Geosciences* (1999) 185-204.
165. Ramey, H.J., Jr.: "Non-Darcy Flow and Wellbore Storage Effects in Pressure Build-Up and Drawdown of Gas Wells," *JPT* (February 1965) 223.
166. Wattenbarger, R.A.: "Well Performance Equations," *Petroleum Engineering Handbook,* Bradley (ed.), Society of Petroleum Engineers, Richardson, Texas, USA(1987) Chap. 35, 1-21.
167. Vairogs, J. and Rhoades, V.W.: "Pressure Transient Tests in Formations Having Stress-Sensitive permeability," *JPT* (August 1973) 965.

168. Avila, C.E. and Evans, R.D.: "The Effect of Temperature and Overburden Pressure upon the non-Darcy Flow coefficient in Porous Media," *Proc.* 27th U.S. Symp. Rock Mech., Univ. Alabama (1985) 623-634.
169. Tiss, M. and Evans, R. D.: "Measurement and Correlation of Non-Darcy Flow Coefficient in Consolidated Porous Media," *J. Pet. Sci. Eng.* (1989) 3, 19-33.
170. Zeng, Z., Grigg, R. and Ganda, S.: "Experimental Study of Overburden and Stress on Non-Darcy Gas Flow in Dakota Sandstone," paper SPE 84069 presented at 2003 SPE Annual Technical Conference and Exhibition, Denver, Colorado, 5-8 October.
171. Bass, D.M., Jr.: "Properties of Reservoir Rocks," *Petroleum Engineering Handbook*, Bradley (ed.), Society of Petroleum Engineers, Richardson, Texas, USA(1987) Chap. 26, 1-33.
172. Wei, K.K., Morrow, N.R., and Brower, K.R.: "Effect of Fluid, Conditioning Pressure and Temperature on Absolute Permeabilities of Low-Permeability Sandstones," *SPEFE*, (August 1986) 413–423.
173. Jarrell, P.M., Fox, C.E., Stein, M. H. and Webb, S.L.: *Practical Aspects of CO_2 Flooding*, Monograph Vol. 22, Society of Petroleum Engineers, Richardson, Texas (2002).
174. Zeng, Z., Grigg, R.B, and Gupta, D.B.: "Laboratory Investigation of Stress-Sensitivity of Non-Darcy Gas Flow Parameters," paper SPE 89431 presented at 2004 SPE/DOE Fourteenth Symposium on Improved Oil Recovery, Tulsa, Oklahoma, 17–21 April.
175. Grigg, R.B, Zeng, Z. and Bethapudi, L. V.: "Comparison of Non-Darcy Flow of CO2 and N2 in a Carbonate Rock," paper SPE 89471 presented at 2004 SPE/DOE Fourteenth Symposium on Improved Oil Recovery, Tulsa, Oklahoma, 17–21 April.
176. Forchheimer, P.: "Wasserbewegung durch Boden," *Zeit. Ver. Deutsch. Ing.* (1901) 45, 1781-1788.
177. Green, L., Jr. and Duwez, P.: "Fluid Flow through Porous Metals," *J. Appl. Mech.* (March 1951) 39-45.
178. Katz, D.L. Cornell, D., Kobayashi, R. Poettman, F.H., Vary, J.A., Elenbaas, J.R. and Weinaug, C.F.: *Handbook of Natural Gas Engineering*, McGraw-Hill Book Co., Inc., New York City (1959).
179. Golubev, I.F.: *Visocity of Gases and Gas Mixtures a Handbook*, Moskva (1959), Translated from Russian by R. Kondor (1970).

180. Polakowski, N.H. and Ripling, E.J.: *Strength and Structure of Engineering Materials*, Prentice-Hall, Inc., Englewood Cliffs, New Jersey (1966) 104-113.
181. Ugural, A.C. and Fenster, S.K.: *Advanced Strength and Applied Elasticity* (Second Edition), Elsevier, New York, (1987) 55-57.Fahlman, B. D.: "Supercritical Fluid Technology: Green Chemistry for the 21st Century," *Today's Chemist at Work* (2002**)** 11(2), 81.
182. Jaeger, J.C. and Cook, N.G.W.: *Fundamentals of Rock Mechanics* (Third Edition), Chapman and Hall, London (1979)17-45.
183. McMain,, W. D. Jr.: *The Properties of Petroleum Fluids* (Second Edition), PennWell Publishing Company, Tulsa, Oklahoma (1990)46-84.
184. Metcalfe, R.S.: "Gas Properties and Correlations," *Petroleum Engineering Handbook*, Bradley (ed.), Society of Petroleum Engineers, Richardson, Texas (1987) Chap. 20, 1-18.
185. Lewis, F.N. and Randall, M,: *Thermodynamics* (Second Edition), revised by Pitzer, K.S. and Brewer, L, McGraw-Hill Book Company, New York (1961) 46-50.
186. Pawar, R.J., Warpinski, NR., Lorenz, J.C., Benson, R.D., Grigg, R.B., Stubbs, B.A., Stauffer, P.H., Krumhansl, J.L., Cooper, S.P., and Svec, R.K.: "Overview of a CO_2 Sequestration Field Test in the West Pearl Queen Reservoir, New Mexico," *Environmental Geosciences*, **V.13**, NO. 13 (September 2006), pp. 163-180.
187. Tiab, D. and Donaldson, E.C. Petrophysics: *Theory and Practice of Measuring Reservoir Rock and Fluid Transport Properties* (Second Edition). Elsevier Ltd, Amsterdam (2006) 87-202.
188. Roegiers, J-C.: "Elements of Rock Mechanics," *Reservoir Stimulation* (Second Edition), M.J. Economides and K.G. Nolte (eds.), Prentice Hall, Englewood Cliff, New Jersey, (1989) Chap. 2, 1-22.
189. Haimson, B.C.: "The Hydraulic Fracturing Method of Stress Measurement: Theory and Practice," *Comprehensive Rock Engineering, Principles, Practice and Projects (Vol 3)* Hudson (ed.) Pergamon Press Ltd. (1993) Chap. 14, 395-412.
190. Zhang, L.: *Engineering Properties of Rocks,* Elsevier Ltd., Amsterdam (2005) 17-30.

National Energy Technology Laboratory

626 Cochrans Mill Road
P.O. Box 10940
Pittsburgh, PA 15236-0940

3610 Collins Ferry Road
P.O. Box 880
Morgantown, WV 26507-0880

One West Third Street, Suite 1400
Tulsa, OK 74103-3519

1450 Queen Avenue SW
Albany, OR 97321-2198

2175 University Ave. South
Suite 201
Fairbanks, AK 99709

Visit the NETL website at:
www.netl.doe.gov

Customer Service:
1-800-553-7681